Oppervlakteversterkte Ramanspectroscopie voor intracellulaire metingen
en de detectie van protease-activiteit: van chiptechnologie tot toepassingen

Surface-Enhanced Raman Spectroscopy for Intracellular Sensing
and Protease Activity Detection: From Chip Technology to Applications

Pieter Wuytens

UNIVERSITEIT
GENT

FACULTEIT INGENIEURSWETENSCHAPPEN
EN ARCHITECTUUR

UNIVERSITEIT
GENT

Department of Information Technology

FACULTEIT
BIO-INGENIEURSWETENSCHAPPEN

Department of Molecular Biotechnology

Promotoren:
Prof. Dr. Ir. Roel Baets   Universiteit Gent - *INTEC, Photonics Research Group*
Prof. Dr. Andre Skirtach   Universiteit Gent - *Dept. of Molecular Biotechnology*

Examencommissie:

Prof. Dr. Ir. Patrick De Baets (Voorzitter)	Universiteit Gent *Dept. of Electr. Energy, Systems and Automation*
Prof. Dr. Ir. Roel Baets (Promotor)	Universiteit Gent *INTEC, Photonics Research Group*
Prof. Dr. Andre Skirtach (Promotor)	Universiteit Gent *Dept. of Molecular Biotechnology*
Prof. Dr. Ir. Liesbet Lagae	KU Leuven - *ESAT* imec - *Director Life Science Technologies*
Dr. Monica Marro Sanchéz	Institut de Ciències Fotòniques (ICFO), Barcelona *Super-resolution Light Microscopy* & *Nanoscopy*
Prof. Dr. Ir. Winnok De Vos	Universiteit Antwerpen *Lab. of Cell Biology and Histology*
Dr. Stephane Clemmen	Université Libre de Bruxelles *Lab. d'Information Quantique (OptiQ)*
Prof. Dr. Mohamed Lamkanfi	Universiteit Gent - *Dept. of Internal Medicine* VIB - *Center for Inflammation Research*
Prof. Dr. Kevin Braeckmans	Universiteit Gent - *Gener. Biochem. and Phys. Pharm., Biophotonic Imaging Group*
Prof. Dr. Ir. Nicolas Le Thomas	Universiteit Gent *INTEC, Photonics Research Group*

Voorwoord - Preface

Zes uur 's ochtends, pakweg twee jaar geleden. Herinnering aan maand noch weersomstandigheid. In de cleanroom is het twintig graden, gelig, een matig gezoem. Hier zijn geen seizoenen meer, enkel smurfen. De vochtigheidsgraad is als gewoonlijk en een lichte solventgeur gooit een waas over vele misbaksels en sporadische successen. De ochtendstond heeft goud in de mond; bij monde van Yannick de Koninck: 'De aanhouder wint!'. Al was zelfs bij deze Mechelse optimist een vleug van tanend enthousiasme te bespeuren na maandenlang tevergeefs lasers bakken. Doch valt op deze verder roemloze ochtend het meest waardevolle advies dat ik gedurende dit doctoraat opgepikt heb. Een vijftigtal celculturen, éénennegentig processing runs en honderdtweeënegentig Raman experimenten leiden tot een bescheidde aantal successen, op één hand te tellen. Volharding is onontbeerlijk om dit soort onderzoek tot een goed einde te brengen. Al ligt de dwaasheid steeds op de loer. Doctoreren is een bij wijlen eenzame stiel, en de natuurlijke habitat van een experimenteel doctorandus in de fotonica is een aan daglicht afgezonderd hok, in tijden van chips bakken afgewisseld met de hierboven beschreven stofvrije ruimte. De resultaten na een kleine vijf jaar in deze biotoop liggen hier netjes neergeschreven voor uw neus. In een vlaag van kortzichtigheid durft de gedachte opkomen dat dit, afhankelijk van hoe hoog de lat die dag ligt, ten volle te wijten is aan persoonlijk falen dan wel succes. Dit is je reinste onzin, en daar zijn drie goede redenen voor.

Vooreerst was er een niet te onderschatten *head start*. Verkregen in eerste plaats dankzij papa - 'Laat zien dat ge ne Wuytens zijt' - en mama - 'Doe wat je graag doet'. Bedankt om mij een hoop bagage en kansen te geven om tot dit moment te komen. Verder ook dankzij de kritische wetenschappelijkheid die op enthousiaste wijze gedoceerd wordt aan de ingenieursfaculteit van de Vrije Universiteit Brussel - mijn officiële Alma mater - én de zelfstandigheid, chaotische gestructureerdheid en verantwoordelijkheid, volgens het doelkrachtige kop-tegen-de-muur principe gestimuleerd door Scouts Sint Paulus Bonheiden - mijn officieuze Alma mater.

Vanuit deze startpositie sta ik op maandag 20 augustus 2012 om 8u op de gang van blok B te wachten om aan dit doctoraat te beginnen, onwetend dat de vroege vogels in de academische wereld pas twee uur later ontwaken. De eerlijkheid ge-

bied mij op te biechten dat het interdisciplinaire avontuur waarvoor ik stond te popelen in mineur aanslaat: op de *Moleculaire Biotechnologie (MoBi)* krijg ik een vergeten lokaal aan het einde van de gang, bij de *Photonics Research Group (PRG)* is er nog plaats vrij in een aan lager wal geraakt kamertje op het gelijkvloers. Een hartelijk ontvangst bieden, het blijft een werkpuntje. Doch verder niets dan goeds over deze *PRG*, een zootje ongeregeld dat er tegen wil en dank niet in slaagt om tegen 9u30 op de bureau te zijn, maar wel herhaaldelijk excellent onderzoek aflevert. Deze vrijruimte voor onderzoek en ontwikkeling in de wondere wereld van het foton wordt in de eerste plaats mogelijk gemaakt door prof. Roel Baets, een bewonderenswaardig persoon die een zeldzame combinatie van wetenschappelijke kennis en people managament ten berde brengt. Roel, bedankt voor de vrijheid en het vertrouwen, je minimalistische maar doeltreffende begeleiding en ten gepaste tijde motiverende woorden en acties. *Thanks to Ashim, Ananth, Nicolas, Haolan, Frédéric, Stephane, Ali and Nina for at moments lengthy discussion in the Raman team. Ali and Nina, this is a challenging research subject and I wish you good courage in bringing the complicated marriage of diagnostics, vibrational spectroscopy, plasmonics and integrated photonics to the next level.*
Na enkele weken promoveer ik bij *PRG* naar de eerste verdieping van het Technicum en kom ik in een uiterst gezellig bureau terecht tussen zeer straffe mannen, waaronder de eerder vermelde Yannick de Koninck en Bartje 'championsleague' Kuyken. Het blijft me een mysterie hoe het permanent bespreken van de actualiteit binnen en buiten de onderzoeksgroep kan leiden tot zulk een sterke kennis en productiviteit in het veld van respectievelijk lasers en niet-lineaire optica. Een gewoonte die bij naam van Koen en Kasper al snel opgepikt werd door een jongere, maar even straffe generatie en het heeft er alle schijn naar dat Kamiel en Isaac de traditie nog ettelijke jaren zullen verderzetten. *Luckily Utsav proved that also without participating in the hourly chitchat one can excel in academic research. I cherished hope that Lukas may honor that respectful attitude, but he seems tipping over to the chitchat side. Thank you boys for keeping the office an environment where technological, scientific and socio-economical solutions for important and trivial issues can be found.* Niet in dezelfde bureau terug te vinden, maar toch van groot belang in diezelfde categorie: Meester Raphael Van Laer - geboren voor het ongeluk maar via een optoacoustische vloedgolf tot in Stanford geraakt. Eva - combineert een aanstekelijk enthousiasme met een verfrissende professionaliteit. Daan - zet belangrijke discussies tijdens de lunch om in een kwantitatieve doch niet representatieve volksbevraging. Thijs - iemand moet de voetjes op de grond houden. Andreas - de Groot(t)e om op zijn eentje een *Photonics Valley* uit te bouwen alsook co-organisator van de betere teambuilding. Sarah - wij bakken de lekkerste lasers. Sören en Peyskens - of was het Waldorf en Statler?-, respectievelijk verantwoordelijk voor een gebrek aan cursief gedrukte eenheden in dit werk en een geestig verblijf in Chemnitz. *Ashim - a touch of crazy with hearth in the right place. Ananth - someone has to keep these guys motivated.* Liesbet - professioneel focused-ion-beam kunstenaar en cleanroompsycholoog in bijberoep. Steven - rots in de branding van processbaaien één tot zes. Ilse, Ilse en Kristien - excuses voor het vernietigen van alle nietjesmachines.

Bij *MoBi* val ik onder de vleugels van prof. Andre Skirtach in het *nano* onderzoeksteam. *Andre, thanks for giving me a first exposure to Raman and SERS microscopy at the Max Planck Institute of Colloids and Interfaces and the best of luck with further establishing your research group. Alexey and Bat-El, I strongly appreciate all the advice during my visits to Golm.* Als enig *nano*-kind word ik deels geadopteerd door drie musketiers die zichzelf na lang nadenken het acroniem *CSI (Cells Cystems and Imaging)* hebben toegewezen. Musketier 1: Winnok, professor, wielrenner en retoricus, jouw advies en enthousiasme zijn zeer belangrijk geweest in de eerste jaren van dit werk. Ik geloof dat wij goed zouden kunnen samenwerken en zal er niet rouwig om zijn als onze professionele paden zich later nog kruisen. Bij deze ook mijn excuses voor het uitstippelen van Vlaanderen's lelijkste fietsroute. Musketier 2: Tom - 'Is uit die Raman nu ooit al iets goed gekomen?' - je was een onmisbaar klankbord voor mislukte experimenten en straalt een te koesteren hartelijkheid uit. Musketier 3: Tobias, een Wevelgemse DJ volgens wie witloof objectief vies is en de klinkers van het alfabet uit drie e's, a en o bestaan. Excuses Tobias voor het opsluiten in een donker lokaaltje in Golm. Bedankt jongens. Over opsluiten gesproken, bedankt Geert om laat op de avond een door mezelf abusievelijk opgesloten dame te bevrijden uit het celcultuur-labo. Bedankt ook Fien en Sofie, luisterend oor voor het occasioneel beklag over de stand van zaken en portiers in tijden van badge-loosheid.

Bart Geers - toekomstig CEO van een groot biotechbedrijf - lag mede aan de wieg van een belangrijke heroriëntatie van dit onderzoek, en opende de deuren naar een beloftevolle samenwerking met het *Vlaams Instituut voor Biotechnologie* (VIB), met name Prof. Mo Lamkanfi, Prof. Kris Gevaert en Hans Demol. Ik ben ervan overtuigd dat er muziek zit in een verdere samenwerking, en waardeer jullie bereidheid tot interdisciplinair onderzoek ten zeerste.

Van niet te onderschatten belang zijn de vrienden en familie tegen wie ik tussen pot en pint kon mekkeren over de zin en onzin van doctoreren in het algemeen en dit werk in het bijzonder. De kans is groot dat u daar deel van uitmaakt: bedankt als luisterend oor of advocaat van de duivel. In dit werk tracht ik u duidelijk te maken dat het onderzoek waarvan ik wel eens zei dat het op niets trok toch zo slecht nog niet is.

Mijn humeur durft mee te schommelen met het succes van mijn onderzoek, en Tom heeft dit vanop de eerste rij mogen meemaken. Al is deze oscillatie met de jaren lichtjes gedempt, enkele zinnen in dit dankwoord zijn een schrale bedanking voor je geduld, begrip en liefde. Ik ben ontzettend gelukkig dat jij mijn man bent.

Nu u hier toch bent, koester ik de hoop dat u op tijd en stond verder in dit boek zal bladeren. Laat u niet afschrikken door de titel, de aanhouder wint!

Enjoy reading,

Gent, Oktober 2017
Pieter C. Wuytens

Table of Contents

List of Acronyms

AS	anti-symmetric
AB	antibody
ABP	activity based probes
Abz	2-aminobenzoic acid
AEF	analytical enhancement factor
ALD	atomic layer deposition
AMC	7-amino-4-methylcoumarin
AFC	7-amino-4-trifluoromethylcoumarin
APTES	(3-aminopropyl)triethoxysilane
CARS	coherent anti-stokes Raman scattering
CASPases	cysteine-dependent aspartate directed proteases
CCD	charge-coupled device
CMOS	complementary metal oxide semiconductor
CV	coefficient of variation
DMAB	dimercaptoazobenzene
DFT	density functional theory
DTT	dithiothreitol
e-beam	electron beam
EVA	ethyl vinyl acetate
ELISA	enzyme-linked immunosorbent assay
FIB	focused-ion beam
FS	free space
FWHM	full width at half maximum
GABA)	gamma-aminobutyric acid
HCP	hexagonally close packed
HPLC	high-performance liquid chromatography
HRP	horseradish perodixdase
HSPP	hybrid surface plasmon polarition
IPA	isopropyl alcohol
LoD	limit of detection
lpmm	lines per milimeter
LPS	lipopolysaccharide
LSPP	localized surface plasmon polarition
LSPPR	localized surface plasmon polariton resonance
LSPR	localized surface plasmon resonance
MALDI-TOF	matrix assisted laser desorption/ionisation time-of-flight

MDM	metal-dielectric-metal
MFON	metal film over nanoparticle
MMF	multimode fiber
MS	mass spectrometry
NA	numerical aperture
NIR	near infrared
NP	nanoparticle
NSL	nanosphere litography
NT	nanotriangle
PECVD	plasma-enhanced chemical vapor deposition
PEG	polyethylene glycol
PEI	polyethyleneimine
PML	phase matched layer
pNA	para-nitroaniline
pNTP	para -nitrothiophenol
PP	polypropylene
PS	polystyrene
PSPP	propagating surface plasmon polariton
Q	quality factor
QE	quantum efficiency
R6G	rhodamine 6G
RB	rhodamine B
RIE	reactive ion etch
rp-HPLC	reversed-phase high-performance liquid chromatography
S	symmetric
SA	single antenna
SAM	self-assembled monolayer
SC-1	standard clean 1
SERS	surface-enhanced Raman scattering
SM	single mode
SMEF	single molecule enhancement factor
SMF	single mode fiber
SNR	signal to noise ratio
SOI	silicon on insulator
SPP	surface plasmon polariton
SRS	stimulated Raman scattering
SSEF	SERS substrate enhancement factor
TE	transverse electric
TM	transverse magnetic
VIB	Vlaams Instituut voor Biotechnologie
WB	Western blotting
WERS	waveguide-enhanced Raman spectroscopy
WG	waveguide

SAMENVATTING

Reeds eeuwenlang werpen optische technieken licht over het mysterie van het leven. Denk bijvoorbeeld aan de ontdekking van de cel als bouwsteen van levende organismes met behulp van de eerste microscopen midden zeventiende eeuw. Sinds eind negentiende eeuw is dit in een stroomversnelling terechtgekomen. Wetenschappelijke vooruitgang leidde tot inzicht in het elektrodynamische en deeltjeskarakter van licht. Hieruit volgde een beter begrip van de interactie tussen licht en materie, en de daarmee samenhangende beschrijving van fysische fenomenen als (Raman) verstrooiing en plasmonen. Dit vooruitschrijdend wetenschappelijk inzicht zorgde in de tweede helft van de twintigste eeuw voor een ongekende technologische vooruitging. Enkele voorbeelden zijn de ontdekking van de laser en CCD beeldsensoren, alsook de ontwikkeling van fluorescente proteïnes en superresolutie-microscopie. Sindsdien is het arsenaal aan beschikbare (optische) methodes spectaculair toegenomen, en vandaag zijn optische beeldvormingstechnieken en sensoren onmisbaar in het biologisch onderzoek en de medische diagnostiek. Uit onze toenemende kennis van steeds ingewikkeldere biologische processen op steeds kleinere dimensies, blijkt in het bijzonder dat we slechts een fractie van de immense complexiteit van het leven begrijpen, en zelfs op het niveau van een enkele cel blijven veel vraagstukken onopgelost. Om hier een antwoord aan te bieden, is er een grote nood aan nieuwe diagnostische- en beeldvormingstechnieken die in staat zijn gelijktijdig verschillende parameters met een hoge gevoeligheid en selectiviteit op te volgen. Daarnaast staat de technologische vooruitgang op het gebied van nano-elektronica en nanofotonica, die in het voorbij decennium de manipulatie van licht op een nanometerschaal mogelijk gemaakt heeft. De huidige beschikbaarheid van nanotechnologie biedt ongekende opportuniteiten voor het ontwerpen van nieuwe biosensoren.

Het is dan ook een bijzonder vruchtbare tijd in de delta waar biotechnologie, nanotechnologie en fotonica samenvloeien. Deze thesis tracht in die grensoverschrijdende discipline een kleine doch belangrijke bijdrage te leveren. Dit door nieuwe methodes te ontwikkelen die gebruik maken van oppervlakte-versterkte Ramanspectroscopie voor intracellulaire metingen en de detectie van protease-activiteit. We starten dit onderzoek met de ontwikkeling van de noodzakelijke technologie voor deze toepassingen en bespreken vervolgens een aantal succesvolle metingen in proefopstellingen. Ten slotte bespreken we hoe deze technologie geminiaturiseerd kan worden op een geïntegreerde fotonische chip. Maar eerst geven we u zeer beknopte korte introductie tot Raman en versterkte Ramanspectroscopie.

Raman- en oppervlakte-versterkte Ramanspectroscopie
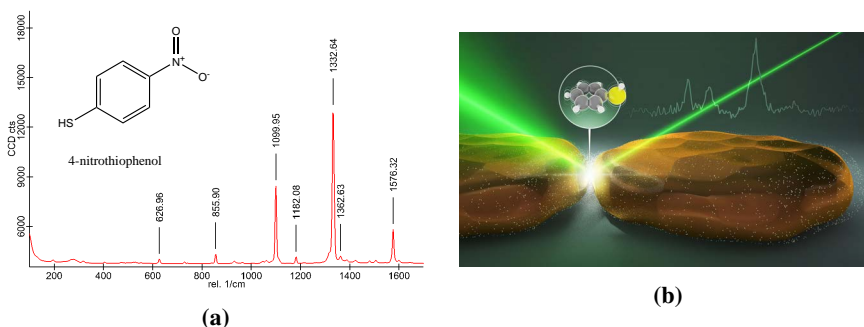
Figuur 1 (a) Raman spectrum van 4-nitrothiophenol. (b) Impressie van single-molecule detectie in een SERS hotspot. *(figuur van N. Antille/EPFL)*

Wanneer een foton met een bepaalde frequentie invalt op een molecule kan een foton met een andere frequentie verstrooid worden. Het frequentieverschil is daarbij exact gelijk aan de vibratie-frequentie van deze molecule. Dit fenomeen heet Ramanverstrooiing. Aangezien de trillingsfrequenties van een bepaalde molecule afhangen van de atomen waaruit deze bestaat en de sterkte waarmee deze atomen gebonden zijn, biedt het Raman-verstrooide spectrum een unieke optische vingerafdruk van deze molecule, zie bijvoorbeeld figuur 1a. Aangezien elke molecule een nauwbanding Ramanspectrum heeft, biedt Ramanverstrooiing ongekende mogelijkheden voor selectieve, labelvrije en spectraal veelvuldige metingen. Hiermee biedt het oplossingen voor de beperkingen van, bijvoorbeeld, fluorescente verstrooiing. Er is echter één gigantisch probleem: voor elk biljoen fotonen dat uitgezonden wordt door een fluorescent label, zal een typische molecule slechts enkele fotonen verstrooien met een vibrationele frequentieverschuiving. In complexe biologische omgevingen zal dit signaal in vele gevallen bovendien overwoekerd worden door dat afkomstig van de hele soep aan andere aanwezige molecules. Oppervlakte-versterkte Raman verstrooiing (*Surface-Enhanced Raman Scattering* of kortweg SERS) biedt een uitweg voor dit euvel. SERS maakt gebruik van de immense versterking van het elektrisch veld in de nabijheid van goud of zilver deeltjes van enkele tientallen nanometers groot. Wanneer een laserbundel met de juiste frequentie invalt op deze nanodeeltjes, drijft het inkomende elektromagnetische veld een resonante oscillatie van de vrije elektronen in het metaal die op hun beurt het elektromagnetisch veld versterken. Deze collectieve resonantie van elektronen en fotonen kan ervoor zorgen dat een molecule die niet meer dan enkele nanometers van een goud- of zilveroppervlak verwijderd is een miljard keer meer Raman fotonen verstrooit. De grootste versterking van Ramanverstrooiing vindt plaats voor moleculen die zich in openingen van enkele nanometers tussen twee nanostructuren bevinden. Deze openingen met gigantische veldversterkingen worden ook wel 'SERS hotspots' genoemd. Figuur 1b geeft een illustratie van deze situatie, waarbij het zelfs mogelijk is om het Ramansignaal van slechts één molecule te detecteren. De veldversterking in deze hotspots is echter extreem

gevoelig aan minieme geometrische variaties. Bijgevolg is het uitermate moeilijk om een SERS-substraat te maken dat een homogene, stabiele en hoge versterking biedt aan nabije moleculen. Om deze reden is het verre van vanzelfsprekend om kwantitatieve informatie te verkrijgen uit een SERS-experiment, dé limiterende factor voor het succes van deze techniek buiten het wetenschappelijk laboratorium. Nanogestructureerde SERS-oppervlakken kunnen bottom-up gemaakt worden via colloïdale goud of zilver nanodeeltjes, al dan niet geclusterd, of top-down door middel van nanolithografische technieken als elektronenbundellithografie. Bij aanvang van dit onderzoek bood geen van de beschikbare technieken een voldoende oplossing voor de te ontwikkelen toepassingen. Enerzijds zijn een uniforme versterkingsfactor en toegankelijke hotspots moeilijk te verkrijgen met behulp van geaggregeerde nanodeeltjes. Anderzijds vraagt onze technologieontwikkeling en toepassing te veel SERS substraten voor een dure en arbeidsintensieve methode als elektronenbundellithografie.

Resultaten

Toolbox 1.0: Een gouden nanodome structuur als SERS oppervlak.
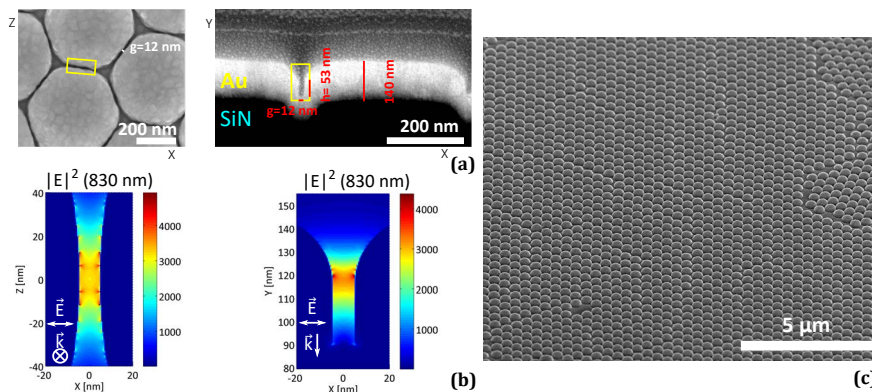
Figuur 2 (a) Elektronenmicroscopische beelden van een goudoppervlak met nanodome structuur, in bovenaanzicht en doorsnede. (b) Gesimuleerde intensiteit van het elektrisch veld in de openingen tussen twee nanokoepels. (c) Overzicht van een typisch nanodome-oppervlak.

De eerste stap in dit doctoraat bestond uit het ontwerp en de fabricage van een SERS-oppervlak dat een sterke en reproduceerbare versterking geeft in toegankelijke hotspots. Bovendien moet dit relatief eenvoudig gemaakt kunnen worden om voldoende chips te voorzien voor de hierna besproken toepassingen. Om dit te bereiken maakten we gebruik van nanosfeerlithografie, een proces waarbij een hexagonaal patroon, gevormd door zelf-geassembleerde microbeads, gebruikt wordt als masker voor een materiaal-depositie of ets-stap. Voor de fabricage van een goud oppervlak met nanodome structuur maken we eerst een monolaag van polystyreen

microbeads op een silicium wafer met diameter van 10 cm. Vervolgens etsen we dit patroon in een onderliggende silicium-nitride (SiN) laag. Na het verwijderen van de beads wordt goud gedeponeerd op de SiN structuur. Het resultaat is een periodische structuur waarbij een grote versterking van het elektromagnetisch veld optreedt in de opening tussen twee naburige nanokoepels. De exacte dimensies van deze opening kunnen op nanometerschaal gecontroleerd worden in het fabricageproces, bijgevolg kan dit SERS-oppervlak aangepast worden in functie van een specifieke toepassing. Bij extreem smalle openingen (~5 nm) werd de Raman-verstrooiing van een monolaag molecules op het goudoppervlak met een factor 10^7 versterkt, met een variatie van 7% over het volledige oppervlak. De nauwe openingen die noodzakelijk zijn voor deze maximale versterkingsfactor zijn echter moeilijk bereikbaar voor grotere biomolecules als proteïnes. Bij een beter toegankelijke opening van 10-15 nm observeren we een versterking van ongeveer 10^6. Het is belangrijk te vermelden dat deze gemeten waarden niet de hoogste zijn die in de literatuur gerapporteerd worden. Een 4 inch wafer met gouden-nanodome oppervlak biedt daarentegen wel een grote hoeveelheid chips met een homogene versterking en een chemisch en fysisch robuust oppervlak. Hierdoor is het een uiterst nuttig werktuig gebleken voor, in het bijzonder, de ontwikkeling van SERS-technologie voor het meten van protease-activiteit.

SERS microchips voor de intracellulaire detectie van vreemde molecules
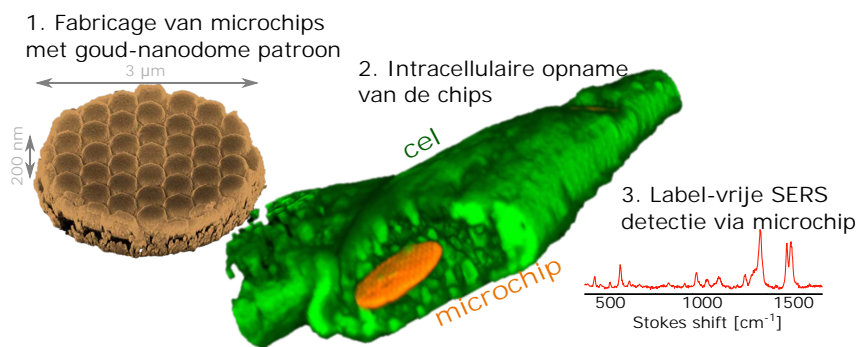
Figuur 3 Microschijfjes met een gouden-nanodome patroon als stabiel en homogeen SERS-oppervlak voor intracellulaire SERS. (links) Rasterelektronenmicropisch beeld van zulk microschrijfje. (midden) Doorsnede van cel met inwendige microchip, opname gemaakt met confocale fluorescentiemicroscopie. (rechts) SERS spectrum van rhodamine 6G gedetecteerd via de intracellulaire chip.

Door gouden nanostructuren te introduceren in levende cellen, kan belangrijke informatie verkregen verkregen worden over het organel waarin deze goudstructuur zich bevindt via SERS spectra uit zijn onmiddellijke omgeving. Belangrijke voorbeelden zijn het meten van intracellulaire parameters als pH en redoxpotentiaal met behulp van gefunctionaliseerde gouden nanodeeltjes, een labelvrije studie van

endocytotische routes en het opsporen van externe molecules. Dit laatste is bijvoorbeeld van belang om de opname van geneesmiddelen door het celmembraan te bestuderen. Om intracellulaire SERS spectra te verzamelen worden typisch gouden nanodeeltjes geïntroduceerd in de cel. Probleem hierbij is dat deze nanodeeltjes aggregeren en de gevormde clusters niet stabiel zijn. Hierdoor is de versterking van het Ramansignaal uitermate wisselvallig. Zoals reeds eerder aangehaald kunnen top-down gefabriceerde SERS-oppervlakken een meer uniforme en stabiele versterking geven. Door het uitsnijden van schijfjes met een diameter van enkele micrometers en een hoogte van honderd nanometer met daarop de gouden-nanodome structuur slaagden we erin een soort coloïdale microschijfjes te maken met een vaste nanostructuur en dus een stabiele, gekende versterkingsfactor. Na het toevoegen van de microschijfjes aan menselijke bindweefsel- of kankercellen werden deze spontaan opgenomen door de cellen. Hierbij merkten we geen overmatige invloed op de viabiliteit van de cel, noch de frequentie van de celdeling. Via deze intracellulaire SERS microchips konden we het spectrum van extern toegevoegde moleculen opmeten. In dit proof-of-concept experiment werd rhodamine 6G gebruikt, een molecule met een sterke Ramanverstrooiing die eenvoudig door celmembranen kan penetreren. Deze methode mag dan wel het probleem van een variabele versterkingsfactor oplossen, twee andere problemen bemoeilijken een kwantitatieve, labelvrije detectie van moleculen met behulp van nano- en micropartikels. Enerzijds hebben we zo goed als geen controle over het finale lot van het microschijfje in de cel. Hoogstwaarschijnlijk bevindt het zich in een fagocytotische capsule waarin het omgeven is door een dubbellaags vetmembraan. Anderzijds zorgt de adsorptie van verschillende moleculen op het goudoppervlak voor een vaak moeilijk doordringbare 'protein corona', die ook zal bijdragen tot het SERS signaal. Beide effecten verhinderen in veel gevallen een gevoelige en kwantitatieve meting van processen in het cytosol. Om deze redenen hebben we het onderzoek naar labelvrije intracellulaire SERS metingen niet verdergezet. Niettegenstaande kunnen er andere interessante toepassingen bestaan voor onze redelijk exotische, 'quasi-colloïdale', SERS microschijfjes.

SERS platform voor de detectie van protease-activiteit

Proteasen zijn enzymen die de hydrolyse van peptidebindingen katalyseren. Bijgevolg zijn proteasen van cruciaal belang voor de post-translationale modificatie van proteïnen, alsook de afbraak tot hun elementaire bouwstenen, zijnde aminozuren. Proteasen spelen ook een centrale rol in verschillende signaalroutes. Het hoeft dan ook niet te verbazen dat een gevoelige en kwantitatieve analyse van proteaseactiviteit van kritisch belang is voor onder andere medische diagnose, de ontwikkeling van geneesmiddelen en de analyse van enkelvoudige cellen. Er zijn intussen meer dan vijfhonderd verschillende genen geïdentificeerd die protease-activiteit encoderen in het menselijk genoom. Er is dan ook nood aan een selectieve methode voor het gelijktijdig observeren van de activiteit van verschillende proteasen. Ook hier is SERS een beloftevolle kandidaat: de peptides waarop proteasen actief zijn hebben een gelijkaardige grootte als de SERS hotspots en het specifieke Ramans-

pectrum biedt veel mogelijkheden tot spectrale multiplexing.

In dit doctoraat ontwikkelden we een generische methode voor het rechtstreeks meten van protease-activiteit. Hiervoor werd een monolaag met peptiden aangebracht op het goudoppervlak van de nanodome structuur. Deze peptiden bevatten een bepaalde aminozuursequentie die herkend wordt door een specifiek protease. Het actieve protease hydrolyseert een binding in deze herkenningssite, waarna de afgeknipte fractie van aminozuren wegdiffundeert uit de SERS-hotspot. Aan beide kanten van de knipplaats zorgen aromatische aminozuren voor specifieke banden in het SERS-spectrum. De verhouding van deze signalen vormt een robuuste metriek voor protease-activiteit. We toonden het principe van deze methode aan via een realtime observatie van trypsine-hydrolyse. Door het wijzigen van de herkenningssequentie kan een analoog peptide gemaakt worden dat selectief is voor een ander protease. Recente experimenten brachten ons zeer dicht bij een meervoudige meting van protease-activiteit, we verwachten hier een doorbraak in de nabije toekomst.
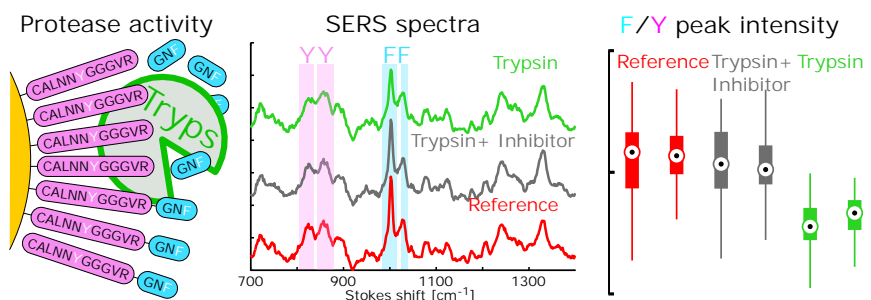
Figuur 4 Een monolaag van een specifiek peptide gebonden op een gouden-nanodome oppervlak maakt het mogelijk om protease-activiteit te meten via de verhouding in SERS-signalen van verschillende aromatische aminozuren.

Een gevoelige en meervoudige detectie van protease-activiteit is van bijzonder belang voor de analyse van inflammasoomactivatie op het niveau van enkelvoudige cellen. Het gedrag van één cel onder externe stimuli kan namelijk sterk verschillen van het gemiddelde gedrag van een populatie. In de laatste jaren werd een bijzonder sterke heterogeniteit vastgesteld in processen die gerelateerd zijn aan celdood en celgemedieerde immuniteit. Het protease caspase-1 speelt een centrale rol in deze cellulaire immuniteit. Bij het meten de activiteit van caspase-1 met onze SERS methode werden we sterk gehinderd door problemen met de goud-peptidebinding in de reducerende omgeving waarin het protease actief is. Door het ontwikkelen van een zichzelf-assemblerende monolaag peptides werd dit probleem grotendeels verholpen, maar we zijn er nog niet in geslaagd om ondubbelzinnig caspase-1 activiteit op te meten.

Toolbox 2.0: Nanofotonische golfgeleiders voor on-chip Raman en SERS

De miniaturisatie van ontelbare elektronische systemen tot nanometergrote componenten op een geïntegreerde CMOS-chip is zonder twijfel één van de groot-

ste technologische succesverhalen van de laatste decennia. Hierdoor geïnspireerd tracht geïntegreerde fotonica verschillende optische componenten samen te brengen op één chip. Silicium-fotonica, waarbij gebruikt gemaakt wordt van dezelfde materialen en technologieën als bij CMOS-elektronica, is hiervoor een uiterst geschikt platform gebleken en staat op het punt door te breken in verscheidene sectoren, gaande van telecom tot biosensing. In de laatste vijftal jaar werd een analoog platform in siliciumnitride (SiN) ontwikkeld, wat geïntegreerde fotonica bij zichtbare golflengtes mogelijk maakt. Gedurende de laatste jaren heeft ons onderzoeksteam belangrijke doorbraken verwezenlijkt waarbij Ramanspectra opgevangen worden via nanofotonische SiN golfgeleiders. Door bovendien gouden nanoantennes te integreren op deze golfgeleiders zijn we er ook in geslaagd om on-chip SERS aan te tonen. In de nabije toekomst kan het gebruik van geïntegreerde fotonica voor de miniaturisatie van SERS experimenten de mogelijkheid bieden om honderden parallelle metingen te integreren op dezelfde chip. Dit is onder meer interessant voor de analyse van enkelvoudige cellen, waarbij een zeer groot aantal verschillende cellen tegelijkertijd moet opgevolgd worden. Aangezien de huidige oplossingen voor on-chip SERS ontoereikend zijn, zowel op vlak van gevoeligheid als complexiteit van het fabricageproces, stellen we hier een vereenvoudigde methode voor om SiN waveguides te decoreren met gouden nanostructuren.
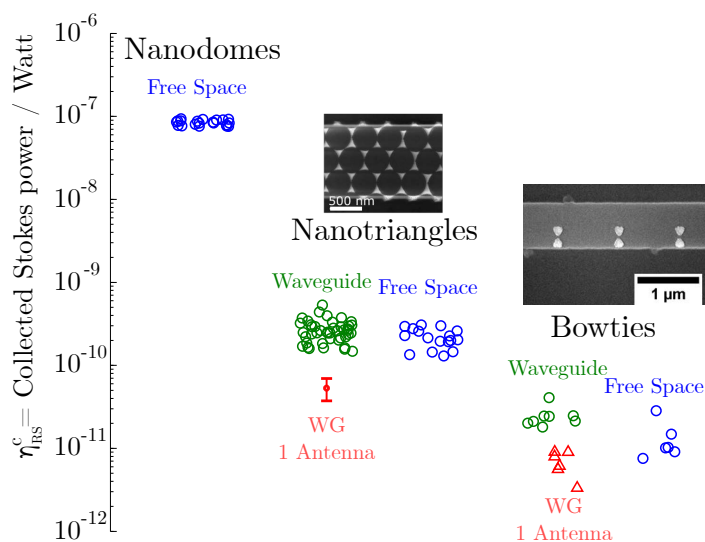
Figuur 5 Vergelijking van het opgevangen SERS-signaal afkomstig van een monolaag molecules op verschillende SERS-oppervlakken. Dit gebruik makend van een golfgeleider of microscoop.

We maken andermaal gebruik van nanosfeerlithografie, waarbij de polystyreen microbeads deze keer dienen als lift-off masker voor gouddepositie. Op deze manier verkrijgen we een patroon van gouden nanodriehoeken op de onderliggende golfgeleiders. Deze nanostructuur versterkt het Raman signaal van een monolaag molecules op het goudoppervlak met een factor 2.5×10^5. Het totale Raman-

verstrooide vermogen opgevangen door de golfgeleider is hierbij tienmaal hoger dan in de bestaande oplossingen. Dankzij deze verbeteringen slaagden we erin het Ramanspectrum van een monolaag peptides op het goudoppervlak op te vangen via de golfgeleider, een cruciale stap naar een geïntegreerde meting van protease-activiteit. Bovendien is het met deze fabricagemethode mogelijk om *deep-UV* geschreven chips te voorzien van een SERS-oppervlak, wat noodzakelijk is voor een toekomstige integratie van het volledige Raman systeem. Een verdere verbetering is mogelijk, de gevoeligheid van SERS op golfgeleiders is nog een eind verwijderd van die op de hierboven besproken nanodomes ten gevolge van een verhoogd achtergrondsignaal en een honderdmaal lagere versterkingsfactor.

Het gebruik van golfgeleiders voor het opmeten van Ramanspectra heeft nog enkele unieke eigenschappen. Het totale vermogen aan opgevangen Ramanverstrooiing is sterk verhoogd door de vergrootte interactielengte met molecules in het evanescente veld van een centimeterlange golfgeleider. Dit evanescente veld meet molecules binnen een honderd nanometer groot gebied rond de golfgeleider, wat nieuwe toepassingen mogelijk maakt voor geïntegreerde Ramanspectroscopie. Als mogelijke toepassing onderzoeken we beknopt hoe SiN golfgeleiders kunnen gebruikt worden voor de detectie van CO_2 moleculen en de identificatie van verschillende isotopen van deze molecule. Ondanks een redelijk hoge detectielimiet blijkt dat, mits het coaten van deze golfgeleiders met een absorberend polymeer of monolaag, golfgeleider-gebaseerde Ramanspectroscopie mogelijkheden biedt voor het detecteren van gasmoleculen.

Conclusies en vooruitzichten

De belangrijkste verwezenlijkingen in dit doctoraat zijn:

- Het ontwerp en de fabricage van een SERS-oppervlak met een periodische structuur van gouden nanodomes, dat fabricatiegemak combineert met een homogene en hoge versterking van het Ramansignaal en bovendien een robuust platform is dat aangepast kan worden in functie van een specifieke toepassing. Dit platform bood een cruciale technologie voor de ontwikkeling van de hier beschreven toepassingen.

- Door gebruik te maken van een microschijfje met nanodome structuur konden we voor het eerst aantonen dan het mogelijk is om SERS signalen vanuit een cel op te meten met behulp van een stabiel, top-down geschreven oppervlak. Dit biedt een alternatief voor goud nanodeeltjes en de hiermee gepaarde variabiliteit van het SERS signaal.

- We hebben een generische methode ontwikkeld voor het opmeten van protease-activiteit via een verhoudingsgewijze meting van het SERS-signaal van aromatische aminozuren. Hiermee konden we de activiteit van trypsine in real-time opvolgen.

- We hebben een aantal noodzakelijke stappen gezet om deze SERS-gebaseerde metingen in de toekomst te kunnen gebruiken voor het bestuderen van inflammasoomactivatie in enkelvoudige cellen via de activiteit van caspase-1.

- Het aanbrengen van gouden nanodriehoeken op *deep-UV* geschreven SiN golfgeleiders zorgde voor een sterk vereenvoudigde fabricage van geïntegreerde SERS golfgeleiders met een tienmaal hogere gevoeligheid.

Gebaseerd op het onderzoek in deze thesis, alsook de interactie met de verschillende betrokken onderzoekdisciplines en gemeenschappen, ben ik van mening dat er twee uitermate interessante pistes zijn voor verder onderzoek en ontwikkeling.

1. Verschillende verbeteringen kunnen aangebracht worden om de gevoeligheid van onze methode voor het meten van protease-activiteit te verhogen. Idealiter slagen we er in een gelijktijdige en kwantitatieve meting van de activiteit van meerdere proteasen bij fysiologische concentraties in een complexe buffer te verwezenlijken.

2. SERS-gebaseerde diagnostiek en celonderzoek vereist dat grote aantallen cellen of condities onderzocht worden. Sequentiële microscopische methodes zijn hiervoor te traag. Een verdere ontwikkeling van een geïntegreerde chip met parallelle golfgeleiders kan deze analyse drastisch versnellen door het gelijktijdig opmeten van SERS spectra op verschillende kanalen. Bovendien zal dit dankzij de on-chip integratie van, onder andere, filters en spectrometers mogelijk zijn op een klein oppervlak tegen een beperkte kostprijs. Dit kan tot doorbraken leiden in verscheidene toepassingen, onder meer de single-cel analyse van inflammasoomactivatie.

Dit zijn zeer ambitieuze doelstellingen die een sterk multidisciplinaire aanpak vragen. Verschillende onderzoekers in het 'Raman-on-chip' team werken aan deze uitdagingen. Ik wens hen oprecht veel inspiratie, moed, creativiteit en een niet verwaarloosbare portie geluk toe om dit te bereiken.

SUMMARY

For centuries, optical sensing and imaging has provided an indispensable tool for unraveling the secrets of life. Think for example of the first compound microscope revealing the cell as an essential building block of living organisms in the 17th century. Scientific progress in the late 19th to mid 20th century brought, amongst others, a vastly improved understanding of the electromagnetic and quantum behavior of light and a concurrent description of various light-matter interactions. Here, the foundations were laid for scientific fields like (Raman) spectroscopy and plasmonics. Forthcoming technological advances, including the nobel-prize awarded inventions of the laser and charge-coupled device image sensors, as well as the discovery of fluorescent proteins and super-resolution light microscopy techniques, have tremendously expanded and improved the methods and tools available for optical biosensing in the last decades. These advances helped to understand increasingly complex biological processes on ever reducing size-scales. To date, optical microscopy and optical biosensors are omnipresent in both fundamental research as well as medical diagnostics or drug development. The progressive insight enabled by these technologies has only presented us a glimpse of the vast complexity of life, even on a single-cell level. In parallel, advances in nano-electronic and -photonic components allow for an unprecedented control of light on the nanoscale. While there is clearly a need for sensitive and selective biosensors with the capability to simultaneously monitor multiple parameters, nanophotonic fabrication and characterization tools provide new opportunities for tackling this challenge. Needless to say, these are exciting times in field of nano- and biophotonics. It is at the crossroads of these disciplines that this thesis aims to provide a modest yet significant contribution.

More specifically, we use surface-enhanced Raman spectroscopy (SERS) for label-free intracellular sensing and a selective detection of protease activity. This thesis starts from the development and fabrication of a gold nanostructured SERS substrate, which provides a technology platform for developing the aforementioned applications. Furthermore, we take steps towards the development of an integrated photonic chip for these applications.

Raman and surface-enhanced Raman spectroscopy

Raman spectroscopy probes the vibrations of a molecule through frequency shifts in the scattered light. As every molecule has specific vibration frequencies depending on its constituting atoms and their bond strength, its Raman spectrum provides
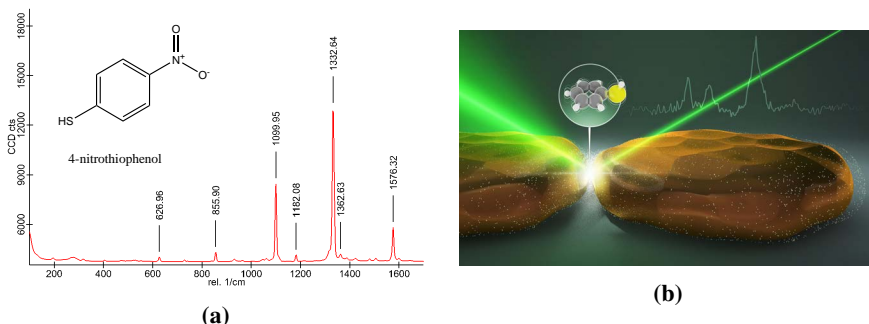
Figure 6 (a) Raman spectrum of 4-nitrothiophenol. (b) Artist impression of single molecule detection in a SERS hotspot. *(figure from N. Antille/EPFL)*

an optical fingerprint with unrivaled selectivity as shown in 6a. In contrast to fluorescence-based methods, Raman spectroscopy furthermore eliminates the need for fluorescent labels, while the narrow-banded emission spectrum enables spectrally multiplexed measurements. Unfortunately, a typical molecule emits about one Raman scattered photon for every trillion fluorescent photons emitted by an efficient fluorescent dye. In complex biological systems, the Raman scattering from the molecules of interest is not only weak, it is also overwhelmed by the contribution of a soup of different molecules. Surface-enhanced Raman scattering provides a solution to combine the specificity of a spectral fingerprint with a locally increased sensitivity. SERS is based on a resonant oscillation of incoming photons with the abundant free electrons in a noble metal. On nano-structured gold or silver surfaces, this can result in an ultra-tight confinement of the electromagnetic field. Squeezing all the energy of the field in a small volume leads to a strongly increased field intensity, which can result in a billion-fold increase of the Raman scattering from molecules located in this enhanced field, typically within a nanometer-range from the gold surface.

The strongest Raman enhancement occurs in nanometer-sized gaps and crevices in between metal nanostructures, as illustrated in figure 6b. In these so-called 'hotspots', even the Raman scattering of a single molecule can be detected. However, these strong enhancements are extremely sensitive to nanometer variations in the geometry of the nanostructure. Therefore, the fabrication of reproducible SERS-substrates with a uniform and high enhancement factor is extremely challenging, and the resulting lack of quantitative information has obstructed the acceptance of SERS as an analytical technique outside of the research lab. Nanostructured SERS substrates can be fabricated bottom-up using clusters of colloidal gold or silver nanoparticles or top-down using nanophotonic fabrication tools like electron-beam lithography. The fabrication of uniform and accessible hotspots in nanoparticle assemblies is difficult, while electron-beam lithography is an expensive and low-throughput method. At the initiation of this research neither of both provided a sufficient solution for our envisaged applications.

Results

Toolbox 1.0: Gold nanodome SERS substrates.

We developed a nanosphere-lithography based method for the fabrication of a SERS substrate with high and uniform enhancement. Briefly, a self-assembled monolayer of polystyrene nanobeads was used as an etching mask for patterning a hexagonal topography into the underlying silicon nitride layer. This structured surface was subsequently covered with gold, resulting in a periodically gold-nanodome patterned substrate. An external electromagnetic field induces a localized surface plasmon resonance in the gap between two neighboring nanodomes, resulting in a strong field enhancement. Because the fabrication process allows for an accurate control over the dimensions of this gap, the spectral location and field enhancement of the plasmonic resonance can be tuned. When designed for maximal enhancement, this SERS substrate increases the average Stokes scattering of a molecule bound to the gold surface by a factor 10^7, with a signal variation of 7% over the surface area of the chip. This maximal enhancement requires extremely narrow (~5 nm) gaps, which are poorly accessible for larger biomolecules. At a 10-15 nm wide gap, we measured an enhancement factor of 10^6. While we do not claim that our nanodome-patterned surfaces are among those with the highest enhancement factors reported in literature, they do provide a performant SERS substrate that is chemically and physically robust. These nanodome chips can be fabricated on a 4" wafer at a minimal cost and effort, thereby providing ample SERS substrate for developing single-cell and protease-sensing applications.
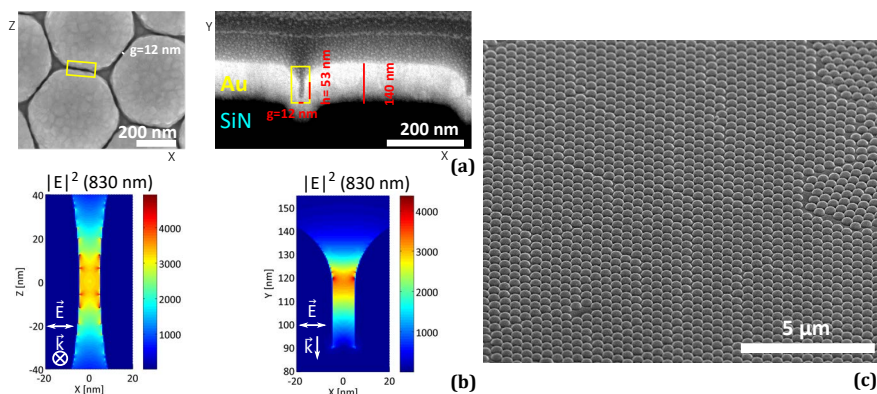
Figure 7 The nanodome SERS platform, with a strong local field enhancement in the gap between two nanodomes. (a) Scanning electron microscope close-up and focused-ion beam cross-section. (b) Simulated electric field intensity in the gap. (c) Large area SEM view of a typical nanodome-patterned surface.

Gold nanodome-patterned microchips for intracellular SERS detection of extraneous molecules

Surface-enhanced Raman spectra acquired from within a living cell can provide a valuable source of information about the organelle from where the spectra originate. For this purpose, gold nanoparticles have been introduced into the cytosol, nucleus or, most commonly, vesicles related to endocytosic pathways. However, the use of gold nanoparticles suffers from a poor reproducibility as the enhancement changes in space and time due to movement of the particles and the formation of aggregates. With the idea of enabling more quantitative intracellular SERS experiments, we cut micrometer-sized disks out of the nanodome SERS substrate and introduced them into mammalian cell lines. We observed a spontaneous intracellular uptake of these structures and found no immediate influence on cell viability or cell division. In a proof-of-concept experiment, we demonstrated that these microdisks can act as a sensor for a label-free intracellular detection of extraneous molecules. However, absorption of molecules on the SERS substrate severely complicates a label-free, quantitative sensing. Also, we have little control over the intracellular location and environment of the SERS microdisk. Upon intracellular uptake, the disk is very likely to be encapsuled by a vesicle. In this case, the surrounding bilipid membrane inhibits a sensitive sensing of processes in the cytosol. For these reasons, we did not continue research on microparticles for label-free intracellular detection, although there may be other applications for these nanostructred, 'quasi-colloidal' microdisks.
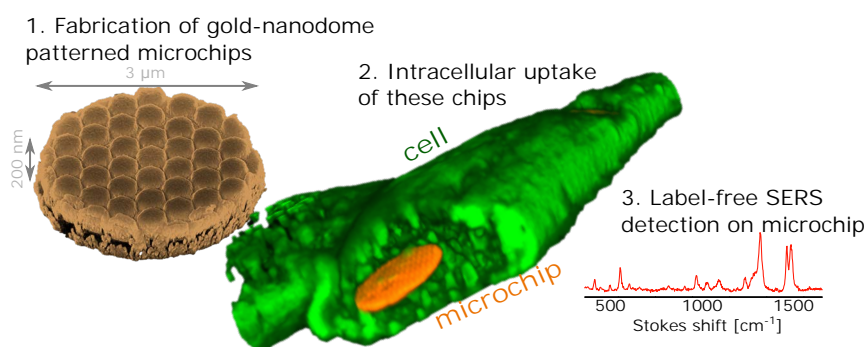
Figure 8 Gold nanodome-patterned microchips as a reproducible and uniform SERS substrate for intracellular surface-enhanced Raman spectroscopy. (left) SEM image of a 3 µm diameter gold-nanodome patterned microchip. (middle) Cross-section of a 3D rendering from a fluorescent confocal microscopy image on a cell with incorporated microchip. (right) SERS spectrum of rhodamine 6G, acquired from the intracellular microchip.

SERS platform for detecting protease activity.

Proteases, enzymes catalyzing the hydrolysis of peptide bonds, play a crucial role in the modification of proteins and their breakdown into constituent amino acids. Proteases are also of vital importance in numerous signaling pathways. A sensitive and quantitative analysis of protease activity is of critical importance for, amongst others, medical diagnostics, drug development and single cell analysis. As over 500 different genes encoding for proteases have been identified in the human genome, there is large interest in a detection technology that allows for a selective and multiplexed measurement of protease activity. SERS provides a promising candidate: peptides and plasmonic hotspots have a similar size while Raman fingerprints hold large potential for spectral multiplexing.

We propose a new method for a label-free and selective analysis of protease activity. For this purpose, we functionalized a gold nanodome surface with a short peptide containing a cleavage site for a specific protease. Aromatic amino-acids provide different contributions to the SERS spectrum on both sides of the cleavage site. Upon protease activity, the cleaved-off fraction diffuses away from the nanometer-sized hotspot and consequently its SERS signal disappears. A ratiometric measurement of SERS peaks from both sides of the cleavage site thus provides a robust metric for the protease activity. Using this method, we demonstrated a real-time detection of trypsin activity. The generic design of the experiment and peptide allows to easily incorporate a cleavage site for different proteases. Therefore, we are close to a truly multiplexed measurement of protease activity.
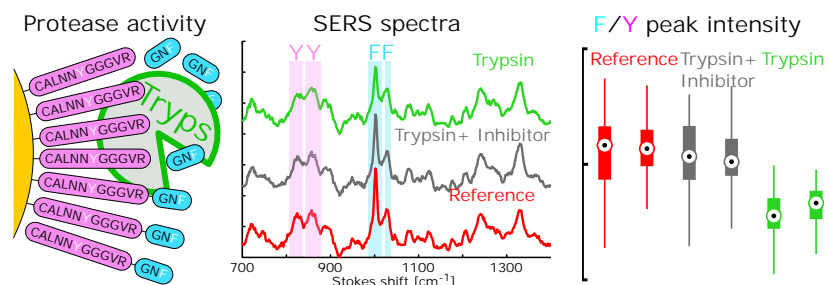
Figure 9 Proteolytic cleavage of a gold-nanodome bound substrate measured in real-time through the ratio of SERS signals from aromatic amino acids.

A sensitive and multiplexed detection of protease activity is of particular importance for monitoring inflammasome-activation on a single-cell level. In recent years, it was demonstrated how the behavior of a single cell can significantly differ from the average response of a population. A particularly high degree of heterogeneity was observed in processes related to cell death and cellular immunity. We took important steps towards using our SERS platform for monitoring activity of the inflammatory protease caspase-1, which plays a central role in cell immunity. However, we could not yet unambiguously demonstrate the detection of caspase-1 activity, largely due to problems with the gold-peptide bond in a reductive environment.

Toolbox 2.0: SiN waveguides for on-chip Raman and SERS

Inspired by the massive success of miniaturizing bulk electronics to nanometer-sized components on an integrated CMOS electronic chip, photonic integration aims to bring various free-space optical components to a single chip. In recent years, our research team has done pioneering work on the development of an integrated silicon nitride photonics platform for waveguide-excited and collected Raman spectroscopy. A hybrid integration of nanoplasmonic antennas with dielectric waveguides does not only result in miniaturized chips for surface-enhanced Raman spectroscopy, integrated photonics also offers opportunities for parallel measurements on a single chip, which will enable high-throughput SERS assays on low sampling volumes. Waveguide-excited and collected SERS is highly promising for monitoring protease activity for single-cell analysis or drug screening, as a parallel readout of multiple conditions or cells is required to speed up the analysis. However, the current state-of-the-art integrated SERS platforms are inadequate for such applications, they provide insufficient sensitivity and heavily rely on electron-beam fabrication.

We developed a nanosphere-lithography based fabrication process for patterning gold nanotriangles on deep-UV lithography fabricated silicon nitride waveguides. The resulting nanotriangles enhance the Raman scattering of gold-bound molecules by a factor 2.5×10^5. The total collected Raman scattered power is ten times higher as compared to the existing platform. This enabled the waveguide-based detection of a peptide monolayer. However, the sensitivity of SERS using nanophotonic waveguides is not yet at the level of free-space measurements on gold nanodomes, because of an increased background and a 100 times lower enhancement.
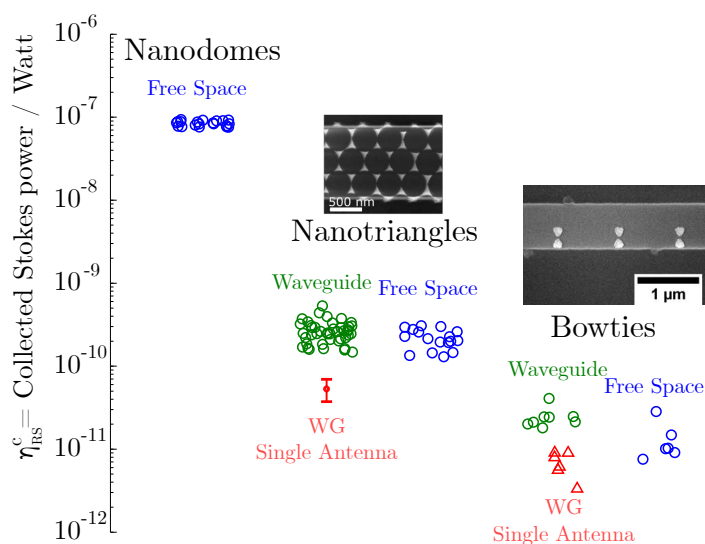
Figure 10 Collected Raman scattering from a para-nitrothiophenol monolayer on waveguides patterned with nanosphere-lithography fabricated nanotriangles compared to waveguide-excited gold bowties and free-space excited nanodomes.

We also investigated the use of SiN slot waveguides for the detection of CO_2 molecules and the identification of its different isotopes. Despite a relatively poor detection limit, we calculated that the functionalization of these waveguides with a hypersorbent polymer or CO_2 monolayer would make waveguide-enhanced Raman spectroscopy a promising platform for trace gas sensing or radioactive-labeled assays.

Conclusions and perspectives

In conclusion, the most important achievements in this work are:

- The design and fabrication of a nanodome-patterned SERS substrate that combines ease-of-fabrication, a uniform and strong enhancement and a robust gold interface. This platform is the workhorse for different applications developed in this thesis.

- A proof-of-concept demonstration of intracellular, label-free detection of extraneous molecules using a nanodome-patterned SERS microchip, thereby eliminating the variability inherent to nanoparticle-based intracellular SERS.

- The development of a generic SERS-based method for a real-time monitoring of protease activity using a ratiometric readout.

- Important progress towards a single-cell measurement of caspase-1 activity, including the design and testing of stable peptide-gold monolayers.

- The fabrication of nanotriangle-patterned SiN waveguides that increase the sensitivity of on-chip SERS and are compatible with a deep-UV lithography fabricated SiN platform.

The presented research and progressive insight acquired during this work open many routes for future research. In my view, the most promising perspectives include:

- An incremental improvement and rigorous quantification of the SERS-based platform for detecting protease activity, which will enable multiplexed measurements on physiological concentrations.

- Further advances on increasing the sensitivity of waveguide-based Raman and SERS spectroscopy, together with the on-chip integration of filters, spectrometer and detector will enable high throughput analysis of protease activity. This may lead to breakthrough applications like a single-cell analysis of inflammatory activation.

Multiple challenges have to be tackled for achieving these goals. Our Raman-on-chip research team is continuously working towards this end and I wish them much inspiration and courage, as well as a fair proportion of luck.

1

INTRODUCTION

1.1 Background and challenges

For centuries, optical sensing and imaging has provided an indispensable tool for unraveling the secrets of life. Think for example of the first compound microscope revealing the cell as an essential building block of living organisms in the 17th century. Scientific progress in the late 19th to mid 20th century brought, amongst others, a vastly improved understanding of the electromagnetic and quantum behavior of light and a concurrent description of various light-matter interactions. Here, the foundations were laid for scientific fields like (Raman) spectroscopy and plasmonics. To date, optical microscopy and sensing are omnipresent in both fundamental life-sciences research as well as medical diagnostics or drug development. The interaction of photons with biomolecules allows for local and sensitive measurements in a non-invasive manner, providing a distinct advantage over other methods, such as chemical or electrical sensing. The advent of fluorescent labels has arguably been one of the biggest driver for new technological development and forthcoming scientific discoveries in bio-imaging over the last 50 years. Thanks to the selectivity and strong intrinsic signal of fluorescent labels, dynamic intracellular processes can now be studied using confocal fluorescence microscopy at resolutions far below the diffraction limit, the expression of genes can be investigated using fluorescent proteins or the presence of enzymes can be sensitively detected using fluorescent immunoassays. These are just a few examples of the long list of technologies that presented us a glimpse of the vast complexity of life. However, fluorescent labels also come with disadvantages. A specific label is required for

each molecule, which limits the range of applications. Moreover the labels bind to the molecules of interest, hence one is looking at artificial entities. Also the toxicity of fluorescent dyes can be problematic. Furthermore, a simultaneous measurement of different molecules and processes (multiplexing) is limited because of the broad emission spectrum of fluorescent dyes. In contrast, the inelastic scattering of light by the vibration of molecules provides a highly specific molecular fingerprint. Raman spectroscopy probes these intrinsic molecular vibrations, but is limited by the extremely low number of photons that is Raman scattered. These weak Raman signals demand long acquisition times and high excitation powers. In the nanometer vicinity of metal nanostructures, an increased electromagnetic field can lead to a more than million-fold enhancement of the Raman scattering. This effect is exploited in surface-enhanced Raman scattering (SERS), a technique that allows to combine the fingerprint specificity of Raman scattering with a sensitive measurement. Despite its discovery over 40 years ago [1], a breakthrough of SERS out of the research lab is still inhibited by the variability encountered in SERS experiments. This obstructs quantitative and reproducible SERS experiments. In this thesis, we develop nanophotonic technology for improved SERS biosensing. In short, we address the following challenges:

- Can we fabricate a SERS platform with high and uniform enhancement using a low cost, scalable method?

    Impact: We developed a gold-nanodome structured surface that provided an enabling technology for the hereafter mentioned applications.

- Is it feasible to use nanophotonic microchips in living cells for in vitro quantitative, label-free sensing?

    Impact: By bringing top-down, gold-nanodome patterned SERS substrates to intracellular applications, we set a step towards time- dependent and quantitative intracellular SERS.

- Can we develop a SERS-based method as a selective and sensitive technology with multiplexing capability for a single-cell analysis of protease activity?

    Impact: We developed a generic method for protease activity sensing using gold nanodomes functionalized with substrate peptides to detect protease-activity in real-time. Important advantages of this method are the label-free measurements, the inherent control against ligand exchange and the use of a low-cost SERS platform. Further research is needed to measure the proteases excreted by individual cells.

- Does integrated photonics allow to develop a lab-on-a-chip for the latter application using waveguide-based sensing?

Impact: We improved the sensitivity of SiN-waveguide excited and collected SERS using deep-UV lithography written waveguides in combination with nanosphere-lithography patterned gold antennas. We show that a monolayer of peptides can be detected through the waveguide.

1.2   Outline

Chapter 2 introduces Raman scattering and provides a qualitative description of surface-enhanced Raman scattering, both following a classical approach. We pay special attention to the Raman scattering cross section and its correct quantification, as this is often the origin of inconsistent reports in literature. We also describe the experimental equipment required for acquiring Raman spectra, in particular applied to the confocal Raman microscope used in this work. We also touch upon different factors that complicate SERS experiments, like photochemical effects and the SERS background. At the start of this thesis, Raman spectroscopy and SERS were new topics in our research group, therefore part of this chapter is intended to help future researchers with optimizing their Raman imaging experiments.

Chapter 3 starts by introducing the field of plasmonics - the interaction of photons with metals - again from a classical electromagnetic picture. First, the frequency-dependent response of metals to an external electromagnetic field is derived. Next we describe the existence of surface-plasmon polaritons on metal-dielectric interfaces and we gradually confine this propagating wave in a three dimensional cavity to introduce the concept of a localized surface plasmon polariton resonance. Subsequently we explain how this 3D metal-air-metal cavity provides an approximate analytical solution for the resonant modes in a gold nanodome structure. The fabrication and characterization of such gold nanodome structures is described in the last two sections. We rigorously measure a SERS-substrate enhancement factor and compare analytical, simulated and experimental results based on the extinction curves and field enhancement.

Chapter 4 discusses evanescent-wave based Raman sensing. First, we investigate the use of SiN slot waveguides for gas sensing using conventional Raman scattering. Next, we describe the combination of nanosphere-lithography fabricated gold nanotriangles with deep-UV written SiN waveguides. The performance of this integrated SERS-platform is experimentally compared to both free-space sensing and existing integrated SERS platforms.

Chapter 5 introduces intracellular SERS and describes how the technology developed in chapter 3 - gold nanodome-patterned microdisks - is used for label free detection of extraneous molecules in living mammalian cells. We also investigate

the effect of these microdisks on cell viability.

In chapter 6 we introduce a SERS-based method for detecting protease activity, again using the technology platform from chapter 3. First, we briefly introduce existing methods for a direct and indirect detection of protease activity. Next, we explain the measurement principle and pay special attention to the choices made when designing a suitable peptide substrate. We investigate the expected spectral changes using rp-HPLC separated peptide fractions and demonstrate a real-time detection of trypsin activity. Subsequently, we explain current achievements and remaining issues for using this technology as a single-cell analysis tool for studying inflammasome activation. We also demonstrate the detection a peptide-monolayer using these nanotriangle-patterned waveguides described in chapter 4, a first step towards an integrated photonics platform for protease activity measurement.

Finally, in chapter 7 I give a critical analysis of the results described in this work and describe the most promising directions for future research and development.

1.3   Research context

This PhD was initiated as a first collaboration between the department of Molecular Biotechnology (UGent, prof. A. Skirtach) and the Photonics Research Group (imec-UGent, prof. R. Baets) in the framework of the center for Nano- and Bio-Photonics (NB-Photonics), with the mindset of using nanophotonic technology for improving label-free intracellular sensing. In the last two years of this work, we extended this collaboration, bringing on board the expertise of the Inflammation Research Center (VIB-UGent, prof. M Lamkanfi) and the Center for Medical Biotechnology (VIB-UGent, prof. K. Gevaert) to develop a generic SERS-based platform for detecting protease activity. Parallel to this work, we developed an integrated photonics platform at the Photonics Research Group (under the InSpectra ERC-advanced grant of prof. R. Baets). The future may bring the extremely promising combination of an integrated platform for lab-on-a-chip detection of protease activity.

1.4   List of Publications

1.4.1   Patent Applications

1. **P.C. Wuytens**, M. Lamkanfi, R. Baets and K. Gevaert, "Label free detection of protease activity", UK patent application number GB 1710401.9, filed on 29 June 2017

1.4.2 Papers published in International Journals (A1)

1. E. Lengert, M. Saveleva, A. Vsevolod, **P.C. Wuytens**,, R. Kamyshinsky, A. Vasiliev, D. Gorin, G. Sukhorukov, A. G. Skirtach, B. Parakhonskiy, "Silver alginate hydrogel micro- and nano- containers for theranostics: synthesis, encapsulation, remote release and detection", ACS Applied Materials & Interfaces, vol. 9(26), pp. 21949-21958, June 2017

2. **P.C. Wuytens**, H. Demol, N. Turk, K. Gevaert, A.G. Skirtach, M. Lamkanfi, R. Baets, "Gold Nanodome SERS platform for label-free detection of protease activity", Faraday Discussions, accepted for publication, Aug. 2017.

3. **P.C. Wuytens**, A.G. Skirtach, R. Baets, "On-Chip Surface-Enhanced Raman Spectroscopy using Nanosphere-Lithography Patterned Antennas on Silicon Nitride Waveguides", Optics Express, vol. 25(11), pp. 12926-12934, May. 2017.

4. A. Dhakal, **P.C. Wuytens**, A. Raza, N. Le Thomas, R. Baets, "Silicon Nitride Background in Nanophotonic Waveguide Enhanced Raman Spectroscopy", Materials, vol. 10(140), Feb. 2017.

5. A. Dhakal, **P.C. Wuytens**, F. Peyskens, K. Jans, N. Le Thomas, R. Baets, "Nanophotonic waveguide enhanced Raman spectroscopy of biological sub-monolayers", ACS Photonics, vol. 3(12), pp. 2141-2149, Oct. 2016.

6. A. Dhakal, F. Peyskens, S. Clemmen, A. Raza, **P.C. Wuytens**, H. Zhao, N. Le Thomas, R. Baets, "Single mode waveguide platform for spontaneous and surface-enhanced on-chip Raman spectroscopy" (invited), Interface Focus, vol. 6(4), p. 20160015, Aug. 2016.

7. **P.C. Wuytens**, A. Subramanian, W. H. De Vos, A. G Skirtach, R. Baets, "Gold nanodome-patterned microchips for intracellular surface-enhanced Raman spectroscopy", Analyst, vol. 140(24), pp. 8080-8087, Dec. 2015.

8. B.E. Pinchasik , J. Steinkuehler, **P.C. Wuytens**, A. G Skirtach, P. Fratzl, H. Mhwald, "From Beetles in Nature to the Lab: Actuating Underwater Loco-motion on Hydrophobic Surfaces", Langmuir, vol. 31(51), pp. 1373413742, Dec. 2015.

9. Subramanian, E.M.P. Ryckeboer, A. Dhakal, F. Peyskens, A. Malik, B. Kuyken, H. Zhao, S. Pathak, A. Ruocco, A. De Groote, **P.C. Wuytens**, D. Martens, F. Leo, W. Xie, U.D. Dave, M. Muneeb, Pol Van Dorpe, Joris Van Campenhout, W. Bogaerts, P. Bienstman, N. Le Thomas, D. Van Thourhout, Zeger Hens, G. Roelkens, R. Baets, "Silicon and silicon nitride photonic circuits for spectroscopic sensing on-a-chip" (invited), Photonics Research, vol. 5(3), pp. B47-49, May. 2015.

10. **P.C. Wuytens**, B. Parakhonskiy, A. Yashchenok, M. Winterhalter, A. Skirtach, "Pharmacological aspects of release from microcapsules - from polymeric multilayers to lipid membranes", Current Opinion in Pharmacology, vol. 18, pp. 129-140, Oct. 2014.

11. A. Dhakal, A. Subramanian, **P.C. Wuytens**, F. Peyskens, N. Le Thomas, R. Baets, "Evanescent excitation and collection of spontaneous Raman spectra using silicon nitride nanophotonic waveguides", Optics Letters, vol. 39(13), pp. 4025-4028, Jun. 2014.

1.4.3 Papers published in Local Magazines

1. Geers, B. Kuyken, **P.C. Wuytens**, R. Van Laer, T. Van Vaerenbergh, "Laat er licht zijn: Fotonica", Eos magazine, vol. 32(9), pp. 82-85, Dec. 2014.

1.4.4 Papers presented at International Conferences

[*] *Presenting Author*

1. **P.C. Wuytens**[*], H. Demol, N. Turk, K. Gevaert, A.G. Skirtach, M. Lamkanfi, R. Baets, "Gold Nanodome SERS platform for label-free detection of protease activity", SERS: Faraday Discussions, Glasgow, United Kingdom, Aug. 2017. *Oral Presentation*

2. **P.C. Wuytens**[*], A.G. Skirtach, R. Baets, "Nanotriangle Decorated Silicon Nitride Waveguides for Integrated Surface-Enhanced Raman Spectroscopy", CLEO: Science and Innovations, vol. STh1M(8), San Jose, United States, May. 2017. *Oral Presentation*

3. A. Raza[*], F. Peyskens, **P.C. Wuytens**, S. Clemmen, P. V. Dorpe, R. Baets, "Detection of Surface-enhanced Raman Signals from a Single Nanoplasmonic Antenna Integrated on a Single Mode Waveguide", CLEO: Science and Innovations, vol. SM4D(6), CLEO, United States, May. 2017. *Oral presentation*

4. A. Raza[*], **P.C. Wuytens**, F. Peyskens, S. Clemmen, P. V. Dorpe, R. Baets, "On-chip Enhanced Raman spectroscopy using metal slot waveguide", ECIO, vol. 19(T7.4), ECIO, Netherlands, Jan. 2017. *Oral presentation*

5. S. Clemmen[*], A. Raza, A. Dhakal, F. Peyskens, A. Subramanian, P, Van Dorpe, **P.C. Wuytens**, H. Zhao, E.M.P. Ryckeboer, S. Severi, N. Le Thomas, R. Baets, "Spectroscopic sensing with silicon nitride photonic integrated circuits" (invited), Proc. SPIE 10106, Integrated Optics: Devices, Materials, and Technologies XXI, San Francisco, United States, p. 101060T, Jan. 2017. *Oral Presentation*

6. A. Dhakal[*], **P.C. Wuytens**, F. Peyskens, A. Skirtach, N. Le Thomas, R. Baets, "Microscope-less Lab-on-a-chip Raman Spectroscopy of Cell Membranes", Photonics Conference (IPC2016), Hawai, United States, pp. 144-145, Oct. 2016. *Oral Presentation*

7. A. Dhakal[*], A. Raza, **P.C. Wuytens**, F. Peyskens, A. Skirtach, R. Baets, "Lab-on-a-chip Raman sensors outperforming Raman microscopes", CLEO, San Jose, United States, vol. SM2O.3, Jun. 2016. *Oral Presentation*

8. A. Dhakal[*], **P.C. Wuytens**, F. Peyskens, A. Subramanian, A. Skirtach, N. Le Thomas, R. Baets, "Nanophotonic Lab-On-A-Chip Raman Sensors: a Sensitivity Comparison with Confocal Raman Microscope", BioPhotonics 2015, IEEE Photonics Society, Florence, Italy, p. Th6.3, Oct. 2015. *Oral Presentation*

9. S. Clemmen[*], H. Zhao, F. Peyskens, A. Dhakal, **P.C. Wuytens**, A. Subramanian, N. Le Thomas, R. Baets, "Coherent anti-Stokes Raman spectroscopy on chip", 28th IEEE Photonics Conference (IPC 2015), IEEE Photonics Society, Reston, Virginia, United States, pp. 623-624, Oct. 2015. *Oral Presentation*

10. **P.C. Wuytens**[*], W.H. Vos, A. Skirtach, R. Baets, "Nanodome coins for intracellular surface-enhanced Raman spectroscopy", 3rd International Conference on BioPhotonics, Florence, Italy, p. paper P1.30, May. 2015. *Poster Presentation*

11. R. Baets[*], A. Subramanian, A. Dhakal, F. Peyskens, **P.C. Wuytens**, E.M.P. Ryckeboer, G. Roelkens, N. Le Thomas, "Spectroscopic sensing enabled by silicon photonics" (invited), Asia Communications and Photonics Conference (ACP), Shanghai, China, Nov. 2014. *Oral Presentation*

12. **P.C. Wuytens**[*], A. M. Yashchenok, A. Subramanian, A. G. Skirtach, R. Baets, "Micron - sized dielectric chips with gold nanostructures for intracellular label - free SERS", 19 th Annual Symposium of the IEEE Photonics Society Benelux Chapter, IEEE Photonics Benelux, Nov. 2014. *Oral Presentation*

13. R. Baets[*], A. Dhakal, F. Peyskens, **P.C. Wuytens**, A. Skirtach, N. Le Thomas, A. Subramanian, "Resonant enhancement mechanisms in lab-on-chip raman spectroscopy on a silicon nitride waveguide platform" (invited), IEEE Photonics Conference 2014 (IPC), San Diego, United States, pp. 500-501, Oct. 2014. *Oral Presentation*

14. A. Dhakal[*], **P.C. Wuytens**, F. Peyskens, A. Subramanian, N. Le Thomas, R. Baets, "Evnascent Raman spectroscopy using photonic waveguides", International Conference on Raman Spectroscopy- ICORS 2014, Jena, Germany, pp. WeA-O-006, Aug. 2014. *Oral Presentation*

15. **P.C. Wuytens**[*], A. M. Yashchenok, A. Subramanian, R. Baets, A. G. Skirtach, "Label-free monitoring of microcapsule-enabled intracellular release using gold-nanoparticle coated microchips", International Conference on Raman Spectroscopy, Jena, Germany, pp. Mop-HS4-1, Aug. 2014. *Poster Presentation*

16. **P.C. Wuytens**[*], A. M. Yashchenok, A. Subramanian, R. Baets, A.G. Skirtach, "Label-free monitoring of microcapsule-enabled intracellular release using goldnanoparticle coated microchips", Surface Enhanced Spectroscopies 2014, Chemnitz, Germany, p. 158, Aug. 2014. *Poster Presentation*

17. F. Peyskens[*], A. Subramanian, P. Neutens, A. Dhakal, **P.C. Wuytens**, P. Van Dorpe, N. Le Thomas, R. Baets, "Enhancement of Raman scattering efficiency by on-chip nanoplasmonic antennas", Surface-Enhanced Spectroscopies 2014 conference, Chemnitz, Germany, Aug. 2014. *Poster Presentation*

18. A. Dhakal[*], **P.C. Wuytens**, F. Peyskens, A. Subramanian, N. Le Thomas, R. Baets, "Silicon-nitride waveguides for on-chip Raman spectroscopy", SPIE Photonics Europe 14, SPIE, Brussels, Jun. 2014. *Oral Presentation*

19. **P.C. Wuytens**[*], A. M. Yashchenok, A. Subramanian, A. G. Skirtach, R. Baets, "Gold Nanoparticle Coated Silicon Nitride chips for Intracellular Surface-Enhanced Raman Spectroscopy", CLEO, vol. STh4H.7, San Jose, United States, Jun. 2014. *Oral Presentation*

20. A. Dhakal[*], **P.C. Wuytens**, F. Peyskens, A. Subramanian, N. Le Thomas, R. Baets, "Raman spectroscopy using photonic waveguides", IPS Benelux 2013, IEEE Photonics Society, Eindhoven, Netherlands, Nov. 2013. *Oral Presentation*

1.4.5   Presentations at Local Conferences

1. **P.C. Wuytens**, A. Raza, H. Zhao, N. Turk[*], F. Peyskens, X. Nie, A. Dhakal, E.M.P. Ryckeboer, S. Clemmen, N. Le Thomas, R. Baets, "On-chip Raman Spectroscopy", FEA Research Syposium 2017, Gent, Belgium, Feb. 2017. *Poster Presentation*

References

[1] M. Fleischmann, P. J. Hendra, and A. J. McQuillan. *Raman spectra of pyridine adsorbed at a silver electrode*. Chemical Physics Letters, 26(2):163–166, 1974.

2

INTRODUCTION TO RAMAN AND SURFACE-ENHANCED RAMAN SPECTROSCOPY

By probing the vibrational frequencies of molecules, Raman spectroscopy acquires a unique spectral fingerprint without the need for external labels. But only a tiny fraction of incident photons are Raman scattered. To overcome these extremely weak Raman signals, surface-enhanced Raman spectroscopy (SERS) uses the field enhancement on metal nanostructures to achieve a more than millionfold enhancement of the Raman scattering. As such, it enables sensitive measurements, while retaining the unrivaled selectivity of Raman scattering. In this chapter we explain the basic concepts behind Raman scattering following a classical approach. We pay special attention to the Raman scattering cross section and its correct quantification. We also describe the experimental equipment required for acquiring Raman spectra, in particular applied to our own confocal Raman microscope. Next, we give a qualitative introduction to Surface-enhanced Raman Scattering and touch upon a number of factors that complicate SERS experiments, such as photochemical effects and the SERS background. We finish with a short, critical discussion of SERS and its applications.

2.1   Introduction to Raman spectroscopy

2.1.1   Light-matter interaction in a two-atom molecule

All scattering processes are the results of an interaction of light with atoms. A correct description of Raman scattering thus requires quantum theory to derive the energy levels of these atoms and molecules, illustrated for a two-atom molecule in figure 2.2. Next, the interaction of photons on these energy states should be calculated from an interaction Hamiltonian. Fortunately, a classical theory of light-matter interaction describes Raman scattering and SERS on a sufficient level to understand this thesis. First, we will describe the vibrational modes of the most simple, diatomic molecule as a harmonic oscillator. Next, we explain the generation of Stokes and anti-Stokes Raman scattering under an incident electromagnetic wave on this molecule. This more educational approach is largely based on [1] and [2].
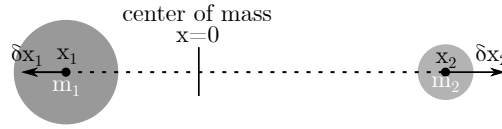
Figure 2.1 An elementary molecule consisting of two bound atoms.

A two-atom molecule   Consider the most elementary molecule, consisting of two bound atoms with mass m_1 and m_2 as shown in figure 2.1. We will approximate the molecular bond as if this were two atoms on a spring with spring constant K. We take the center of mass as origin and place the atoms on the X-axis at positions x_1 and x_2. Under an external force, these atoms are respectively displaced over a distance δ_1 and δ_2, but the center of mass is conserved:

$$\delta_1 = \frac{m_2}{m_1}\delta_2 \tag{2.1}$$

We assume that the restoring force F_s of the bond is linear with the dislocation of the molecules. This is correct for limited dislocations of the atoms. This approximation is not always valid, for example in silicon the first overtone of the $520\,\mathrm{cm}^{-1}$ band is observed at $941\,\mathrm{cm}^{-1}$ (figure A.15). From (2.1), we can write $F_s = -K(\delta_1 + \delta_2)$ as:

$$F_s = -K\frac{m_1 + m_2}{m_2}\delta_1 = -K\frac{m_1 + m_2}{m_1}\delta_2 \tag{2.2}$$

From Newton's second law we get the equation of a harmonic oscillator:

$$\frac{m_1 m_2}{m_1 + m_2}\left(\frac{\mathrm{d}^2\delta_1}{\mathrm{d}t^2} + \frac{\mathrm{d}^2\delta_2}{\mathrm{d}t^2}\right) = -K(\delta_1 + \delta_2) \tag{2.3}$$

$$\mu\frac{d^2 q}{dt^2} = -Kq \tag{2.4}$$
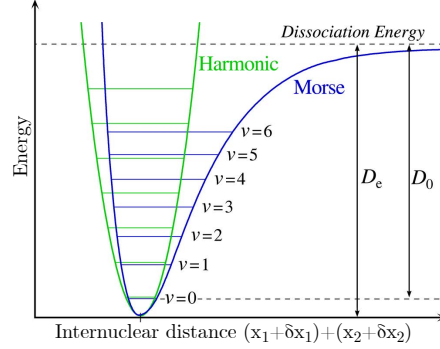
Figure 2.2 Harmonic oscillator potential well with equally spaced vibrational modes (green) and the Morse potential (blue), a better approximation of the real molecule. *(figure adapted from en.wikipedia.org/wiki/Morse_potential)*

Here, we introduced the reduced mass $\mu = \frac{m_1 m_2}{m_1 + m_2}$ and displacement $q = \delta_1 + \delta_2$. The solutions of this equation is an harmonic oscillation with angular frequency $\omega_s = 2\pi\nu_s$:

$$q = q_0(e^{i\omega_s t} + e^{-i\omega_s t}) \tag{2.5}$$

The fundamental vibrational frequency of this oscillation ν_s is given by:

$$\nu_s = \frac{1}{2\pi}\sqrt{\frac{K}{\mu}} \tag{2.6}$$

The potential energy V for this harmonic oscillation forms a parabolic well:

$$V = \frac{1}{2}Kq^2 \tag{2.7}$$

Figure 2.2 compares the vibrational modes of the diatomic molecule in this classical harmonic oscillator potential well to that in a Mores potential well, calculated from a quatum-mechanical interaction model.

A two-atom molecule under an external electromagnetic field   Now consider an electromagnetic wave oscillating with angular frequency ω_0

$$\vec{E} = \vec{E_0}e^{i\omega_0 t} + \vec{E_0}e^{-i\omega_0 t} \tag{2.8}$$

This electromagnetic wave will drive the oscillation of dipoles in the molecule, inducing a dipole moment $\vec{p}$.

$$\vec{p} = \bar{\bar{\alpha}}\vec{E} \tag{2.9}$$

Here, $\bar{\bar{\alpha}}$ is the polarizability tensor. This is a material- and frequency-dependent parameter, which can have nonlinear components. In this work we focus on linear scattering processes, which is valid for modest field strengths. We also assumed

that the polarization depends linearly on the electric field. In nonlinear scattering processes such as stimulated Raman scattering (SRS) and coherent anti-Stokes Raman scattering (CARS), it is necessary to consider higher (third) order components. For an electric field parallel to a diatomic molecule with a zero depolarization ratio (see equation (2.23)), we can further simplify the vector to a scalar polarizability α. The polarizability is the sum of a static contribution determined by the molecule at equilibrium position α_0 and a component depending on the displacement q:

$$\alpha = \alpha_0 + \frac{\mathrm{d}\alpha}{\mathrm{d}q}q + ... \tag{2.10}$$

Inserting (2.10) and (2.5) in (2.9) gives:

$$\vec{p} = \alpha_0 \vec{E}_0 e^{-i\omega_0 t} + \frac{\mathrm{d}\alpha}{\mathrm{d}q}q\vec{E}_0 e^{-i(\omega_0-\omega_s)t} + \frac{\mathrm{d}\alpha}{\mathrm{d}q}q\vec{E}_0 e^{-i(\omega_0+\omega_s)t} + c.c. \tag{2.11}$$

We thus find three frequency components for the induced dipole moment:

$$\vec{p} = \vec{p}^{\,r}_{(\omega_0)} + \vec{p}^{\,s}_{(\omega_0-\omega_s)} + \vec{p}^{\,as}_{(\omega_0+\omega_s)} \tag{2.12}$$

The first term represents the dipole oscillating at the frequency of the incident wave ω_0, which will re-radiate light at the same frequency. This elastic scattering process is called Rayleigh scattering. This is the dominant scattering process responsible for the propagation and scattering of light in media. The second and third term give rise to inelastic scattering. Light is radiated at a frequency shifted by the vibrational frequency of the molecule. The scattering with a lower energy $\omega_0-\omega_s$ is called Stokes scattering, that at the higher frequency $\omega_0+\omega_s$ anti-Stokes scattering.

Raman selection rules   We can extend (2.11) to more complex molecules with multiple vibrational frequencies ω_j:

$$\vec{p} = \alpha_0 \vec{E}_0 e^{-i\omega_0 t} + \vec{E}_0 \sum_j \Big[\frac{\mathrm{d}\alpha}{\mathrm{d}q_j} q_j e^{-i(\omega_0-\omega_s)t} + \frac{\mathrm{d}\alpha}{\mathrm{d}q_j} q_j e^{-i(\omega_0+\omega_s)t} \Big] + c.c. \tag{2.13}$$

The total power radiated P_{rad} by a dipole $\vec{p}$ in a medium with refractive index n_m can be derived from Maxwell's equations [2]:

$$P_{rad} = \frac{(\omega_0 + \omega_s)^4 n_m \sqrt{L_m}}{12\pi\epsilon_0 c^3}|\vec{p}|^2 \tag{2.14}$$

Here, L_M is a local field correction factor relating the microscopic field felt by the molecules to the macroscopic electromagnetic field:

$$\sqrt{L_M} = \Big[\frac{\epsilon_m + 2}{3}\Big]^2 \tag{2.15}$$
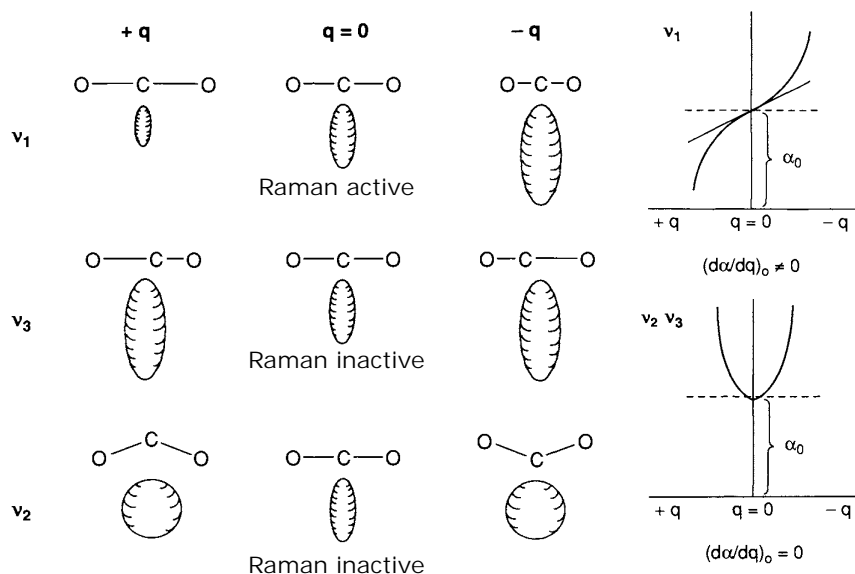
Figure 2.3 Changes in polarizability during the vibration of a CO_2 molecule. The symmetric vibration ν_1 ($1340\,\text{cm}^{-1}$) is Raman active, while the asymmetric vibrations ν_2 ($667\,\text{cm}^{-1}$) and ν_3 ($2350\,\text{cm}^{-1}$) are Raman inactive. *(figure adapted form [1])*

Thus, the radiated power is proportional to ω^4 and increases when the dipole is in a larger refractive index environment. From (2.13), we find that only photons will be emitted for those vibrational frequencies ω_j were $\mathrm{d}\alpha/\mathrm{d}p_j \neq 0$. This means that the induced displacement of the atoms around their equilibrium position must change the polarizability of the molecule to make the mode 'Raman active'. On the other hand, one can derive that a mode will be 'IR-active' if vibration changes the dipole moment of the molecule. For example, consider the three-atom molecule CO_2 in figure 2.3, which has three vibrational modes. The polarizability tensor $\bar{\bar{\alpha}}$ is here represented by a polarizability ellipsoid with axis lengths $\alpha_{xx}^{-1}, \alpha_{yy}^{-1}, \alpha_{zz}^{-1}$. These are proportional to the inverse size of the electron clouds along these axes. Linear molecules are typically more polarizable along the axis of the bond. For ν_1, the extremes of the displacement $-q$ and $+q$ lead to a different polarizability, thus this mode is Raman active. For the other two cases ν_2 and ν_3, the extremes of q give an equal polarizability. This reasoning becomes less trivial for more complicated molecules, for more details we refer to [1]. In this work, it is sufficient to remember that not all vibrations are Raman active. The activity of a specific mode depends on its symmetry, and a change in the environment can influence the activity of a mode. For example, different Raman modes can become (in)active when a free molecule gets bound to a surface. As we will explain later, this is often the case in SERS.
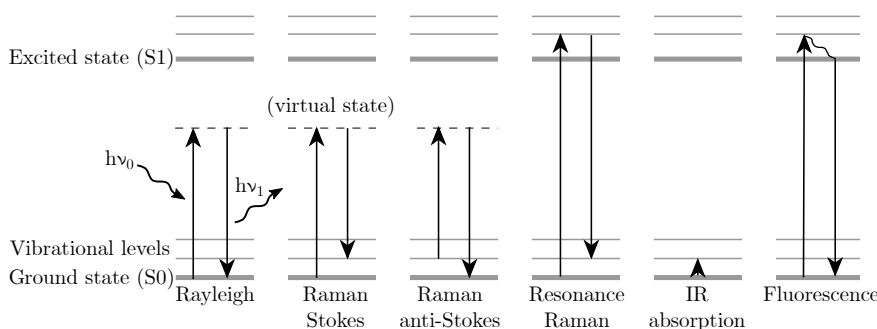
Figure 2.4 Simplified Jablonski diagram of different linear scattering or absorption processes occurring upon the interaction of a photon with a molecule. Note that the 'virtual' energy level does not really exist, the electron immediately falls back to the ground state.

2.1.2   Linear scattering processes

It is instructive to look at different scattering processes with respect to the energy levels of the molecule in a simplified Jablonski diagram (figure 2.4). For an intuitive reasoning, we introduce a 'virtual' state to which the electron is excited when an incoming photon $h\nu_0$ is annihilated. Note that this virtual state is purely introduced for an instructive reasoning, no such thing exists physically.

Rayleigh Scattering   The electron can fall back to the original state, thereby emitting a Rayleigh scattered photon with the same frequency.

Stokes and anti-Stokes Raman scattering   The electron can also fall back to a higher or lower energy vibrational mode of the ground state, emitting respectively a Stokes or anti-Stokes scattered photon. The ratio between Stokes and anti-Stokes scattered power is determined by the Maxwell-Boltzmann factor:

$$\frac{P_{aS}}{P_S} = \frac{(\omega_0 + \omega_s)^4}{(\omega_0 - \omega_s)^4} \cdot e^{-\frac{\hbar\omega_s}{k_B T}} \tag{2.16}$$

Here k_b is the Boltzmann constant, $\hbar$ the reduced Planck constant and ω_s the angular frequency of the molecular vibration. At room temperature, Stokes scattering is much stronger than anti-Stokes scattering. For example, the anti-Stokes scattering will be approximately 400 times weaker than the Stokes scattering for the 1003 cm^{-1} Raman band of phenylalanine excited with a 785 nm pump laser. At higher temperatures, molecules vibrate stronger and the higher vibrational energy levels are more populated. Thus the amount of anti-Stokes scattering, which takes energy away from the vibration, will increase. In this work, we exclusively measured Stokes scattering because it is the dominant component of an already weak scattering process. Anti-Stokes scattering is more of interest when fluorescent back-

ground is an issue. Because fluorescent processes exclusively scatter photons with lower energies, the anti-Stokes spectrum is completely free of any fluorescence.

Fluorescence and absorption   If the energy of the incoming photon is equal or greater than that of an electron transition, the photon can be absorbed and excite an electron to a vibrational mode of the excited state (S1). The electron can either completely decay non-radiatively through heat or re-emit part of its energy as a redshifted photon. The latter process is called fluorescence, which is the result of a two-step decay. First, part of the absorbed energy is non-radiatively dissipated in the molecule. Hereby the electron decays to the lowest energy excited state (S1). Next, the electron falls back to the ground state, a spontaneous emission process whereby a photon with lower energy is re-emitted, resulting in a redshifted Stokes scattering. In contrast to Raman and Rayleigh scattering, the presence of a real energy level here results in a finite time of a few nanoseconds between electron excitation and fluorescence emission. The number of fluorescent emitted photons per excited electron is called the fluorescence quantum yield, which can be up to 0.9 for dyes such as rhodamine 6G (R6G) or as low as 5×10^{-5} for crystal violet (CV).

In contrast to Raman scattering, fluorescence occurs only at specific wavelengths in specific molecules. Therefore fluorescent labels are usually conjugated to detect the molecule of interest. An important reason for the widespread success of fluorescence in (bio)imaging application is the large scattering cross section of these labels: their fluorescent scattering is 10^{10-14} times stronger than the normal Raman scattering of a comparable molecule. Another major driver for this success is the existence of fluorescent proteins like GFP (green fluorescent protein, 2008 Nobel Price in Chemistry), which can be genetically encoded. In this thesis, fluorescence and absorption spectroscopy are used as routine tools in multiple experiments. For example, we used confocal fluorescence microscopy for visualizing cell membranes (chapter 5), fluorescent and absorption spectroscopy for monitoring peptide cleavage in (chapter 6) and UV-absorption for quantifying the peptide concentration in liquid chromatography fractions (chapter 6).

Resonance Raman scattering   If the energy of the pump photons exciting a Raman mode is close to that of electron transition, the Raman scattering efficiency can increase by several orders of magnitude. This usually comes at the cost of an increased fluorescence background, limiting the signal to noise in resonant Raman spectroscopy. For example, dyes like R6G give rise to resonant Raman bands when excited around 530 nm, but at this wavelength the fluorescence emission will still be about 10^8 times stronger than the resonant Raman scattering. In combination with SERS, the fluorescent background can be quenched if the molecule is in the nanometer proximity of a Ag or Au nanostructure. The scattering cross section in surface-enhanced resonance Raman scattering (SERRS) can be as high as that of a fluorescent molecule. Note that a pre-resonant effect can extend to redshifted wavelengths. For example, the Raman scattering of R6G is still increased at 633

nm [3].

Infrared absorption   When the frequency of an incoming photon equals a vibration frequency ν_s of the molecule, it can be absorbed, thereby exciting an electron to a higher vibrational state. This frequency dependent process provides a spectroscopic technique that is complimentary to Raman spectroscopy. It can be shown that vibrations resulting in a changed dipole moment are IR active. For example, modes ν_2 and ν_3 in figure 2.3 are IR active, while mode ν_1 is IR inactive. As vibrational frequencies ν_s are typically in the 5-100 THz range, IR spectroscopy requires sources and detectors in the mid-IR region at wavelengths of 3-50 µm. Important advantages of IR over Raman spectroscopy are the larger scattering cross section and the increased spectral resolving power of different vibrational and rotational modes. Disadvantages include the strong absorption of water in the mid-IR region and the lower spatial resolution when using longer wavelengths. From a cost perspective, sources and detectors in the mid-IR region are more expensive, but the larger scattering cross section relaxes the system requirements.

Rather than referring to the vibrational frequency, a specific Raman mode is typically expressed in terms of a relative inverse wavelength shift with units [cm^{-1}]:

$$\delta\nu_s = \frac{1}{\lambda_0} - \frac{1}{\lambda_R} \tag{2.17}$$

Here, λ_0 is the excitation wavelength and λ_R the Stokes scattered wavelength. The resulting $\delta\nu_s$[1] is independent of the excitation wavelength, simplifying a comparison of Raman and IR spectra acquired at different wavelengths. Generally, organic molecules have their most prominent Raman bands in the 600-1800 cm^{-1} and 2600-2900 cm^{-1} region. The 600-3000 cm^{-1} wavelength region roughly corresponds to:

- A vibrational frequency ν_s of 20-100 THz.
- IR absorption wavelengths of $2.5 - 15\,\mu$m.
- Stokes scattered wavelengths λ_R of 820-1020 nm for a 785 nm pump.

2.1.3   Raman scattering cross section

Definition   The scattering cross section σ [m^2] of a molecule is defined as the total scattered power P_s^t it generates for a given irradiance I. As shown in figure 2.5a, σ represents the equivalent area that a particular molecule would absorb and convert to scattered photons if illuminated by a beam with uniform irradiance.

$$P_S^t = \sigma I \tag{2.18}$$

Unless integrating spheres are used, most configurations only capture a small fraction of the scattered light. Furthermore, the radiation pattern of the oscillating

---

[1]For simplified notation, $\delta\nu_s$ is often written as ν
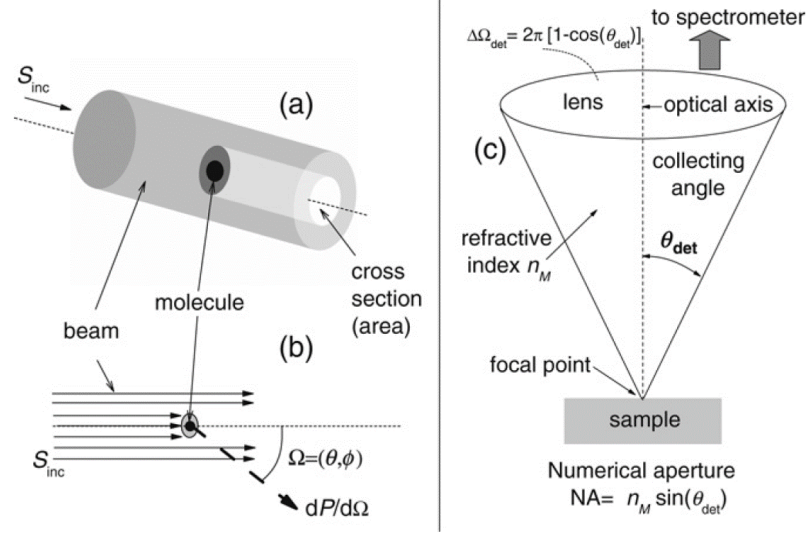
Figure 2.5 (a) The Raman cross section σ of a molecule equals the equivalent area that gives rise to the total Raman scattered power in a beam with uniform irradiance. (b) The Raman scattering is orientation dependent. (c) Solid angle of collection of a lens. *(figure from [2])*

dipoles is not uniform and depends on the direct environment and the orientation of the molecule with respect to the polarization of the incoming light. Therefore it is more correct and practical to use a differential scattering cross section $d\sigma/d\Omega$ [$cm^2 sr^{-1}$]:

$$P_s^c = \int_{\delta\Omega} \frac{d\sigma(\Omega)}{d\Omega} d\Omega \cdot I \qquad (2.19)$$

Here P_s^c is the collected Stokes scattered power through an optical system with solid angle $\delta\Omega$. The solid collection angle $\delta\Omega$ can be calculated from the numerical aperture (NA) of the lens (figure 2.5b):

$$NA = n_M \sin(\theta_{det}) \qquad (2.20)$$

$$d\Omega = 2\pi(1 - \cos(\theta_{det})) \qquad (2.21)$$

$$d\Omega = 2\pi[1 - \cos\left(\sin^{-1}(\frac{NA}{n_M})\right)] \qquad (2.22)$$

Table 2.1 lists $\delta\Omega$ for the different objectives used in this thesis. In the best case, 28% of the maximum solid angle is captured. In many bulk measurements, the molecules will have an average orientation. However, the emission profile is still not uniform because of the polarization of the pump light. As a consequence, the collected scattered power P_s^c does not necessarily scale linearly with $\delta\Omega$.

The absolute and differential Raman cross section are linked via the Raman depolarization ratio ρ_r, which is the ratio of the Raman scattered power with a polarization perpendicular to the incident polarization ($P_s^\perp$) over that parallel to the incident polarization ($P_s^\parallel$), measured in a forward, backward or 90° scattering configuration:

$$\rho_r = \frac{\mathrm{d}P_s^\perp/\mathrm{d}\Omega}{\mathrm{d}P_s^\parallel/\mathrm{d}\Omega} \tag{2.23}$$

$$\sigma = \frac{8\pi}{3}\frac{1+2\rho_r}{1+\rho_r}\frac{\mathrm{d}\sigma}{\mathrm{d}\Omega} \tag{2.24}$$

One can show that the depolarization ratio always has a value between 0 and 3/4 [2]. If for a particular vibrational mode all the Raman scattered power is polarized parallel to the incident polarization, $\rho_r = 0$ and $\sigma = \frac{8\pi}{3}\frac{\mathrm{d}\sigma}{\mathrm{d}\Omega}$. This is the case if the Raman tensor is isotropic.

Table 2.1: Solid angle, fraction of the maximum solid angle (4π) and matched pinhole diameter (PH) for optimal axial resolution for the objectives used in this work.

Objective	N.A.	n_d	$\delta\Omega$	$\frac{\delta\Omega}{4\pi}$	PH
Nikon CFI Plan Fluor 10x $\infty/0.16$	0.3	1	0.29	2.3%	21 μm
Zeiss W N-Achroplan/W 20x $\infty/0$	0.5	1.33	0.46	3.7%	25 μm
Nikon PlanFluor 20x $\infty/0.16$	0.5	1	0.84	6.7%	25 μm
Nikon S Plan Fluor 40x ELWD $\infty/0 - 2.0$	0.6	1	1.26	10%	42 μm
Zeiss EC Epiplan Neofluar 100x $\infty/0$	0.9	1	3.54	28%	69 μm
Zeiss W Plan-Apochromat 63x $\infty/0$	1	1.33	2.14	17%	39 μm

Determining cross sections The absolute differential scattering cross section is defined as the backscattered power per solid angle for an orientation averaged molecule. Unfortunately, little data is available on the absolute differential Raman cross section of molecules excited with a 785 nm pump, and the available data is spread out over different publications. Often, the distinction between the absolute cross section σ and absolute differential cross-section $\mathrm{d}\sigma/d\Omega$ is not made, or values are erroneously extrapolated from far blueshifted wavelengths using the λ^{-4} rule. The best characterized differential Raman cross section is that of N_2, but gases are an impractical reference. We believe the values mentioned in table 2.3 for benzene and methanol are reliable, the latter being less toxic. The unknown Raman cross section of the other molecules was measured relative to that of methanol under identical acquisition settings:

$$\left(\frac{\mathrm{d}\sigma}{\mathrm{d}\Omega}\right)_? = \left(\frac{\mathrm{d}\sigma}{\mathrm{d}\Omega}\right)_{mOH} \times \frac{I_? * c_{mOH}}{I_{mOH} * c_?} \tag{2.25}$$

Table 2.2 lists the absolute differential Raman cross section for molecules used in this thesis and a few other frequently used molecules in the field of Raman and SERS. At 785 nm, the differential Raman cross section is typically within a

range of 10^{-32} to 10^{-28}. Table 2.3 compares the absolute Raman cross section to the typical (larger) cross sections observed in other scattering or absorption mechanisms. Important to remember here is that fluorescence cross sections are a factor 10^{12-14} stronger than 785 nm pumped Raman cross sections of comparable molecules.

Direct measurement of the absolute Raman cross sections It is an interesting exercise to directly measure the Raman cross section of para-nitrothiophenol (pNTP) dissolved in ethanol, a molecule used throughout this work for characterizing the performance of a SERS substrate. This measurement also allows to verify the measured Raman cross sections of pNTP and ethanol relative to the literature values of methanol and ethanol in table 2.2. It furthermore provides a good insight in the actual strength of Raman signals and the losses of the microscope. In order to determine the absolute Raman cross section of pNTP, we prepare a 50 mM solution of this molecule in ethanol. The Raman spectrum of this solution is acquired through an objective with a numerical aperture of 0.3, corresponding to a solid angle $\delta\Omega$ of 0.29 sr (table 2.1). For a pump laser with a power P_0 of 100 mW on the sample and a 785 nm wavelength, we calculate the photon flux F_{ph} for the 1339 cm^{-1} vibration ($\nu_s = 342$ THz) of pNTP from the number of counts in this Raman band on the CCD camera (I_{1339}) multiplied with the overall conversion rate of the spectrometer ζ. This conversion rate equals the product of the transmission of the spectrometer, the quantum efficiency of the camera and its analog to digital conversion factor. We measured a ζ of 5.2 at a wavelength of 785 nm. Taking the difference in QE at the Stokes scattered wavelength into account (figure 2.9b), we find a ζ of 5.9 ± 0.2 photons/count at 870 nm. The collected photon flux for the 1339 cm^{-1} peak of 50 mM pNTP solution becomes:

$$F_{ph}^c = I_{1339}\zeta = 3.8 \cdot 10^5 \text{ photons.s}^{-1} \tag{2.26}$$

The total Stokes scattered power P_s^t is calculated from the photon flux, the transmission of the objective ($T_o = 0.76$) and microscope ($T_m = 0.8 \pm 0.1$) at the Stokes scattered wavelength and the fraction of light collected in the solid angle of the objective (2.3%):

$$P_s^t = F_{ph}h(\nu_0 - \nu_s)\frac{4\pi}{\delta\Omega}n^2 T_m^{-1} = 11.1 \text{ pW} \tag{2.27}$$

Here, $h(\nu_0 - \nu_s)$ is the energy of the Stokes scattered photons and $n = 1.335$ is the refractive index of the ethanol solution. We have made the assumption that the radiation has a uniform profile. This is not necessarily true and for a correct determination we should measure the depolarization ratio of the Raman mode. Our current setup does not allow for this, which results in an additional error up to a factor 1.5 on the final cross section.

The conversion factor η_{rs} from the 100 mW pump to Stokes power becomes:

$$\eta_{RS} = \frac{P_s^c}{P_0} = 1.1 \cdot 10^{-10} \tag{2.28}$$

Table 2.2: <u>Absolute differential</u> **Raman cross sections for different molecules excited with a 785 nm pump laser. See appendix A for the corresponding molecular structure and Raman spectra. Cross sections marked with '∗' are based on own measurements, either relative to the literature value of methanol as in equation** (2.25) **or an absolute direct measurement. The cross-sections of the Raman bands in rhodamine 6G and the CFGVR-pNA/YVADGFC peptides (used in chapter 6) are less reliable, respectively because of autofluorescence and low sample concentration.**

Molecule	$\delta\nu_{\mathbf{s}}[\mathbf{cm^{-1}}]$	$\frac{\mathrm{d}\sigma}{\mathrm{d}\mathbf{\Omega}}[\mathbf{cm^2sr^{-1}}]$	Reference
		Gases	
N_2	2331	$5.9 \cdot 10^{-32}$	[2] ν^4 from 633
CO_2	1285	$4.1 \cdot 10^{-32}$	[4] ν^4 from 633, rel. to N_2
	1388	$6.5 \cdot 10^{-32}$	[4] ν^4 from 633, rel. to N_2
		Liquids	
Methanol	1030	$2.1 \cdot 10^{-31}$	[2] ν^4 from 633 nm
		$2.2 \cdot 10^{-31}$	∗ Abs. meas.
Ethanol	882	$3.3 \cdot 10^{-31}$	[5] ν^4 from 532 nm
		$3.2 \cdot 10^{-31}$	∗ Abs. meas.
Isopropanol	819	$7.9 \cdot 10^{-31}$	[6] ν^4 from 488 nm
		$5.8 \cdot 10^{-31}$	∗ Abs. meas.
Chloroform	667	$1.2 \cdot 10^{-30}$	[7] ν^4 from 514
Benzene	992	$2.4 \cdot 10^{-30}$	[8] Abs. meas.
DMSO	668	$3.1 \cdot 10^{-30}$	∗ Abs. meas.
		Aromatic molecules in solution	
Benzenethiol	1584	$7 \cdot 10^{-31}$	[8] Abs. meas.
pNTP	1339	$1.83 \cdot 10^{-29}$	∗ Rel. meas. in eOH
		$1.87 \cdot 10^{-29}$	∗ Abs. meas.
pNA	1316	$6.9 \cdot 10^{-29}$	∗ Rel. meas.
Rhodamine 6G	1366	$1.5 \cdot 10^{-28}$	∗ Rel. meas. in eOH
	1510	$2.1 \cdot 10^{-28}$	∗ Rel. meas in eOH
		Aromatics in peptides in solution	
CGFVR-**pNA**	1597	$3.6 \cdot 10^{-30}$	∗ Rel. meas. in DMSO
	1342	$1.4 \cdot 10^{-29}$	∗ Rel. meas. in DMSO
CGFVR-pNA	1003	$9.6 \cdot 10^{-31}$	∗ Rel. meas. in DMSO
YVADGFC	847	$6.4 \cdot 10^{-31}$	∗ Rel. meas. in DMSO
YVADG**F**C	1207	$3.0 \cdot 10^{-31}$	∗ Rel. meas. in DMSO

Table 2.3: Exemplary <u>absolute</u> cross sections of different scattering and absorption processes

Molecule	Scattering Process	λ_0[nm]	σ[cm^2]	Reference
R6G	Absorption	514	$2.5 \cdot 10^{-16}$	[2]
R6G	Fluorescence	514	$2 \cdot 10^{-16}$	[2]
R6G	Resonance Raman	532	$2 \cdot 10^{-24}$	[3]
R6G	Raman	785	$2 \cdot 10^{-27}$	measured

We find that 1.10×10^{-10} times the incident power is converted into Raman scattered photons by a molecule density ρ of 3.01×10^{25} molecules $\cdot$ m^{-3} over an effective length H_{eff} (see equation (3.53) on 3-36) of 150 μm when using 200 μm diameter pinhole. Note that these calculations are only valid if the pinhole diameter is much larger than the projected focal spot of the laser, characterized by the parameter v_p (figure 2.7a) [9]. The absolute and differential Raman cross sections of a single molecule of pNTP equal:

$$\sigma = \frac{\eta_{RS}}{H_{eff} \cdot \rho} = 2.4 \cdot 10^{-28} \, \text{cm}^2 \tag{2.29}$$

$$\frac{\mathrm{d}\sigma}{\mathrm{d}\Omega} = 1.9 \cdot 10^{-29} \, \text{cm}^2\text{sr}^{-1} \tag{2.30}$$

We measured an identical cross section for a 10 mM solution with a 20 mW laser power to verify that there is no photobleaching, quenching, absorption or limited dissolution that would reduce the measured cross section. We make the same calculation for the $882 \, \text{cm}^{-1}$ peak from the ethanol (eOH) in which the pNTP is dissolved, again with an excitation power of 100 mW. The concentration of ethanol in a pure ethanol solution is 17.5 M, or 1.03×10^{28} molecules.m^{-3}:

$$F_{ph}^{eOH} = 2.16 \cdot 10^6 \, \text{photons.s}^{-1} \tag{2.31}$$

$$P_s^{eOH} = 62.0 \, \text{pW} \tag{2.32}$$

$$\eta_{RS}^{eOH} = 6.02 \cdot 10^{-10} \tag{2.33}$$

$$\sigma_{eOH} = \frac{4.94 \cdot 10^{-10}}{150 \, \mu\text{m} \times 1.03 \cdot 10^{28} \, \text{molecules.m}^{-3}} = 4.01 \cdot 10^{-30} \text{cm}^2 \tag{2.34}$$

$$\frac{\mathrm{d}\sigma_{eOH}}{\mathrm{d}\Omega} = 3.19 \cdot 10^{-31} \, \text{cm}^2\text{sr}^{-1} \tag{2.35}$$

Similar calculations were made for methanol and isopropanol. We measured a differential Raman cross section of 2.2×10^{-31} for the $1030 \, \text{cm}^{-1}$ mode of ethanol, which is in excellent agreement with the 2.1×10^{-31} cross section in [2]. The latter was extrapolated to 785 nm from 633 nm according to the ν^4 law, which is reliable for small molecules and small wavelength shifts. From these absolute measurements, we believe the cross sections mentioned in table 2.2 are reliable.

Qualitative estimation of Raman cross section From (2.13), we know that the Raman cross section of a particular vibrational mode is large if there is a strong

change in polarizability under an applied electric field. Density functional theory (DFT) can be used to calculate the electronic structure of a molecule, from which the vibrational modes and corresponding Raman cross sections can be derived [2]. Qualitatively, the following guidelines based on the amount and mobility of electrons, provide an indication about the magnitude of the absolute cross-section σ [1, 7]:

- As all scattering processes, σ scales with λ^{-4}. For example, exciting Raman modes at 532 nm is about five times more efficient than at 785 nm. For small molecules such as N_2, this dependence can be used to extrapolate the Raman cross section to other wavelengths. However, for more complex molecules this is not generally true and one should be careful with extrapolating Raman cross sections characterized at shorter wavelengths to the near-infrared, especially when resonance effects are at play.

- Liquids typically have a 2-4 times higher σ than gases because of their higher refractive index. Molecules in a liquid experience an increased microscopic field and a stronger dipole radiation.

- Resonant effects, occurring when the pump energy is close to that of an electron transition, can result in a huge Raman cross section.

- Molecules with only single bonds and small atoms such as *C-H*, *C-O*, or *C-C* typically have a small σ.

- Small molecules without electron-rich atoms, such as N_2 and H_2, have a small σ.

- Molecules with larger atoms (e.g. S, I) typically have a larger σ.

- Molecules with electron-rich atoms have a larger σ, for example $C - CL_4$ stretches.

- Molecules with extended π systems have delocalized electrons which are easily polarized, resulting in a large σ. A well-known example of this is the benzene ring. Multiple conjugated extended π systems further increase the Raman cross-section. For example, the Raman cross section of anthracene, consisting of three fused benzene rings, is even 20 times higher than that of benzene.

- Multiple bond stretches generally have a larger σ. For example, the relative intensity of the *C≡C, C=C and C-C* stretches is roughly 3:2:1. A very large cross-sections can be found for multiple bond stretches conjugated with an extended π system.

We will briefly discuss this from lowest to highest σ for the most important molecules used in this thesis, all excited at 785 nm. The Raman spectra and chemical structure of these molecules are given in appendix A, and some of the absolute differential cross sections were calculated in table 2.3. The symmetric *O=C=O* stretching mode of CO_2 molecules (measured in chapter 4.2.2) has a small cross section

because the molecules in the gas phase and consist of small atoms. The CO stretching mode in liquid isopropanol, used as a reference molecule for quantifying waveguide-enhanced Raman [6], has a larger σ. Other alcohols like ethanol and methanol have a comparable σ to that of isopropanol, as do small amino acids such as glycine. The extended π systems in the aromatic amino acids phenylalanine, tyrosine and tryptophan (chapter 6) give rise to ring breathing modes with further increased σ. An even larger σ is found in the symmetric O-N=O stretch of para-nitrothiophenol (pNTP, used for quantifying SERS enhancement in chapter 3), a multiple bond stretch bound to a benzene ring. Multiple conjugations to the ring can further increase σ [10]. A comparable cross-section is found for rhodamine 6G, containing multiple aromatic groups. This molecule would be the cross-section champion at shorter wavelengths, with resonant effects occurring when exciting with a 500-633 nm pump, resulting in a $\mathrm{d}\sigma/\mathrm{d}\Omega$ of $10^{-24}\,\mathrm{cm}^2\mathrm{sr}^{-1}$ at 532 nm [3].

Note that a large Raman cross section often comes with a strong chemical activity of the molecule. As a consequence, many strong Raman scatterers are toxic molecules and should be handled with care.

2.2 Confocal Raman Microscopy

Although Sir Chandrasekhara Raman may have used nothing more than sunlight and a set of colored filters to measure inelastic scattering of organic vapors [11], technological developments in the last decades have tremendously increased the sensitivity and spectral resolution with which Raman spectra can be acquired. In the most elementary Raman setup, a laser is incident on the sample and scattering of this sample is collected under a 90 or 180 °angle. The collected light passes through a notch filter, removing the Rayleigh scattered photons and is sent to spectrometer. Many alternatives to this basic principle exist, such as fiber-based excitation and collection or FT-Raman. In this thesis, all experiments are done using a commercial confocal Raman microscope (WITec Alpha300 R+). A Raman microscope is very similar to a conventional laser-scanning confocal fluorescence microscope, except for the fact that the collected light is directed to a spectrometer instead of the typical photomultiplier tube. Also, the 10^{12-14} times lower scattering cross section as compared to fluorescence poses a number of different requirements on the different components. Figure 2.6 schematically shows the optical path of the microscope used in this work, we will step by step discuss the different components and motivate some the choices made in our experiments. We will also describe the particulars of our Raman microscope, necessary to find optimal acquisition settings and intended as a guide for future researchers.

Laser   The most important characteristic of the pump source for exciting Raman spectra is its **wavelength**. Raman shifts are independent of the excitation wavelength, but the intensity of the acquired spectrum is strongly wavelength dependent. Scattering processes scale with λ^{-4} (2.14), which favors shorter excitation
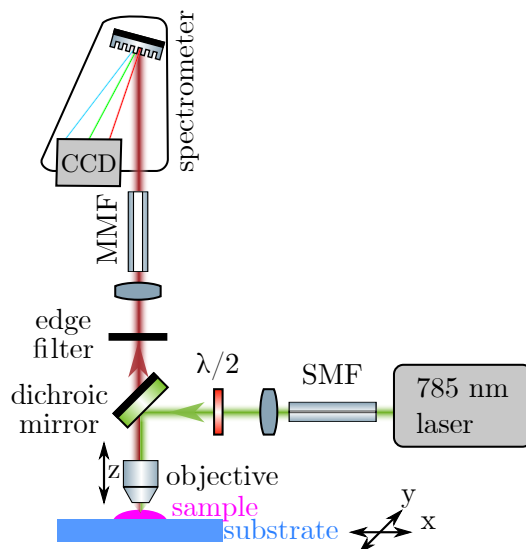
Figure 2.6 Schematic of the WITec Alpha 300 R+ upright confocal Raman microscope, using a multi-mode fiber as pinhole and entrance facet to the spectrometer.

wavelengths. But there are more arguments to be considered for the choice of a wavelength region:

Ultraviolet - Visible excitation (250-650 nm):

+ Highest Raman cross section because of λ^{-4} dependence.

+ Resonance Raman spectra for many biological molecules at UV wavelengths.

+ Excellent chromatically corrected objectives available at visible wavelengths.

+ High spatial resolution in confocal microscopy.

- Strong fluorescent background signal.

- Damage to biological specimen.

Near-Infrared (650-800 nm):

+ Strongly reduced fluorescent background.

+ Limited absorption in cells and tissue in this 'near-infrared' therapeutic window [12].

+ Ideal for SERS on gold nanostructures because of optimal Q-factor of localized surface plasmon polariton resonances (see figure 3.2 on page 3-7).

- Reduced Raman cross section.

- Lower quantum efficiency of Si detectors (figure 2.9b) at larger wavelength shifts. For example, at a 785 nm excitation the $2950\,\mathrm{cm}^{-1}$ CH_3 stretch will emit photons at 1022 nm with an energy of 1.21 eV, close to the 1.1 eV bandgap of Si.

Typical Raman bands of organic molecules have a linewidth larger than $5\,\mathrm{cm}^{-1}$ or $150\,\mathrm{GHz}$. For many applications, it is sufficient to sample these Raman bands

with a spectral resolution of $\approx 1\,\mathrm{cm}^{-1}$. To avoid **linewidth** broadening or peak shifts due to laser instability, the laser linewidth and **frequency drift** should typically be below $10\,\mathrm{GHz}$. For specific applications such as the characterization of crystalline materials, a $< 1\,\mathrm{GHz}$ stability can be necessary, but no such experiments are done in this thesis. Because of the weak nature of Raman scattering, the signal is often increased by using high laser powers. In normal Raman spectroscopy at NIR wavelengths, a **laser power** of a few 100 mW is often used. In SERS experiments, the combination of high power densities with the local field enhancement and absorption of the gold will excessively heat and destroy most molecules. Typically, $< 1\,\mathrm{mW}$ powers are sufficient for acquiring SERS spectra. In our microscope, we use a Toptica XTRA II 785 nm pump laser with a $< 10\,\mathrm{MHz}$ linewidth and $<< 30\,\mathrm{GHz}$ frequency drift. This laser is fiber coupled to a single mode fiber (SMF), with a maximum output power of 200 mW through the fiber. At the entrance of the microscope, a lens collimates the output beam of the fiber and a half-wave plate allows to rotate the linear polarization of the light.

Objective   The choice of an objective follows similar arguments as in confocal fluorescence. The **numerical aperture** determines the size of the focal spot, and the combination of pinhole and **magnification** of the objective will influence the confocality of the measurement. Because of the longer acquisition times, Raman images are usually not acquired at the same spatial resolution as a fluorescence image. Therefore, one can tolerate slightly larger optical aberrations. However, **chromatic aberrations** are often problematic for high resolution or quantitative Raman imaging in the near-infrared. Apochromats are typically corrected for equal focal points across visible wavelengths, but the focal length may drift strongly above 800 nm. This can easily be noticed from a change in the overall shape of the Raman signal when adjusting the focus on a planar sample (e.g. a SERS substrate). Furthermore the **transmission** of objectives designed for visible applications often decreases above 800 nm. For these reasons, special near-IR objectives are often preferred. Because all materials have some Raman background, Raman spectra are often acquired in an upright setup where there is no cover slip in between the sample and objective. Thus, **zero-coverslip** corrected objectives are preferable. Table 2.1 lists the objectives used in this work.

Pinhole and spectrometer entrance slit   After passing through a dichroic mirror and edge or notch filter removing the Rayleigh scattered light, the Stokes scattered light is collected by a confocal pinhole. The rejection of light scattered outside of the focal plane is crucial in Raman microscopy. If there would be no confocality, all materials in the optical path would contribute to the Raman background signal. With respect to lateral and axial resolution, the functioning of the pinhole is exactly the same as in a confocal fluorescence microscope. For an objective with magnification M and numerical aperture NA, the optimal diameter of the pinhole can be calculated for optimal axial ($v_p \leq 2.5$) or lateral ($v_p \leq 0.5$) resolution [13]:

$$\frac{M}{NA} \geq \frac{\pi d_0}{v_p \lambda} \tag{2.36}$$

Table 2.1 lists the optimal pinhole radii at optimal axial resolution for the ob-
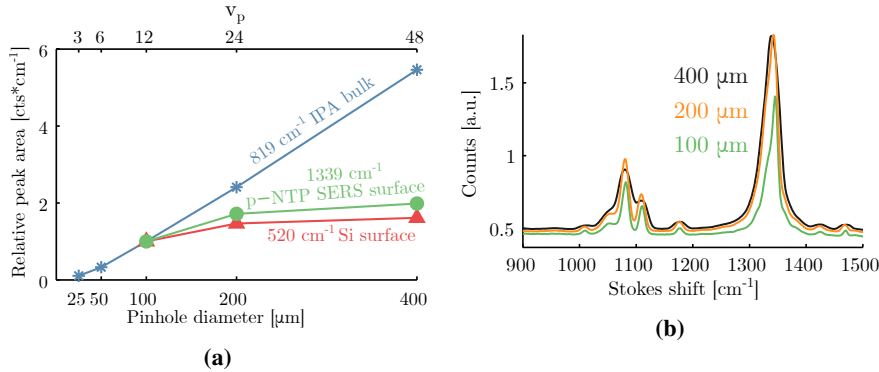

(a)

(b)

Figure 2.7 Influence of the core diameter of the multimode collection fiber functioning as confocal pinhole. (a) Signal increase with pinhole size (equalized for 100 μm pinhole diameter) for bulk and surface scattering collected with a 10x/0.3 objective. (b) SERS spectra of an NTP monolayer acquired with different core diameters. Because the multimode fiber also functions as entrance slit of the spectrometer, the spectral resolution decreases slightly for the 200 μm pinhole and severely for the 400 μm pinholes, visible from the peak doublet around $1100 \ \mathrm{cm}^{-1}$.

jectives used in this thesis. Because of the low Raman cross section, in many Raman experiments resolution is sacrificed in favor of larger signal intensity by using a larger pinhole diameter. For SERS on planar substrates, the Raman signal originates from the nanometer region of the substrate. As a consequence, the measurement inherently has an 'axial resolution' of a few nanometers. In these cases, it often makes sense to use a pinhole with a $v_p > 4$ to acquire maximum signal, as long as this does not compromise the spectral resolution of the spectrometer. In the Raman system (figure 2.6) used in this work, a multimode fiber is used as a confocal pinhole. This fiber also guides the light and serves as an entrance slit of the spectrometer. Figure 2.7a shows the effect of the multimode fiber core diameter on the collected Raman signal in bulk and surface scattering samples, measured for a 10x/0.3 objective. For surface-measurements, the signal saturates with increasing pinhole diameter because the pinhole size becomes much larger than the projected beam radius of the focal spot. In a bulk measurement, the signal keeps increasing up to the largest available multimode fiber because the axial collection volume keeps increasing. For these larger pinhole diameters, the wider input slit of the spectrometer results in a decreased spectral resolution (figure 2.7b). The effect of the pinhole is a somewhat controversial issue in the comparison of waveguide-based versus microscope-based Raman collection [14], see chapter 4.2.2.

While the use of a multimode fiber as pinhole has the practical advantage that the spectrometer can be placed anywhere, it severely complicates tuning the pin-
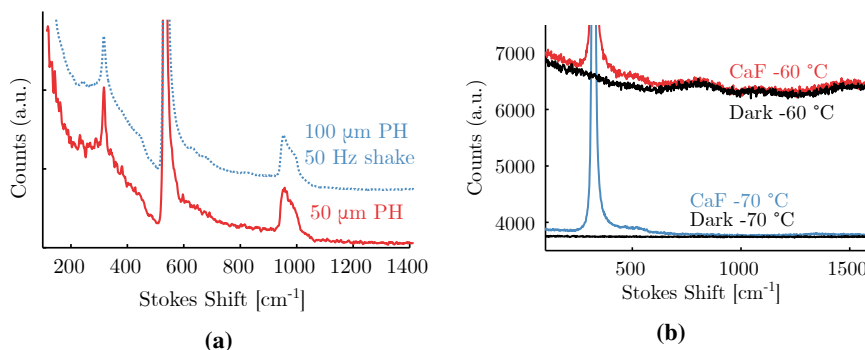
Figure 2.8 (a) Effect of shaking the MM collection fiber to average out non-uniform output profiles, illustrated on the Raman spectrum of Si. Spectra are cascaded and normalized for clarity.(b) Detecting weak Raman peaks on a low background requires a reduction in dark noise, here illustrated for CaF_2. Spectra shown to scale and not cascaded, 10 s acquisition time.

hole diameter. Even more problematic is that these fibers generate a ripple on the acquired spectrum. We attribute this to either the non-uniform radiation pattern of these multimode fibers or multimode interference, a similar effect to the one observed when using multimode waveguide for collecting SERS spectra, as discussed in section 6.5. If the radiation pattern is non-uniform, the light entering the spectrometer will not have a Gaussian beam profile, but will be a capricious spot that is the superposition of multiple modes in the fiber. As long as there exist multiple modes, a lower number of modes in the fiber generates a beam profile that deviates stronger from the Gaussian shape. As a consequence, the ripple is stronger for smaller core fibers. Using a single mode fiber with a core diameter of approximately 5 µm could solve this problem, but this would result in a very low signal collection. Practically, we mitigate the problem by shaking the collection fiber with a 20-100 Hz frequency, which will make the temporally averaged beam profile closer to the Gaussian. For the 25 µm and 50 µm core collection fibers, it is necessary to use an intermediate larger core fiber (e.g. 100 µm) and shake that one before the Stokes scattered light goes into the spectrometer. Figure 2.8a shows how this shaking is crucial to reveal small Raman peaks on a large background signal. In my opinion, the use of multimode collection fibers is a major design flaw in the WITec confocal Raman microscopes.

Spectrometer   The Stokes scattered light is incident on a diffraction grating and imaged onto a CCD camera. The spectral resolution of the the spectrometer depends on the input slit, size of the spectrometer and periodicity of the grating. The effect of the input slit was shown in figure 2.7a. Because the size of the spectrometer is usually fixed, the only way to increase the spectral resolution is to use a different grating. Our system has two different gratings. The 600 lpmm grating allows to acquire an inverse frequency span of approximately 1800 cm^{-1} (at a center wavelength of 1800 nm) with a spectral resolution of approximately 1.5 cm^{-1}. The 300 lpmm gives an inverse frequency span of 3400 cm^{-1} and a spectral reso-
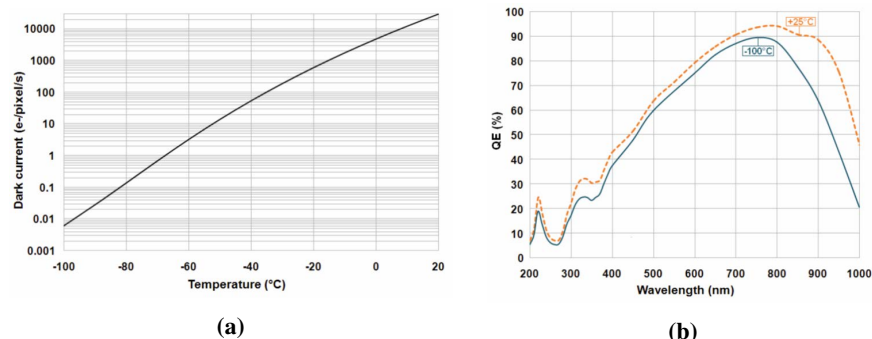
(a) **(b)**

Figure 2.9 Specifications of the CCD camera installed on the confocal Raman system used in this thesis. (a) Dark current (b) Quantum efficiency. *(Copied from Andor documentation)*

lution of approximately $2 \, \text{cm}^{-1}$. Because the quantum efficiency of our Si detector is low at longer wavelength shifts, this frequency span is usually excessively wide at the cost of spectral resolution. Remember that the dispersion of a grating is not linear, meaning that a linear spectral interpolation is often necessary before any data processing is done on the Raman spectra.

CCD camera   Because Raman signals are weak, spectra acquired at room temperature are overwhelmed by thermal noise. A **low dark current** is crucial for sensitive Raman measurements. For this reason, CCD cameras cooled below -60 °C are typically used. For the spectral camera used in this work (Andor iDus 401 BR-DD), the dark current decreases from a Poisson distribution of 4 to 0.9 electrons/pixel per second when cooling the camera from -60 °C to -70 °C (figure 2.9a). For the lower temperatures and limited integration times, the **readout noise** becomes dominant. At the most sensitive setting, we get a Poisson distribution of 4.5 electrons/pixel per readout for our camera. The **quantum efficiency** of silicon-based CCD detectors can be above 0.9, but drops sharply above 900 nm as illustrated for our camera in figure 2.9b. As the total readout- and dark-noise fluctuations scale linearly with the number of pixels, reading less pixels per spectral point helps to reduce it. Our CCD camera is a 2D matrix with 1024 columns and 128 rows. The Stokes scattered light will only illuminate the center rows of the camera, therefore it is sufficient to read only the 10-20 center rows at each spectral point or column. In fact, a large part of the 2D camera is unused because the Raman spectrum is a 1D array of information. In a slit scanning microscope [15], confocal Raman imaging is speed up by simultaneously acquiring multiple spectra an multiple rows of the CCD camera. Figure 2.8b illustrates the effect of dark- and thermal noise on a weak Raman spectrum.

Upright or inverted   As mentioned before, an upright collection gives the best signal to noise ratio in a Raman measurement. However, an inverted setup is often preferred from a practical viewpoint, especially with live-cell imaging. Because there is no direct contact with the sample, inverted microscopy makes sterile ex-

periments and sample handling much easier. Furthermore multiple experiments with low sample volumes can simultaneously be ran and imaged with high numerical aperture objectives using thin-bottom multi-well plates. For these reasons, inverted microscopy is the method of choice for fluorescent imaging. Because of the strong local field enhancement on a nanometer scale, SERS experiments are usually not hindered by the signal from a glass or calcium-fluoride thin substrate and can be conducted on an inverted microscope. For example, for the live-cell SERS experiments described in chapter 5 we converted our Raman microscope to an inverted system.

Substrate   When imaging a thin sample ($< 2\,\mu$m), the underlying substrate will contribute to the Raman signal even when using high NA objectives. Its contribution can be reduced by reduce the pinhole size for maximum lateral resolution and using an optimal substrate material. Figure A.16 compares the Raman background of frequently used substrates. Calcium Fluoride (CaF_2) is usually preferred, with an extremely low Raman background (figure 2.8b) from 400-3000 cm^{-1}. Quartz is also acceptable in the 900-3000 cm^{-1} region. The conventional glass coverslide has a rather strong Raman background, especially in the 1200-1700 cm^{-1} region . Unfortunately, the price increases from €0.02 for a cover glass to €20 for a CaF_2 slide. Note that there are large differences in Raman background with CaF_2 from different suppliers. We found the *Raman Grade* CaF_2 from *Crystran Ltd.* to have the lowest Raman background among the samples we measured.

2.3   Surface-enhanced Raman scattering

The extremely low cross section of Raman scattering urges for a method to increase the sensitivity of Raman spectroscopy. The strongly enhanced electric field intensities close to metal nanostructures provide such a solution. Molecules within the nanometer range of these nanostructures can emit up to 10^{10} times more Stokes scattered photons as compared to the same molecules in vacuum. Because of the necessary proximity of the molecule to the (metal) surface, this process is called surface-enhanced Raman scattering (SERS). The localized surface plasmon resonance responsible for the enhancement in SERS is most commonly phrased as a resonant oscillation of free electrons at the frequency of incident photons, depicted in figure 2.10. The incoming electromagnetic wave drives the oscillation of the electrons. These moving electrons will in turn generate an electromagnetic field, and so on. Here, we give a qualitative description of surface-enhanced Raman scattering, which provides a sufficient background for understanding the application of SERS for intracellular sensing (chapter 5) and single-cell protease sensing (chapter 6) discussed in this work. For a more extensive introduction to the subject and its applications, we refer to the recent review article of Schlücker [16] and the excellent reference book of Le Ru and Etchegoin [2]. In chapter 3, we describe the presence of plasmonic modes in the nanodome SERS platform and the related
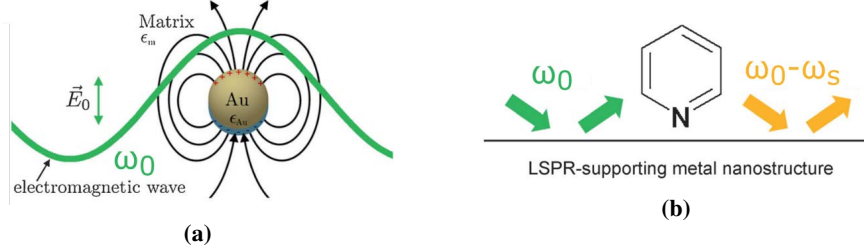
Figure 2.10 (a) The collective resonance of the incident electromagnetic wave and the free electrons in the metal nanoparticle creates a localized surface plasmon polariton resonance (LSPR). (b) Both the incoming field ω_0 and dipole power $\omega_0 - \omega_s$ are enhanced by the metal nanostructure (Image adapted from [16]).

field enhancement in more detail.

2.3.1 SERS enhancement mechanism

Consider again a molecule with angular vibrational frequency ω_s in vacuum . An external electromagnetic field with frequency ω_0 generates a dipole $\vec{p}$ (2.13):

$$\vec{p}(\omega_0 + \omega_s) = \alpha_0(\omega_0, \omega_0 + \omega_s)\vec{E}_0(\omega_0) \tag{2.37}$$

Now, consider the same dipole inside or very close to an optically responsive material ($\epsilon \neq 1$). The presence of the material has three effects. (1) It modifies the electric field profile at the location of the molecule. (2) It also influences the electron structure, hence the polarizability or even the vibrational frequency of the molecule. The induced dipole becomes:

$$\vec{p}_m(\omega_0 + \omega_s) = \alpha_m(\omega_0, \omega_0 + \omega_s)\vec{E_m}(\omega_0) \tag{2.38}$$

(3) In addition, an increased local density of states will lead to a modified spontaneous emission of the dipole. This enhances the total power radiated by the dipole. From the optical reciprocity theorem, one can show that this enhanced emission is proportional to the intensity of the electric field [17]. Because the power P_r radiated by the dipole at frequency $\omega_0 + \omega_s$ is proportional to $|\vec{p}|^2$ (2.14), we find that the total Stokes scattered power by the dipole close to the material relative to that in vacuum becomes:

$$\frac{I_{SERS}}{I_{Raman}} \propto \frac{P_r^m}{P_r^0} = \underbrace{\frac{|\alpha_m|^2}{|\alpha_0|^2}}_{\text{Chemical factor}} \times \underbrace{\frac{|\vec{E_m}(\omega_0)|^2}{|\vec{E_m}(\omega_0)|^2}}_{\text{Field enhancement}} \times \underbrace{\frac{|\vec{E_m}(\omega_0 + \omega_s)|^2}{|\vec{E_m}(\omega_0 + \omega_s)|^2}}_{\text{Radiation enhancement}} \tag{2.39}$$

We can separate the increase in Raman scattering into three different contributions: a chemical factor, an increase of the local electric field at ω_0 and a radiation enhancement at $\omega_0 + \omega_s$. Remind that Raman scattering is an instantaneous process,

there is no separation in time between the local field and the radiation enhancement. We will briefly discuss the different contributions below. First we repeat the approximations made to arrive at (2.39):

- We assumed that the molecule has a scalar polarizability and is aligned with the polarization of the incoming field.

- Equation (2.39) neglects the changes in polarization to the local field induced by the presence of the material or surface.

- In addition to enhancing the total radiated power of the dipole, the presence of the material will also modify the dipole radiation pattern and one should speak of directional radiation enhancement. Usually a fraction of the total scattered power is collected, thus the measured SERS enhancement can be different from (2.39).

Experimentally, these assumptions are correct when measuring Raman spectra in a backscatter configuration (same excitation and collection optics) from molecules aligned to the incident polarization with a zero depolarization ratio. Because of reciprocity, under this geometry Maxwell solvers can be used to calculate the directional radiation enhancement from the local field enhancement at the Raman scattered frequency .

Electromagnetic enhancement

The multiplied effect of the local field enhancement and radiation enhancement is usually referred to as the electromagnetic enhancement. This enhancement is independent of the presence of the molecule, except for the minor changes to the local refractive index induced by the molecule itself. Because any surface with $\epsilon \neq 1$ influences the propagation of the electromagnetic field, in basically any situation where a molecule is close to a surface, there will be some degree of electromagnetic enhancement. For example, enhanced Raman scattering has been demonstrated for molecules in a nanophotonic slot waveguide [6] and in resonant dielectric cavities such as a whispering gallery mode resonator [18] or a dielectric grating [19]. However, non-resonant modes provide modest field enhancements, while in dielectric resonators a strong evanescent field comes with a spectrally narrow resonance. As a consequence, there is either excitation or emission enhancement.

As explained in the next chapter, localized surface plasmon polariton resonances (LSPRs) in the gaps between metal nanostructures result in field intensities enhanced up to a factor 10^5 over a wide wavelength range. Because this resonance can be broad enough to encompass both ω_0 and ω_s, the electromagnetic enhancement is often simplified to an $|E|^4$ approximation:

$$\frac{I_{SERS}}{I_{Raman}} \propto \frac{|\vec{E_m}(\omega_0)|^4}{|\vec{E_m}(\omega_0)|^4} \tag{2.40}$$

This equation provides a useful tool to estimate the maximum single-molecule (chapter 3.4.1) enhancement factor from the simulated electric field profile of a metal nanostructure (see for example figure 3.34 on 3-41). Remember that it is only valid for smaller Stokes shifts and broad resonances.

Chemical effects

Many articles about SERS and its applications briefly mention that *'SERS is the multiplied effect of an electrochemical enhancement and a chemical enhancement. ... The chemical enhancement is responsible for an additional factor 10-100'*. Often this is followed by a statement that the latter effect is poorly understood. In my opinion, the term chemical *enhancement* is misleading and makes some people think of SERS as some kind of wizardly hocus-pocus. There seems to be no such thing as an overall chemical enhancement [20] [9]. Rather, the polarizability of the molecule, and hence its Raman cross section can change due to the binding of the molecule to a noble-metal surface. This can change the internal electron structure, altering the relative strength and vibration frequencies of the different modes. Also, the molecule-metal band can give rise to new vibrational modes. These interactions can either reduce or increase the Raman cross section of a particular mode. Bonds may become resonant or, vice versa, resonant bonds can be quenched. These effects typically have an effect of a factor 0.1-10. The particularities of these interactions are described in a critical review by Jensen et al. [21], we will not further discuss them here. Note that chemical effects are not purely reserved to metal-molecule interactions. Binding a molecule to any surface or other molecule, or even dissolving it will change its polarizability (figure 2.11). Obviously the chemical effect will be different for each molecule and each Raman band within that molecule.

For the particular case of a pNTP molecule bound to one or multiple silver atoms, the effect of the so-called 'chemical enhancement' was investigated by Thomas et al. [22] through electron density functional theory. They found significant changes in relative peak strength and newly emerging bands in the pNTP-Ag complex, but no overall chemical enhancement. Figure 2.11 shows the effect the gold-sulfur bond on the SERS spectrum of pNTP. Although we do not observe the same changes as reported in [22], there is clearly a change in peak position and relative peak intensity.

2.3.2   Photochemical effects in Raman and SERS

In a simplified description, photobleaching in fluorescent molecules is the result of inter-system crossing of an excited electron in the S1 state to a triplet state. An electron in this triplet state is highly reactive, especially with oxygen. This can result in an abrupt disappearance of the fluorescence. For a typical fluorescent dye such as R6G, this means that on average 10^6 fluorescent photons are emitted before it bleaches. When fluorescence spectroscopy is done on a large
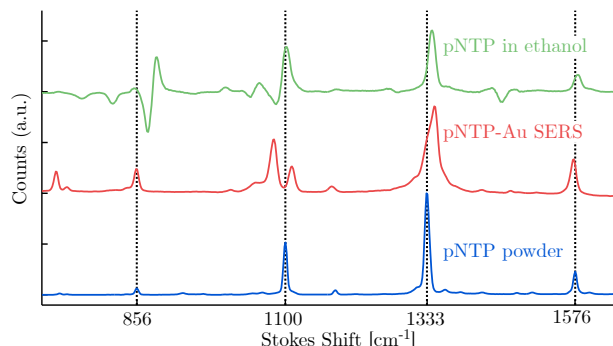
Figure 2.11 The gold-sulfur bond changes the relative strength and exact position of the Raman bands for pNTP in a SERS measurement. Note that also dissolving the powder in ethanol changes the spectrum. Black dashed lines highlight the vibrational modes of pNTP peaks in its powderous form.(Spectra are normalized and cascaded for clarity. An ethanol reference spectrum was subtracted from the top curve to retrieve the spectrum of pNTP dissolved in ethanol).

collection of molecules, this results in a gradual decrease of the fluorescent signal. Although specific techniques use bleaching in a smart way for super-resolution microscopy [23] or for studying system dynamics (e.g. fluorescent recovery after photobleaching or FRAP), in most cases photobleaching hinders fluorescence microscopy. As described in figure 2.4, Raman scattering is an instantaneous process where the electron is not excited to a next energy level and this inter-crossing can not appear. For many molecules, this is true when using an infrared excitation wavelength. Therefore, in contrast to fluorescence, Raman and SERS signals are not (or much less) prone to photobleaching. Indeed, SERS tags have been developed that show a superior photostability to conventional fluorescent dyes or even quantum dots [24]. Figure 2.12 shows how the background fluorescence in a peptide is bleached using a long exposure, revealing its Raman spectrum. Note that this bleaching is irreversible.

The reduced photobleaching does not mean that molecules inside plasmonic hotspots are inert to all photochemical phenomena. On the contrary, as compared to fluorescence, SERS experiments require significantly increased laser powers and/or longer acquisition times. Even for a strong (non resonant) Raman scatterer such as pNTP in a hotspot with a 10^8 electromagnetic enhancement, the equivalent 'SERS cross-section' is still a factor $10^4 - 10^5$ lower than a fluorescent dye. Furthermore, exactly because of the electromagnetic enhancement, the local field intensity felt by the molecule will be dramatically increased. To make things worse, the absorption of gold (or silver) of at the wavelength of this enhanced field can strongly heat up the hotspot.

A comprehensive overview and physical understanding of all possible photochemical effects in SERS experiments is outside the scope of this thesis. Rather, we describe a few phenomena that we repeatedly observed experimentally. In most
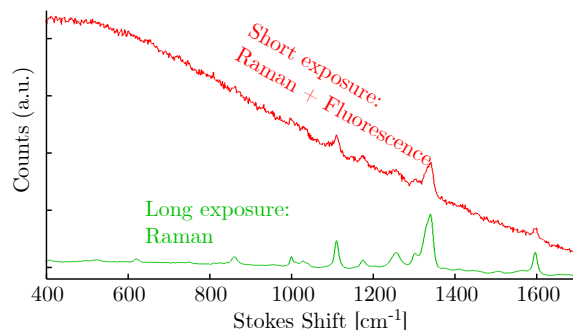
Figure 2.12 Fluorescence bleaching and stable Raman spectrum of the lyophilized Ac-CGGGGGFGVR-pNA peptide (see chapter 6) acquired before and after exposing for a few minutes with $20\,\mathrm{mW}/\mu\mathrm{m}^2$ at 785 nm.

SERS experiment in this work, we used an irradiance of $50-1000\,\mu\mathrm{W}/\mu\mathrm{m}^2$ with an exposure time of 0.1-10 s. The irradiance at which a specific phenomenon occurs depends strongly on the electromagnetic enhancement, the geometry of the plasmonic antenna, the surrounding medium and the molecule itself. We list them roughly from highest to lowest irradiance for a gold-sulfur bound monolayer of molecules:

Burning   Under excessive irradiance, the SERS spectrum of all molecules will disappear and one observes a strong overall rise in 'Raman background', eventually saturating the detector over a broad Stokes shifted range. This effect is easily spotted and aspecific of the measured molecules. We believe this is a heating effect that, in our experience, irreversibly damages the SERS substrate.

SERS blinking   Especially with label-free SERS experiments in complex media, the SERS signal fluctuates in time, even when acquired on a fixed nanostructure. This can be explained by dynamic processes such as Brownian motion and competitive adsorption and desorption of molecules. These processes would also occur without incident irradiation. At increased irradiance however, the fluctuations in the SERS spectra can increase dramatically, often resulting in a 'blinking' behavior where a specific spectrum is only visible during the short time span (e.g. 100 ms) of a single acquisition, as illustrated in figure 2.13. Multiple photochemical and photo-thermal effects are at play, the latter probably predominant. Localized heating increases the Brownian motion and drags molecules into the hotspot. The de-adsorption rate can be increased or molecules may be fragmented in the strong electromagnetic field. Also, sub-nanometer mechanical changes to SERS hotspots in plasmonic gaps are possible [2]. Whatever the source may be, excessive blinking is a sign that one should strongly reduce the irradiance.
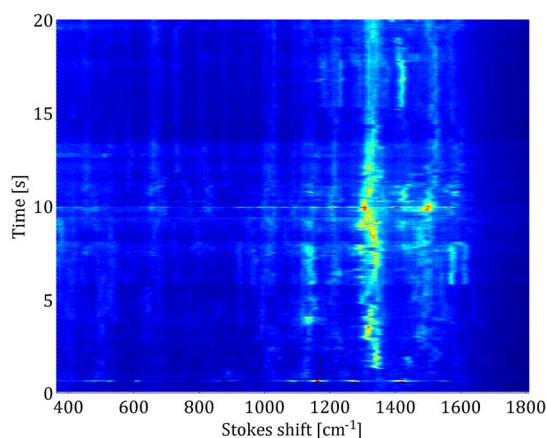
Figure 2.13 SERS 'blinking' observed from time-dependent spectra of clustered gold nanoparticles (stabilized with 4-dimethylaminopyridine) in an intracellular environment, excited using excessive laser power with a 50 ms interval.

Photoreduction of the signaling molecule

Two-Photon Absorption   Nonlinear optical processes such as two-photon absorption usually require power densities far higher than the typical $100\,\mu\mathrm{W}/\mu\mathrm{m}^2$ used in our SERS experiments. However, the strong field enhancement in the hotspot can lead to significant two-photon absorption even at these low power densities [26]. Frequency doubling implies that the energy of this transition corresponds to a wavelength of 390 nm, at which many molecules have electron transitions. As a consequence, two-photon absorption may induce photochemical processes in SERS experiments at near-infrared wavelengths.

We also repeatedly observed a relative peak change and overall signal reduction in the SERS spectrum of aromatic peptides, as shown in figure 2.15. upon prolonged laser exposure. We have not yet identified the origin of this problem. These peptides are used for monitoring protease activity in chapter 6.

2.3.3   SERS background

As can be seen from figure 2.14b, SERS spectra are superimposed on a broad background. In all gold or silver nanostructures (table 3.2) we measured, such a background was present. In many publications, including this thesis, the SERS background is subtracted and only SERS peaks are shown. This background signal, also called the SERS continuum, limits the signal to noise ratio (SNR) of SERS experiments. As a consequence the SNR of a SERS spectrum is not simply that of the pure Raman spectrum of that molecule multiplied by the enhancement factor.
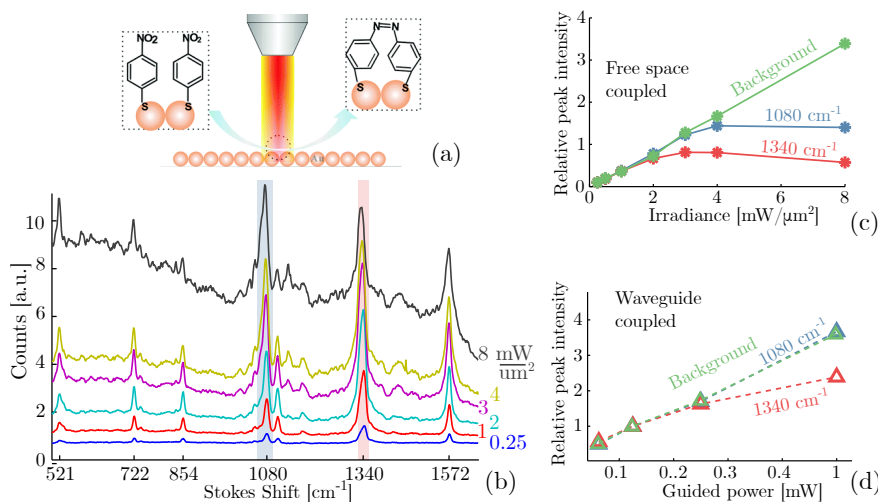
Figure 2.14 (a) Photoinduced reduction of pNTP into DMAB (schematic from [25]). (b) Irradiance-dependent SERS spectra acquired through a high NA objective on a nanotriangle substrate. (c) Relative strength of the background and $1080\,\mathrm{cm}^{-1}$ and $1340\,\mathrm{cm}^{-1}$ peaks derived from these SERS spectra (c) Relative peak strength for the same nanotriangle pattern excited through a waveguide.

Many different origins of this SERS continuum have been described and, although the presence of the SERS continuum was described as early as the first SERS experiments 40 years ago [27], to the best of our knowledge there is no scientific consensus on the origin of this phenomena. An obvious source of background is the material on which the gold or silver nanostructure is deposited. Part of the plasmonic hotspot can be located in this material, leading to surface-enhanced Raman scattering or -fluorescence. Think for example of gold nanoparticles on a (SiO_2) carrier, where the broad Raman spectrum of the latter (figure A.16) contributes to the continuum. It is not always straightforward to recognize the material's Raman spectrum from the shape of the background, as it is convoluted with the enhancement spectrum of the LSPR. In certain experimental situations, part of the background may originate from carbonaceous contaminants burned onto the sample, for example under high temperature or laser irradiance as described in the previous section. Other, less trivial, contributions to this background signal have been described in literature. The molecule under study or any contaminants can contribute to a surface-enhanced fluorescence [28]. Also, due to the presence of the metallic 'mirror' Raman dipoles can have a strongly damped radiating image dipole in the metal surface [29, 30]. Electronic inelastic light scattering from electrons in the noble metal structure in plasmon modes has also been suggested as a major contributor [31].

In the gold-nanodome SERS platform discussed in chapter 3, a contribution of the underlying SiN is unlikely. We use an approximately 150 nm thick gold layer that screens the electromagnetic field in the dielectric material. We did not observe
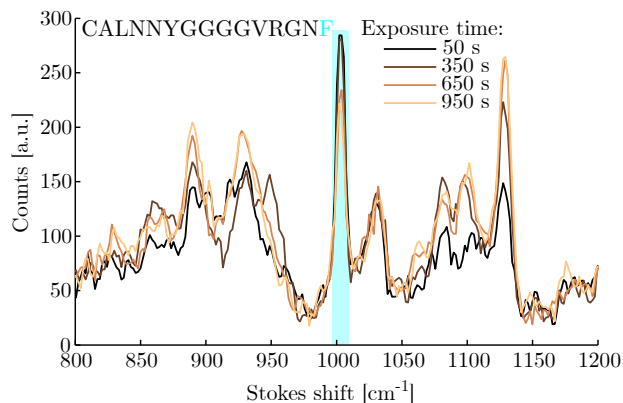
Figure 2.15 Relative peak changes in SERS signal of Ac-CALNNYGGGGVRGNF-COOH peptide upon prolonged exposure at $0.4\,\mathrm{mW\mu m^{-2}}$. Degradation of the F-related 1003 cm^{-1} peak is highlighted in blue (spectra are background subtracted).

an decrease in background when using a 20 nm thicker Ti adhesion layer. We have not done a systematic study on the Raman background in the nanodome SERS platform, but our observations are consistent with some of the proposed origins. The background is linear with excitation power and clearly correlated to the presence of a LSPR [32] . We also observe a SERS continuum on clean samples, but it increases in the presence of molecules or dirt. Apart from an increased shot noise, which scales with the square root of the total intensity, in the particular case of our Raman microscope the output profile of the MMF generates an extra ripple on the spectrum, as explained in section 2.2).

2.4 A critical view on SERS applications

The number of applications and related research papers using SERS has grown tremendously over the last decades. By no means we can provide a comprehensive overview of the field, not even in the subfields of SERS for intracellular or single-cell sensing. Nevertheless, it is useful to get insight in different applications of SERS on a higher-level. It is also important to be aware of some common pitfalls encountered in SERS literature. Experimental surface-enhanced Raman spectroscopy is a very complicated topic, and results should be interpreted with caution. Excellent starting points for developing this mindset are the lucid review by Moskovits on persistent misconceptions in SERS [20] and the comprehensive reference book by Le Ru. and Etchegoin [2]. I urge the reader to also apply this critical mindset to the results reported in this thesis.

Most SERS experiments can be grouped in one of the three categories represented in figure 2.16:

(a) A completely **label-free detection** of molecules close to the gold surface

or in the gap (hotspot) between two nanostructures, used in chapter 5. This way specific molecules can be directly detected, for example used for the intracellular detection of extraneous molecules [33] [34]. Also, information about the environment of the SERS nanostructure can be obtained, for example about endo-lysosomes [35] or exosomes [36]. This modality of SERS is extremely prone to experimental variations. Only a tiny volume of roughly 10nm^3 is sampled in a SERS hotspot, which is not necessarily a representative measurement for the complete environment. Furthermore, molecules adsorb on the gold layer through charge-based interactions, and many organic molecules have similar Raman bands. On top of that, the spectra are often contaminated by stabilizers used for fabricating the nanoparticles. Some of these problems can be solved by using nanoparticles isolated by a nanometer thin inert shell [37]. In many manuscripts reporting label-free SERS measurements in a complex biological environment, one finds a tentative assignment of SERS peaks to specific proteins, DNA, RNA, etc. These are often based on a single (the best matching?) SERS spectrum. One has to be very careful with these peak assignments, the spectral position of SERS peaks can deviate slightly from the normal Raman bands. Given a margin of $5-10\,\text{cm}^{-1}$, it is almost always possible to attribute a peak to some organic vibration in the $600\,\text{cm}^{-1}$ to $1700\,\text{cm}^{-1}$ Stokes region.

In short, it is extremely challenging to obtain quantitative or reproducible information from completely label-free SERS experiments in a complex environment.

(b) The detection of **spectral changes in a surface-bound monolayer**, used in chapter 6. The gold layer can be functionalized with reporter molecules. These provide a SERS spectrum that changes depending on the environment, for example the local pH [38], redox potential [39] or protease activity (chapter 6). As the surface is fully coated with a monolayer of molecules, this method is much less prone to the spectral variations encountered in a completely label-free detection. Nevertheless, the stability of the coating can be problematic in complex environments (see chapter 6.4). Note that this monolayer sensing is sometimes also referred to as a label-free measurement, in the sense that there are no fluorescent labels used for detection. This is a debatable, semantic issue.

(c) The fingerprint specificity of Raman spectra can be used to make '**SERS tags**' [24, 40], not used in this thesis. They usually consist of a silver or gold core, functionalized with a strong Raman scatterer and sealed by a thin dielectric shell. These SERS tags are analogous to fluorescent labels or quantum dots, but allow for a dense spectral multiplexing of 10-100 labels using a single excitation wavelength. They may also be more inert to photobleaching. Figure 2.16 shows an exemplary imaging experiment using SERS tags, where multiple tags with a distinguishable SERS spectrum are targeted towards different regions in the cell. One of many interesting applications is the use of SERS nanotags in a multiplexed endoscopic imaging
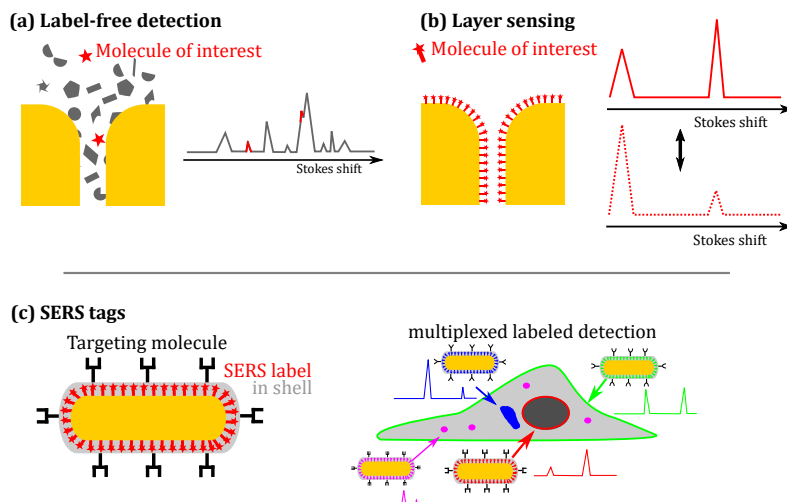
Figure 2.16 Modalities of SERS experiments. (a) Label-free sensing of the environment. (b) Detection of spectral changes in a surface-bound monolayer. (c) SERS tags.

technique for detecting colon cancer [41].

Out of the three modalities discussed here, SERS labels clearly provide the most stable signal and easiest data analysis. They are likely to enable a first commercial success of SERS.

References

[1] John R. Ferraro, Kazuo Nakamoto, and Chris W Brown *Introductory Raman Spectroscopy* Elsevier, 2 edition, 2003.

[2] Eric C Le Ru and Pablo G Etchegoin *Principles of Surface-Enhanced Raman Spectroscopy and related plasmonic effects* Elsevier, Amsterdam, jan 2009.

[3] Stefan A. Meyer, Eric C.Le Ru, and Pablo G. Etchegoin *Quantifying resonant raman cross sections with SERS* Journal of Physical Chemistry A, 114(17):5515–5519, 2010.

[4] H.W. Schrotter, H.W., Klockner *Raman scattering cross sections in gases and liquids* In Springer, editor, Raman scattering cross sections in gases and liquids, pages 123–166. Springer, Berlin, 1979.

[5] N Abe and M Ito *Effects of Hydrogen Bonding on the Raman Intensities of Methanol, Ethanol and Water* Raman Spectrosc., 7(3):161–167, 1979.

[6] Ashim Dhakal, Ali Raza, Frédéric Peyskens, Ananth Z Subramanian, Stéphane Clemmen, Nicolas Le Thomas, and Roel Baets *Efficiency of evanescent excitation and collection of spontaneous Raman scattering near high index contrast channel waveguides.* Optics express, 23(21):27391–404, 2015.

[7] Richard L. Mccerry *Raman spectroscopy in chemical bioanalysis.*, volume 1 John Wiley & Sons, 2000.

[8] R L Aggarwal, L W Farrar, E D Diebold, and D L Polla *Measurement of the absolute Raman scattering cross section of the 1584-cm 1 band of benzenethiol and the surface-enhanced*

Raman scattering cross section enhancement factor for femtosecond laser-nanostructured substrates Journal of Raman Spectroscopy, 2009(April):1331–1333, 2009.

[9] E.C. Le Ru, M Meyer, and P.G. Etchegoin *Surface Enhanced Raman Scattering Enhancement Factors: A Comprehensive Study* Journal of Physical Chemistry C, 111(37):13794–13803, 2007.

[10] Zegen Zheng, Seiichiro Higuchi, and Shigeyuki Tanaka *Raman Scattering Intensities of the NO2 Symmetric Stretching Vibration Band of Some Aromatic Nitrocompounds* Spectroscopy Letters, 15(9):773–787, 1982.

[11] C. V. Raman *A Change of Wave-length in Light Scattering*, 1928.

[12] Ralph Weissleder *A clearer vision for in vivo imaging.* Nature biotechnology, 19(4):316–317, 2001.

[13] Wolfram Ibach and Olaf Hollricher *High Resolution Optical Microscopy* WITec, 2002.

[14] Ashim Dhakal, Ali Raza, Pieter C. Wuytens, Frédéric Peyskens, Andre G. Skirtach, and Roel Baets *Lab-on-a-chip Raman sensors outperforming Raman microscopes* In CLEO 2016, page SM2O.3, 2016.

[15] Almar F Palonpon, Jun Ando, Hiroyuki Yamakoshi, Kosuke Dodo, Mikiko Sodeoka, Satoshi Kawata, and Katsumasa Fujita *Raman and SERS microscopy for molecular imaging of live cells.* Nature protocols, 8(4):677–92, apr 2013.

[16] Sebastian Schlücker *Surface-enhanced raman spectroscopy: Concepts and chemical applications* Angewandte Chemie - International Edition, 53(19):4756–4795, 2014.

[17] E. C. Le Ru and P. G. Etchegoin *Rigorous justification of the —E—4 enhancement factor in Surface Enhanced Raman Spectroscopy* Chemical Physics Letters, 423(1-3):63–66, 2006.

[18] Logan K Ausman and George C Schatz *Whispering-gallery mode resonators: Surface enhanced Raman scattering without plasmons.* The Journal of chemical physics, 129(5):054704–054704–10, aug 2008.

[19] Peipeng Xu, Qiangsheng Huang, and Yaocheng Shi *Silicon hybrid plasmonic Bragg grating reflectors and high Q-factor micro-cavities* Optics Communications, 289:81–84, oct 2012.

[20] Martin Moskovits *Persistent misconceptions regarding SERS* Physical Chemistry Chemical Physics, 15(15):5301, 2013.

[21] Traci R Jensen, Michelle Duval Malinsky, Christy L Haynes, and Richard P Van Duyne *Nanosphere Lithography : Tunable Localized Surface Plasmon Resonance Spectra of Silver Nanoparticles* Journal of Physical Chemistry B, 104(May):10549–10556, nov 2000.

[22] Martin Thomas, Stefan Muhlig, Tanja Deckert-Gaudig, Carsten Rockstuhl, Volker Deckert, and Philipp Marquetand *Distinguishing chemical and electromagnetic enhancement in surface-enhanced Raman spectra: The case of para-nitrothiophenol* Journal of Raman Spectroscopy, 44(11):1497–1505, 2013.

[23] M.P. Gordon, T. Ha, and P.R. Selvin *Single-molecule high-resolution imaging with photobleaching* PNAS, 101(17):6462–465, 2004.

[24] Yunqing Wang, Bing Yan, and Lingxin Chen *SERS Tags: Novel optical nanoprobes for bioanalysis* Chemical Reviews, 113(3):1391–1428, 2013.

[25] Pan Li, Bingbing Ma, Liangbao Yang, and Jinhuai Liu *Hybrid single nanoreactor for in situ SERS monitoring of plasmon-driven and small Au nanoparticles catalyzed reactions* Chem. Commun., 51(57):11394–11397, 2015.

[26] Oleksii Ivashenko, Jochem T. Van Herpt, Ben L. Feringa, Petra Rudolf, and Wesley R. Browne *UV/Vis and NIR light-responsive spiropyran self-assembled monolayers* Langmuir, 29(13):4290–4297, 2013.

[27] Ronald L. Birke, John R. Lombardi, and Joel I. Gersten *Observation of a continuum in enhanced Raman scattering from a metal-solution interface* Physical Review Letters, 43(1):71–75, 1979.

[28] Eric C. Le Ru, P G Etchegoin, Paris Denis Diderot, Cnrs Umr, and De Brosse *Mechanisms of Spectral Profile Modification in Surface-Enhanced Fluorescence* J. Phys. Chem. Lett., 111:16076–16079, 2007.

[29] Stephen M. Barnett, Nadine Harris, and Jeremy J. Baumberg *Molecules in the mirror: how SERS backgrounds arise from the quantum method of images* Physical Chemistry Chemical Physics, 16(14):6544, 2014.

[30] Sumeet Mahajan, Robin M Cole, Jonathon D Speed, Suzanne H Pelfrey, Andrea E Russell, Philip N Bartlett, Stephen M Barnett, and Jeremy J Baumberg *Understanding the Surface-Enhanced Raman Spectroscopy Background* J. Phys. Chem. C, 114(16):7242–7250, 2010.

[31] James T Hugall and Jeremy J Baumberg *Demonstrating photoluminescence from Au is electronic inelastic light scattering of a plasmonic metal: the origin of SERS backgrounds.* Nano letters, 15(4):2600–4, 2015.

[32] Cosmin Farcau and Simion Astilean *Evidence of a surface plasmon-mediated mechanism in the generation of the SERS background.* Chemical communications (Cambridge, England), 47:3861–3863, 2011.

[33] Stefan Bálint, Satish Rao, Mónica Marro Sánchez, Veronika Huntosová, Pavol Miskovský, and Dmitri Petrov *Diffusion and cellular uptake of drugs in live cells studied with surface-enhanced Raman scattering probes.* Journal of Biomedical Optics, 15(2):027005(1–7), 2010.

[34] Pieter C Wuytens, Ananth Z Subramanian, Winnok H De Vos, Andre G Skirtach, and Roel Baets *Gold nanodome-patterned microchips for intracellular surface-enhanced Raman spectroscopy* The Analyst, 140(24):8080–8087, 2015.

[35] Anna Huefner, Wei-Li Kuan, Karin H. Müller, Jeremy N. Skepper, Roger A. Barker, and Sumeet Mahajan *Characterization and Visualization of Vesicles in the Endo-Lysosomal Pathway with Surface-Enhanced Raman Spectroscopy and Chemometrics* ACS Nano, page acsnano.5b04456, 2015.

[36] Stephan Stremersch, Monica Marro, Bat-el Pinchasik, Pieter Baatsen, An Hendrix, Stefaan C. De Smedt, Pablo Loza-Alvarez, Andre G Skirtach, Koen Raemdonck, and Kevin Braeckmans *Identification of Individual Exosome-Like Vesicles by Surface Enhanced Raman Spectroscopy* Small, 12(24):3292–3301, 2016.

[37] Jian Feng Li, Yi Fan Huang, Yong Ding, Zhi Lin Yang, Song Bo Li, Xiao Shun Zhou, Feng Ru Fan, Wei Zhang, Zhi You Zhou, De Yin Wu, Bin Ren, Zhong Lin Wang, and Zhong Qun Tian *Shell-isolated nanoparticle-enhanced Raman spectroscopy* Nature, 464(7287):392–395, 2010.

[38] Stefan Bálint, Satish Rao, Mónica Marro Sánchez, Pavol Miskovský, and Dmitri Petrov *Monitoring of local pH in photodynamic therapy-treated live cancer cells using surface-enhanced Raman scattering probes* Journal of Raman Spectroscopy, 2011(January):1215–21, 2011.

[39] Craig A R Auchinvole, Patricia Richardson, Catherine McGuinnes, Venkatesh Mallikarjun, Ken Donaldson, Hamish McNab, and Colin J Campbell *Monitoring intracellular redox potential changes using SERS nanosensors.* ACS nano, 6(1):888–96, jan 2012.

[40] Magdalena Gellner, Karsten Kömpe, and Sebastian Schlücker *Multiplexing with SERS labels using mixed SAMs of Raman reporter moleucles* Analytical and bioanalytical chemistry, 394(7):1389–1844, 2009.

[41] C. L. Zavaleta, E. Garai, J. T. C. Liu, S. Sensarn, M. J. Mandella, D. Van de Sompel, S. Friedland, J. Van Dam, C. H. Contag, and S. S. Gambhir *A Raman-based endoscopic strategy for multiplexed molecular imaging* Proceedings of the National Academy of Sciences, 110(25):E2288–E2297, 2013.

3

PHYSICS, FABRICATION AND CHARACTERIZATION OF THE NANODOME SERS PLATFORM

Sensitive and quantitative SERS experiments demand a uniform, stable and reproducible SERS platform with a high enhancement factor. We developed a gold nanodome platform to meet these requirements. These gold nanodomes, fabricated using a cheap and scalable method on 4" wafers, enhances the Raman scattering of molecules bound to the gold surface with an average factor of 10^7. The gold nanodomes platform is the workhorse for different applications discussed in chapters 5 and 6.
In this chapter, we in particular discuss following issues:

1. *What are propagating and localized surface plasmon polaritons?*

2. *Can we understand the physics of the nanodome structure from the plasmonic modes in a metal/dielectric/metal cavity?*

3. *How to fabricate and characterize these gold nanodomes?*

4. *Which parameters allow to tune the plasmonic resonances in these nanodomes?*

5. *How does the performance of these gold nanodomes compare to other SERS substrates?*

3.1 Propagating surface plasmon polaritons at metal-dielectric interfaces

In this section, we provide a minimal theoretical background on plasmonics, sufficient to reason on the plasmonic modes present in the gold-nanodome structured SERS platform described in later sections of this chapter. For a more extensive introduction to plasmonics and its applications, we refer to the reference books of Maier [1] and Le Ru [2]. As mentioned in the previous chapter, the localized surface plasmon-polariton responsible for the electromagnetic enhancement in SERS is a resonant interaction between an electromagnetic (photon) mode and a charge-density (plasmon) mode. This effect can be described purely from Maxwell's electromagnetic equations without directly describing the charge oscillations. The response of the electrons in a material to the incident electromagnetic wave is fully included in the frequency-depended, complex dielectric function of the material. Thus, we start this section with deriving the optical properties of metals from the Drude model and use this to describe the surface plasmon-polariton modes at metal-dielectric interface. But first, we provide the definition of a few essential terms for plasmonics.

3.1.1 Photons, plasmons and polaritons

Photon Quantum particle representing the elementary excitation of electromagnetic field oscillations.

Plasmon Quantum quasi-particle that represents the elementary modes of a charge-density oscillation in a plasma. According to its first definition:

> *The valence electron collective oscillations resemble closely the electronic plasma oscillations observed in gaseous discharges. We introduce the term 'plasmon' to describe the quantum of elementary excitation associated with this high-frequency collective motion.* [3]

In contrast to a photon, which is a real quantum particle, a plasmon is a quasi particle in an absorbing medium that decays in the absence of external excitations.

Polariton A photon coupled to an optically responsive medium, or the interaction of an electromagnetic wave with the electric or magnetic dipoles of a material. According to this definition any photon that is not in vacuum is associated with a polariton rather than a pure electromagnetic wave. In practice, the term polariton is often reserved for photons in media with a strong optical response such as metals.

Plasmon-Polariton (PP) The quasi-particle related to the mixed photon-plasmon modes generated by an electromagnetic wave in a metal.

Surface Plasmon-Polariton (SPP)   Mixed state of a charge density wave (plasmon) and an electromagnetic wave (photon) at a metal-dielectric interface. As described in further in this section, they are excited by transverse-magnetic (TM) electromagnetic modes at the interface of a material with negative re(ϵ), typically a metal.

Localized Surface Plasmon-Polariton (LSPP, LSPR)   A surface plasmon that is confined in three dimensions. One can make the analogy with localized electron states in a quantum dot or localized optical modes in a 3D photonic bandgap structure. In contrast to the latter two, LSPP resonances have a broad spectrum. This is a consequence of the dispersion of the used noble metals, where the imaginary part of the refractive index strongly damps the resonant mode. In section 3.2, we will stepwise describe the confinement of surface plasmons on a metal dielectric layer to arrive at the localized surface plasmon polaritons in a nanodome cavity. The term LSPP is often abbreviated to localized surface plasmons (LSP) or localized plasmon (LP), or referred to as a localized surface plasmon resonance (LSPR).

3.1.2   Metal dispersion calculated from the Drude model

The optical properties of materials can be calculated using the Lorentz model, following a classical approach. Under an externally applied electric field $\vec{E}(t) = \mathrm{Re}\left[\vec{E_0}e^{-i\omega t}\right]$[1] oscillating at frequency ω, negatively charged electrons e with mass m will move. Think of this as an externally driven, damped harmonic oscillator where the lighter electron is bound with a spring to a fixed (heavier) positively charged ion. This implies a position-dependent restoring force $m\omega_0^2\vec{r}$ and a velocity-dependent friction force $m\gamma\frac{\mathrm{d}\vec{r}}{\mathrm{d}t}$ under an external driving force $-e\vec{E}$:

$$m\frac{\mathrm{d}^2\vec{r}}{\mathrm{d}t} + m\gamma\frac{\mathrm{d}\vec{r}}{\mathrm{d}t} + m\omega_0^2\vec{r} = -e\vec{E} \tag{3.1}$$

For metals, we consider a 'sea' of free electrons moving against the positively charged background of ion cores. Their motion is damped due to collisions occurring with a frequency $\gamma = 100\,\mathrm{THz}$ at room temperature. Because the electrons are free, we can neglect the position-dependent restoring force and simplify the differential equation to the Drude model:

$$m\frac{\mathrm{d}^2\vec{r}}{\mathrm{d}t} + m\gamma\frac{\mathrm{d}\vec{r}}{\mathrm{d}t} = -e\vec{E} \tag{3.2}$$

The frequency-dependent oscillation of the electron becomes:

$$\vec{r_0}e^{-i\omega t} = \frac{e}{m(\omega^2 + i\gamma\omega)}\vec{E_0}e^{-i\omega t} \tag{3.3}$$

From $\vec{r} = \vec{r_0}e^{-i\omega t}$, we calculate the macroscopic polarization $\vec{p} = N\vec{d}$ with dipole moment $\vec{d} = -e\vec{r}$. Here N is the number of free electrons per unit volume. $\vec{P}$

---

[1]To simplify the notation, we will write $\mathrm{Re}\left[\vec{E_0}e^{-i\omega t}\right]$ as $\vec{E_0}e^{-i\omega t}$

links the dielectric displacement $\vec{D}$ to the electric field $\vec{E}$:

$$\vec{D} = \epsilon_0 \vec{E} + \vec{P} \tag{3.4}$$

$$= \epsilon_0 \epsilon \vec{E} \tag{3.5}$$

The dielectric function ϵ of the free electrons becomes:

$$\epsilon(\omega) = 1 - \frac{Ne}{m\epsilon_0} \frac{1}{w^2 + i\gamma\omega} \tag{3.6}$$

For now, we have neglected the fixed background of the positive ions. This contributes to a constant, real dielectric function $\epsilon_\infty \geq 1$:

$$\epsilon(\omega) = \epsilon_\infty - \frac{\omega_p^2}{\omega + i\gamma\omega} \tag{3.7}$$

We have introduced the plasma frequency $\omega_p^2 = \frac{ne^2}{m\epsilon_0}$. It can be shown that this corresponds to the natural oscillation frequency of the electron sea in a bulk metal [1]. For most Drude metals, this plasma frequency is in the UV-range, for Ag ω_p equals $1.4 \cdot 10^{16} \, \mathrm{rad\,s^{-1}}$, corresponding to a plasma wavelength λ_p of 136 nm. The complex dielectric function can be split into its real and imaginary components $\epsilon(\omega) = \epsilon_r + i\epsilon_i$:

$$\epsilon_r = \epsilon_\infty \left(1 - \frac{\omega_p^2}{\omega^2 + \gamma^2}\right) \tag{3.8}$$

$$\epsilon_i = \epsilon_\infty \frac{\omega_p^2 \gamma}{\omega(\omega^2 + \gamma^2)} \tag{3.9}$$

In non-magnetic materials, the real and imaginary parts of the refractive index $(n + i\kappa)^2 = \epsilon$ become:

$$\epsilon_r = n^2 - \kappa^2 \tag{3.10}$$

$$\epsilon_i = 2n\kappa \tag{3.11}$$

$$n = \sqrt{\frac{\epsilon_r + |\epsilon|}{2}} \tag{3.12}$$

$$\kappa = \frac{\epsilon_i}{\sqrt{2}\sqrt{\epsilon_r + |\epsilon|}} \tag{3.13}$$

Here, the refractive index n represents the effect of the material on the phase velocity of the light, and κ is a number for its absorption with an absorption coefficient $\alpha = 2k_0\kappa$, with $k_0 = \omega/c$ the wavenumber in vacuum. Because all the work described in this thesis uses a Raman excitation laser of 785 nm, we limit ourselves to describing light-metal interactions at visible to near-infrared wavelengths (600-1000 nm), where $\omega < \omega_p$. We consider two extreme cases. First, when $\omega \ll \gamma$,
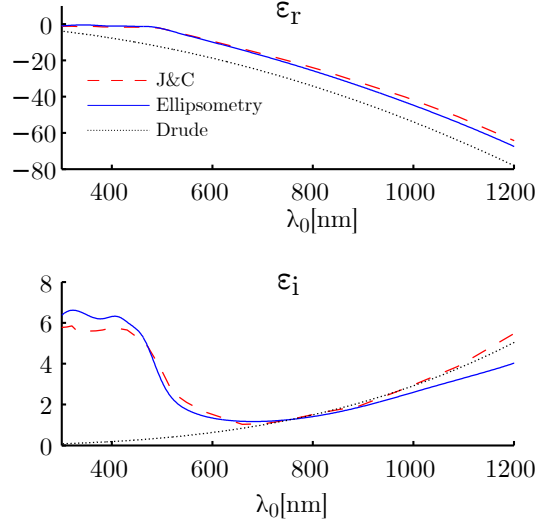
Figure 3.1 Dispersion of gold calculated from the Drude model compared to experimental values measured in this work and those measured by Johnson and Christy [4].

the dielectric constant is mainly imaginary. In this regime, metals are strongly absorbing.

$$\alpha = 2k_0\sqrt{\frac{\epsilon_i}{2}} = \sqrt{\frac{2\epsilon_\infty \omega_p \omega}{c^2 \gamma}} \tag{3.14}$$

This comes as no surprise. If the electromagnetic field - which is the driving force for the oscillation of the electrons in (3.1) - has a much lower frequency than the collision frequency of the electrons, the movement of the electrons will be strongly damped by these collisions.

The opposite argument explains why ϵ is predominantly real if $\omega \gg \gamma$. There is little damping, and ϵ decreases to strongly negative values with decreasing ω:

$$\epsilon = 1 - \frac{w_p^2}{w^2} \tag{3.15}$$

This is the interesting regime for the surface plasmon-polariton resonances lying at the basis of SERS. They require a negative ϵ_r and, for most applications, benefit from a small ϵ_i. However, in this frequency region the behavior of many metals is influenced by interband absorption. While for Ag the dielectric function at visible wavelengths largely follows (3.8) and (3.9), the dispersion of gold is strongly affected by interband transitions at 470 nm and 325 nm. Figure 3.1 compares ϵ_i and ϵ_r calculated from the Drude model to the literature standard of Johnson and Christy [4] and the gold we used for fabricating the nanostructures described this thesis, whose dispersion was measured with ellipsometry. The increased ϵ_i and related absorption renders gold a poor material for SERS below 600 nm. Notice that there is a significant variation between our ellipsometric data that from the Johnson and Christy model. We also observed such differences when characterizing

the dispersion of Au from different sources in our own cleanroom. In general, it is difficult to have exact values for the dielectric function of highly dispersive metals like gold. It is important to keep this in mind when using FDTD or FEM methods to simulate plasmon resonances. There is little use in finding the exact position of a plasmonic resonance with sub 50 nm accuracy, while simulated field intensities will usually only tell the order of magnitude of the eventual SERS-enhancement factor. All calculations in the rest of this chapter are based on the measured dielectric function of the sputtered gold, unless mentioned differently.

In the next sections, we look into the existence of transverse-magnetic (TM) propagating surface plasmon polaritons (PSPPs) at a metal-dielectric interface. From the dispersion relation of a metal-insulator-metal sandwich, we explain how this PSPP can be confined in three dimensions to a localized surface plasmon polariton (LSPP) through the example of coupled gold nanowires. Rather than introducing LSPPs via the textbook example of a metal nanoparticle, we choose this approach for two reasons. First, it provides an stepwise and more intuitive reasoning towards the confinement of a PSPP. Thereby we avoid some of the more complex mathematics used in the electrostatic approximation or Mie theory, necessary for explaining the existence of LSPPs in spherical metal nanoparticles. These are excellently described in [5] and [2] . Second, this approach provides us with an analytical solution for explaining the LSPPs present in the nanodome SERS-platform which will be introduced in section 3.2.

Nevertheless, we must briefly mention two important results of the electrostatic approximation for a single metal nanosphere in a dielectric medium ϵ_d. Under a uniform external electric field, the electric field inside the sphere E_{in} is proportional to the incident field E_0:

$$E_{in} = \frac{3\epsilon_d}{\epsilon(w) + 2\epsilon_d} E_0 \tag{3.16}$$

Hence the field enhancement would be infinite if $\epsilon(w) = -2\epsilon_d$, which for a particle in air implies that $\epsilon_r = -2$ and $\epsilon_i = 0$. In reality, the metal absorption is never zero, thus the field enhancement at resonance remains finite. The quality factor of the LSPP resonance in a metal/air nanoparticle can be directly calculated from the metal's dispersion:

$$Q = \frac{\omega \frac{d\epsilon_r}{d\omega}}{2\epsilon_i^2} \tag{3.17}$$

Figure 3.2 shows Q in function of wavelength for nanoparticles of different materials. This figure provides an excellent starting point for choosing a material for SERS at a specific wavelength. For examples, Ag nanostructures can provide a strong electromagnetic enhancement from 300 to over 1200 nm, with the strongest resonances occurring at visible wavelengths. Gold on the other hand is only an interesting SERS-material for wavelengths above 600 nm.
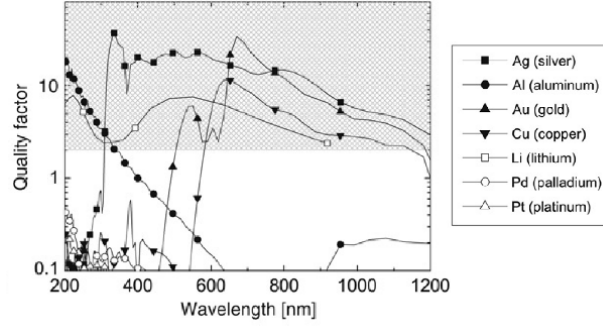
Figure 3.2 Quality factor Q of the LSPP resonance (LSPR) for a metal nanoparticle in air (Figure from [2])

3.1.3 PSPPs at a Metal-Dielectric interface

Except for effects starting to play a role in gaps narrower than 2-3 nm, classical electromagnetism provides an excellent framework for a quantitative description of photon-plasmon effects responsible for surface-enhanced Raman scattering. Only at the distances below a few nanometers, quantum effects have to be taken into account. These are outside the scope of this work. Thus, surface plasmonics is nothing else than applying Maxwell's equations on the interface of a metal and a dielectric. Hereto, we largely follow the description in [1]. We start from Maxwell's equations:

$$\nabla \cdot \vec{D} = \rho \tag{3.18}$$

$$\nabla \cdot \vec{B} = 0 \tag{3.19}$$

$$\nabla \times \vec{E} = -\frac{\delta \vec{B}}{\delta t} \tag{3.20}$$

$$\nabla \times \vec{H} = \vec{J} + \frac{\delta \vec{D}}{\delta t} \tag{3.21}$$

With constitutive relations:

$$\vec{D} = \epsilon_0 \epsilon \vec{E} \tag{3.22}$$

$$\vec{B} = \mu \mu_0 \vec{H} \tag{3.23}$$

The Helmholtz equation in non-magnetic (relative permeability $\mu = 1$) media can be derived from Maxwell's curl equations (3.20) and (3.21) for an electric field with harmonic time dependence $\vec{E}(\vec{r}, t) = \text{Re}\left[\vec{E}(\vec{r})e^{-i\omega t}\right]$:

$$\nabla^2 \vec{E} + k_0^2 \epsilon \vec{E} = 0 \tag{3.24}$$

We look at the most elementary interface between a metal and dielectric material. Figure 3.3 shows the geometry, consisting of a dielectric half-space ($z > 0$) with
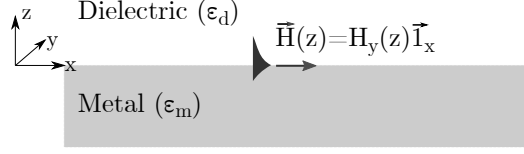
Figure 3.3 A transverse magnetic wave can propagate at the interface between a dielectric and metal semi-infinite space.

dielectric constant $\epsilon_d \in \mathbb{R}^+$ and a metal half-space ($z < 0$) with dielectric function $\epsilon_m \in \mathbb{C}$, and $\mathrm{Re}(\epsilon_m) < 0$. Now consider an electromagnetic wave propagating in the positive x-direction. Because $\epsilon(x, y, z) = \epsilon(z)$, $\vec{E} = \vec{E}(z)e^{ik_x x}$ and the Helmholtz equation becomes:

$$\frac{\delta^2 \vec{E}(z)}{\delta z^2} + (k_0^2 \epsilon - k_x^2)\vec{E} = 0 \tag{3.25}$$

Again using Maxwell's curl equations (3.20) and (3.21), one can derive the wave equation for transverse-magnetic (TM, only H_y, E_x and E_z non-zero) and transverse-electric (TE, only E_y, H_x and H_z non-zero) modes:

$$TM: \qquad \frac{\delta^2 H_y}{\delta z^2} + (k_0^2 \epsilon - k_x^2)H_y = 0 \tag{3.26}$$

$$TE: \qquad \frac{\delta^2 E_y}{\delta z^2} + (k_0^2 \epsilon - k_x^2)E_y = 0 \tag{3.27}$$

We look again at figure 3.3 and only consider solutions that are bound to the metal surface. This implies that the field decays exponentially when moving away from the interface (z=0) with a characteristic evanescent decay length in the metal $z_m = 1/|k_m^\perp|$ and dielectric layer $z_d = 1/|k_d^\perp|$, with $k_m^\perp$ and $k_d^\perp$ the components of the wavevector perpendicular to the interface. Consider a TM wave:

$$z > 0 (dielectric): \qquad H_y(z) = A_d e^{ik_x x} e^{-k_d^\perp |z|} \tag{3.28}$$

$$z < 0 (dielectric): \qquad H_y(z) = A_d e^{ik_x x} e^{-k_m^\perp |z|} \tag{3.29}$$

Analogous expressions for E_x and E_z can be derived from (3.20). From the TM-wave equation (3.26) and the continuity of H_y and ϵE_z, one can derive the dispersion relation for these surface-bound waves, called surface-plasmon polaritons (SPP):

$$k_{SPP} = k_x = k_0 \sqrt{\frac{\epsilon_d \epsilon_m}{\epsilon_d + \epsilon_m}} \tag{3.30}$$

Using a similar reasoning, one can show that there are no non-zero solutions for a TE-polarized SPP because of the continuity of E_y. Thus, only TM-polarized surface plasmon polaritons exist. The dispersion relation (3.30) of a SPP at an air ($\epsilon_d = 1$) - metal interface is plotted for a Drude metal following (3.8) and

(3.9) in figure 3.4. Remember that the dispersion shown in this figure takes the absorptive character of the Drude metal into account ($\epsilon_i \neq 0$), but does not include the interband transitions. Nevertheless it is instructive to take a closer look at the resulting SPP dispersion. We find three different regimes. Radiative modes occur when $\omega > \omega_p$, where the solutions for k_x lie above the light line $k = \frac{\omega n}{c}$. We are more interested in the bound modes below the light line $\omega < \omega_{sp}$. For the smaller wavevectors, k_{SPP} is very close to $\frac{\omega n}{c}$, implying that the modes are almost radiative and stretch over multiple wavelengths into the dielectric material. At large wavevectors, the frequency of the SPP approaches the characteristic surface plasmon frequency $\omega_{sp} = \omega_p/\sqrt{(1 + \epsilon_d)}$. For these modes, the group velocity $v_g = \frac{d\omega}{dk}$ approaches zero and the mode requires the properties of an electrostatic surface plasmon. There also exists an intermediate regime $\omega_{sp} < \omega < \omega_p$, where k_{SPP} is mainly imaginary. We will not further discuss these so-called quasi-bound modes.

The dispersion of SPPs a Ag/air interface strongly resembles that of the Drude model in figure 3.4. For gold however, interband absorption below 600 nm completely alter the dispersion relation. Figure 3.5 shows the dispersion relation of $Re(k(\omega))$ and $Im(k(\omega))$ for a gold-air and gold-water interface, using the dielectric function of the gold sputtered in our cleanroom (see figure 3.1). Although less pronounced, we can still distinguish the different regions described before, including the bound SPP modes below the light line.

The confinement of the SPP to the metal-dielectric interface can be quantified from the inverse components of the wavevector perpendicular to the interface $z_m = |k_m^\perp|^{-1}$ and $z_d |k_d^\perp|^{-1}$. These are calculated from the TM wave-equation (3.26):

$$k_m^\perp = \sqrt{k_{SPP}^2 - \epsilon_m \frac{\omega^2}{c^2}} \tag{3.31}$$

$$k_d^\perp = \sqrt{k_{SPP}^2 - \epsilon_d \frac{\omega^2}{c^2}} \tag{3.32}$$
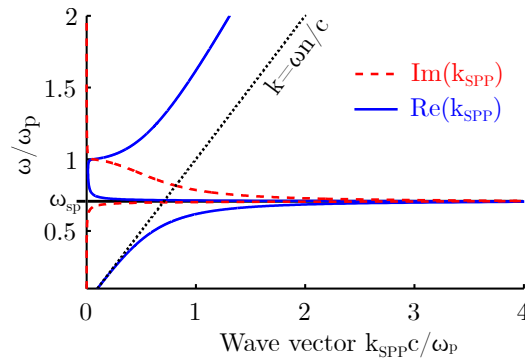

Figure 3.4 Dispersion relation of a SPP on an air-metal interface for a Drude metal.
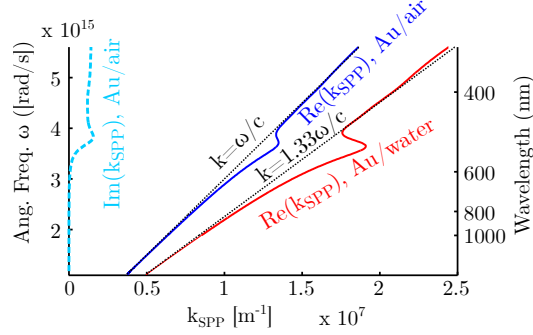
Figure 3.5 Dispersion relation of a SPP on an gold-air and gold-water interface based on the measured dielectric function of the in-house sputtered gold used in this work.

From the imaginary part of the wavevector parallel to the interface, we can also calculate the propagation length L of the SPP. In non-ideal metals, the SPP is attenuated by absorption, resulting in a finite propagation length:

$$L = \frac{1}{2\,\text{Im}(k_{SPP})} \qquad (3.33)$$

Figure 3.6a shows the field confinement and figure 3.6b the SPP-propagation length for an air/gold interface based on the measured dispersion of our sputtered gold. At 785 nm $z_m \cong 25\,\text{nm}$, $z_d \cong 0.6\,\mu\text{m}$ and the propagation length $L \cong 50\,\mu\text{m}$. Above ω_{sp}, modes that have a shorter extend in the dielectric layer also have a reduced propagation length because they extend longer into the metal. A larger fraction of the mode in the metal will result in a stronger absorption.
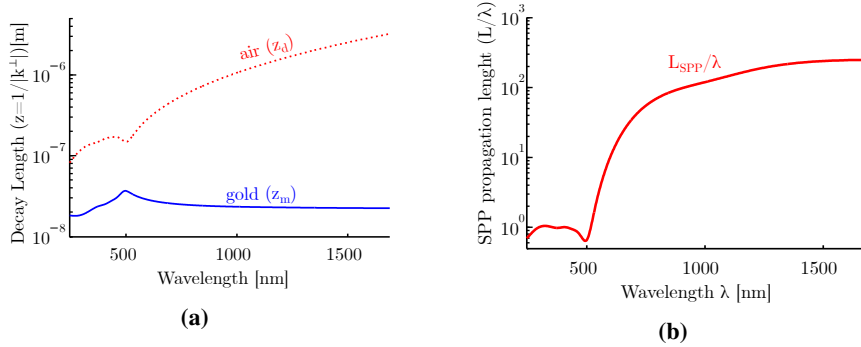

Figure 3.6 (a) Confinement of the SPP to an air/gold interface, quantified by its extend into the metal layer z_m an dielectric layer z_d. (b) Propagation length L of an SPP attenuated by an absorptive gold layer. In both figures, we used the dispersion relation of in-house sputtered gold.

3.1.4   PSPPs in a Metal-Dielectric-Metal structure

Now consider a three-layer system consisting of a thin layer of dielectric with thickness g sandwiched in between two identical semi-infinite metal layers, as
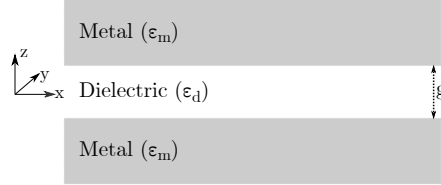
shown in figure 3.7.

Metal (ε_m)

Dielectric (ε_d)

g

Metal (ε_m)

Figure 3.7 The MDM structure: A thin dielectric layer (thickness g) sandwiched between two metal half-spaces.

One can again write the field components H_z, E_x and E_z in each layer and apply the boundary conditions requiring continuity of H_y and $\epsilon_i E_z$. The dispersion relation has two possible solutions:

$$Symmetric: \qquad \tanh\left(k_d^{\perp}\frac{g}{2}\right) = -\frac{\epsilon_d k_m^{\perp}}{\epsilon_m k_d^{\perp}} \qquad (3.34)$$

$$Anti-Symmetric: \qquad \tanh\left(k_d^{\perp}\frac{g}{2}\right) = -\frac{\epsilon_m k_d^{\perp}}{\epsilon_d k_m^{\perp}} \qquad (3.35)$$

It can be shown that these solutions correspond to a symmetric (S) mode (E_x S, H_y and E_z AS) and an anti-symmetric (AS) mode (E_x S, H_y and E_z AS). This mode degeneracy and the corresponding symmetry can be understood from figure 3.8. The arguments are analogous to that of bonding and anti-bonding states in coupling atom orbitals. Opposite charges attract each other in the S (bonding) mode, requiring less excitation energy and thus occurring at lower frequencies. In the next section, we will explain that the AS mode will not be excited in an end-fire coupled MDM configuration and thus is not of interest for the rest of this study. Hence, we focus on the symmetric mode.
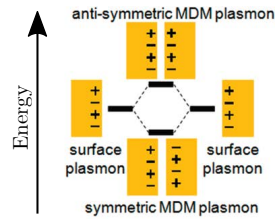

Figure 3.8 Hybridization of the SPP modes in a metal-dielectric-metal layer (adapted from [6])

The relation between $k_d^{\perp}$, $k_m^{\perp}$ and k_{SPP} was derived from the TM wave equation in (3.31) and (3.32). We substitute these in the symmetric dispersion relation (3.34) and solve this equation numerically using the dielectric function of our sputtered gold. Figure 3.9 shows the dispersion for the symmetric mode for widths g ranging from 160 nm to 10 nm. A thinner dielectric layer results in a better confined mode (further away from the light line) with a lower frequency. For wider layers, the

dispersion converges to that of the metal-dielectric cavity, while for narrower gaps ($\leq$40 nm), the dispersion becomes strongly dependent on the gap size. As the mode gets more confined with thinner dielectric layers, the decay length of the field in the metal decreases (figure 3.10a). Nevertheless, a larger fraction of the mode will be in the metal layers. As a consequence, the propagation length L, calculated from (3.33) in figure 3.10b, decreases to a few micrometers for a 10 nm thick layer.
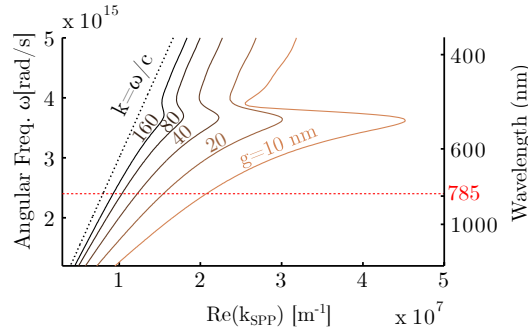

Figure 3.9 Dispersion relation for an air layer with thickness g sandwiched between two semi-infinite gold planes. A smaller gap gives a lower frequency for the same k_{SPP}. The dashed line shows the 785 nm pump laser used in all our SERS experiments.
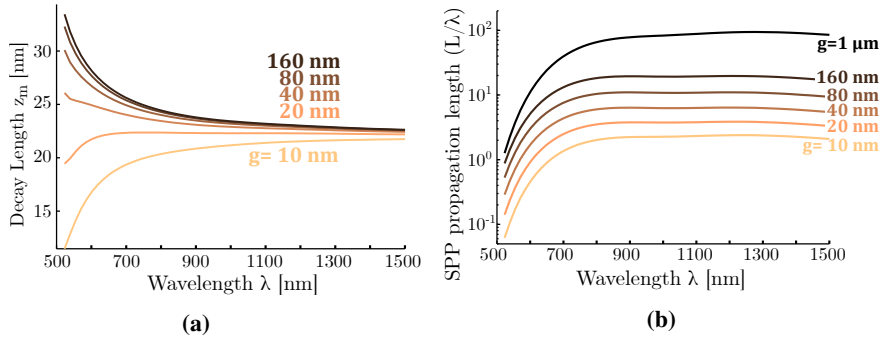

(a)   **(b)**

Figure 3.10 Thinner dielectric layers have more confined modes with shorter propagation lengths. (a) Calculated decay length z_m of the SPP mode in the metal layer in a gold/air/gold sandwich for different thicknesses g of the dielectric.(b) Calculated propagation length L of the SPP.

3.1.5   Excitation of surface plasmon polaritons

As can be seen from figures 3.5 and 3.9, the dispersion curve of SPPs lies below the light line. Thus confined SPPs have a k_{SPP} which is larger than $k = \frac{wn}{c}$. Because of momentum conservation, a SPP on an infinite metal/dielectric interface, as shown in figure 3.3, can not be directly excited by a free-space electromagnetic wave in the dielectric layer. Nevertheless, different techniques exist to excite PSPPs. Prism-coupling using a Kretschmann configuration is conceptually one of

the easiest approaches for a phase-matched excitation of SPPs. In this configuration (figure 3.11a), a thin metal layer is evaporated on a glass prism ($\epsilon_{g=2.1}$). This creates a glass-metal-air sandwich. An incident wave from the glass side under an angle θ will have an increased $k_x = k\sqrt{\epsilon_g}sin(\theta)$, which can excite a SPP at the air-metal interface at a specific frequency. This principle is used in commercially available surface-plasmon resonance biosensors (e.g Biacore SPR$^{\text{TM}}$), where variations in the refractive index of the top dielectric layer are monitored through changes in the angle under which a SPP is excited for a specific frequency. Figure 3.11b shows the dispersion relation for a SPP on a gold-air interface, where a SPP is excited at a wavelength of 785 nm using prism coupling under an angle θ of 45°. For simplicity, the influence of the glass on the dispersion relation is neglected here.
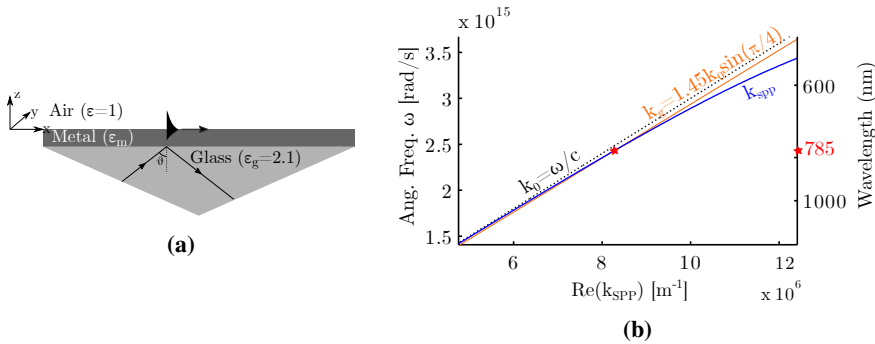

(a)

(b)

Figure 3.11 (a) Kretschmann configuration using a glass prism coated with a thin metal layer to excite SPPs at the metal/air interface. (b) Dispersion equation for gold-air interface. Phase matching is satisfied for exciting an SPP at 785 nm using the Kretschmann configuration with an angle of incidence $\theta = \pi/4$.

Various alternative approaches for a phase-matched excitation of SPPs exist. Similar to the Kretschmann coupling, one can use prism coupling from the top dielectric layer in an Otto configuration. Alternatively, the prism can be replaced by an oil-immersion, high numerical aperture objective, or the wavevectors can be matched using periodic gratings. A variant of the latter can occur in periodic nanodome structures, described in section 3.2.4

End-fire coupling offers an entirely different approach for an efficient and broadband excitation of SPPs. The coupling efficiency is determined by the spatial overlap between the free-space exciting mode and the SPP-mode. Using tightly-focused beams edge-coupled to a silver/air interface, couping efficiencies of up to 90% can be achieved [7]. For those familiar with integrated photonics, we can make the analogy to vertical coupling using grating couplers and horizontal coupling through the facet of a cleaved chip. Horizontal coupling can have a high coupling efficiency over a broad spectral range, while grating-couplers typically have a bandwidth limited to approximately 10 nm.

We look again at the MDM structure, but now it is semi-infinite along x, starting at $x = 0$ (figure 3.12).

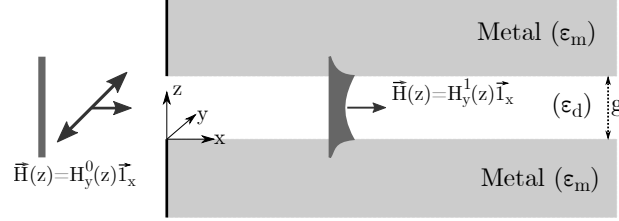Remember that only TM-polarized SPPs exist, whose wave equation is given by

Figure 3.12 End-fire coupling can be used to excite symmetric SPPs in a metal-dielectric-metal structure.

(3.26). Now consider the end-fire coupling of this structure by an incident plane wave $H_y^0(z)\vec{1}_x$ at $x \leq 0$. The coupling efficiency η between this plane wave and the SPP can be calculated from the spatial overlap of the modes [8]:

$$\eta = \frac{\left[\int H_y^0(z) H_y^{1*}(z)\mathrm{d}z\right]^2}{\int H_y^0(z) H_y^{0*}(z)\mathrm{d}z \int H_y^1(z) H_y^{1*}(z)\mathrm{d}z} \qquad (3.36)$$

Here, $H_y^0(z)$ and $H_y^1(z)$ are the field distributions of H_y for respectively the incident plane ($x \leq 0$) wave and the gap-SPP mode($x \geq 0$). For the incident plane wave, $H_y^0(z)$ is uniform across the gap as long as $g \ll \lambda_0$. This condition is satisfied in an MDM sandwich with strongly coupled modes, where g is typically smaller than 40 nm (figure 3.9). From (3.36) we see that η is zero if $H_y^1(z)$ is symmetric, which explains why the anti-symmetric solution in equation (3.35) (E_x AS, H_y and E_z S) cannot be excited in this configuration. Hence $H_y^1(z)$ has to be anti-symmetric. Sun et al. [8] calculated that the funneling coefficient $Q_f = \sigma/g$ increases with decreasing gap width (within the validity of an electromagnetic model, $g > 3$ nm). Here σ is a coupling cross section defined as the fraction of the incident beam that equals the guided power in the SPP ($\sigma = P_1/I_0$). In other words, coupling into smaller gaps results in a higher irradiance inside the gap.

3.2 Localized surface plasmon polaritons in gold nanodomes

The field enhancement in a nanodome-structured surface can to a large extend be explained from the dispersion relation of the metal-dieletric-metal sandwich derived in the previous section. In this section, we make a stepwise transition from the 1D confined plasmonic modes in a MDM sandwich to a 3D confined plasmonic mode in a nanodome. It is worth to first take a sneak peek at figure 3.18, showing this nanodome surface.

3.2.1 Resonances in a MDM cavity

Until now, we have considered SPPs that are one-dimensionally bound to the metal-dielectric interface. For an ideal metal ($\epsilon_i = 0$) these would propagate

over an infinite distance. For a realistic metal, the propagation is attenuated, with a characteristic propagation length L of 1-10 μm in a MDM sandwich (figure 3.10b). Now we make a transition from the MDM structure to the two-dimensional cavity shown in figure 3.13, following a reasoning inspired by [6].
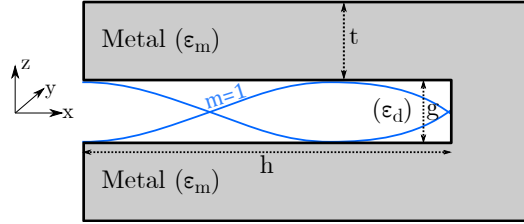

Figure 3.13 A metal-dielectric-metal cavity with width g and length h is open on one side and closed with a metal mirror on the other side. The cavity will resonate for SPP waves with an antinode on the metal end and a node on the open end.

The cavity has an open dielectric end on the left side and a closed, reflective metal end on the right side. Similar to figure 3.12, a SPP is end-fire coupled and propagates over a distance h until it reflects with a π phase-shift at the metal end. Light will resonate in the cavity for wavelengths that allow the formation of a standing wave with an anti-node at the metal surface and a node at the open end. This implies that k_{SPP} satisfies the following relationship:

$$hk_{SPP} = \pi(m + \frac{1}{2}) \tag{3.37}$$

Here $m \in \mathbb{N}^+$ is the mode of the resonance, illustrated for $m = 1$ in figure 3.13. As long as the thickness t of the metal layer is larger than the penetration depth z_m of the field in the metal, the symmetric dispersion relation for a MDM-sandwich is valid (3.34). From figure 3.10a, we know that this assumption is definitely valid for $t > 50\,\text{nm}$ (which is the case for the gold nanodomes). Equation (3.34) and the cavity resonance condition (3.37) allow to calculate the resonance position for a given length h and width g. Figure 3.14a shows the influence of h in a gold/air cavity with fixed gap width ($g = 20$ nm). With increasing length h, the resonant wavelength redshifts and higher order modes appear. The influence of cavity width g on different lengths is plotted in figure 3.14b. As mentioned before (see figure 3.9), decreasing the thickness of the dielectric layer in an MDM-sandwich leads to SPPs with lower excitation frequencies.

We compare the calculated resonant wavelength for a gold/air cavity to the results of a two-dimensional FDTD-simulation for different cavity lengths h and gaps g in figure 3.15. Both simulated and analytical solutions used the measured dielectric function of the cleanroom-sputtered gold. From the simulation, we derive two parameters for determining the resonant wavelengths: the absorption cross section σ_{abs} ([m]) and the normalized field amplitude $|E|/|E_0|$ along the cavity in the middle of the gap ($z = 0; x = 0 \rightarrow h$, along the red dashed line in figure 3.15a). Here, $|E_0|$ is the amplitude of the electric field without cavity. For all geometries,
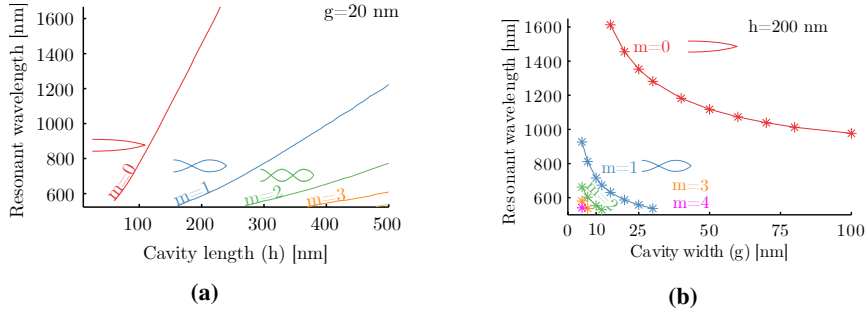
Figure 3.14 Resonant modes for a gold/air cavity with width g and length h (a)The resonant wavelength λ_R redshifts with increasing h for a fixed gap width ($g = 20\,nm$). Higher order modes appear for longer cavities (b) λ_R redshifts with decreasing width of the dielectric layer for a fixed cavity length ($h = 200$ nm).

there is a strong correlation between the field enhancement and absorption cross section: both allow to identify the spectral position of the resonances. This can be expected from the coupling η of the incident photon field to the cavity, which is proportional to the squared average field (3.36). At resonance, light will couple more efficiently into the cavity. Hence the free-space resonant wavelength λ_0 can be experimentally measured from a reflective absorbance measurement, as used for characterizing the nanodome SERS substrates in section 3.4. The increasing absorption below 600 nm is a consequence of the interband-transitions of the gold, as was shown in figure 3.1. The dashed vertical lines show the calculated resonance position. For the 2 µm long cavity (3.15e), there is an excellent agreement between the calculated resonance and the simulated field profile or absorption cross section. As expected from figure 3.14, the modes blueshift for shorter cavities and narrower gaps. Furthermore we see that the field enhancement is stronger for lower order modes. This field enhancement further increases with decreasing the gap width, illustrated for a 200 nm long cavity with 50, 20 and 10 nm wide gaps in the right column of figure 3.15.

The simulated and calculated resonance positions start to diverge for shorter cavities with lower order modes. For example, in a 100 nm long cavity with 20 nm gap the simulated fundamental resonant mode is redshifted by 200 nm with respect to the predicted resonance position (3.15a). We believe this is due to the non-pure TM-modes at the open end of the cavity. The dispersion equation (3.34) assumes an infinitely long MDM-sandwich, this approximation becomes decreasingly valid for shorter cavities. A higher fraction of the mode is also concentrated at the open end of the cavity for lower order modes. It is especially this case that is of most interest for SERS because the magnitude of the E-field is highest for the lowest order resonant mode. In order to tune this fundamental resonance to a 785-900 nm wavelength region of Raman pump and Stokes emission, the cavity length (h) has to become smaller than 100 nm.
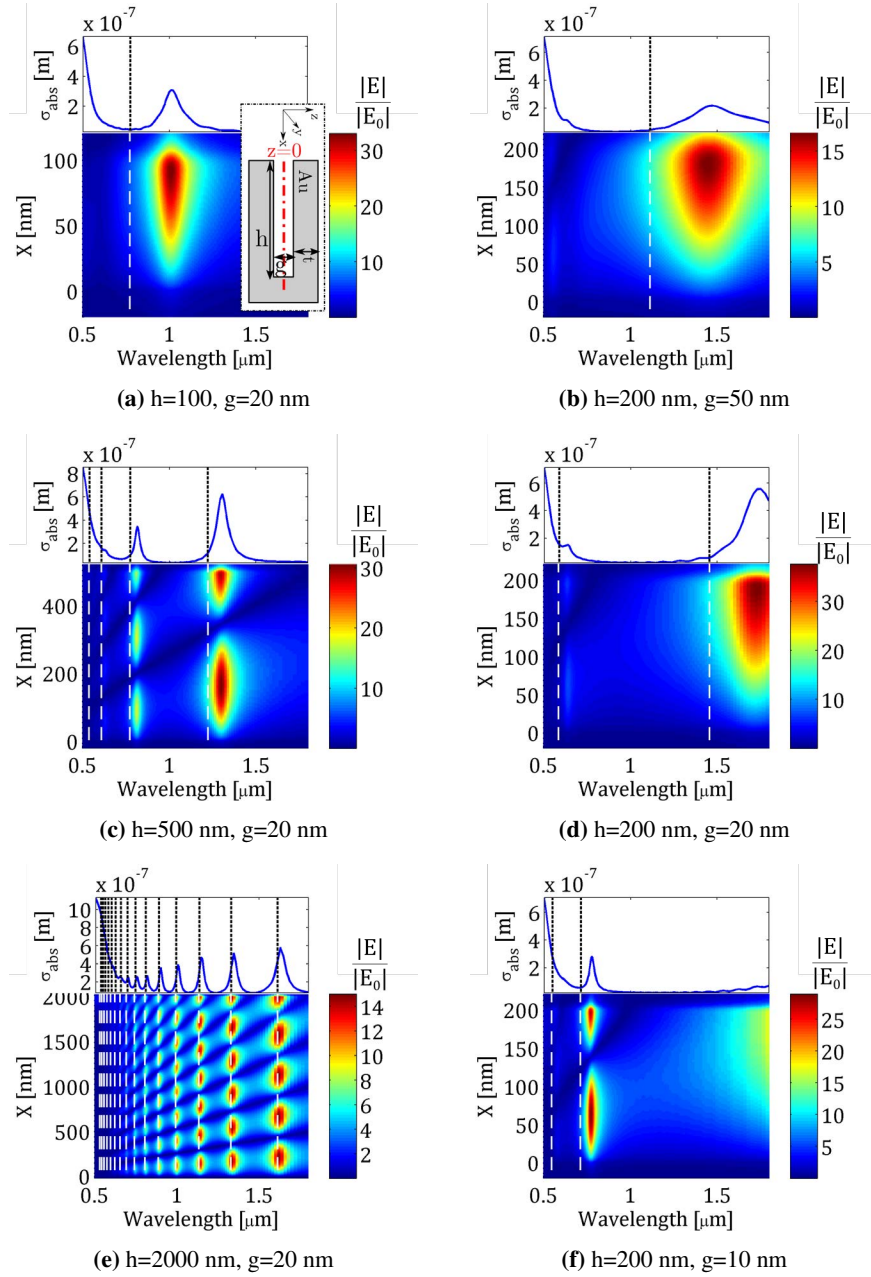
(a) h=100, g=20 nm

(b) h=200 nm, g=50 nm

(c) h=500 nm, g=20 nm

(d) h=200 nm, g=20 nm

(e) h=2000 nm, g=20 nm

(f) h=200 nm, g=10 nm

Figure 3.15 Simulated and calculated resonances of the SPP in a 2D MDM cavity for increasing cavity length h (a,c,e) and decreasing cavity width g (b,d,f). The absorption cross section σ_{abs} (blue curves) correlates well with the field intensity across the center of the cavity (color plots). The dashed lines show the calculated resonant positions from the symmetric MDM dispersion relation and the cavity resonance condition.
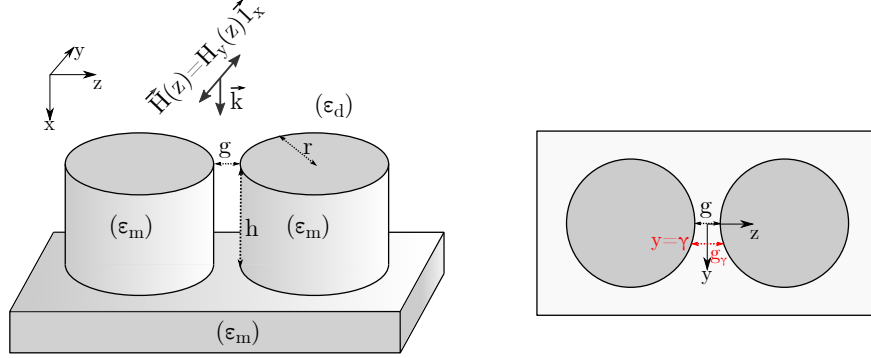
Figure 3.16 A pair of metal nanowires with gap g and height h forms a three dimensional cavity for SPPs in the interwire-gap.

3.2.2 3D confinement in a two-nanowire cavity

We make the transition from a two-dimensional MDM-cavity to a three-dimensional pair of parallel gold nanowires with height h and radius r separated by gap g, shown in figure 3.16. We again assume $r > z_m$. This geometry can be considered as a continuum of infinitesimally thin MDM layers with decreasing gap size, as argued by Bora et al. [6][2]. From the dispersion relation of SPPs in a MDM-sandwich (figure 3.9), we have seen that the energy of a SPP is lower in structures with smaller gaps. Thus the electromagnetic field will be confined to the energetically favorable region with the smallest nanowire separation. From a charge density perspective (figure 3.8), opposite charges in both wires will minimize the dipole energy at shorter distances. The smaller the radius of curvature, the stronger the intensity gradient will be, or the more the mode will be confined to the inter-wire gap. The efficiency η with which the incident plane wave couples to the SPP mode is still given by (3.36). If the incoming field is constant across the gap ($g \ll \lambda$), η is quadratically proportional to the average magnetic field of the plasmon mode H_y^1 at position $y = \gamma$ at the open end of the cavity ($x = 0$):

$$\eta(y = \gamma) \propto \Big[\int H_y^1(0, \gamma, z)\mathrm{d}z \Big]^2 \tag{3.38}$$

The total coupling η_t to the pair of nanowires, a parameter that can be experimentally determined using a reflective absorption measurement, is then given by:

$$\eta_t = \int \eta(y)\mathrm{d}y \tag{3.39}$$

We can also define an effective gap g_{eff} for which the coupling to the MDM cavity is as close as possible to the nanowire pair:

$$g_{eff} = \int \eta(y)g(y)\mathrm{d}y = \int_y g(y)\Big[\int_z H_y^1(0, \gamma, z)\mathrm{d}z \Big]^2 \mathrm{d}y \tag{3.40}$$

---

[2]This approach does not capture multipole modes present in the nanowires [9]

Figure 3.17 shows the results of a 3D FDTD simulation on the two-nanowire cavity ($h = 200\,\mathrm{nm}$, $g = 20\,\mathrm{nm}$, $r = 224\,R$, $\epsilon_d = 1$, $\epsilon_m(\omega) = Au(sputtered)$). The simulated results of an equivalent 2D metal-dielectric-metal cavity were shown in figure 3.15d, whose σ_{abs} is replotted for comparison in figure 3.17a (red dashed curve). In both cases there is a fundamental (m=0) and first order (m=1) resonance. From the absorption cross section and field amplitude (figure 3.17a), we can see that both resonances are blueshifted in the nanowire cavity. This was expected, the increased effective gap size g_{eff} (3.40) implies that a higher photon energy is needed for the excitation of SPPs. Furthermore the spectral range of the fundamental resonance has broadened, which can also be explained by the different gap sizes across the y-axis. This spectral broadening, which results in a decreased quality factor Q, is not accompanied by a decrease in field amplitude. On the contrary, the mode confinement perpendicular to the gap ($\vec{1}_y$) reduces the mode volume V, resulting in an increased field enhancement. This three-dimensional mode confinement is visible from the field-profile cross sections shown for resonant both modes in figure 3.17b-c. It is worth to take a closer look at the XZ-field profiles. Notice that the field amplitude is fairly constant across the gap (not considering the nm-environment of the infinitely sharp top-edges, which do not exist in a physical structure). Inside this gap molecules will experience a field enhancement that depends weakly on the distance to the gold surface. This characteristic is in strong contrast to the SERS distance dependence for isolated nanostructures [10].This limited distance dependence is important for detecting protease activity on gold-bound peptide substrates, as explained in chapter 6.

We have now defined a structure in which the surface plasmon polaritons are confined in all three dimensions. Parallel to the gap (z), the mode is confined by the charges on the metal-dielectric interfaces. Perpendicular to the gap (y), an energy gradient confines the mode to the region with the smallest gold separation. Along the nanowire axis (x), a half-open cavity creates resonant modes. In other words, the propagating surface plasmon polariton (PSPP) of the metal-dielectric interface has now become a localized surface plasmon polariton (LSPP). In this 3D cavity, confined modes exist at discrete frequencies satisfying the resonance condition (3.37). We therefore speak of a localized surface plasmon polariton resonance, commonly abbreviated as LSPR.

Even though the MDM dispersion relation (3.34) and cavity resonance condition (3.37) poorly predict the exact resonance position for geometries that are most interesting for SERS, they do provide useful inside into the behavior of LSPRs in the nanowires. Together with other findings in this sections such as the gap-dependent coupling efficiency, decay length in the metal and SPP propagation length, we can obtain a qualitative understanding of the SERS platform. Important parameters for tuning the resonant wavelength of the zero-order resonant mode are the gap width g, cavity length h, radius of curvature r and dielectric constant of the surrounding material ϵ_d. The confinement of the electromagnetic field to the inter-wire gap increases for smaller gaps and smaller radii of curvature. This increased field enhancement is the main responsible for surface-enhanced Raman scattering. Remember that the derivations made here are valid for only for metal layers thicker
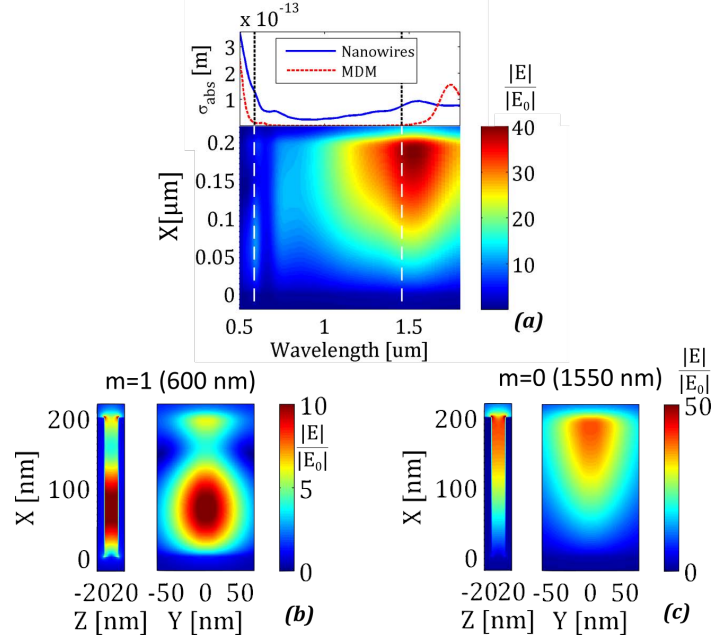
Figure 3.17 A 3D FDTD simulation of a gold double nanowire cavity in air ($h = 200$ nm, ,$g = 20$ nm, $r = 224$ nm) shows broadened and blueshifted LSPP resonances compared to a 2D metal-dielectric-metal cavity. (a) The absorption cross section and field amplitude along the center axis of the cavity show a first order resonance at 600 nm and a zero order resonance at 1550 nm. Dashed lines show the resonance positions calculated from the MDM cavity- and dispersion equation. (b) Amplitude of the electric field enhancement ($|E|/|E_0|$) for the first order mode in the plane parallel (ZX) and perpendicular (YX) to the nanowire gap. (c) $|E|/|E_0|$ for the fundamental mode.

than the penetration depth of the field into the metal($z_m > 50$ nm) and sufficiently wide gaps ($g > 3$ nm). Furthermore we only considered a single nanowire-pair on a metal surface.

3.2.3   From a nanowire pair to a nanodome pair

The two-nanowire cavity has strong similarities to the geometry of the gold nanodome SERS platform (figure 3.18). The fabrication and characterization of these structures is described in sections 3.3 and 3.4. Compared to the two-nanowire cavity, there are two significant differences with the gold nanodome platform: the top edge of the domes is rounded with radius of curvature r_d and the nanodomes are packed in a hexagonal periodic structure. We first discuss the influence of r_d. Consider the nanodome pair presented in figure 3.18a. Rounding the top edge of the nanowires will decrease the effective cavity length $h_0 < h_{eff} < h$, where h_0 is the length of the straight part of the cavity. From the cavity resonance condition (3.37), we know that this rounding will results in a blueshift of the resonant modes. We also know that the mode will still be confined to the region with the smallest
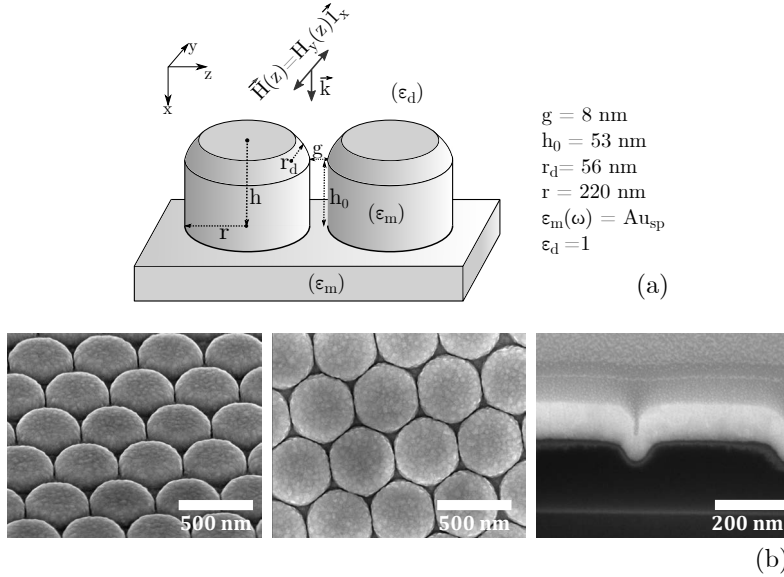
Figure 3.18 (a) A nanodome dimer can be modeled as a nanowire pair where the top edges are rounded with radius r_d. The mentioned values of the geometrical parameters are derived from (b), which shows an SEM tilted view, top view and cross section of a gold-nanodome patterned surface.

gap because this is energetically more favorable. Figure 3.19 shows the field amplitude and absorption cross section for a two-nanodome cavity with 10 nm gap width g, 70 nm height h_0 a 30 nm radius of curvature r_d, realistic dimensions for a fabricated nanodome pair. These results are compared to equivalent nanowire cavities with $h = h_0$ and $h = h_0 + r_d$, all calculated from a 3D FDTD simulation. As expected, the resonant wavelength of the fundamental mode in the nanodome cavity lies in between that of these nanowire cavities. For the rounded nanodomes, both the absorption cross section and field amplitude plot show a broadened resonance. This time, the decrease in Q-factor is not compensated by a reduction in mode volume. Hence the field enhancement decreases in comparison to the non-rounded nanowires, as can be seen from figure 3.19b. For example, the 100 nm long nanowire cavity, shown in the rightmost plot of figure 3.19b, has a fundamental resonance centered around 1000 nm. Based on the wavelength-dependent maximum intensity of the electric field in the cavity $|E|^2/|E_0|^2$ (figure 3.20), this resonance has a Q-factor ($\delta\omega/\omega$) of 6.2, a bandwidth of 150 nm at FWHM and a maximum field enhancement $|E|^2_{max}/|E_0|^2$ of 7.3×10^3. In contrast, the nanodome cavity with $h_0 = 70$ nm and $r_d = 30$ nm has a Q-factor of 3.9, bandwidth of 225 nm and $|E|^2_{max}/|E_0|^2$ of 3.9×10^3.

Note that a further broadening of the plasmonic resonance is not necessarily bad for SERS experiments, even at the cost of a lower field enhancement. Obviously, a narrower resonance would further tighten the fabrication tolerances. Furthermore, larger Raman shifts may require a broad resonance to enhance both pump

and Stokes wavelengths. For example, lipids have characteristic Raman peaks around $2900 \, \mathrm{cm}^{-1}$ and the SiN used as a waveguide material in chapter 4 can be identified by a Si-H stretch at $2330 \, \mathrm{cm}^{-1}$ [11]. At an excitation wavelength of 785 nm, these large Stokes shifts correspond to an emission wavelength of respectively 1016 and 961 nm, demanding a resonance broader than 200 nm for both excitation and radiation enhancement. However, the quantum efficiency of silicon detectors decreases rapidly above 950 nm (figure 2.9b) and therefore our Raman system is poorly suited for a study of such large Stokes shifts. We are mostly interested in Stokes shifts of organic molecules in the 600 - 1800 cm^{-1} range, corresponding to a 39 - 129 nm wavelength shift. For these smaller Stokes shifts, r_d should be as small as possible to achieve a maximal SERS enhancement. Unfortunately our fabrication process offers little control over this parameter.
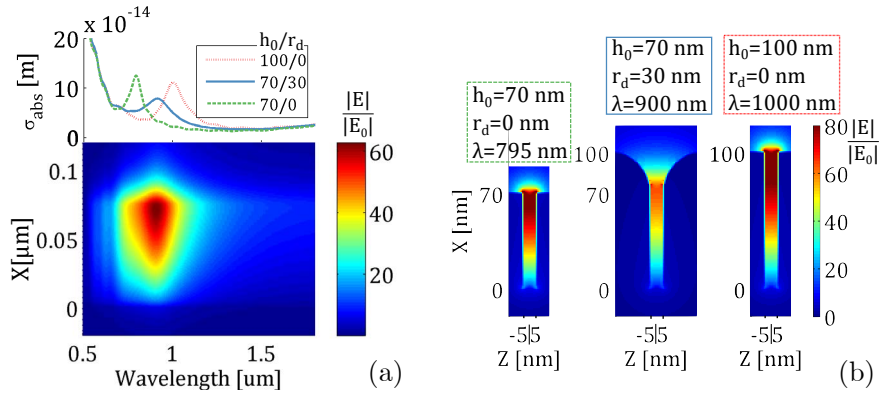

Figure 3.19 The rounded edges in a two-nanodome cavity result in a broadened LSPR with decreased field enhancement. This is simulated here for a $g = 10 \, \mathrm{nm}$, $h_0 = 70 \, \mathrm{nm}$ and $r_d = 30 \, \mathrm{nm}$ two-nanodome gold/air cavity (a) Field amplitude at the center of the nanodomes showing the spectral position of the broadened fundamental resonance. A comparison of the nanodome's absorption cross section to that of nanowire cavities with $h = h_0 + r_d$ and $h = h_0$ shows that the nanodome resonance is located in between that of the latter two. (b) Field amplitude in the XZ-plane for a (left) $h = 70 \, \mathrm{nm}$ nanowire cavity, (middle) a $h_0 = 70 \, \mathrm{nm}$ and $r_d = 30 \, \mathrm{nm}$ nanodome cavity and (right) a $h = 100 \, \mathrm{nm}$ nanowire cavity
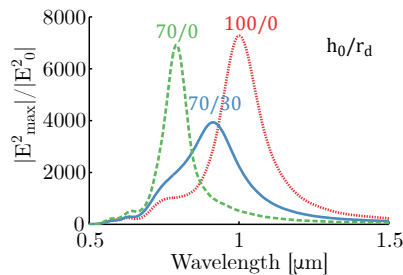

Figure 3.20 Maximum field intensity in the gap for two-nanodome (blue, solid) and two-nanowire cavities (green dashed and red dotted). Rounding of the nanodomes ($\uparrow r_d$) spectrally broadens the resonance, lowering the Q-factor and field enhancement.

3.2.4   From a nanodome dimer to a periodic nanodome structure

In the previous sections we looked at a single cavity consisting of two coupled nanowires or -domes in air without considering the influence of other structures in the vicinity. This approach is justified by the fact that the electromagnetic field is strongly confined to the gap, with decay lengths that are much smaller than the surrounding metal layers. However, a periodic structure can also excite a Bloch wave SPP on the gold/dielectric interface in the YZ plane [12]. Here, we investigate how the periodicity of the structure could be used to further optimize the enhancement of the nanodome SERS platform.

The wavevector for a propagating surface plasmon on a metal/dielectric interface was calculated in equation (3.30). We call this wavevector $\vec{\beta}_{SPP} = \beta_y \vec{1}_y + \beta_z \vec{1}_z$. This is not to be confused with the wavevector of the localized surface plasmon mode in the cavity $\vec{k}_{LSPP} = k_x \vec{1}_x$. Momentum conservation is satisfied if a combination of the in-plane wavevector for a wave incident under angle θ (normal to the surface) $k_\parallel = nk_0 sin(\theta)$ and the reciprocal grating vectors matches the SPP wavevector. Here θ is the angle between the incident wavevector and the normal to the surface.

$$\vec{k}_\parallel + m\vec{G_1} + n\vec{G_2} = \vec{\beta}_{SPP} \tag{3.41}$$

$$|\beta_{SPP}| = k_0 \sqrt{\frac{\epsilon_d \epsilon_m}{\epsilon_d + \epsilon_m}} \tag{3.42}$$

The nanodomes form a 2D hexagonal crystal with lattice vectors $\vec{a_1}$ and $\vec{a_2}$ that make an angle of 120° and both have magnitude $2r_0$. Here, $r_0 = r + g/2$ is the radius of the polystyrene beads used for fabricating the nanodome pattern, as explained in the next section. The lattice and its unit cell are shown in figure 3.21a. Figure 3.21b shows the reciprocal lattice, its first Brillouin zone and the irreducible Brillouin zone. The magnitude of the reciprocal lattice vectors $|\vec{G_1}|$ and $|\vec{G_2}|$ equals $\frac{2\pi}{r_0\sqrt{3}}$. The dispersion of the SPP modes for $r_0 = 224$ nm is shown in figure 3.21c (not considering band splitting). All modes are degenerate for perpendicular incidence($\mathbf{\Gamma}, k_\parallel = 0$) because of the equal magnitude of $\vec{G_1}$ and $\vec{G_2}$. For a gold nanodome pattern with a 448 nm period in water, a PSPP with an angular frequency of 3.3×10^{15} rad/s ($\lambda_0 = 577$ nm) is excited at normal incidence (3.21c). For the same structure in air, the dispersion equation (3.41) has no solution below the plasmon frequency. The situation becomes more complicated for non-normal incidence. In our particular case where self-assembled nanospheres are used as an etch mask, there is no control on the orientation of the crystal axes. Furthermore, line defects in the packing of the polystyrene particles can result in a rotation of the crystal axes (figure 3.21d). Typically the orientation is maintained over tens of micrometers. This is in the same range as the propagation length of the SPP mode (figure 3.6b). Therefore propagating SPPs can still be excited in the structure, however they will scatter strongly at these defect boundaries. Because of
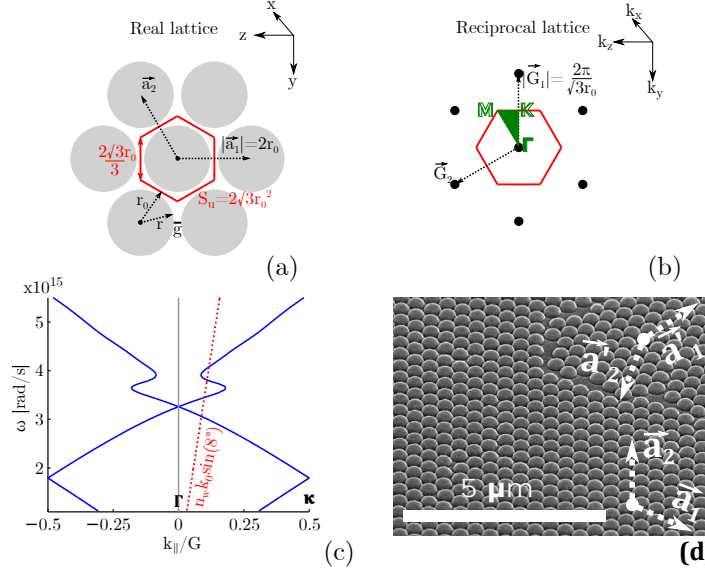
Figure 3.21 The nanodomes are arranged in a hexagonal lattice with periodicity $2r_0$. (a) Lattice in real space with lattice vectors $\vec{a_1}$ and $\vec{a_2}$. The red lines show the unit cell, a hexagon with side length $\frac{2}{3}\sqrt{3}r_0$. (b) Reciprocal space with reciprocal lattice vectors $\vec{G_1}$ and $\vec{G_2}$. The red hexagon marks the first Brillouin zone, with the irreducible Brillouin zone marked in green. (c) Dispersion of the SPP modes for a gold nanodome structure with $r_0 = 224$ nm in water. The red dashed line represents $k_\parallel$ for $\theta = 8°$, as used in the Vis/IR reflection measurements. (d) Tilted SEM image of a nanodome pattern. The orientation of lattice vectors changes at line defects.

this finite periodicity, the spectral range of the excited SPPs will broaden. Experimentally, we determine the presence of PSPP and LSPP modes from the far field specular reflection of a nanodome chip. In our experimental setup, the sample is illuminated by a spot with a diameter of approximately 4 mm. Over the entire area of the spot, we assume that the lattice vectors will have all possible orientations. Hence the measured absorption spectrum will be an average of all the possible orientations of the wavevector of the incoming field projected on the reciprocal lattice vectors $\vec{G_1}$ and $\vec{G_2}$. This implies that the narrowband SPP will present itself as a broadened feature for $\vec{k}_\parallel$ going from the **Γ-K** edge to the **Γ-M** edge in the irreducible Brillouin zone. In other words, PSPPs will be excited 'locally' within regions with the same crystal orientation at wavelengths satisfying (3.41) for the following in-plane wavevectors:

$$\mathbf{\Gamma - K} : \quad \vec{k}_\parallel = -nk_0\sin(\theta)\vec{1}_y \tag{3.43}$$

$$\mathbf{\Gamma - M} : \quad \vec{k}_\parallel = -\cos\left(\frac{\pi}{6}\right)nk_0\sin(\theta)\vec{1}_y + \sin\left(\frac{\pi}{6}\right)nk_0\sin\theta\vec{1}_z \tag{3.44}$$

The corresponding dispersion equation 3.42 for the lowest energy modes at the

two extremes becomes:

$$\mathbf{\Gamma - K}: \qquad k_0 \sqrt{\frac{\epsilon_d \epsilon_m}{\epsilon_d + \epsilon_m}} = \left| \frac{2\pi}{\sqrt{3} r_0} - n k_0 \sin(\theta) \right| \tag{3.45}$$

$$\mathbf{\Gamma - M}: \qquad k_0 \sqrt{\frac{\epsilon_d \epsilon_m}{\epsilon_d + \epsilon_m}} = \left[n^2 k_0^2 \sin^2(\theta) - \frac{2\pi}{r_0} n k_0 \sin(\theta) + \frac{4\pi^2}{3 r_0^2} \right]^{\frac{1}{2}} \tag{3.46}$$
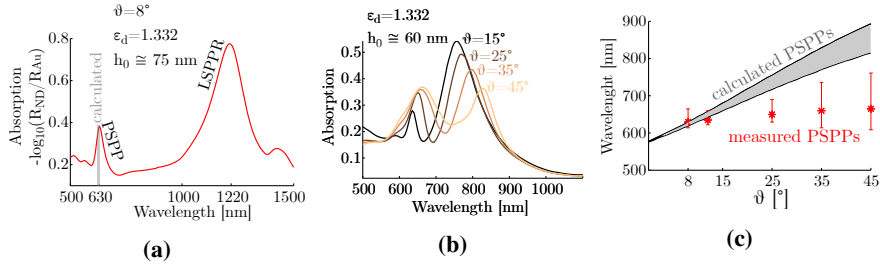

Figure 3.22 Spectral absorption of nanodome samples derived from a specular reflection measurement under different angles of incidence θ. (a) A gold-nanodome chip ($h_0 \approx 75$ nm, $r_0 = 224$ nm, $\theta = 8°$) in water shows a peak around 630 nm, attributed to a PSPP, and a broad absorption centered around 1220 nm, attributed to a LSPR. The wavelength of the PSPP corresponds exactly with the analytically calculated solution. (b) The absorption spectra of nanodomes ($h_0 \approx 60$ nm) measured at larger θ show a broadening of the PSPP and anti-crossing behavior of the PSPP and LSPR modes. (c) Because of the anti-crossing, the measured wavelength of the PSPP deviates from the calculated values for larger θ.

The absorption of the nanodomes is derived from their specular reflection R_{ND} relative to that of a plane gold layer R_{Au} as $A = -\log_{10} \frac{R_{ND}}{R_{Au}}$. In our setup, the minimal angle of incidence θ is $8°$. Figure 3.22 shows the absorption spectrum for a gold nanodome pattern with 448 nm period in water under this angle. We attribute the broadband absorption around 1220 nm to the LSPP resonance in the nanodome gaps and the narrowband absorption at 630 nm to the excitation of PSPPs at the gold/air interface in the XY-plane This is in excellent agreement with the calculated PSPP wavelength from 622 nm to 630 nm from equations (3.45) (red dashed line in figure 3.21c) and (3.46) . The effect of increasing θ is shown in figure 3.22b for a second nanodome-patterned chip, which again has a 448 nm periodicity but a LSPR centered around 755 nm for small θ ($h_0 \approx 60$ nm). As expected, the peak attributed to the PSPP redshifts and broadens for increasing angles of incidence. However, the redshift going from $\lambda_{PSPP} = 635$ for $\theta = 15°$ to $\lambda_{PSPP} = 665$ for $\theta = 45°$ does not follow the calculated dispersion, as shown in figure 3.22c. At the same time, the LSPR also redshifts with increasing angles of incidence, while in a non-periodic structure the spectral position of this resonance should be independent of the angle of incidence. These are two indications of a strong coupling between both modes for non-perpendicular incidence. The PSPP mode is pushed to higher energies and the LSPR mode to lower energies, an anti-crossing behavior also called Rabi splitting [12–14] resulting in a hybrid plasmon mode. Zhou et al. [13] provided an excellent experimental demonstration of this behavior, summarized in figure 3.23.
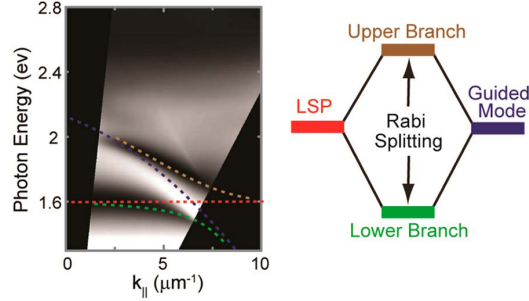
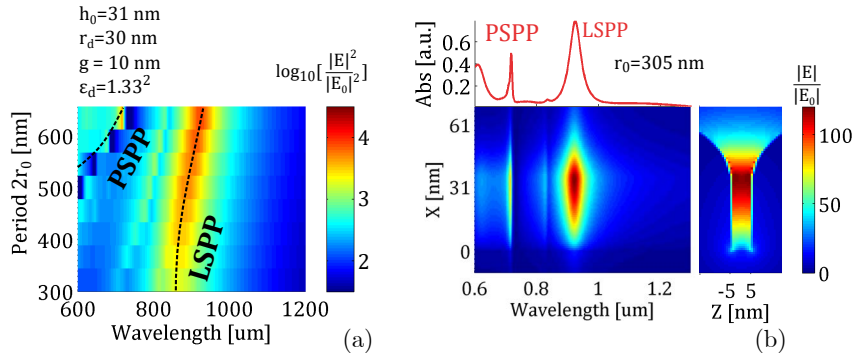**Figure 3.23** Anti-crossing behavior of plasmonic modes. *(Figure copied from [13])*

Figure 3.24 Influence of the hexagonal lattice on the local field enhancement on gold nanodomes ($g = 10\,nm$, $h_0 = 31\,nm$, $r_d = 30\,nm$) in water, simulated using 3D FDTD. The geometry of the structures was chosen to have an LSPR around 830 nm. (a) Average squared field enhancement in the gap (in the XZ plane) versus wavelength for different periods ($2r_0$), showing the anti-crossing behavior of the LSPP and PSPP modes and correlated increase in field enhancement. (b) Absorption and field-enhancement along the center of the gap for a 610 nm period. Strong coupling results in field enhancements $|E|/|E_0| > 10^2$ for the LSPR at 933 nm.

To further investigate this effect, we run a 3D FDTD simulation for periodic nanodomes with different radii r_0, and hence a different periodicity $|a| = 2r_0$. The other geometrical parameters are set such that the simulated LSPR of the isolated nanodome pair lies in the spectral region between the 785 nm pump and 870 nm Stokes wavelengths ($h_0 = 31$ nm, $r_d = 30$ nm, $g = 10$ nm). Figure 3.24a shows the squared field enhancement averaged across the center of the gap in the XZ plane. The strong coupling between the modes is visible at larger periods, where we observe an anti-crossing behavior of the PSPP and LSPP modes, and correlated increase in field enhancement. This is illustrated for $r_0 = 305$ nm in figure 3.24b. At the center of the gap, $|E|/|E_0|$ reaches up to 120 for the fundamental LSPR. In an $|E|^4$ approximation, the local electromagnetic enhancement factor in the hotspot would be 2×10^8.

In conclusion, the periodicity of the nanodome structure $2r_0$ provides an extra parameter to manipulate the plasmonic modes in the nanodome substrate and pos-

sibly achieve an increased enhancement factor. In contrast to the dimensions of the interdome-gap (h and g), we have not experimentally investigated the influence of the bead radius. All experiments described in this thesis use a r_0 of 224 nm. As explained in the next section, the radius r_0 of the nanodomes is determined by the size of the spincoated polystyrene beads. Beads with different sizes are commercially available, thus the influence of this parameter could be studied with relative ease. According to the simulated results from figure 3.24, a larger bead radius would increase the maximum field enhancement. However, this will also have a contrary effect on the SERS substrate enhancement factor (SSEF, see section 3.4.1) because the density of hotspots will decrease proportionally to r_0^{-2}. Also, a further reduction of h_0 below 30 nm is required to blueshift the resonance back to the 785-870 nm range, as the anti-crossing results in a redshifted resonance. It is not trivial to fabricate structures with even shorter MDM cavities because of the rounding of the nanodomes ($r_d = 30 - 50\,\mathrm{nm}$, depending on the gold deposition parameters).

The strong coupling between the 'grating' PSPP mode and the LSPR mode has been used to fabricate strongly enhancing SERS-substrates [15, 16]. The mode coupling can furthermore result in a directional emission of the scattered light [17]. This has, amongst others, been exploited for making plasmonic lasers [12].
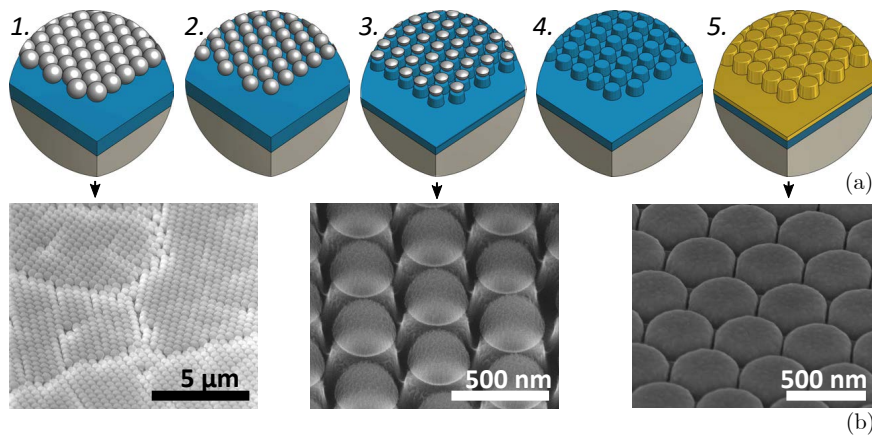
3.3   Fabrication of gold nanodomes

Figure 3.25 (a) Schematic and (b) corresponding tilted SEM figures of the gold-nanodome-array fabrication flow. A monolayer of polystyrene beads (1-2) forms a mask for reactive ion etching (RIE) into the underlying SiN (3-4), resulting in an array of nanopillars that serve as template for gold deposition (5).

We developed a process based on nanosphere lithography (NSL) to fabricate periodic arrays of gold nanodomes, as depicted in figure 3.25. Nanosphere lithog-

raphy is based on the self-assembling of microbeads into a hexagonal (or rectangular) close-packed monolayer. These microbeads are usually polystyrene (PS) or silica spheres with a diameter of 100-1000 nm, which act as a template for etching or material deposition. One of the simplest and most famous applications of NSL is the fabrication of Ag or Au nanotriangles [18] or -dots, shown in figure 3.26b-c. The power of NSL lies in the controllable and scalable fabrication of nanometer-sized structures without the need for expensive and labor-intensive tools such as e-beam lithography. As such, it combines the ease of fabrication of colloidal methods with the reproducibility and substrate uniformity of top-down fabrication methods. However, the technique also has its shortcomings. The uniformity of the pattern is limited by point- or line defects in the monolayer, as well as the formation of multilayer stacks (figure 3.26a). Furthermore, only hexagonal or rectangular periodic structures can be made and there is limited control on the exact position of the nanostructure. Nevertheless, with some creativity a myriad of different structures can be made through NSL [19–22]. Furthermore the controlled fabrication of nanosized gaps we achieved with our NSL-based nanodomes has by far not been reached using e-beam lithography in our lab. We will now describe the different steps in the fabrication process and discuss their influence on the final nanodome substrate. A technical summary of the process flow is given in the methods section.
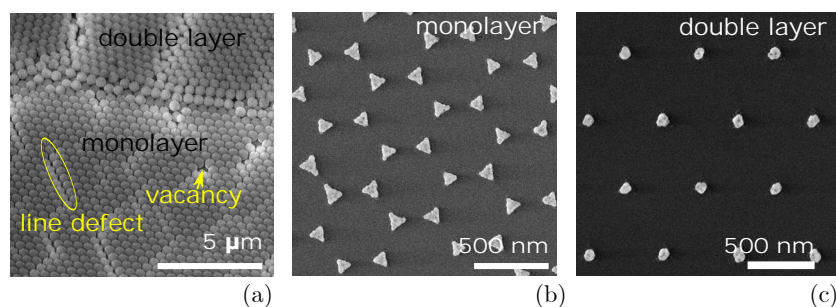

Figure 3.26 Typical applications of nanosphere lithography. (a) Polystyrene beads can form HCP-packed monolayers or multilayers. As in any natural crystal, the 2D lattice has point and line defects. (b) Nanotriangles appear after directional gold deposition and liftoff of a monolayer mask. (c) A double layer mask results in gold nanodots.

3.3.1 Step 1: Spincoating a monolayer of close-packed nanobeads

Various techniques have been described for the formation of a hexagonally close-packed (HCP) monolayer of polystyrene beads on glass or Si wafers, including Langmuir-Blodgett pulling [23], tilted controlled solvent evaporation [24], drop coating [25] and spin coating [26–29]. Here, we opt for spin coating because of its ease of fabrication: spin coating a sample with polystyrene beads takes only a few minutes, regardless of the sample size. The quality of the monolayer depends on the beads, sample, solvents, spin coating parameters and environmental con-

ditions. For a more detailed study on the forces involved in the formation of the monolayer and the influence of each individual parameter, we refer to the systematic studies of Chen et al. [27] and Colson et al. [26]. Here, we only describe our experimentally optimized procedure and briefly discuss the most important hurdles for achieving a good monolayer (figure 3.28).

We start from a 4″ Si wafer on top of which a 200 nm layer of PECVD SiN is deposited. A clean and hydrophilic surface is of crucial importance for the formation of a monolayer. The microbeads will stack against impurities on the wafer and radially obstruct the formation of a monolayer in the spincoating process (figure 3.28c). The surface of the wafer is rendered hydrophilic with oxygen plasma, after which it is stored in water until a few seconds before spin coating. Through an experimental optimization, we acquired a good monolayer quality on 4″ wafers using a three-step spin coating with 700 µl (≈ 10 µl/cm^2) of a 5 $w\%$ solution of 448 ± 13 nm diameter polystyrene beads dissolved in a 2/1 methanol/water mixture:

1. The solution of beads is spread evenly over the wafer during 10 s, accelerating with 100 rpm/s to a spin speed of 400 rpm.

2. A HCP monolayer is formed by accelerating with 450 rpm/s to 900 rpm and spinning for 90 s.

3. The spinning is further accelerated with 300 rpm/s to 5000 rpm for 50 s to remove all solvents and spin off excessive beads that pile up at the edges.

The parameters in the second step are critical for an optimal HCP-monolayer coverage (figure 3.28a-3.28b). The third step is important to generate a dry SiN-PS interface, which avoids the formation of 'micro-explosions' in the vacuum chamber of the RIE (figure 3.28d). Figure 3.27 shows a typical spin-coated wafer, with monolayer coverage of 80-90 % across the surface. Note that the optimal settings can be different in another environment; we achieved poor results when using experimental parameters described in other papers [26, 28] in our cleanroom. The optimal spin speed also depends on the sample size. Smaller substrates require faster spinning and higher accelerations in the second spin-coating step, for example on 4 cm^2 chips an optimal monolayer coating was found when spinning 40 µl at 1400 rpm and 1400 rpm/s for 60 s. Surfactants like Triton X-100 are often suggested for an improved wetting of the substrate [18]. However, these surfactants are not removed during the spin coating and stick in between the polystyrene beads, as shown in figure 3.28e for a $0.15 \, v/v\%$ Triton X-100 in methanol. These remaining surfactants would inhibit etching a well defined inter-dome gap in the next section.

After monolayer formation, two well known SERS substrates can be fabricated by directly depositing Ag or Au on the polystyrene template [18, 25]. Figure 3.26b shows nanotriangles fabricated by evaporating a thin ($< r_0/2$) gold layer followed by removing the polystyrene beads. In chapter 4 we use this method to develop a
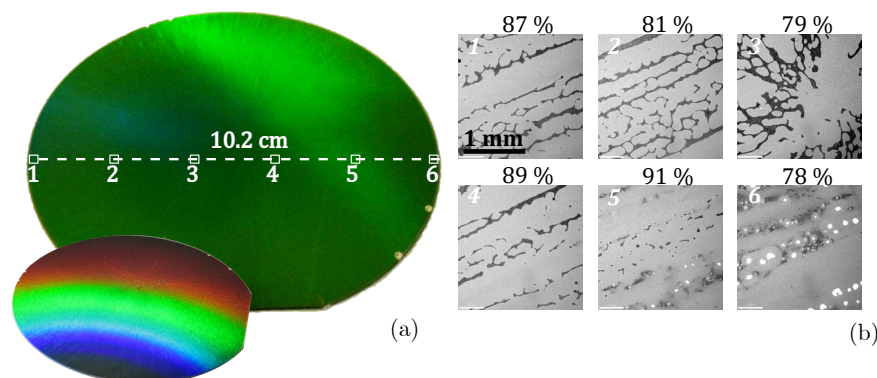
Figure 3.27 (a) Spincoated HCP layer of 448 nm diameter polystyrene beads on a 4″ SiN on Si wafer. The inset shows white light diffraction on this periodically patterned wafer under grazing incidence. (b) Microscope images taken at different positions across the wafer, giving a monolayer coverage of 78 − 91%. The light-gray regions represent HCP-monolayers, the darker consist of a double layer and the white dots at position 5-6 are empty spots on the wafer.

waveguide-based SERS platform. The same method used on a double HCP-layer results in nanodots with a size of approximately 80 nm for 448 nm polystyrene beads (figure 3.26c). These structures have a strongly blue-shifted resonance, un-suited for Raman excitation at 785 nm. If on the other hand a thick metal layer ($> r/2$) is evaporated or sputtered on the polystyrene beads, one obtains a metal-film-over-nanoparticle surface (see table 3.2 on page 3-44). Depending on the deposited metal these are often referred to as AuFON or AgFON [30–32]. Such MFON structures have a strong SERS enhancement in the crevices between the different polystyrene particles.

Instead of direct gold deposition, we introduce an extra etching step to fabricate nanodome samples that offer a superior enhancement and tunability over MFON and nanotriangle substrates. The resulting substrates are also more chemically stable and offer a better control over the accessibility of the gap. In Table 3.2 we compare the SSEF for these different structures, which we fabricated ourselves and characterized using identical procedures.

3.3.2   Step 2: Transferring the bead pattern into a SiN layer

The HCP pattern of polystyrene beads is transferred into the underlying SiN layer using two reactive-ion etches (RIE, step 2-4 in figure 3.25). First, the polystyrene beads are thinned down in an O_2 plasma. A relatively low power and high pressure (75 W, 100 mTorr) are used to obtain a more chemical, isotropic etching. The exact time of this etch will determine the width g of the nanodome gaps, whose influence is experimentally investigated in figure 3.33 on page 3-41. Next, the pattern of the thinned beads is etched into the SiN layer by a highly anisotropic reactive-ion
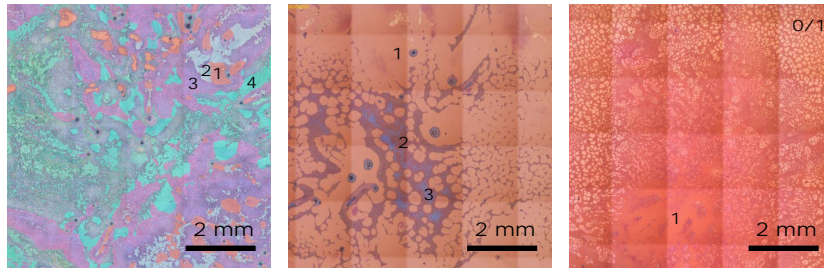
(a) Spin speed (left) Multilayer formation means the spin speed needs to be increased. (middle) A slightly too slow spinning gives a considerable fraction of double layers. (right) Excessive spin speed results in sub-monolayer coverage.
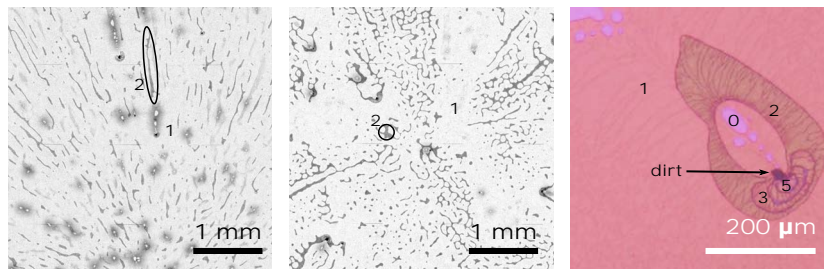
(b) Acceleration (left) High acceleration (1200 rpm/s) leaves radial patterns of double layers (right) Low acceleration (300 rpm/s).

(c) Dirt particles lead to multilayer stacking.
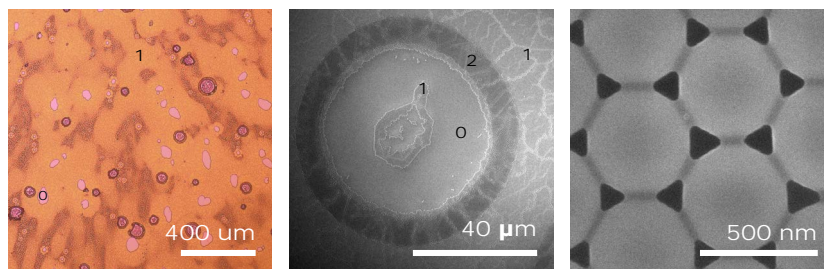
(d) Wet surfaces lead to explosions in the vacuum chamber of the RIE. Flash-drying, a > 5000 rpm spinning step or waiting >24 hours can help.

(e) Surfactants such as Triton X-100 leave a trace between the PS beads.

Figure 3.28 Hurdles encountered when spin coating HCP monolayers of polystyrene beads. The small digits **0-4** give the number of stacked polystyrene layers.

etch ($80 \, \mathrm{sccm} \, CF_4 \, / \, 3 \, \mathrm{sccm} \, H_2$, 210 W, 20 mT, 160 s). Specific details on the anisotropic etching of SiN can be found in [33]. Briefly, the low pressure results in a more physical etching which simultaneously thins down the polystyrene beads while etching the SiN surface in between the beads. The addition of H_2 further increases anisotropicity due to the formation of a polymer protective layer on the SiN side walls. The time of this etching step will determine the depth h of the inter-dome gap, whose influence is experimentally investigated in figure 3.35 on page 3-42. We typically cleave the $4''$ wafer in different samples and use a sweep on both the O_2 (30-70 s, etch rate 0.6 ± 0.12 nm/s) and CF_4/H_2 (70-100 s, etch rate 1.6 nm/s) etch times, because there is an inaccuracy of approximately 20 nm on the thickness of the gold layer that will be deposited in the last step. After etching, the beads are washed off in an ultrasonic bath with ethanol or dichloromethane (carcinogenic!) and the nanostructured chip is cleaned using piranha (dangerous!) and O_2 plasma. Any contamination of the chip surface at this stage is likely to be present in the SERS spectra, so a clean surface is of crucial importance.

3.3.3   Step 3: Gold deposition

First, a 2-5 nm thin adhesion layer is sputtered because gold poorly adheres to the SiN surface. Immediately after, 150 nm gold is sputtered. We typically use a titanium adhesion layer, except if this is not compatible with post processing steps. For example, a sputtered nickel layer was used to withstand the potassium-hydroxide etched Si undercut used for releasing nanodome-patterned microdisks in chapter 5. Recently, a number of studies highlighted that these metallic adhesion layers can strongly damp the plasmonic resonance [34, 35]. They suggested the use of organic layers such as (3-mercaptopropyl)trimethoxysilane as alternative and observed an increase in Q-factor and enhancement factor. Here, the effect of the adhesion layer is minimal because we cover it with a 150 nm thick gold layer. This gold thickness is much longer than the penetration depth z_m of the LSPR in the metal (figure 3.10a), thus the mode does not reach the adhesion layer. We indeed measured no change in SSEF when increasing the thickness of the Ti adhesion layer from 5 nm to 20 nm. The gold can either be thermally evaporated or physically sputtered onto the patterned SiN. Figure 3.29 shows a close up of the gold surface for different deposition methods. The evaporated gold has a poor sidewall coverage and high surface roughness, especially at the bottom of the nanodomes. The sputtered gold offers a more uniform coating and reduced surface roughness, although there are large differences depending on the used sputtering tool. A smooth gold layer is sputtered form the Alcatel SCM600 DC Magnetron sputter tool (partial pressure Argon= 10^{-2} mbar, 1000 W sputter power). This machine also provides the most uniform gold coverage over the entire surface of the wafer, as it uses a large $7''$ Au target (99.99 % pure) and rotating substrates. We did not manage to reach a comparable surface roughness with a Leybold Univex sputterer when varying the Argon partial pressure or sputter power. Furthermore this sputter target has a diameter of only $3''$ (99.999%), therefore the gold thickness will not be uniform on larger samples. For these reasons, we used the Alcatel
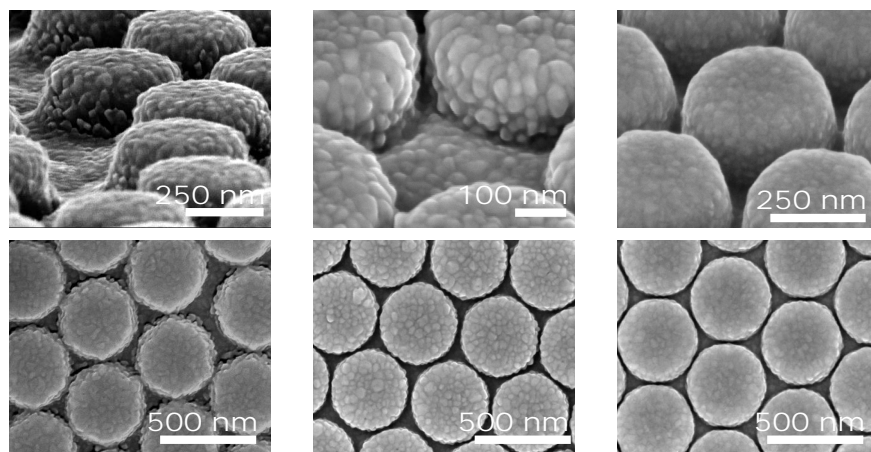
(a) Evaporated from Leybold L560

(b) Sputtered from Leybold Univex

(c) Sputtered from Alcatel SCM600

Figure 3.29 Nanodomes made from sputtered gold have a lower surface roughness than the evaporated layers, especially when the Alcatel SCM600 sputtering tool was used.

SCM600 sputter tool for all gold nanodome substrates described in this thesis except for the nanodome-patterned microdisks in chapter 5, which were fabricated using an evaporated gold layer as we did not have access to gold sputtering at the time of fabrication.

3.4   Characterization of plasmonic resonances

We use two metrics to experimentally characterize a SERS substrate. The first is a broadband specular (or diffuse) reflection measurement, which provides the absorption (or scattering) spectrum. These measurements, already introduced in section 3.2, help gaining a qualitative understanding of the SERS platform. The second is a quantitative measurement of the SERS signal originating from molecules close to the gold layer. This is a crucial parameter, signal enhancement is the reason why we use SERS in the first place. However, Raman and SERS experiments are typically single pump-wavelength measurements. Combined, absorption and enhancement measurements can provide a good insight in the properties of a SERS substrate. It is however important to realize that the absorption or scattering spectra do not always provide an accurate indication of the wavelength-dependent enhancement of a SERS substrate [36]. Think for example of a monodisperse solution with a thousand colloidal gold nanoparticles. Two of these particles are clustered, providing a hotspot with a 5 nm gap. This cluster may produce a stronger SERS signal than the other 998 isolated nanoparticles combined, but will contribute negligibly to the absorption spectrum of the solution. Ideally, one could directly measure a wavelength-dependent enhancement factor, but this requires expensive tunable lasers and filters.

In this section, we quantify the enhancement factor of the nanodome substrate and compare this to other SERS substrates. Furthermore, we experimentally investigate the dependence of the absorption spectrum and enhancement factor on g and h, and interpret these results based on the model developed in the previous sections. But first we need to correctly define the enhancement factor.

3.4.1   Definition of SERS enhancement factors

Before determining a SERS enhancement factor, I strongly recommend reading the comprehensive study on quantifying SERS enhancement by Le Ru et al. [37]. Quantifying the enhancement of a SERS substrate is less straightforward than it may seem. Different metrics have been defined in literature and the naming of these is not always consistent. To make things worse, many papers do not clearly mention the exact method used for quantifying the enhancement. This confusion has lead to erroneous reports of single-molecule enhancement factors up to 10^{15}. These insensibly huge enhancement factors were inexplicable using electromagnetic enhancement. As a result, theories on chemical enhancement were developed, in vain trying to explain these wrong results. Thanks to the rigorous definition of the problem by Le Ru. et al. [37] and the advent of new technology for simulating and visualizing plasmon resonances in individual antennas, it is now widely accepted that electromagnetic enhancement is the dominant enhancement mechanism [36–38] and single-molecule enhancement factors do not exceed 10^{11-12}. Except for specific molecules, SERS enhancement factors can be explained purely by plasmon modes.

We repeat the definition of three different enhancement factors: one for bulk, one for single-molecule and one for monolayer measurements. The latter, named SERS substrate enhancement factor (SSEF) is used throughout this work and, if correctly measured, allows for a quantitative comparison of different SERS substrates.

Analytical Enhancement factor (AEF)   The analytical enhancement factor simply calculates the ratio of total SERS over Raman signal for a solution of identical molecules, divided by their respective concentrations. It is a metric for the enhancement of the Raman signal in a bulk volume of analyte:

$$AEF = \frac{I_{SERS}\, c_{Raman}}{I_{Raman}\, c_{SERS}} \tag{3.47}$$

Measuring the AEF is fairly straightforward, but the metric has important shortcomings. First, the measured enhancement factor strongly depends on experimental conditions. For example, for planar SERS substrates all the signal originates from a nanometer region on the gold surface and changing the numerical aperture of the objective will change the AEF. Second, the AEF neglects any kind of physical or chemical interactions on the metal surface. For example, in combination with a negatively charged metal surface, a positively charged molecule such

as rhodamine 6G (R6G) will give a much higher AEF than a negatively charged molecule. Unless special precautions are taken, such as a passivation of the gold layer using polymer [39] or dielectric shells [40], there will be surface interaction. Therefore, I_{SERS} is in general not linear with concentration. Nevertheless the AEF provides the easiest benchmark for comparing equally charged SERS substrates if all measurement conditions and concentrations are identical.

Single molecule enhancement factor (SMEF)   The enhancement of the Raman scattered signal originating from a single molecule is defined as the ratio between the SERS signal of this molecule over the orientation averaged Raman signal of the same molecule:

$$SMEF = \frac{I_{SERS}^{SM}}{< I_{Raman}^{SM} >}$$ (3.48)

This definition seems trivial. Nonetheless, the myth of $> 10^{12}$ SMEFs was partially created by normalizing the signal of a R6G molecule to that of ethanol [41], while the Raman cross section of R6G can be 6 orders of magnitude larger, with resonant Raman effects in the visible wavelengths. The enhancement factor experienced by a single molecule depends strongly on the position and orientation of that molecule. The field intensity over a SERS substrates is extremely heterogeneous because of the small mode volume of the LSPR. Furthermore, the excitation a particular Raman mode in the molecule is polarization depended. The proximity of a molecule to a surface will also influence the dipole radiation profile of the Stokes scattering for that mode. Only the fraction of radiated Stokes power collected by a particular detection system will contribute to the measured SMEF. This makes both the numerical and experimental calculation of a SMEF a difficult task. To simplify the problem, the SMEF is often calculated from the local fields in a FDTD/FEM simulation in the $|E_R|^2|E_S|^2$ approximation (see section 2.3.1):

$$SMEF(\omega_R, \omega_S) \cong \frac{|E_{loc}(\omega_R)|^2}{|E_0(\omega_R)|^2} \frac{|E_{loc}(\omega_R)|^2}{|E_{loc}(\omega_S)|^2}$$ (3.49)

Remind that this doesn't take molecular orientation into account and approximates the directional radiation enhancement by the local field enhancement at the Stokes frequency. If the difference between the Raman frequency ω_R and the Stokes scattered frequency ω_S is small compared to the spectral bandwidth of the LSPR, this can be simplified to:

$$SMEF(\omega_R, \omega_S) \cong \frac{|E_{loc}(\omega_R)|^4}{|E_0(\omega_R)|^4}$$ (3.50)

One typically refers to the maximum possible SMEF for a SERS substrate, implying that the molecule would be ideally positioned at the position with the strongest field enhancement. For example, we estimate a maximum SMEF for the nanodome substrate with 10 nm gap in figure 3.24 of 2×10^8. The maximum achievable SMEF is in the order of 10^{11-12}, which has been observed from hotspots

in aggregated clusters of Ag colloids at visible wavelengths [37]. These maximal SMEFs occurred in irreproducible, sub 4 nm gaps in between these clustered silver nanoparticles. Such SMEFs are out of range for structured gold at near-infrared wavelengths. Single molecules with a differential SERS cross section ($d\sigma/d\Omega \times SMEF$) down to $10^{-21}\,\mathrm{cm}^2\mathrm{sr}^{-1}$ have been detected with a 1s integration time. Hence the single molecule spectrum of strong Raman scatterers such as R6G ($d\sigma_R^{785}/d\Omega = 2.1 \cdot 10^{-28}\,\mathrm{cm}^2\mathrm{sr}^{-1}$) may be detectable on the nanodome platform. Although single molecule detection is interesting from a theoretical perspective and advocates the ultimate SERS detection limit, it has little applications in complex biological samples because the signal of the single molecule will be overwhelmed by a soup of other nearby molecules. Therefore we did not experimentally investigate single molecule detection on our SERS substrates.

SERS substrate averaged enhancement factor (SSEF)   Where the AEF quantifies the enhancement of bulk analytes and the SMEF that of single molecules, the SSEF gives a figure for the enhancement of a monolayer of molecules on the metal surface. The SSEF is particularly suited for characterizing planar SERS substrates such as the nanodome surface. Under the correct assumptions, its value is independent of the experimental conditions.

$$SSEF = \frac{I_{SERS}}{I_{Raman}} \times \frac{N_{Vol}}{N_{Surf}} \qquad (3.51)$$

The tricky part in determining the SSEF is to relate the number of molecules in the excitation volume for spontaneous Raman scattering to the number of molecules adsorbed on the gold layer in the SERS experiment. This ratio can be calculated from the bulk molecule density ρ (molecules/m^3), the effective height of the collection volume H_{eff} (m), the density of the molecules on the gold surface μ_{NTP} (molecules/m^2), the surface area of a single nanostructure A_{Au} (m^2) and the density of the metal nanostructures μ_{Au} (m^{-2}):

$$SSEF = \frac{I_{SERS}}{I_{Raman}} \times \frac{H_{eff}\rho}{\mu_{Au}\mu_{mol}A_{Au}} \qquad (3.52)$$

The effective height of the collection volume H_{eff} can be measured from an axial scan on a thin layer:

$$H_{eff} = \int \frac{\mu_{\perp}(z)}{\mu_0}\mathrm{d}z \qquad (3.53)$$

Here, μ_0 and $\mu_{\perp}(z)$ are respectively the Raman intensity in focus and at a distance z from the focal plane. H_{eff} depends on the magnification and numerical aperture of the objective, as well as the diameter of the confocal pinhole. It can be measured from the z-dependent Raman intensity of a thin film in an axial scan. Here, we used a 50 nm thin layer of ALD-deposited TiO_2 on CaF_2 (figure 3.30). Note that silicon is a poor choice at NIR wavelengths. Although plain Si samples are often used for measuring effective heights and widths of collection volumes, the penetration depth of the incoming field at $\lambda_p = 785\,\mathrm{nm}$ in Si is approximately 8
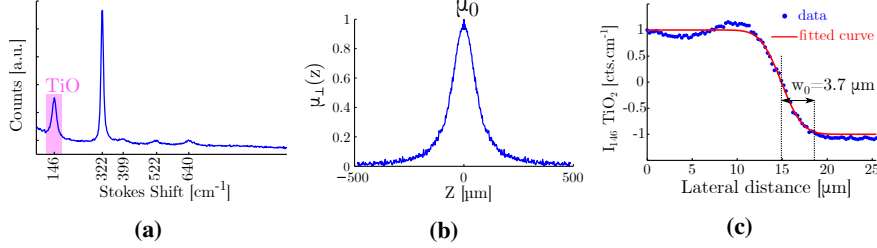
Figure 3.30 The effective height of the collection volume H_{eff} equals 150 μm for a 10x/0.3 objective and 200 μm pinhole, determined from an axial scan over a 50 nm TiO_2 on CaF_2 layer. (a) Raman spectrum of TiO_2 on CaF in the focal plain. (b) Integrated peak intensity of the $146\,cm^{-1}$ peak versus axial distance (c) Beam width $w_0 = 3.7$ μm in the focal plane, measured from a fitted error function to a lateral scan using a 100 μm pinhole

μm.

3.4.2   Nanodome absorption and uniformity

Substrate averaged enhancement

We used para-nitrothiophenol (pNTP) to measure the SSEF of various SERS substrates. Through its thiol group, this molecule will form a monolayer on Ag or Au surfaces with a density μ_{mol} of 4.4×10^6 molecules/μm^2 [42]. We measured a H_{eff} of 150 μm for a 10x magnification and 0.3 numerical aperture objective in combination with a 200 μm multimode fiber as confocal pinhole (figure 3.30). The conventional Raman signal of the molecule was determined from a 50 mM solution of pNTP in ethanol ($\rho = 3.01 \times 10^7$ molecules/μm^3), as shown in figure 3.31b. From a Lorentzian fit to the $1339\,cm^{-1}$ peak, we found an I_{Raman} of 1.12×10^3 cts.cm^{-1}mW^{-1}s^{-1}. Thus (3.52) becomes:

$$SSEF = 0.92 \frac{I_{SERS}}{A_{Au}\mu_{Au}} \tag{3.54}$$

We now have an equation that easily allows to experimentally compare the SSEF of different substrates. It is important to remember that, although the final enhancement factor is independent of the optical setup, we need to use exactly the same conditions (objective, microscope, pinhole etc.) for acquiring the SERS and Raman spectra. For our particular Raman system, these are outlined in detail in the methods section. The product $A_{Au}\mu_{Au}$ represents the projected Au surface area, which depends on the geometry of the SERS substrate. In the case of HCP nanodomes, the area of a unit cell ($S_u = \mu_{Au}^{-1}$ in figure 3.21) equals $2\sqrt{3}r_0^2$. The total gold surface area of the nanodome (figure 3.18) in this unit cell is:

$$A_{Au}^{ND} = 2\sqrt{3}r_0^2 + 2\pi r_0(h_0 + (\frac{\pi}{2} - 1)r_d) \tag{3.55}$$

For a nanodome substrate with $r_0 = 224$ nm, $h_0 = 45$ nm and $r_d = 50$ nm, the

projected surface area becomes:

$$A_{Au}^{ND}\mu_{Au}^{ND} = \frac{2\sqrt{3}r_0^2 + 2\pi r_0(h_0 + (\frac{\pi}{2}-1)r_d)}{2\sqrt{3}r_0^2} = 1.59 \qquad (3.56)$$

We also determine I_{SERS} from a Lorentzian fit to the 1339 cm^{-1} peak as shown in figure 3.31. Using (3.54) and (3.56), we measured a maximum SSEF for a gold nanodome substrate in air of $9.8 \pm 0.5 \times 10^6$. Here, 'maximum' refers to the nanodome chip showing this strongest enhancement averaged over its entire surface, not to be confused with the local maximum SMEF mentioned before.
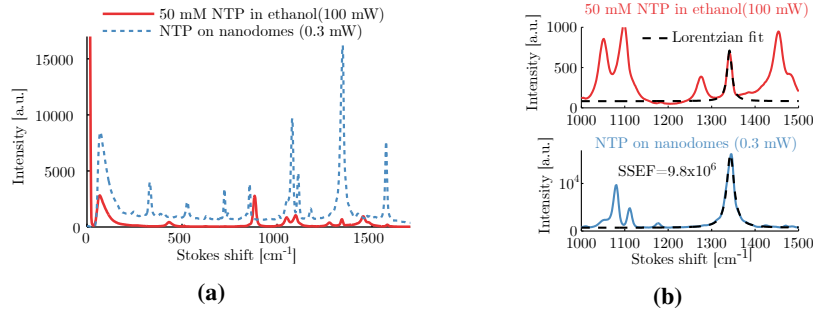

Figure 3.31 (a) The SSEF is calculated by comparing the Raman signal of a solution of molecules (red curve, 50 mM pNTP in ethanol, 100 mW, 0.133 s) to the SERS signal of a gold adsorbed monolayer of the same molecules (dashed blue, 0.3 mW, 0.133 s). (b) The area of the 1339 cm^{-1} peak is calculated from a Lorentzian fit to the measured data. The maximum measured SSEF in this work was 9.8×10^6.

Because SSEF is the average enhancement for a molecule on the SERS substrate, it depends on the total gold area with which molecules can interact. For example, for NSL-fabricated nanotriangles with the same periodicity, used for patterning waveguides in chapter 4, the projected surface area of a single nanotriangle becomes ($A_{Au} = 0.023\,\mu m^2$ and $\mu_{Au} = 11.5\,triangles/\mu m^2$):

$$A_{Au}^{NT}\mu_{Au}^{NT} = 0.26 \qquad (3.57)$$

Hence a nanotriangle substrate giving the same I_{SERS} as a nanodome substrate will have a 6 times higher enhancement factor. In other words, there is a large fraction 'superfluous' gold in the nanodome pattern, surface area to which thiol-containing molecules will bind without contributing to the SERS signal.

Substrate uniformity

SERS has only partially been able to live up to the expectations that rose since its discovery and especially since the regained interest after the first demonstration of single-molecule sensing. This is largely due to difficulties with acquiring truly quantitative information out of SERS experiments. A necessary (but not sufficient) demand for quantitative experiments is a reproducible SERS substrate with a uniform enhancement factor. A proper characterization of the SERS enhancement
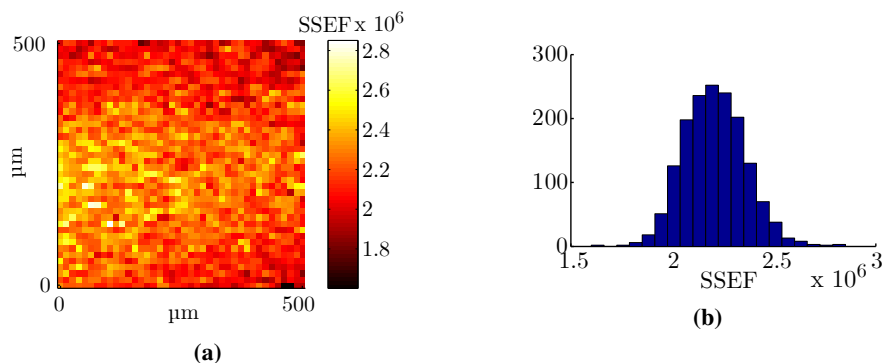
(a)

(b)

Figure 3.32 The coefficient of variation on the SSEF of the nanodome substrate is 7%. (a) Intensity of the 1339 cm^{-1} peak over a 500 μm x 500 μm area (b) Histogram of the position-dependent SSEF in this area.

factor is only useful to the extent that this EF is uniform across the entire SERS substrate, or even over different fabrication runs. The latter is problematic in our nanodome-fabrication process, because there is a run-to-run variability of 20 nm on the targeted gold thickness of 150 nm. As a consequence, each run requires a limited parameter sweep on the O_2 and CF_4H_2 etch times to fabricate a chips with optimal gap dimensions. With the proper efforts, the fabrication process can undoubtedly be made more reproducible.

The nanodomes do provide a fairly uniform enhancement factor over the same chip. Figure 3.32 shows the variation of the SSEF on a single chip over a 0.5 mm by 0.5 mm area measured using a 10x/0.3 objective. From this map, we find an enhancement factor for this particular chip of $2.2 \pm 0.15 \cdot 10^6$, or a coefficient of variation (CV=standard deviation/mean) of 7%. Part of this variation is not due to variations in the SERS substrate but rather due to shot noise or mechanical instability of the microscope; we measured a CV of 1.7% in a static measurement.

3.4.3 Tuning the nanodome resonances

As explained in section 3.2, multiple geometrical parameters have an influence on the LSPR in the gap between the nanodomes. Table 3.1 summarizes the dominant effects of changing the nanodome geometry (sketched in figure 3.18) on the spectral position of the LSPR λ_r^{LSPP} and the local field enhancement. Except for r_d, the top rounding of the nanodomes, these parameters can be easily controlled during the fabrication process. Here, we take a closer look at how the width g and height h of the inter-dome gap allow to tune[3] the resonance and adjust the enhancement factor.

Figure 3.33 shows the effect of the gap width g, adjusted through the O_2 etch time, on the absorption spectrum and SSEF. As expected, a narrower gap gives a

---

[3]The geometry of the nanodomes is adjusted from changing the fabrication parameters. This is not to be mistaken for active tuning.

Table 3.1: The wavelength and field enhancement of the plasmon polariton modes in a nanodome substrate can be tuned through geometrical parameters g, h = h₀ + r_d, r₀ and r_d. Between brackets we give the reasonable range from a fabrication point of view.

Parameter	Tune	$\lambda_r^{\mathbf{LSPR}}$	Field enhancement	Fabrication control
$g\,[5-50\,nm]$	↓	Redshift	↑↑: Mode coupling	O_2 plasma HCP beads
$h\,[40-200\,nm]$	↓	Strong Blueshift Lower order modes	↑: Lower mode	CF_4/H_2 SiN RIE
$r_0\,[150-350\,nm]$	↑	Redshift: anticrossing	↑: Hybrid SPP ↓: Energy gradient	PS bead radius
$r_d\,[30-70\,nm]$	↑	Blueshift	↓: Energy gradient	(Au deposition)

redshifted LSPR and a stronger enhancement. The smallest gap in this series is approximately 12 ± 3 nm, determined from a SEM measurement (figure 3.33b), resulting in a SSEF of $\approx 8 \times 10^5$. We see that the enhancement drops by more than two orders of magnitude for a 20 ± 3 nm gap size, despite the good overlap of the absorption spectrum with the 785 nm pump and 877 nm Stokes wavelengths. A similar behavior is found from 3D FDTD simulations, for which figure 3.34 shows the average field intensity in the gap, the absorption spectra and the enhanced field profile $|E|/|E_0|$ at the fundamental LSPR resonance. This simulation again confirms that the spectral position and enhancement of the LSPR becomes very sensitive to the exact gap width for smaller gap sizes. For narrow gaps, the discrepancy between the absorption spectrum and the field enhancement becomes prominent. For example, the field enhancement in a 4 nm wide gap is stronger than that in a 30 nm gap at all wavelengths, even at the center of the LSPR resonance in the wide gap. This can not be predicted from the absorption spectrum. The sharp resonances appearing around 600 nm in the simulated absorption spectrum for narrower gaps are most likely multipole modes [9], which were not considered in the MDM-cavity derived model explained in section 3.2.

Figure 3.35 shows the effect of increasing the SiN etch time, and hence the gap depth h_0, on the absorption spectrum and enhancement factor. The same O_2 PS etch was used for all samples, resulting in a fairly constant g. A longer etch results in a deeper cavity which, as expected, results in a strong redshift of the LSPR. The measured SSEF is optimal when there is a maximal overlap between the absorption spectrum and the pump to Stokes wavelengths. Qualitatively we find the same behavior from a 3D-FDTD simulation, for which figure 3.36 plots the average field intensity in the gap for different heights.

Remarkably, in four different fabrication runs the samples with the highest SSEF have an absorption maximum around 620-635 nm (figure 3.37). These maximum enhancements occur in samples with gap width of approximately 5 nm, a dimension quantified from a SEM measurement. Possibly the nanodomes touch on some positions in these extremely narrow inter-dome gaps, reducing h_0 and thereby blueshifting the resonance. Nevertheless, the narrow gap will still have a strong
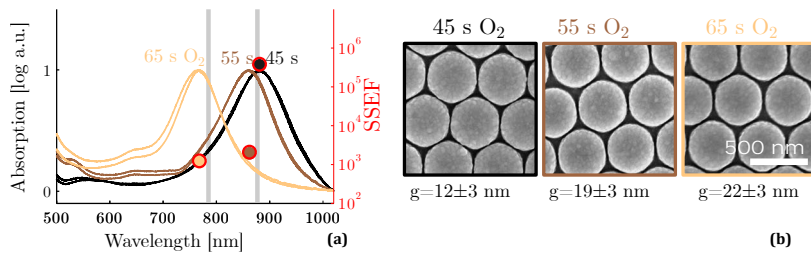
Figure 3.33 Increasing the time of the O_2 polystyrene etch results in a larger g, yielding a blueshifted resonance and a decreased SSEF. (a) UV-Vis absorption of nanodomes in air with increasing O_2 etch time and 90 s CF_4/H_2 SiN etch. Specular reflection was measured using a fiber bundle probe. The red outlined circles give the SSEF for each sample, which increases for narrower gaps. Gray lines mark the pump and Stokes wavelengths. (b) SEM images showing the increase in gap width from 12 to 22 nm. Note that all SSEFs are measured with a 785 nm pump laser, for clarity their value is positioned closest to the respective absorption spectrum.
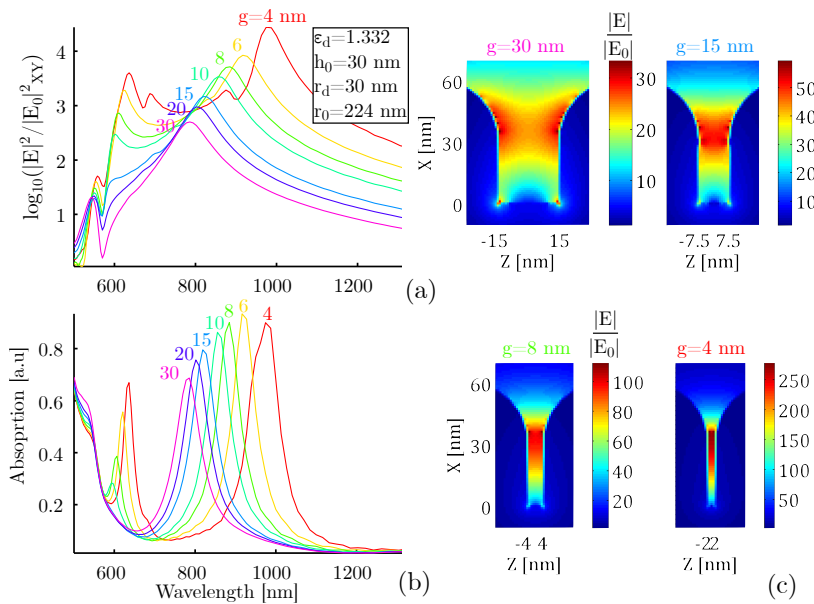

Figure 3.34 3D FDTD simulation of a periodic gold nanodome structure in water with decreasing gap width (g). (a) Average squared field enhancement in the gap (in the XY plane). (b) Corresponding simulated absorption spectra. (c) Electric field magnitude at resonance in the XZ plane for 30, 15, 8 and 4 nm gaps. Notice how the LSPR is very sensitive to nm variations on smaller gap sizes.

and broad enhancement as seen from the simulations in figure 3.34a. In future, it would be interesting to quantify their SSEF at a 633 nm pump wavelength.
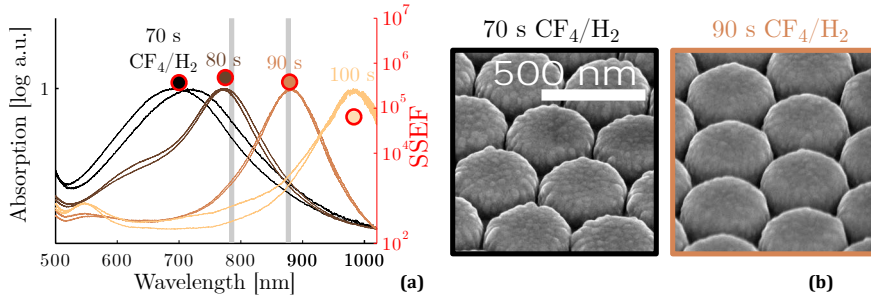

(a)

(b)

Figure 3.35 Increasing the time of the CF_4/H_2 SiN etch results in a larger h_0. This redshifts the fundamental LSPP resonance. (a) UV-Vis absorption of nanodome substrates in air with increasing SiN etch times and a 45 s O_2 polystyrene etch. The SSEF (red outlined circles) decreases when the resonance is redshifted with respect to the pump and Stokes wavelengths (gray lines). (b) SEM images under a 52° angle of the shorter and longer cavities.
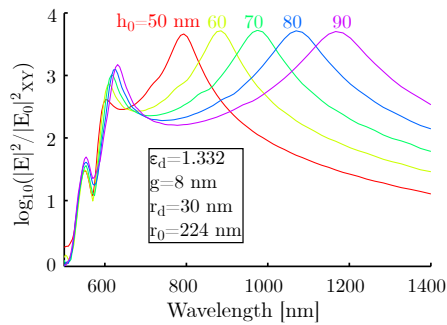

Figure 3.36 Average squared field enhancement in the gap (in the XY plane) calculated from a 3D FDTD simulation of a periodic gold nanodome structure in water, showing a redshift of the resonance with increasing gap height (h_0).
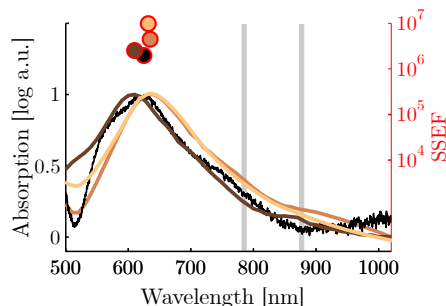
Figure 3.37 Absorption spectra and SSEF for the nanodome chips with maximum SSEF from four different fabrication runs. The absorption is blueshifted with respect to the pump and Stokes wavelength. Note that all SSEFs are measured with a 785 nm pump laser, for clarity their value is positioned closest to the respective absorption spectrum. (SSEF and specular reflection in air. Black curve measured with a Thorlabs fiber bundle probe, others with a PerkinElmer spectrophotometer.)
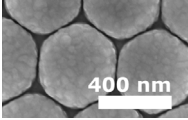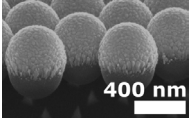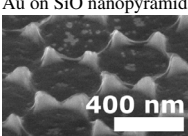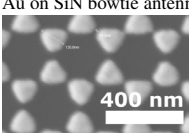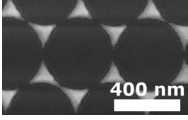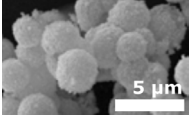
3.4.4 Quantitative comparison of SERS substrates

For our nanodomes we measured a maximum SSEF of $(0.98 \pm 0.07) \times 10^7$. Table 3.2 compares this SSEF and uniformity to the values we measured using an identical procedure on various SERS substrates. From the SERS substrates we could get our hands on, the nanodomes are clearly the best both in terms of enhancement and signal variation. Note that we have not considered any chemical effects that may alter the polarizability of the molecule upon gold-binding (chapter 2.3.1). For a complete analysis, one should redo the experiment for a number of other types of molecules.

A comparison to the SSEF of other SERS substrates reported in literature is difficult. In multiple manuscripts, the performance of the proposed SERS substrate was compared to Klarite®, a SERS substrate that was commercially available until recently. While Klarite® is always outperformed, the reported SSEF at 633 nm pump for this substrate range from 1.5×10^4 [43] over 3.5×10^5 [44] to 1.0×10^6 [45]. Either the reproducibility of Klarite® was extremely bad or, more likely, differences in methodology for determining the SSEF result in this 2 orders of magnitude discrepancy. Similar problems arise when comparing the substrate uniformity. It obviously depends on the numerical aperture of the objective. For a high NA (> 1), the focal spot of the laser becomes smaller than the period of the structure, so individual hot-spots can be visible. Lower NA's on the other hand will intrinsically average the signal over multiple hotspots, resulting in a more uniform signal. This complicates a comparison of the substrate uniformity with literature. Despite the work of Le Ru et al. [37], measuring SSEF remains a challenging task and comparisons should be made with a healthy dose of skepticism. For these reasons, we will not embark on an extensive quantitative comparison with literature. For those insisting, such an attempt was made in a recent review paper [46]. Nevertheless it is worth mentioning two other reproducible and scalable SERS platforms for 785 nm excitation, whose characterization was described with sufficient detail:

Wu et al. [44] reported a SSEF 8×10^7 for their nano-imprinted gold array and Li et al. [43] report a SSEF of $4 \times 10^4 \pm 5\%$ for their gold-capped nanopillars fabricated on 300 mm wafers using deep-UV lithography.

Table 3.2: Highest SSEF of different SERS nanostructures measured in our lab using an identical protocol. Au on SiN bowtie antennas were fabricated with various dimensions by Dr. U. Huebner using e-beam lithography (IPHT Jena). The Ag alginate microparticles were fabricated with Dr. B. Parakhonskiy and E. Lengert [47]. The projected surface area $A \cdot \mu = A_{Au}\mu_{Au}$ was estimated from SEM images.

Substrate	Fabrication	SSEF $\pm$**CV**	Substrate	Fabrication	SSEF $\pm$**C.V.**
Au nanodomes	NSL + RIE In house $A \cdot \mu = 1.6$	$9.8 \cdot 10^6$ $\pm 6\%$	Au-film-over-nanoparticle	NSL In house $A \cdot \mu = 1.9$	$1.2 \cdot 10^6$ $\pm 20\%$
Au on SiO nanopyramids	NSL In house $A \cdot \mu = 0.26$	$7.0 \cdot 10^5$ $\pm 20\%$	Au on SiN bowtie antennas	e-beam IPHT Jena $A \cdot \mu = 0.5$	$4.5 \cdot 10^5$ $\pm 13\%$
Au on SiN nanotriangles	NSL In house $A \cdot \mu = 0.26$	$3.5 \cdot 10^5$ $\pm 28\%$	Ag alginate beads	Colloidal In house $A \cdot \mu = 2.8$	$2 \cdot 10^5$ $\pm 75\%$

3.5   Absolute comparison of simulation and experiment

In section 3.4.3, we showed that the dependence of the plasmonic modes on the geometry of the nanodome substrate can be qualitatively explained from the model developed in this chapter. Here, we try an absolute comparison between the measured absorption spectra and those obtained from a 3D FDTD simulation on a periodic nanodome structure. Figure 3.38 shows this comparison for five different nanodome samples. First, we determine the geometry (g, h, r_d, r_0) of the different nanodome samples from top-view SEM-images (figure 3.38b) and FIB/SEM cross sections (figure 3.38a). Next, we simulate a HCP-periodic nanodome structure with these geometrical parameters in Lumerical FDTD. The calculated absorption spectra are than compared to the measured ones, retrieved from a specular reflection measurement. This comparison is made both in air (figure 3.38c) and water (figure 3.38d). There is a striking blueshift of more than 200 nm for the measured absorption spectra compared to the simulation for all samples. This blueshift may be caused by inaccuracy in determining the nanoscale dimension of the inter-dome gap, there is a 5% systematic and 2 nm measurement error on the SEM-measured dimensions. The plasmon modes are very sensitive to nanometer variations, especially for stronger confined modes in narrow gaps. Remember that a 2 nm variation on a 8 nm wide gap can shift the resonance position by more than 100 nm (figure 3.14b). Furthermore, the modeled geometry as shown in figures 3.18 is still an approximation of the actual nanodomes. For example, it does not take surface roughnesses into account, which can locally modify the gap. Also, an exact modeling of the gold dispersion is not possible in FDTD and there are inaccuracies in the ellipsometric spectrum an fit of the gold dispersion. The simulation and experiment do correspond qualitatively on the relative shifts of the LSPR resonance when changing the gap dimensions or refractive index of the environment. However, we must conclude that the FDTD model does not allow to quantitatively predict the characteristics of the plasmonic modes in a nanodome surface. In general, a quantitative simulation of metal nanostructures for SERS is extremely difficult. If there is one conclusion to draw from this comparison, it would be not to overdo a simulation-based design optimization for nanoplasmonics and to take SERS-papers purely based on simulations with a grain of salt.

S1 g: 6±2 nm   h: 48±5 nm r_d: 71±6 nm

S2 g: 8±2 nm   h: 53±5 nm r_d: 56±5 nm

S3 g: 8±2 nm   h: 74±6 nm r_d: 48±5 nm

S4 g: 12±3 nm   h: 84±6 nm r_d: 67±6 nm

S5 g: 11±3 nm   h: 138±9 nm r_d: 105±10 nm
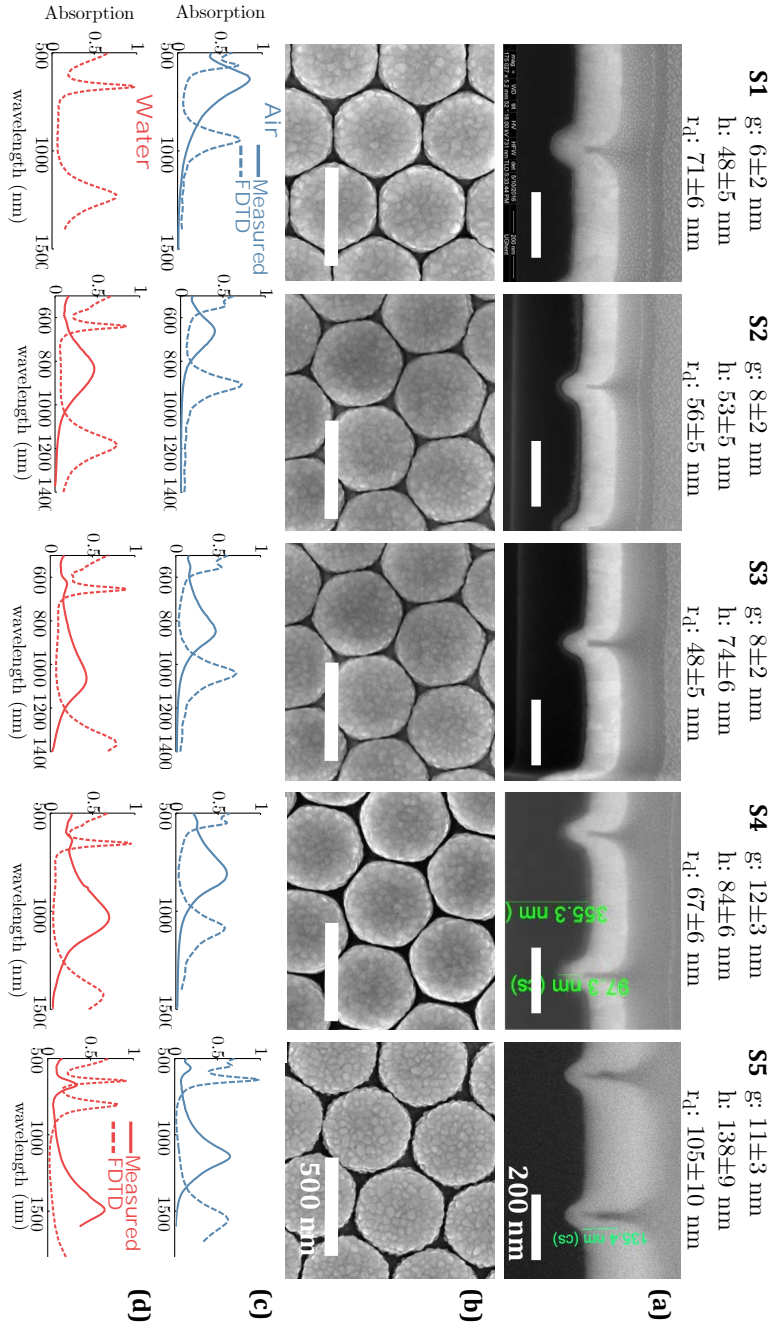
Figure 3.38 Experimental versus simulated specular absorption for five different nanodome samples with fixed radius $r_0 = 224 \pm 6$ nm and varying gap height h, width g and top rounding r_d. We observe a consistent redshift of the simulated result compared to the measurement. (a-b) FIB/SEM cross section and SEM top-view used to determine the geometrical parameters of the nanodomes. (c) Measured (solid) and simulated (dashed) absorption in air. (d) Measured and simulated absorption in water. The gold on sample **S5** was sputtered from Leybold Univex, all other samples used Alcatel SCM600 sputtered gold.

3.6   Conclusions and perspectives

In conclusion, we developed a nanosphere lithography based process to fabricate a gold nanodome SERS platform that provides a SSEF up to 10^7 with a 7% signal variation across a chip. These are competitive numbers compared to other state-of-the art substrates, especially given the relatively easy, cheap and scalable fabrication method. The most important localized plasmon resonances in this system can be derived from a parallel metal nanowire, which in turn is approximated as a layered metal/dielectric/metal cavity. This provides a physical understanding of the modes, and allows to qualitatively predict their behavior. The most important geometrical parameters for the spectral position of the LSPR and the SSEF are the width and height of the inter-dome gap. These can be controlled though etch times in the fabrication process. The periodicity of the nanodome pattern, which allows to excite Bloch wave SPPs in the gold layer, also plays a role. However, further experiments are needed to study this effect in detail. Although the analytic solutions and the 3D FDTD model developed in this chapter correctly predict trends in the absorption spectra and enhancement factor when changing a geometrical parameter, we could not achieve a satisfying quantitative modeling of the gold nanodomes.

The gold nanodome substrate provided a valuable tool for intracellular sensing and protease detection developed in chapters 5 and 6. In future, the enhancement of the platform may be improved by optimizing the periodicity of the hexagonal nanodome structure. A better batch-to-batch reproducibility can be achieved by optimizing the gold deposition process. A wavelength-dependent measurement of the SERS substrate enhancement factor will further improve our understanding of the plasmon polariton modes in the structure and possibly a higher SSEF can be reached using a 633 nm excitation.

Materials and Methods

Finite Difference Time Domain Simulations

Lumerical FDTD solutions was used for simulating the field profile in the plasmonic hotspots. The mesh accuracy settings were optimized for convergent results at a reasonable simulation time. Over the entire simulation region, mesh accuracy '4' was used. A mesh override region with 2 nm mesh size was used on the metal structures themselves, and the gap region was meshed with a 1 nm mesh size. All meshes used conformal variant 0. Constant refractive indices were used for the dielectric layers ($n_{SiN} = 2$, $n_{air} = 1$, $n_{water} = 1.33$) and sampled data from an ellipsometry measurement on a gold sputtered layer was used for n_{Au} and k_{Au}. The source has a wavelength span from 500 nm to 1800 nm.

2D and 3D modeling of a MDM cavity   Figure 3.39 shows the geometry of the 2D simulation. A TM-polarized total-field scattered-field source (TFSF) encompasses the two-nanowire cavity with asymmetric boundary conditions parallel to the gap. Phase-matched layer (PML) boundaries were used in the x direction, and asymmetric/PML boundaries along z. The absorption cross section was calculated from a box of frequency domain field- and power monitors surrounding the structure, but still inside the TFSF source region. A frequency domain field profile monitor was used to capture the mode profile in the gap. A typical 2D simulation required 0.25 million FDTD Yee nodes, corresponding to a simulation time of 1-2 minutes on an 8 core processor. For the 3D simulations, symmetric/PML boundaries were used along y. The number of nodes increased to 20 million, resulting in a simulation time of approximately 2 hours.
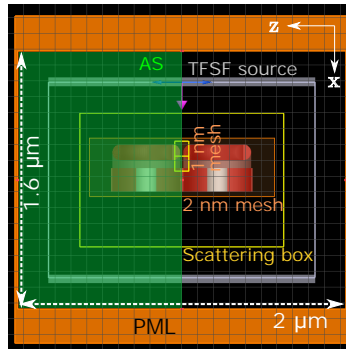

Figure 3.39 Lumerical 2D FDTD simulation geometry of a two-nanowire cavity.

3D simulations of nanodome array with hexagonal periodicity   Figure 3.40 shows the three dimensional geometry of the simulation. A box with side lengths $2r_0 \times 2\sqrt{3}r_0$ is used as unit cell for the periodic structure. A plane wave source with electric field polarized parallel to the gap ($\vec{E} = E\vec{1}_z$, $\vec{k} = k\vec{1}_x$) is incident on the structure. Asymmetric/periodic and symmetric/periodic boundary conditions were used along respectively z- and y boundaries. The absorption was calculated from a frequency domain field- and power monitor located above the plane wave source. A 1 nm mesh-override region was used in all

the interdome-gaps. For a comparison to the experimental specular reflection measurements we used a far-field projection of the reflected field.
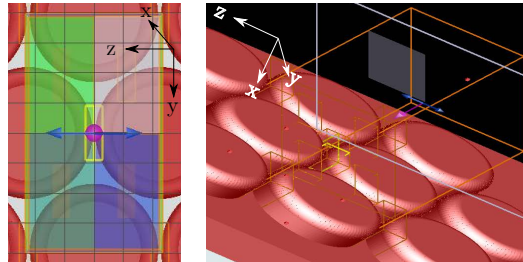

Figure 3.40 Lumerical 3D FDTD simulation geometry for nanodomes with hexagonal periodicity.

Nanodome Characterization

SEM and FIB   Scanning electron microscopy images were acquired on a FEI Nova 600 Nanolab Dual-Beam FIB system, using a voltage of 18 kV and a through the lens (TLD) detection. For cross section analysis, first a thick protective layer of titanium was deposited on the surface, after which the sample was cross-sected using a focused ion beam (FIB) and imaged with SEM under an angle of 52°. To image the nanodome gap as accurate as possible (top row in figure 3.38), progressive FIB sections were made with a 50 nm step.

UV Vis measurements   The absorption was calculated relative to the reflection R_{Au} of a 100 nm thick plane Au on SiN sample:

$$A = -\log_{10}(R_{ND}/R_{Au}) \tag{3.58}$$

Two different setups were used for measuring specular reflection, both giving comparable results:
- **PerkinElmer Lambda 950 UV/Vis spectrometer** with Universal Reflectance Accessory in absolute reflectance mode for measuring specular reflection under an angle of 8° normal to the nanodome substrate, except if mentioned differently. We used a spot size of 4 mm x 4 mm and a 10 nm resolution in the 500 nm - 1500 nm wavelength range. Reflection spectra in water were acquired by squeezing a drop of water in between the substrate and a 170 μm microscope slide.
- **Fiber optic backscatter probe bundle** (Thorlabs RP26) connected to a stabilized Tungsten-Halogen light source (Thorlabs SLS201L) and a compact spectrometer (Thorlabs CCS200/M). This setup, shown in figure 3.41, allows to measure specular reflection close to normal incidence in a 400-1020 nm wavelength range. Reflection spectra in water were acquired by immersing both fiber probe and sample.

Raman experiments   Spectra were acquired on a WITec Alpha 300 R+ confocal Raman microscope equipped with a -65 °C to -70 °C cooled CCD camera (Andor iDus 401 BR-DD) and a 785 nm diode laser (Toptica, XTRA II). All spectra presented in this chapter used a 10x/0.3 Nikon Plan Fluor objective. Stokes scattered light was collected by a 200 μm diameter multimode fiber. This fiber is also the entrance slit to the spectrometer, which used
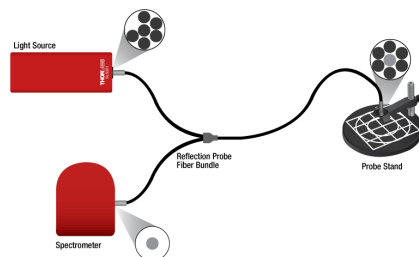
Figure 3.41 Setup for measuring specular reflection using a fiber probe bundle (image from Thorlabs).

a 600 lpmm grating to diffract the Stokes scattered light on the spectral camera. The integration time of this camera was set to 0.13372 s. All lines of the CCD camera were read out (full vertical binning), using a vertical shift speed of 16.25 µs and a horizontal shift speed of 0.033 MHz. The spontaneous Raman signal of pNTP was measured from a 50 mM solution in ethanol using a laser power of 100 mW (spectrum in figure A.11 and 3.31). From a Lorentzian fit to the $1339\,\mathrm{cm}^{-1}$ peak, we found a peak area of $2.5 \cdot 10^4\,\mathrm{cts\,s}^{-1}\mathrm{M}^{-1}\mathrm{mW}^{-1}$. We did not observe photo-bleaching nor quenching at this power and concentration, as the same value was found for 100 mM and 50 mW laser power.

SERS experiments   The microscope, camera and spectrometer configuration is the same as for the normal Raman measurements. Both a 100 µm and 200 µm multimode fiber were used as confocal pinhole. For a planar SERS substrate, the latter collects 1.4 times more Stokes scattered power on the $1339\,\mathrm{cm}^{-1}$ pNTP peak as compared to the 100 µm pinhole.

For all SERS experiments, a laser power of 300 µW and integration time of 0.1337 s was used. The combination of this low laser power with a low NA objective results in a low irradiance ($< 50\,\mu\mathrm{W}\mu\mathrm{m}^{-2}$). This avoids the photoinduced reduction of pNTP into dimercaptoazobenzene [20]. SERS spectra were typically acquired within 48 hours after pNTP labeling. Prior to labeling, planar SERS samples were cleaned with acetone, isopropanol and water and dried with a nitrogen gun. Next, a short oxygen plasma (PVA-TEPLA GIGAbatch 310M, 6000 sccm O_2, 600 W, 750 mTorr, 120 s) was used to further remove organic contaminants and render the surface hydrophilic. Immediately after, the chips are immersed for at least three hours in a 1 mM solution of para-nitrothiophenol (sigma N27209) in ethanol. After incubation, the labeled chips were thoroughly rinsed with ethanol and water to remove excessive pNTP molecules and dried under a stream of nitrogen. Colloidal SERS samples were also incubated in a 1 mM solution for over three hours, after which excessive pNTP was washed out using at least 4 centrifugation steps.

SERS substrate uniformity was derived from a measurement with 40 x 40 pixels in a tilt-compensated 500 µm by 500 µm plane, yielding a CV of $5.6 - 7\%$. In a static measurement with 1000 sequential 0.13372 s measurements on a single spot, the CV was 1.7%.

Nanodome fabrication

First, a 200 nm layer of PECVD SiN was deposited on top of a $4''$ (100) Si wafer (Advanced Vacuum Vision 310-PECVD). Note that Si wafers are clean from the box and any further

wet cleaning efforts often contaminate the surface rather than cleaning it. Nevertheless, dirty samples can be reasonably well cleaned using a Piranha cleaning for 15 minutes at 80 °C (3/1 H_2SO_4/H_2O_2) followed by Standard-Clean 1 (SC-1, 1/1/5 $NH_4OH/H_2O_2/H_2O$) in an ultrasonic bath at $70°C$ for 30 minutes. Make sure to follow the proper safety instructions during these steps. Next, the wafer was dry-cleaned and made hydrophilic by 20 min of O_2 plasma (PVA-TEPLA GIGAbatch 310 M, 6000 sccm O_2, 600W, 750 mTorr) and stored in DI water. Prior to spincoating, the wafer was flash-dried under a stream of nitrogen, followed by spincoating 760 µl of a 5 w/v% in 2/1 methanol/water mixture of 448 nm diameter polystyrene beads (microparticles GMBH, 448 nm) on top of the wafer. This mixture of microparticles was fabricated by centrifuging 1 ml of a 5 w/v% at 2500 g for 20 minutes, after which 670 µl water was replaced by ethanol. The beads were sonicated and vortexed to break potential clusters. The beads solution was spun on the wafer in three steps: (1) 10 s with 100 rpm/s to 400 rpm (2) 90 s with 450 rpm/s to at 900 rpm and (3) 50 s with 300 rpm/s to 5000 rpm. Step (2) needs to be adjusted depending on the environmental humidity and temperature. Next, the wafer was dried under a stream of nitrogen. The HCP-layer of polystyrene beads was then transferred into the underlying SiN using a two-step reactive ion etch. First, the diameter of the beads was reduced using O_2 plasma (Advanced Vacuum Vision 320-RIE, 50 sccm O_2, 75 W, 100 mTorr, 40-70 s), followed by a CF_4/H_2 SiN etch using an optimized recipe for anisotropic etching (80 sccm CF_4, 3 sccm H_2, 210 W, 20 mTorr, 70-100 s). Next, the beads were lifted off using dichloromethane (follow safety precautions, this is a carcinogenic molecule that penetrates nitrile gloves) in an ultrasonic bath. The wafer was cleaned in a piranha solution (H_2SO_4/H_2O_2, 3/1, 15 minutes at 80 °C. Follow safety precautions, highly corrosive and explosive) and 20 min of O_2 plasma (PVA-TEPLA GIGAbatch 310 M, 6000 sccm O_2, 600W, 750 mTorr). Finally, a 2 nm thick Ti adhesion layer (Leybold Univex) and a 130-170 nm thick Au layer (Alcatel SCM600, partial pressure Argon 10^{-2} mbar, 1 kW, rotating substrates) were sputtered on the clean, nanostructured wafer.

References

[1]   Stefan A Maier. *Plasmonics: Fundamentals and applications*. Springer, 2007.

[2]   Eric C Le Ru and Pablo G Etchegoin. *Principles of Surface-Enhanced Raman Spectroscopy and related plasmonic effects*. Elsevier, Amsterdam, jan 2009.

[3]   D. Pines. *Collective energy losses in solids*. Reviews of Modern Physics, 28:184–199, 1956.

[4]   P.B. Johnson and R.W. Christy. *Optical Contstants of Noble Metal*, 1972.

[5]   F. Peyskens. *Surface Enhanced Raman Spectroscopy Using a Single Mode Nanophotonic-Plasmonic Platform*. Ghent University, Ghent, 2016.

[6]   Mihail Bora, Benjamin J. Fasenfest, Elaine M. Behymer, Allan S P Chang, Hoang T. Nguyen, Jerald a. Britten, Cindy C. Larson, James W. Chan, Robin R. Miles, and Tiziana C. Bond. *Plasmon resonant cavities in vertical nanowire arrays*. Nano Letters, 10(8):2832–2837, 2010.

[7]   G. I. Stegeman, R. F. Wallis, and A. A. Maradudin. *Excitation of surface polaritons by end-fire coupling*. Optics letters, 8(7):386–388, 1983.

[8]   Zhijun Sun and Danyan Zeng. *Coupling of surface plasmon waves in metal/dielectric gap waveguides and single interface waveguides*. Journal of the Optical Society of America B, 24(11):2883, 2007.

[9]   Charles J. Choi and Steve Semancik. *Effect of interdome spacing on the resonance properties of plasmonic nanodome arrays for label-free optical sensing*. Optics Express, 21(23):28304, 2013.

[10] Qi Ye, Jianxin Fang, and Li Sun. *Surface-Enhanced Raman Scattering from Functionalized Self-Assembled Monolayers. 2. Distance Dependence of Enhanced Raman Scattering from an Azobenzene Terminal Group*. Journal of Physical Chemistry B, 101(41):8221–8224, 1997.

[11] Ashim Dhakal, Pieter Wuytens, Ali Raza, Nicolas Le Thomas, and Roel Baets. *Silicon Nitride Background in Nanophotonic Waveguide Enhanced Raman Spectroscopy*. Materials, 10(2):140, 2017.

[12] Hsin Yu Wu, Longju Liu, Meng Lu, and Brian T. Cunningham. *Lasing Emission from Plasmonic Nanodome Arrays*. Advanced Optical Materials, 4(5):708–714, 2016.

[13] Wei Zhou, Jae Yong Suh, Yi Hua, and Teri W. Odom. *Hybridization of localized and guided modes in 2D metal-insulator-metal nanocavity arrays*. Journal of Physical Chemistry C, 117(6):2541–2546, 2013.

[14] Mitradeep Sarkar, Mondher Besbes, Julien Moreau, Jean François Bryche, Aurore Olivéro, Grégory Barbillon, Anne Lise Coutrot, Bernard Bartenlian, and Michael Canva. *Hybrid plasmonic mode by resonant coupling of localized plasmons to propagating plasmons in a Kretschmann configuration*. ACS Photonics, 2(2):237–245, 2015.

[15] Luping Du, Xuejin Zhang, Ting Mei, and Xiaocong Yuan. *Localized surface plasmons, surface plasmon polaritons, and their coupling in 2D metallic array for SERS*. Optics express, 18(3):1959–1965, 2010.

[16] S Hamed Shams Mousavi, Ali A Eftekhar, Amir H Atabaki, and Ali Adibi. *Band-edge Bilayer Plasmonic Nanostructure for Surface Enhanced Raman Spectroscopy*. ACS Photonics, 2:1546–1551, 2015.

[17] Haibo Li, Yuejiao Gu, Hongyun Guo, Xinnan Wang, Yu Liu, Weiqing Xu, and Shuping Xu. *Tunable plasmons in shallow silver nanowell arrays for directional surface-enhanced Raman scattering*. Journal of Physical Chemistry C, 116(44):23608–23615, 2012.

[18] John C. Hulteen and Richard P. Van Duyne. *Nanosphere lithography: A materials general fabrication process for periodic particle array surfaces*. Journal of Vacuum Science & Technology A: Vacuum, Surfaces, and Films, 13(3):1553–8, may 1995.

[19] A. Kosiorek, W. Kandulski, P. Chudzinski, K. Kempa, and M. Giersig. *Shadow Nanosphere Lithography: Simulation and Experiment*. Nano Letters, 4(7):1359–1363, jul 2004.

[20] Mohammadali Tabatabaei, Alexandre Sangar, Nastaran Kazemi-Sanjani, Philippe Torchio, Alexandre Merlen, and Francois Lagugné-Labarthet. *Optical Properties of Silver and Gold Tetrahedral Nanopyramid Arrays Prepared by Nanosphere Lithography*. The Journal of Physical Chemistry C, 117:14778–86, 2013.

[21] Pierre Colson, Catherine Henrist, and Rudi Cloots. *Nanosphere lithography: A powerful method for the controlled manufacturing of nanomaterials*. Journal of Nanomaterials, 2013, 2013.

[22] Matthew R Jones, Kyle D Osberg, Robert J Macfarlane, Mark R Langille, and Chad A Mirkin. *Templated techniques for the synthesis and assembly of plasmonic nanostructures*. Chemical reviews, 111(6):3736–827, jun 2011.

[23] Maria Bardosova, Martyn E Pemble, Ian M Povey, and Richard H Tredgold. *The langmuir-blodgett approach to making colloidal photonic crystals from silica spheres*. Advanced materials, 22(29):3104–24, aug 2010.

[24] Rodica Morarescu. *Preparation and Applications of Periodical Gold Nanoparticle Arrays*. PhD thesis, Universitat Kassel, 2009.

[25] Traci R Jensen, Michelle Duval Malinsky, Christy L Haynes, and Richard P Van Duyne. *Nanosphere Lithography : Tunable Localized Surface Plasmon Resonance Spectra of Silver Nanoparticles*. Journal of Physical Chemistry B, 104(May):10549–10556, nov 2000.

[26] Pierre Colson, Rudi Cloots, and Catherine Henrist. *Experimental design applied to spin coating of 2D colloidal crystal masks: a relevant method?* Langmuir : the ACS journal of surfaces and colloids, 27(21):12800–6, nov 2011.

[27] Jian Chen, Peitao Dong, Di Di, Chaoguang Wang, Haoxu Wang, Junfeng Wang, and Xuezhong Wu. *Controllable fabrication of 2D colloidal-crystal films with polystyrene nanospheres of various diameters by spin-coating.* Applied Surface Science, 270:6–15, apr 2013.

[28] Mona J. K. Klein, Franck Montagne, Nicolas Blondiaux, Oscar Vazquez-Mena, Harry Heinzelmann, Raphael Pugin, Juergen Brugger, and Veronica Savu. *SiN membranes with submicrometer hole arrays patterned by wafer-scale nanosphere lithography.* Journal of Vacuum Science & Technology B: Microelectronics and Nanometer Structures, 29(2):021012, 2011.

[29] Jea-Young Choi, T L Alford, and Christiana B Honsberg. *Solvent-controlled spin-coating method for large-scale area deposition of two-dimensional silica nanosphere assembled layers.* Langmuir : the ACS journal of surfaces and colloids, 30(20):5732–8, may 2014.

[30] Douglas A Stuart, Chanda Ranjit Yonzon, Xiaoyu Zhang, Olga Lyandres, Nilam C Shah, Matthew R Glucksberg, Joseph T Walsh, and Richard P Van Duyne. *Glucose sensing using near-infrared surface-enhanced Raman spectroscopy: gold surfaces, 10-day stability, and improved accuracy.* Analytical Chemistry, 77(13):4013–9, jul 2005.

[31] Cosmin Farcau and Simion Astilean. *Mapping the SERS Efficiency and Hot-Spots Localization on Gold Film over Nanospheres Substrates.* The Journal of Physical Chemistry C, 114(27):11717–22, jul 2010.

[32] Jon a. Dieringer, Adam D. McFarland, Nilam C. Shah, Douglas a. Stuart, Alyson V. Whitney, Chanda R. Yonzon, Matthew a. Young, Xiaoyu Zhang, and Richard P. Van Duyne. *Surface enhanced Raman spectroscopy: new materials, concepts, characterization tools, and applications.* Faraday Discussions, 132:9, 2006.

[33] Weiqiang Xie, Yunpeng Zhu, Tangi Aubert, Steven Verstuyft, Zeger Hens, and Dries Van Thourhout. *Low-loss silicon nitride waveguide hybridly integrated with colloidal quantum dots.* Optics Express, 23(9):12152, 2015.

[34] Terefe G. Habteyes, Scott Dhuey, Erin Wood, Daniel Gargas, Stefano Cabrini, P. James Schuck, a. Paul Alivisatos, and Stephen R. Leone. *Metallic adhesion layer induced plasmon damping and molecular linker as a nondamping alternative.* ACS Nano, 6(6):5702–5709, 2012.

[35] Marc Lamy de la Chapelle, Hong Shen, Nicolas Guillot, Benoît Frémaux, Bruno Guelorget, and Timothée Toury. *New Gold Nanoparticles Adhesion Process Opening the Way of Improved and Highly Sensitive Plasmonics Technologies.* Plasmonics, 8(2):411–415, 2013.

[36] Martin Moskovits. *Persistent misconceptions regarding SERS.* Physical Chemistry Chemical Physics, 15(15):5301, 2013.

[37] E.C. Le Ru, M Meyer, and P.G. Etchegoin. *Surface Enhanced Raman Scattering Enhancement Factors: A Comprehensive Study.* Journal of Physical Chemistry C, 111(37):13794–13803, 2007.

[38] S.J. Lee, Z. Guan, H. Xu, and M. Moskovits. *Surface-Enhanced Raman Spectroscopy and Nanogeometry: The Plasmonic Origin of SERS.* Journal of Physical Chemistry C, 111(49):17985–17988, 2007.

[39] R A Sperling and W J Parak. *Surface modification, functionalization and bioconjugation of colloidal inorganic nanoparticles.* Philosophical transactions. Series A, Mathematical, physical, and engineering sciences, 368(1915):1333–1383, 2010.

[40] Jian Feng Li, Yi Fan Huang, Yong Ding, Zhi Lin Yang, Song Bo Li, Xiao Shun Zhou, Feng Ru Fan, Wei Zhang, Zhi You Zhou, De Yin Wu, Bin Ren, Zhong Lin Wang, and Zhong Qun Tian. *Shell-isolated nanoparticle-enhanced Raman spectroscopy.* Nature, 464(7287):392–395, 2010.

[41] K Kneipp, Y Wang, H Kneipp, L T Perelman, and I Itzkan. *Single molecule detection using surface-enhanced Raman scattering (SERS).* Physical review Letters, 78(9):1667–1670, 1997.

[42] L. Baia, M. Baia, J. Popp, and S. Astilean. *Gold films deposited over regular arrays of polystyrene nanospheres as highly effective SERS substrates from visible to NIR.* Journal of Physical Chemistry B, 110(47):23982–23986, nov 2006.

[43] Jiaqi Li, Chang Chen, Hilde Jans, Xiumei Xu, Niels Verellen, Ingrid Vos, Yasuaki Okumura, Victor V. Moshchalkov, Liesbet Lagae, and Pol Van Dorpe. *300 mm Wafer-Level , Ultra-Dense Arrays of Au- Capped Nanopillars with sub-10 nm Gaps as Reliable SERS Substrates.* Nanoscale, 6:12391–96, 2014.

[44] Hsin-Yu Wu, Charles J Choi, and Brian T Cunningham. *Plasmonic nanogap-enhanced Raman scattering using a resonant nanodome array.* Small, 8(18):2878–85, sep 2012.

[45] Jing Jiang, Zhida Xu, Abid Ameen, Fei Ding, Guohong Lin, and Gang Logan Liu. *Large-area, lithography-free, low-cost SERS sensor with good flexibility and high performance.* Nanotechnology, 27(38):385205, 2016.

[46] Zheng Zeng, Yiyang Liu, and Jianjun Wei. *Recent advances in surface-enhanced raman spectroscopy (SERS): Finite-difference time-domain (FDTD) method for SERS and sensing applications*, 2016.

[47] Ekaterina Lengert, Mariia Saveleva, Anatolii Abalymov, Vsevolod Atkin, Pieter C Wuytens, Roman Kamyshinsky, Alexander L Vasiliev, A Dmitry, Gleb B Sukhorukov, Andre G Skirtach, and Bogdan Parakhonskiy. *Silver alginate hydrogel micro- and nano- containers for theranostics : synthesis , encapsulation , remote release and detection.* ACS Applied Materials & Interfaces, 2017.

4

SILICON NITRIDE WAVEGUIDES FOR ON-CHIP RAMAN AND SERS

Inspired by the massive success of miniaturizing bulk electronics to nanometer-sized components on an integrated CMOS electronic chip, photonic integration aims to bring various free-space optical components to a single chip. In recent years, our research team has done pioneering work on the development of an integrated photonics platform for waveguide-excited and collected Raman spectroscopy. Here, we further characterize this platform and present important improvements to on-chip surface-enhanced Raman spectroscopy. In particular, we discuss the following issues:

1. *Is nanophotonic waveguide-enhanced Raman spectroscopy promising for an on-chip detection of gaseous molecules?*

2. *Can we develop an e-beam free technology to functionalize deep-UV patterned SiN waveguides with a SERS substrate?*

3. *How does waveguide excited and collected Raman and SERS compare to their free-space equivalent?*

The results described in this chapter extend on the research done in collaboration with Dr. A. Dhakal[1] and Dr. F. Peyskens [2] on integrated Raman spectroscopy. Section 4.3 was published in Wuytens et al., Optics Letters (2017).

4.1　Silicon and Silicon-nitride photonics

Multiple material platforms for photonic integration have been developed over the past decades of which silicon photonics is rapidly becoming the omnipresent technology for various industrial applications of photonic integrated circuits. The fundamental component in a silicon photonics circuit is the silicon-on-insulator (SOI) waveguide (figure 4.1a). It consists of a high refractive index Si core ($n_{Si} = 3.45$ at 1550 nm) embedded on a SiO_2 ($n_{SiO} = 1.44$) substrate. Because of this high index contrast, light can be tightly confined in the 450 nm wide by 220 nm high Si core. These nanophotonic waveguides allow for a dense integration of different components such as waveguides, resonators, modulators and spectrometers on a minimal surface area (figure 4.1c). The success of the SOI platform is largely due to the use of standard CMOS-fabrication techniques used for integrated electronics, which ensures high-volume manufacturing, reproducible components and potential co-integration with CMOS electronics. Thanks to the transparency of Si in the wavelength band where optical fibers have minimal absorption (1300-1600 nm), SOI has proven to be an excellent platform for telecom applications. But SOI also provides a promising technology for sensing. When light is confined in the waveguide core, part of the electromagnetic mode in the waveguide mode extends out of the Si region. This part, referred to as the evanescent field, enables to sensitively detect changes in the surrounding media. SOI enabled, amongst others, the development of sensitive and compact refractive index [1] and absorption [2] sensors across the telecom and mid-infrared wavelength range.

Silicon has an indirect bandgap of 1.12 eV, which implies that it absorbs light with wavelengths shorter than 1.1 μm. This makes it a great material for solar cells or cameras, but obviously not for guiding light at visible wavelengths. Because the intensity of (Raman) scattering scales with λ^{-4}, silicon is not the ideal material for an integrated detection of optical scattering. This inspired the development of a silicon nitride (SiN) counterpart, a deep-UV fabricated integrated photonics platform that is transparent at visible wavelengths. The SiN waveguide (figure 4.1b) is conceptually similar to the Si waveguide, it has a slightly lower core index ($n_{SiN} = 1.9 - 2$ at 800 nm), which combined with the shorter wavelengths results in single-mode waveguides of comparable size. Of crucial importance is that SiN photonic chips can also be made on wafer-scale in the CMOS-fab. The ongoing improvement of different optical components such as low-loss waveguides [3],

---

[1]Photonics Research Group and Center for Nano- and Biophotonics UGent. Current affiliation: Phutung Research Institute, Nepal

[2]Photonics Research Group and Center for Nano- and Biophotonics UGent. Current afilliation: MIT, USA

spectrometers [5, 6] and hybrid integrated lasers [7] is leading to a maturation of this SiN platform [8]. Being transparent at near-infrared and visible wavelengths, SiN enabled on-chip fluorescence [9] and Raman spectroscopy [10].

4.2   Waveguide-enhanced Raman spectroscopy

Figure 4.2 shows the idea of the future integration of a full Raman system on a SiN nanophotonic chip, including a III/V integrated laser [7], integrated filters, a waveguide collection region [11] and an on-chip spectrometer [12]. Technological improvements on all these different components are ongoing. Here, we focus on the waveguide-based excitation and collection of Raman spectra using SiN slot waveguides (figure 4.3), described in detail in the doctoral thesis of A. Dhakal [13]. Apart from the typical advantages of miniaturizing a Raman spectrometer to a lab-on-a-chip device, such as a reduced cost and size, using guided modes for exciting and collecting Raman spectra can increase the total collected Stokes power by a factor 10-1000. Therefore, by analogy with SERS, we refer to it as waveguide-enhanced Raman spectroscopy (WERS) [14] [15]. The reason for this enhancement is twofold, as illustrated in figure 4.2a-b. First, the strong evanescent field in the confined slot mode results in an increased excitation of dipoles in the slot. Simultaneously, their Stokes radiation coupled to the guided mode is Purcell-enhanced. This is quantified by the parameter $\bar{P}_w$ in figure 4.2a, which represents the total Stokes power coupled into the guided mode for a molecule at a specific position, normalized by that collected by a NA=1 objective. For example, $\bar{P}_w = 1$ implies that the waveguide will collect the Stokes scattering power emitted by an equivalent molecule in free space over a solid angle of $2\pi\, sr$. Second, this efficiently collected Stokes scattering accumulates all along the length of the
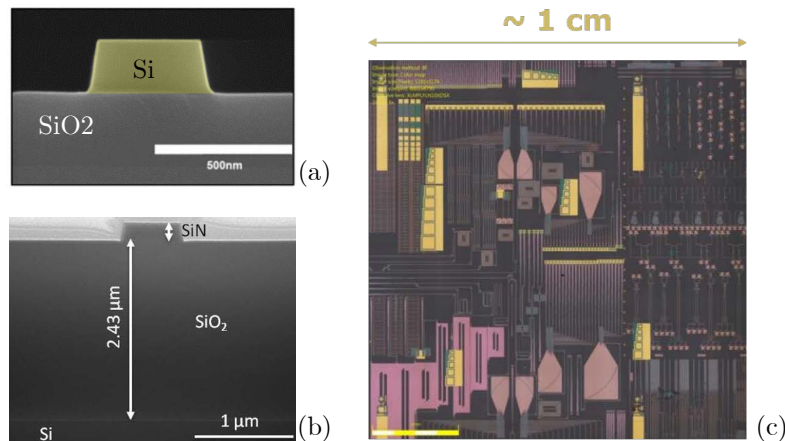

Figure 4.1 (a) SEM cross section of a Si on SiO$_2$ waveguide. (b) SiN on SiO$_2$ waveguide (figure from [3])(c) Example of an integrated photonic chip including waveguides, spectrometers and detectors (figure from [4]).
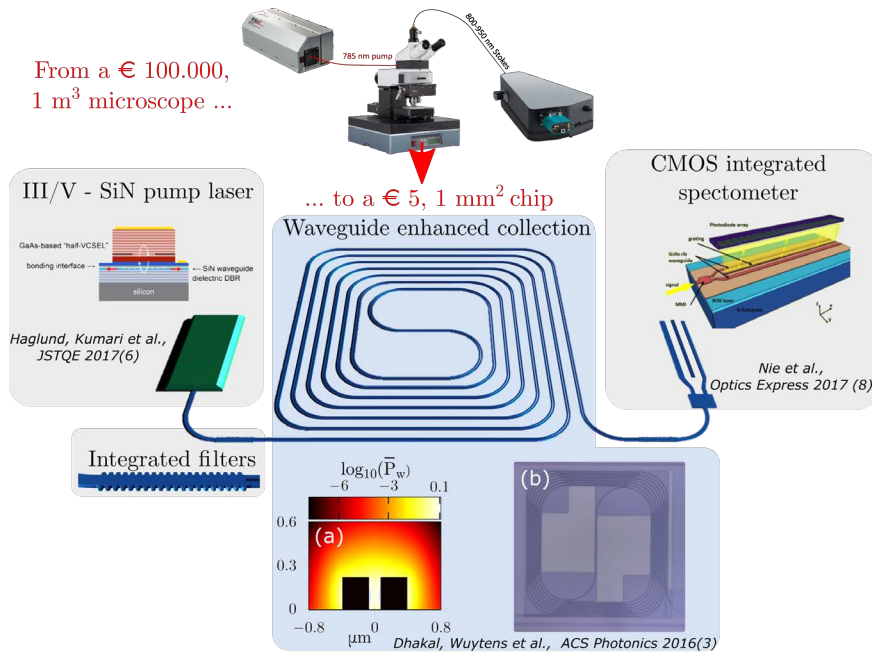
Figure 4.2 Conceptual view of a fully integrated Raman system on a nanophotonic chip. Insets (a) and (b) show the two contributions to the waveguide enhanced excitation and collection: An efficient coupling of dipole radiation to the waveguide and the collection of Stokes power over a long interaction length.

waveguide, for example along the 1 cm long spiral shown in figure 4.2b. For an ideal waveguide, the Raman signal scales linearly with the waveguide length. In reality, the interaction length is limited to a few cm because of propagation loss (1-5 dB/cm) in the waveguide.

Furthermore, WERS is ideal for Raman spectroscopy on objects with dimensions between those measured in SERS (< 10 nm) and confocal microscopy (> 500 nm), as illustrated in figure 4.4. The evanescent field out a SM rib SiN waveguide has a decay length of 10-100 nm, while the slotted waveguides considered here have a gap of 220 nm by 150 nm.
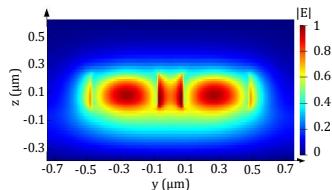
Figure 4.3 Guided TE mode at 785 nm in a slotted SiN waveguide on a SiO$_2$ substrate with a 150 nm air gap sandwiched between two 400 nm wide by 220 nm high SiN ridges. A large fraction of the guided TE mode overlaps with the gap, ensuring a maximal interaction with molecules of interest and a minimal Raman background excitation .
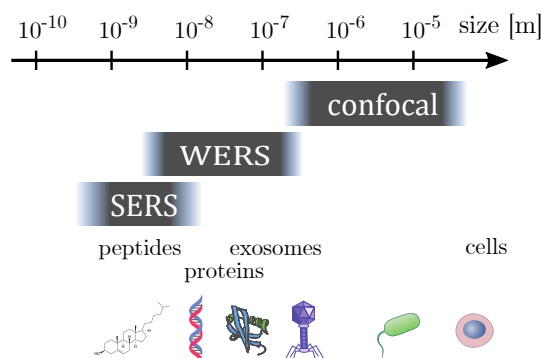

Figure 4.4 Waveguide-enhanced Raman spectroscopy opens a new range of applications because of the 10-100 nm decay length of the evanescent field. (cartoons of biomolecules from [16])

4.2.1 The inevitable Raman background

Over the past few years, three different research groups, including ours, have developed waveguide-based Raman system for detecting bulk liquids [11, 17], gases [14] or monolayers [15]. In all systems, Raman scattering from the waveguide core itself severely limits the sensitivity of the system. As the Stokes scattering of the analyte is acquired along the propagation length of the waveguide, so is the Stokes scattering of the SiN out of which the waveguide is made. As a result, the Raman bands of interest are superimposed on a large background. This strongly increases the shot noise which is proportional to the square root of the total intensity, thereby compromising the detection limit of the waveguide system. The Raman spectrum of our particular SiN (figure 4.5a), an amorphous material, consists of a broad background that decreases monotonically towards longer relative frequency shifts and has a characteristic peak at $2330 \, \text{cm}^{-1}$. Note that the shape and strength of this background depends not only on the waveguide material but also on the exact deposition parameters. We describe the characteristics of this Raman background, which should not be mistaken for background fluorescence, in detail in [18]. Unfortunately the presence of this background is inherent to waveguide-based sensing. The best one can do is to push the guiding mode as much as possible out of the core into the analyte using, for example, the TM mode

in a thin rib waveguide [14] or a nanophotonic slotted waveguide 4.3. Ideally, there exist a material that has a low Raman background, a reasonably high refractive index and is processable on wafer-scale in a CMOS-fab. We have not yet found such a Utopian material. Out of a comparison with atomic layer deposited TiO_2, Al_2O_3 and HfO_2, SiN still came out as the best candidate. Furthermore, of all the different fabricated silicon nitrides we have access to, the PECVD deposited SiN at imec has the lowest Raman background. For example, imec's LPCVD deposited SiN or the PECVD deposited SiN from our cleanroom has an increased background, especially a shorter relative frequencies.

4.2.2   Waveguide-based Carbon Dioxide Sensing

In this section, we explore using WERS for the detection of CO_2 molecules. Spectroscopic methods for detecting CO_2 or other gases can be beneficial over chemical sensors as offer an improved durability over time and can be more robust to environmental variations. Current optical systems rely on non-dispersive IR spectroscopy, using a LED-based light source [19]. Photonic integration can bring a further reduction in size, cost and power consumption, and integrated Raman spectroscopy using visible lasers might be a valuable competitor on these fronts. Apart from measuring airborne concentrations of carbon dioxide, the detection of different CO_2 isotopes is of relevance for multiple applications including breath analysis, radio immuno-assays (similar to ELISA, figure 6.2) and food control. Furthermore the CO_2 detection described here allows us to estimate the general performance of our waveguide-based Raman platform for trace gas detection.

Compared to the waveguide-based acquisition of Raman spectra from bulk liquids [11], we introduced a few changes. We collect the Raman spectrum in reflection rather than transmission. Furthermore, we use a commercial confocal Raman microscope with high NA objective for end-fire coupling the waveguide (figure 4.11a). This allows for an accurate comparison of the performance of the waveguide-excited and collected Raman signal to that using a conventional microscope. The chip and objective are enclosed in a stage-top incubator filled with a 100% concentration of $^{12}CO_2$ or $^{13}CO_2$. Figure 4.5a-b shows the coupling and propagation of the Raman pump light in a slotted waveguide spiral. As explained in the previous section, the collected Raman spectrum contains a strong contribution of the SiN background, as shown in figure 4.5c. After background subtraction, distinguishable Raman spectra of the different CO_2 isotopes are clearly visible (figure 4.6b). Despite the 12-fold increased overall signal in the waveguide-measurement (60-fold when compensating for coupling losses), the signal to noise ratio (SNR) is higher for a free-space measurement (figure 4.6a) under the same power (160 mW) and integration time (300 x 1 s). In the waveguide case, the noise consists of shot noise and multimode-interference in the collection fiber. The latter originates from using a multimode fiber as confocal pinhole and spectrometer entrance slit in our microscope, as explained in chapter 2.2. Its contribution is not inherent to WERS, and can be removed by changing the collection setup. In the
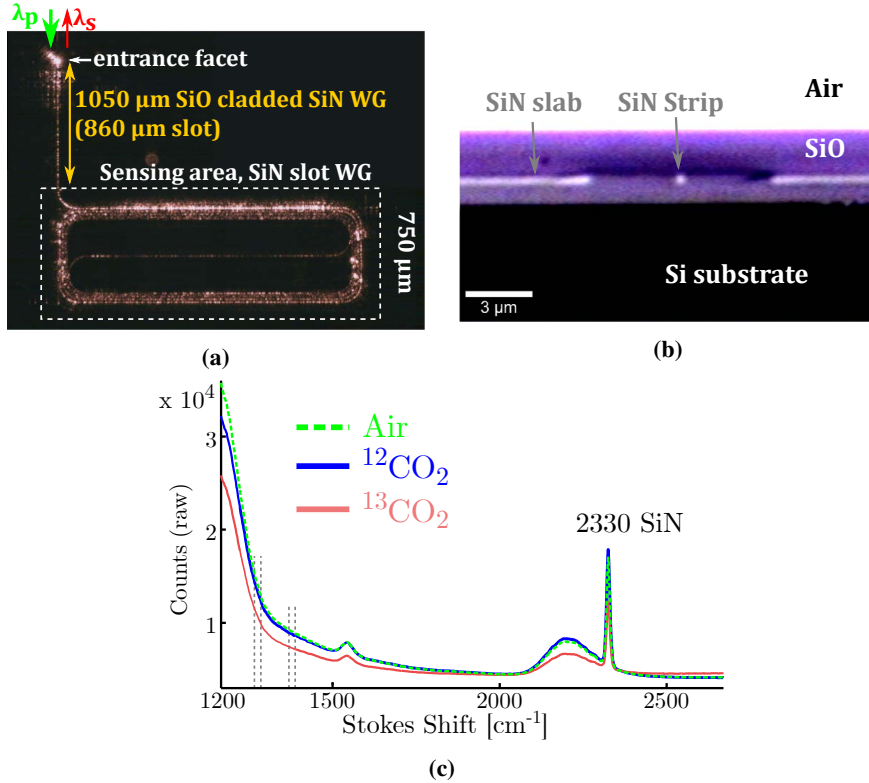
(a)

(b)

(c)

Figure 4.5 (a) Scattering along the propagation of the 785 nm pump light, edge-coupled in a 4 cm long SiN slot waveguide. Starting from the entrance facet, an oxide-clad rib waveguide is tapered into an oxide-clad slot waveguide and finally enters the open-clad sensing spiral. The oxide-clad access waveguide is responsible for a significant part of the SiN background. (b) Cleaved facet of the SiN waveguide seen through the 100x/0.9 microscope objective used for coupling light in- and out of the chip. (c) Unprocessed Raman spectra acquired from the SiN slotted spiral with and without CO_2. The CO_2 peaks (gray dotted lines) are superimposed on the huge SiN background. (The $^{13}CO_2$ measurement could not be optimally aligned because only a limited amount of this gas was available.)

current setup, we observe a 5-fold deterioration of the signal to noise ratio when using the waveguide as compared to the dark-noise limited free-space measurement. Table 4.1 summarizes the comparison between the waveguide and free-space collection geometry, with a limit of detection (LoD) for the CO_2 concentration of respectively 30% and 6.6%.

Our ever-increasing desire for energy has pushed the atmospheric concentration of CO_2 up by 40% since the industrial revolution to 400 ppm (0.04%). Unfortunately the end is not in sight, but even Trumponian measures will not increase the atmospheric CO_2 concentration a level detectable by this waveguide-based Raman measurement. In regard to occupational hazards, the European Union puts the long (8 h) and short term (15 min) exposure limits for CO_2 at respectively
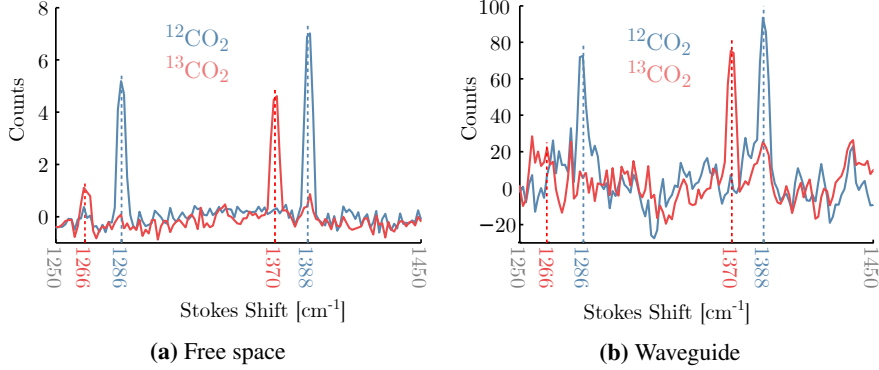
(a) Free space

(b) Waveguide

Figure 4.6 Raman spectra of the $^{12}CO_2$ and $^{13}CO_2$ isotopes in a 100% CO_2 concentration excited and collected through (a) a 100x/0.9 objective (b) a SiN slotted spiral. All spectra are acquired with a 1 s integration time over 300 averages at 170 mW input power. Spectra are background subtracted

Table 4.1: Comparison of waveguide-based and free-space collection of 100 % CO_2 Raman spectra.

	Free Space	Waveguide
Peak height (I, 1389, cm^{-1})	7.1 cts	84 cts
Noise (σ_{BG})	0.23 cts	12.83 cts
SNR ($I/2\sigma$)	15.1	3.3
Dominant noise source	Dark	Shot & MMF
Coupling loss	0 dB	
Relative collected Stokes power	1	60 ± 14
LoD CO_2	6.6%	30.3%

5000 and 15000 ppm [20], which still won't be detectable in the current setup. On Venus our measurement may work today, but luckily there are promising solutions for more earthly applications. In the remainder of this paragraph, we highlight a few ideas for further research.

First we make a simplified comparison between the number of molecules measured in a monolayer sensing experiment to those in a bulk CO_2 measurement for a 100% CO_2 concentration at room temperature under atmospheric pressure. With a mass of 44 g/mol and a density of 1.84 g/L, the minimal detectable CO_2 concentration becomes:

$$C_{CO_2}^{min} = \frac{\rho}{N} LoD = 12.7 \, mM \tag{4.1}$$

We assume that the slot waveguide mode fills the entire slot area and contributions from outside of the slot are neglected. For a 220 nm by 150 nm slot waveguide, the collection volume V^{slot} equals $3.3 \cdot 10^{-13} \, L$ per cm of waveguide (figure 4.7a). The minimal number of detectable molecules becomes:

$$N_{CO_2}^{min} = V^{slot} C_{CO_2}^{min} N_A = 2.5 \cdot 10^9 \text{ molecules/cm}_{wg} \tag{4.2}$$
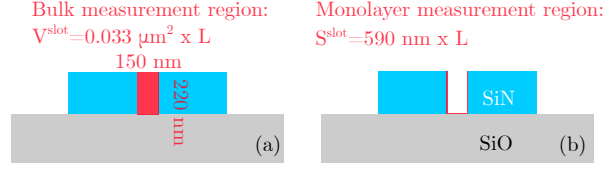
Figure 4.7 Interrogated volume or area in (a) bulk or (b) monolayer WERS using a slotted waveguide.

Now, consider the slot is filled with polyethyleneimine (PEI). This material is known to capture CO_2 out of the ambient air [21]. At atmospheric concentrations, the density of CO_2 in the polymer increases by a factor 10^5 to approximately 70 g/L. This corresponds to a concentration of 1.6 M or $3.2 \cdot 10^{11}$ molecules per cm waveguide, more than 100 times higher than the detection limit of our waveguide system. Thus, in a PEI filled slot waveguide we can expect a sensitivity of 4 ppm CO_2. For stronger Raman scatterers such as DMSO (see table 2.3 on page 2-13) in a comparable system, the detection limit lowers to 10-100 ppb. This anticipated value is similar to the 7.6 ppb detection limit measured by Stievater et al. [14] on a SiN rib waveguide coated with a hybersorbent polymer that increases the concentration by a factor 10^8. The combination of such a hybersorbent polymer with our slotted waveguides could bring the limit of detection of DMSO down to a few 100 ppt.

Next, consider a monolayer of CO_2 isotopes bound to the SiN waveguide. For this purpose, the SiN surface needs to be functionalized with, for example, (3-aminopropyl)-triethoxysilane (APTES). A single CO_2 molecule can bind to the amino group of this molecule, which has a grafting density ρ_{APTES} of approximately 10^{14} cm^{-2}. We calculate the number of probed molecules in a monolayer ($N_{CO_2}^{ML}$) under the assumption that the Stokes signal is collected exclusively from the surface area in the gap (4.7b):

$$S^{slot} = (2 \times 220\,\text{nm} + 150\,\text{nm})/\text{cm}_\text{wg} = 5.9 \cdot 10^{-5}\,\text{cm}^2/\text{cm}_\text{wg} \qquad (4.3)$$

$$N_{CO_2}^{ML} = \rho_{APTES} S^{slot} = 5.9 \cdot 10^9\,\text{molecules}/\text{cm}_\text{wg} \qquad (4.4)$$

According to this back-of-the-envelope calculation, a monolayer of CO_2 molecules will be just detectable, as it provides a similar amount of measured molecules on the waveguide as a 70% concentration. Note that we have made a conservative calculation. Molecules close to the SiN surface, as is the case for the monolayer, will have a stronger Stokes scattering than those in the center of the gap and the outer surface of the slot waveguide will also contribute to the signal. Remember that the situation is different in an objective-based collection. In a collection volume of 3 μm^3, a limit of detection of 6.6 % corresponds to Stokes scattered photons collected from $5 \cdot 10^6$ molecules. However, in a monolayer, we would acquire signal only from a 1 μm^2 spot containing $1 \cdot 10^6$ molecules. As a consequence, the signal will be masked by dark (thermal) noise or background signal of the substrate

material.

When comparing the slot waveguide to a microscope, there is a large discrepancy between the 17.7 ± 1 dB Stokes signal enhancement measured here for CO_2, and the 30 dB enhancement measured and theoretically calculated in [13] for 2-propanol. However, both measurements used the same waveguides. When repeating the experiment for 2-propanol, the measured enhancement was similar to the one measured for CO_2. The 13.3 dB difference can be explained by differences in the diameter of the confocal pinhole (see section 2.2, figure 2.7a). In [13] fully confocal detection is implicitly assumed, where the pinhole matches the diffraction limited beam waist. In contrast, we have used a 100 µm wide pinhole to collect as much Stokes scattering as possible, while optimal axial resolution requires a 14 µm wide pinhole for the 100x/0.9 objective. From the perspective of a chemical analyst, a signal enhancement of 17.7 dB is correct, because there is no reason to reduce the pinhole size in non-imaging applications. From a photonic integration perspective, the 30 dB enhancement makes sense because a future integration of a minimal sized spectrometer requires collection of light with minimal etendue.

We make a final back of the envelope calculation to convince ourselves of the correct values. Assume a waveguide loss of 3 dB/cm at the pump wavelength (785 nm) and 4 dB/cm at the Stokes wavelength (880 nm). The total amount of collected Stokes light is equal to that of an equivalent lossless waveguide of 0.62 cm (equation (4.6)). The coupling efficiency of Stokes scattering to the waveguide mode from CO_2 molecules in the 220 nm high by 150 nm wide slot is comparable to the power collected by a 1.0 NA objective (figure 4.2a). Thus, the waveguide collects Stokes scattering over a volume of $0.033 \ \mu m^2/cm \times 0.62 \ cm = 205 \ \mu m^3$ with a solid angle (equation (2.22)) of $2\pi sr$. In our microscope setup we collect light in a 100 µm pinhole through a 100x/0.9 NA objective. This corresponds to a signal collection over a confocal volume of approximately 3 µm^3 with a solid angle of 3.54 sr. The expected enhancement of collected Stokes signal through the waveguide versus the microscope becomes 20.8 dB, close to the measured 17.7 ± 1 dB.

4.3 Integrated Surface-enhanced Raman spectroscopy

A hybrid integration of nanoplasmonic antennas with silicon nitride waveguides enables miniaturized chips for surface-enhanced Raman spectroscopy at visible and near-infrared wavelengths. This integration can result in high-throughput SERS assays on low sampling volumes. However, current fabrication methods are complex and rely on electron-beam lithography, thereby obstructing the full use of an integrated photonics platform. Here, we demonstrate the electron-beam-free fabrication of gold nanotriangles on deep-UV patterned silicon nitride waveguides

using nanosphere lithography. The localized surface-plasmon resonance of these nanotriangles is optimized for Raman excitation at 785 nm, resulting in a SERS substrate enhancement factor of 2.5×10^5. Furthermore, the SERS signal excited and collected through the waveguide is as strong as the free-space excited and collected signal through a high NA objective.

4.3.1   Introduction

Even though waveguide-based Raman spectroscopy strongly increases the collected Stokes scattering as compared to free-space sensing [14, 17, 18, 22], it remains limited by both the low Raman cross-section of most molecules and the intrinsic background Raman scattering of the waveguide itself [18]. Surface-enhanced Raman scattering (SERS) allows to dramatically increase the Raman signal from molecules in the close vicinity of plasmonic nano-antennas, even up to the limit of single-molecule detection [23]. Recent efforts succeeded in combining plasmonic antennas with Si [24] and SiN [25–27] waveguides, providing proof-of-concept experiments for integrated localized surface plasmon resonance (LSPR) sensing [27] and even waveguide-excited and -collected SERS [26]. However, all these approaches rely on multiple electron-beam lithography steps with critical alignment for writing both the waveguides and the nano-antennas. Apart from being time-consuming and resource-intensive, the use of e-beam lithography inhibits exploiting the full functionality of a mature integrated photonics platform. Alternative approaches combine a waveguide platform with colloidal gold or silver nanoparticles [28–30]. However, colloidal particles lack the reproducibility of top-down fabricated SERS substrates.

In this section, we develop a nanosphere-lithography [31] (NSL) based technology for patterning deep-UV fabricated SiN waveguides with gold nanotriangles. We characterize the plasmonic resonance of these nanotriangles through their absorption spectra and demonstrate efficient waveguide-based excitation and collection of surface-enhanced Raman spectra at a pump wavelength of 785 nm. Furthermore, for an equal input power we experimentally find the Stokes scattered power to be approximately equal when exciting and collecting through the waveguide versus a high numerical aperture objective. To the best of our knowledge, this is the first demonstration of an e-beam free platform for on-chip SERS, an important step towards a complete on-chip SERS-platform combining the sensing area, filters, spectrometer and even the laser on a single chip.

4.3.2   Fabrication of integrated nanotriangles

Figure 4.8 schematically shows how a deep-UV patterned SiN chip is decorated with nanotriangles. The fabrication process is described in more detail in the methods section. First, a $2.5 - 15\,\mu$m wide window is defined across the waveguide using photoresist. This window is thinned down using oxygen plasma to avoid stacking of the polystyrene beads. Next, polystyrene beads with a 448 nm diameter are spin-coated on the chip to form a self-assembled, hexagonally close packed
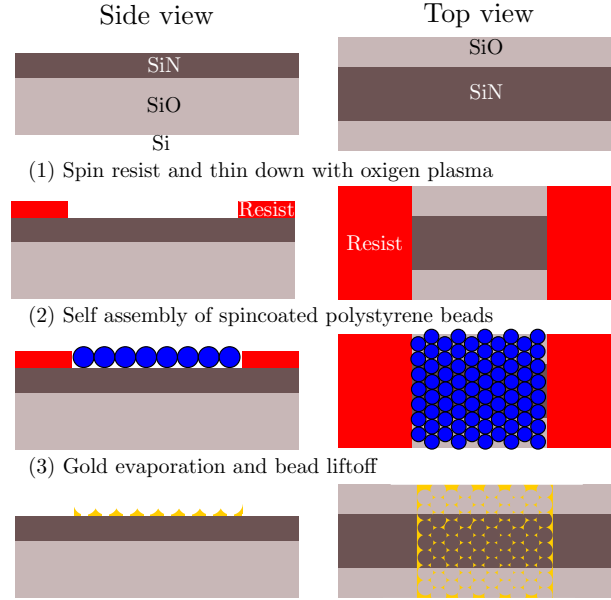
Side view   Top view

(1) Spin resist and thin down with oxigen plasma

(2) Self assembly of spincoated polystyrene beads

(3) Gold evaporation and bead liftoff

Figure 4.8 Simplified processing scheme for patterning SiN waveguides with gold nanotriangles.

monolayer in this window. These beads act as a mask for gold deposition. After lifting of the beads and resist, the waveguide is covered with a repetitive pattern of nanotriangles. Figure 4.9 shows SEM images of the monolayer of beads and resulting gold nanotriangles on the waveguide. Because of the 220 nm height difference between the waveguide and the substrate, the beads form a double layer on the latter. Openings in the double HCP-layer result in the smaller nanodots visible next to the waveguide in figure 4.9b.

4.3.3   Spectral properties of the localized surface plasmon resonance

The nanotriangles and waveguides are designed for a Raman pump laser of 785 nm and Stokes emission at 877 nm, corresponding to the $1339\,cm^{-1}$ symmetric stretching mode (ν_s) of NO_2 in the gold-binding molecule para-nitrothiophenol (pNTP) [32]. A maximal overlap of the LSPR with the wavelength region of the pump laser and Stokes emission is necessary to achieve a high SERS enhancement factor. The spectral location of this resonance strongly depends on geometrical parameters such as the size and aspect ratio of the triangles, as well as the refractive index of the surrounding materials. For uncoupled gold nanostructures, implying a large separation between the antennas, the extinction spectrum provides a reasonable indication for wavelength-dependent enhancement factor [33]. With a gap of approximately 75 nm (figure 4.9d), this condition is met for the nanotriangles. The optimal geometry was experimentally found by varying the radius of the
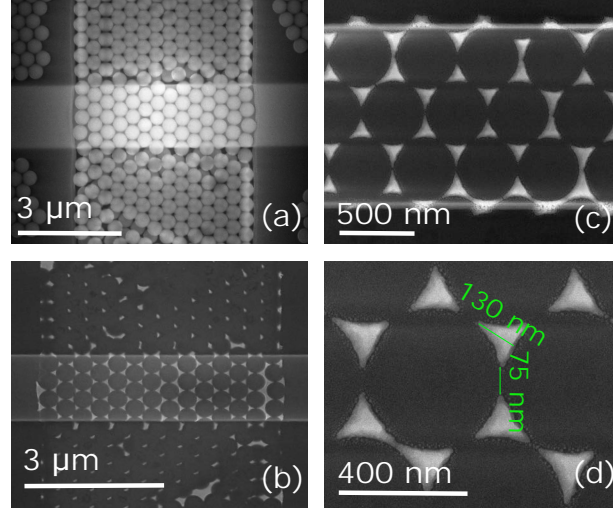
Figure 4.9 SEM image of (a) a hexagonally close-packed monolayer of polystyrene beads in photoresist across the SiN waveguide and (b-d) a typical gold nanotriangle pattern on the waveguide.

polystyrene beads, thinning down the beads with O_2 plasma (figure 4.8, between step (2) and (3)) and adjusting the thickness of the evaporated gold. Optimal values of respectively 224 nm, 15 s and 70 nm were determined from UV-Vis absorption and SERS spectra measured on different geometries using a top-down, free-space excitation (data not shown). These parameters are used for fabricating nanotriangles on a SiN waveguide. Figure 4.10a shows the spectral absorption from different lengths of these nanotriangle patterns on waveguides when excited by a TE polarized supercontinuum source. As expected, the absorbance increases with increasing number of nanotriangles. Furthermore, the 785 nm pump wavelength and $1339\,\mathrm{cm}^{-1}$ Stokes shift overlap well with this spectrum, indicating that these structures are suited for exciting surface-enhanced Raman spectra in the near-infrared. From these data we extract an absorption coefficient for the gold nanotriangles α_p of $1.7 \pm 0.5\,\mathrm{dB}/\mu\mathrm{m}$ at the 785 nm pump and α_s of $2.7 \pm 0.5\,\mathrm{dB}/\mu\mathrm{m}$ at the 877 nm Stokes wavelength. From α_s and α_p we calculate the total collected Stokes power as function of the length of the nanotriangle section:

$$P_{col}^R \propto \gamma_{in}\gamma_{out}\int_0^L P_0 e^{-\alpha_p x}\sigma e^{-\alpha_s x}dx \tag{4.5}$$

$$\propto \gamma_{in}\gamma_{out}P_0\sigma\,\frac{1 - e^{-L(\alpha_p+\alpha_s)}}{\alpha_p + \alpha_s} \tag{4.6}$$

Here, σ is the Raman cross-section of the molecule P_0 is the laser power incident on the entrance facet of the chip. The losses when coupling pump light in and the Stokes light out of the chip are respectively given by γ_{in} and γ_{out}. Because of the strong absorption of pump and Stokes light, after only $2.5\,\mu\mathrm{m}$ of nanotriangles the SERS signal reaches 93% of the maximum value (solid blue curve in figure

4.12b). Hence making the nanotriangle stretch longer does not contribute to a stronger signal. Figure 4.12b also shows the experimentally measured intensity of the $1339\,\mathrm{cm}^{-1}$ SERS peak on 8 waveguides each for lengths of 2.5 μm, 5 μm, 10 μm and 15 μm, indeed showing no significant differences in signal strength with increasing length.
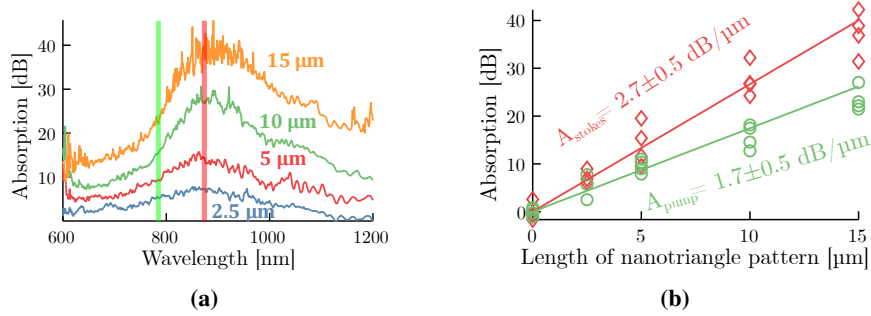

(a)   **(b)**

Figure 4.10 (a) Absorption spectra of waveguides decorated with increasing lengths of nanotriangle patterns. The LSPR-absorption shows a good overlap with a 785 nm pump laser and a $1139\,cm^{-1}$ Stokes shift, respectively green and red shaded. (b) Absorption versus nanotriangle length at pump and Stokes wavelength measured on four different waveguides for each length. A linear fit to the data gives an absorption of $2.7 \pm 0.5\,\mathrm{dB}/\mu\mathrm{m}$ at Stokes and $1.7 \pm 0.5\,\mathrm{dB}/\mu\mathrm{m}$ at the pump wavelength.

4.3.4   Surface-enhanced Raman scattering of waveguide-coupled versus free-space coupled nanotriangles

SERS-spectra of the same nanotriangle patterns are measured using both free-space and waveguide-based excitation. A commercial Raman microscope is used in both cases, with the chip placed respectively perpendicular or parallel to the beam path, as shown in figure 4.11a. This allows for an accurate comparison between the total free-space- and waveguide- collected Stokes scattered power for the same input power. Figure 4.11b shows a camera image of the end-fire coupled chip, placed vertically under a 40x/0.6 objective installed on an upright microscope. Scattering of the waveguide-coupled pump light, propagating along the green arrow in figure 4.11b, can be seen at the entrance facet, at the nanotriangle section and at the other end of the waveguide. The spectra are collected in a reflection mode, meaning that the backscattered Stokes scattered light is collected by the same objective, as indicated by the dashed red arrow. The pump light propagates for approximately 1.5 mm through a multimode SiN rib waveguide before encountering the nanotriangle section. Along this propagation, a strong Raman signal of the SiN core is generated [18]. As a consequence, the Raman spectra collected through the waveguide consist of two major contributions, as highlighted in figure 4.12a. One is the SERS spectrum of NTP, which in the rest of this work will be quantified by its most prominent peak at $1339\,\mathrm{cm}^{-1}$ ($\nu_s\ NO_2$). The other is the SiN background spectrum. Figure 4.12a shows a raw waveguide-excited SERS spectrum, as well as a SiN background spectrum collected from a reference
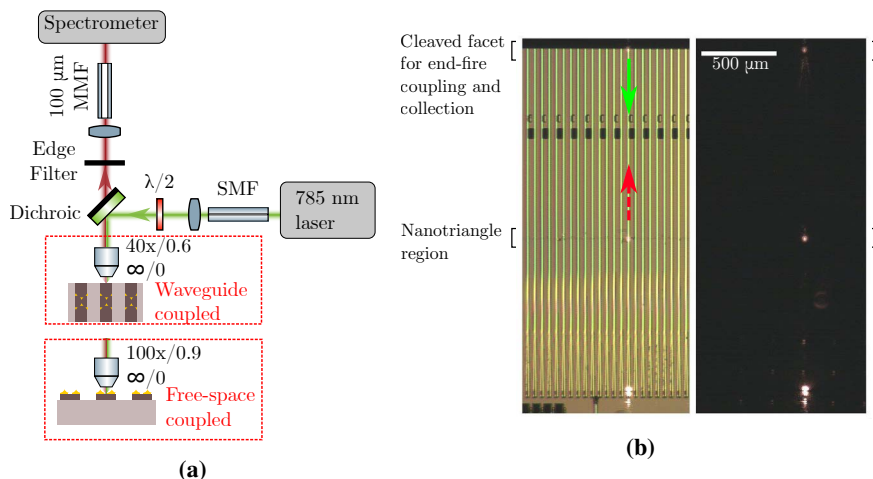
Figure 4.11 (a) Schematic of the confocal microscope used for collecting Stokes scattered light from both waveguide- and free-space coupled nanotriangles. (b) Camera image of the chip in bright field (left) and dark field (right). Light is coupled from the top into the vertically oriented waveguides, and propagates along the waveguide (green arrow) until the nanotriangle section. Stokes scattered light is collected in reflection (red-dashed arrow). Scattering of the pump laser can be seen at the entrance facet and nanotriangle section.

waveguide without plasmonic antennas. The latter is rescaled for equal peak intensity at $2330\,\mathrm{cm}^{-1}$ (figure 4.12a, inset) because of differences in propagation length and absorption. The lack of NTP peaks on the reference spectrum also proves that the NTP peaks indeed originate from gold-bound molecules on the nanotriangles. To compare the waveguide-excited SERS signals to a free-space excitation, we subtract the SiN background and rescale the spectrum to compensate for a total coupling loss ($\gamma_{in}\gamma_{out}$) of 8 dB. The rationale behind compensating for these coupling losses is a future integration of the spectrometer [6] and light source [7] on the chip, eliminating the need for edge-coupling and thus minimizing losses in between components. On a shorter term it is possible to substantially reduce coupling losses by optimizing the waveguide design for a specific coupling geometry. Free-space excited SERS spectra are collected top-down across the same waveguide with the same polarization of the light using a 100x/0.9 NA objective, with the chip placed horizontally under the microscope. This is close to the highest possible etendue using an air objective, and thus results in the strongest possible SERS spectrum collected in free space for this particular SERS substrate. An average spectrum is calculated over the first $2.5\,\mu\mathrm{m}$ of nanotriangle pattern on the waveguide, as this part contributes to over 90% of the waveguide-coupled Raman signal. Figure 4.13a shows both free-space and waveguide excited SERS spectra for a typical waveguide, both having the same shape and approximately equally magnitude. This comparison was made for multiple waveguides on two different chips. The integrated SERS intensity of the $1339\,\mathrm{cm}^{-1}$ peak for each individual nanotriangle-patterned waveguide is shown in figure 4.13b for both free-space and waveguide-based excitation. From this data, we conclude that exciting and collect-

ing surface-enhanced Raman spectra through the waveguide is at least as efficient as through the high NA objective. When the guided power in the waveguide equals the power through the objective, an equal amount of Stokes scattered photons is collected by both systems. Note that this does not imply that both the field intensity and collection efficiency are individually identical in both systems. A difference in mode volume and the asymmetry of the nanotriangles on the SiN waveguide can lead to a different excitation or collection efficiency in both systems [11, 34].
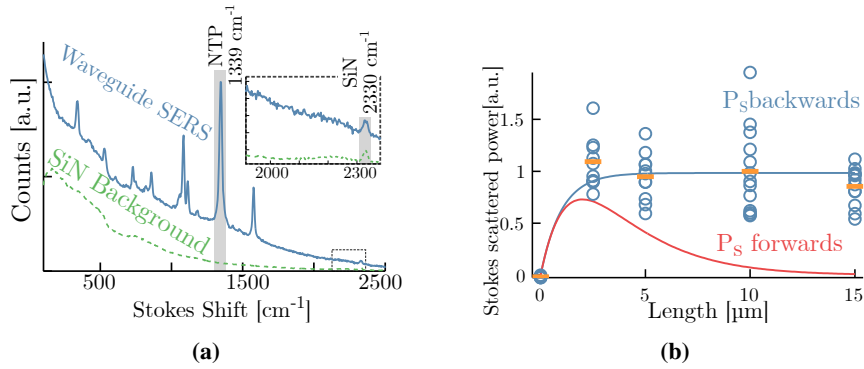

(a)   **(b)**

Figure 4.12 (a) pNTP SERS signal acquired through the waveguide (solid blue) and the SiN background spectrum on a blank reference waveguide (dashed green). The $1339\,\mathrm{cm}^{-1}$ is used for quantifying the enhancement factor. The inset shows a characteristic peak for our SiN at $2330\,\mathrm{cm}^{-1}$. (b) SERS signal strength in function of the length of the nanotriangle section, showing that the maximum signal is already reached for a $2.5\,\mu\mathrm{m}$ length. The orange bars give the average of at least 8 different measurements. The solid blue curve shows the calculated signal strength versus length when collecting the backwards Stokes scattered light in a reflection mode, as used in this work. The red curve shows the forward collected Stokes power in a transmission mode.
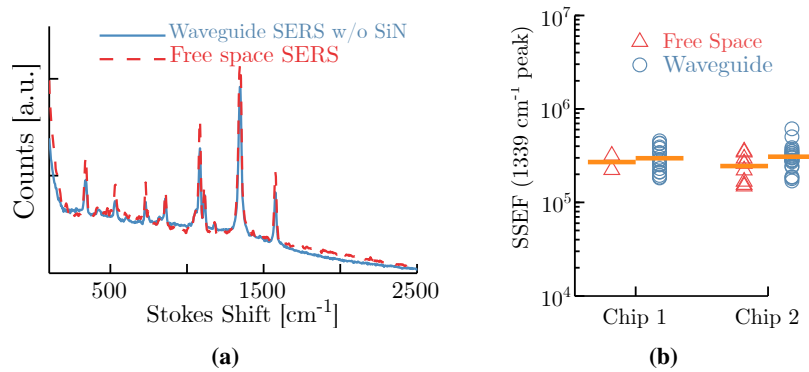

(a)   **(b)**

Figure 4.13 (a) Waveguide collected SERS spectrum (solid blue) after subtracting the SiN background and scaling with the coupling losses, compared to a free-space collected SERS spectrum (dashed red) acquired on the same nanotriangle section. (b) SSEF for free-space excitation and collection compared to the signal strength using a waveguide-based measurement, acquired on multiple waveguides on two different chips.

To enable a quantitative comparison with other (future) integrated SERS platforms, we calculate the SERS substrate-enhancement factor (SSEF) for the gold nanotri-

angle patters as described by Le Ru et al. [35]. The SSEF is defined as the ratio between the average signal per molecule on the SERS substrate and that in a bulk, spontaneous Raman measurement:

$$SSEF = \frac{I_{SERS}}{I_{Raman}} \times \frac{N_{Vol}}{N_{Surf}} \tag{4.7}$$

$$= \frac{I_{SERS}}{I_{Raman}} \times \frac{H_{eff}\rho}{\mu_{Au}\mu_{NTP}A_m} = (2.5 \pm 0.7) \times 10^5 \tag{4.8}$$

In this definition, the intensity of the Raman and SERS signals are scaled to the same excitation power and integration time. The ratio between the number of molecules in a bulk measurement and those adsorbed on the gold surface can be calculated from the bulk molecule density ρ (6.022×10^7 molecules/μm^3), the effective height H_{eff} of the collection volume ($150\,\mu$m), the density of the pNTP molecules on the gold μ_{NTP} (4.4×10^6 molecules/μm^2) [36], the surface area of a single nanotriangle A_m ($0.023\,\mu$m^2) and the density of the metal nanostructures μ_{Au} (11.5 triangles/μm^2). It is important to remember that, although this calculation assumes the use of exactly similar conditions (objective, microscope, pinhole etc.) for acquiring SERS and spontaneous Raman spectra, the final enhancement factor is independent of the optical setup. An exact translation of this free-space enhancement factor to a waveguide-coupled number is not straightforward because of the intrinsic differences in both geometries, and therefore outside the scope of this paper. Qualitatively, we conclude that SERS signals are in the same order of magnitude while the number of molecules excited in both cases is similar.

4.4 Quantitative comparison of waveguide-excited SERS systems

We experimentally compare the nanotriangle-patterned waveguides to bowtie antennas patterned on single-mode, e-beam written SiN waveguides [26]. Hereto, we calculate the ratio of total collected Stokes power over input power η_{RS}^c (similar to the calculation of $d\sigma/d\Omega$ in chapter 2.1.3, equation (2.27)):

$$P_s^c = \gamma_{in}\gamma_{out}F_{ph}h(v_0 - v_s)Tm^{-1} \tag{4.9}$$

$$\eta_{RS}^c = \frac{P_s^c}{P_0} \tag{4.10}$$

For the $1340\,\text{cm}^{-1}$ pNTP peak excited at 785 nm, the Stokes frequency ($v_0 - v_s$) equals 342 THz and the transmission of the microscope T_m is 0.61 at the 870 nm Stokes shifted wavelength. For the particular case of our spectrometer (with settings as described in the methods section) the photon flux F_{ph} equals 5.9 times the number of counts in the Raman spectrum. F_{ph} is multiplied with a total coupling loss $\gamma_{in}\gamma_{out}$ of $8\,\text{dB}$ for the 1.5 μm wide nanotriangle-patterned waveguides and $9.1\,\text{dB}$ for 700 nm wide, e-beam written, bowtie-patterned waveguides. We make

this comparison both for a saturated number of plasmonic antennas and for the case of a 'single antenna'. For the nanotriangle pattern described above, we consider one column of nanotriangles as a single antenna. This corresponds to a length of half a period, or 224 nm. From (4.6), we calculate that this signal column of nano-triangles generates 20% of the saturated value for $\alpha_p = 1.7$ and $\alpha_s = 2.7\,\mathrm{dB}/\mu\mathrm{m}$. Figure 4.14 shows that η_{RS} is approximately 10 times higher for the nanotriangles as compared to the bowtie antennas, both for a saturated number of antennas as for a single antenna. From the difference in SSEF and gold coverage ($A \cdot \mu$, table 3.2 on page 3-44), it is no surprise that η_{RS} is still two orders of magnitude lower as compared to gold nanodomes excited in free-space with a 0.9 NA objective. All measurements in 4.14 were done on the same microscope following an identical pNTP labeling protocol.
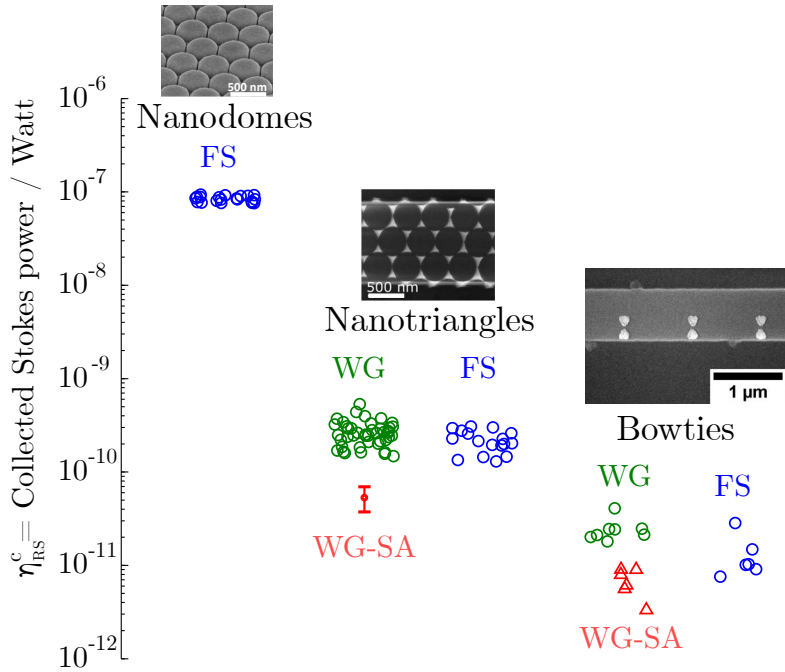

Figure 4.14 Collected Stokes power per watt input power for nanodomes (best chip), nanotriangles (3 chips) and bowtie antennas (best chip) [26] collected using a free-space (FS), 0.9 NA objective or a SiN waveguide (WG), collected from a saturated number of antennas (WG) or a single antenna (WG-SA). Each point corresponds to a different waveguide or a different position on the chip.

4.5 Conclusions and perspectives

In this chapter, we introduced nanophotonic SiN waveguides for integrated Raman- and surface-enhanced Raman spectroscopy. We showed that slotted SiN waveg-uides can be used to detect small Raman cross-section gases like CO_2 and dis-

tinguish between different isotopes, albeit at very high concentrations ($> 30\%$). In a bulk measurement, shot noise and multimode-fiber interference result in a 5-fold deteriorated limit-of-detection for the waveguide measurement as compared to a free-space measurement on a commercial Raman microscope with a -70 °C cooled CCD detector. Nevertheless, we calculated that functionalizing the SiN surface with an absorbent polymer or a CO_2 capturing monolayer make waveguide-enhanced Raman spectroscopy a promising tool for the detection of trace gases or assays with stable CO_2 isotopes as ultra-small labels.

We have also demonstrated a relatively easy process for patterning individual dies of deep-UV waveguides with gold nanotriangles in a post-processing step. The absorption spectrum of this nanopattern is well suited for Raman spectroscopy in the near-infrared, a wavelength region interesting because of its low absorption by biological specimen, reasonably strong scattering and low background fluorescence. SERS data show that the SSEF of this pattern is 2.5×10^5, and that excitation and collection of SERS spectra through the waveguide is at least as efficient as using the best possible air objective. We measured a more than 10-fold improvement of total collected SERS power in comparison to e-beam patterned gold bowties on SiN. Although the enhancement factor of the nanotriangles presented in this manuscript is not among the highest reported in literature, nanosphere-lithography has also been used to fabricate high-performance SERS substrates, at least under free-space excitation [32, 36, 37]. Variations of these can possibly be combined with photonic waveguides. The hybrid integration of nano-plasmonic antennas with a mature integrated photonics platform is a prerequisite for fully integrated SERS sensors. We are convinced that further technological developments on this topic will lead to breakthrough applications that are currently limited to free-space SERS sensing.

Waveguide-integrated SERS using multiple waveguides on a single chip can enable a simultaneous readout of a large number of channels. This dense parallelization is of particular interest for a single-cell analysis of protease activity. This is further explored in chapter 6.5, where we show the detection of a peptide substrate for trypsin hydrolysis on a nanotriangle patterned waveguide.

Materials and Methods

A. SERS on nanotriangle patterned waveguides

Fabrication of nanotriangle patterned waveguides As shown in figure 4.8, we start from a deep-UV patterned die containing 220 nm high by $1.4\,\mu$m wide SiN waveguides. After cleaning the chips, a $2.5 - 15\,\mu$m wide open window is patterned in AZ MiR 701 positive photoresist using UV-contact lithography (SÜSS MA6), resulting in a resist thickness of approximately 700 nm. This resist is thinned down to less than 400 nm using O_2 plasma (Vision 320 RIE, 50 sccm O_2, 75 W, 100 mTorr, 235 s), after which the polystyrene beads are spin-coated on the chip. The resist must be thinner than the size of the polystyrene beads to avoid stacking of the beads at the edges of the window. Typically,

40 μl of a 3.75 w% in 2/1 methanol/water mixture of 448 nm polystyrene beads (Microparticles GMBH) was used for a two-step spin coating. First a HCP monolayer is formed at a speed of 2100 rpm and an acceleration of 1600 rpm/s during 45 seconds, followed by the removal of excessive beads and solvents at 5000 rpm and 1000 rpms during 40 seconds. Note that these parameters should be slightly changed depending on the chip size ($4\,\mathrm{cm}^2$), humidity and temperature in order to acquire an optimal arrangement of the beads into a hexagonally close-packed (HCP) monolayer. After spin-coating, an additional 15 s of O_2 plasma is applied. This reduces the size of the beads such that the resulting nanotriangles will have the optimal dimensions for a LSPR around 785-870 nm. The O_2 plasma also improves the adhesion of metals to the SiN surface. First a 1-4 nm Ti adhesion layer is sputtered, followed by the thermal evaporation of a 70 nm Au layer (Leybold Univex 450). Finally, the polystyrene beads are removed in dichloromethane and the resist is lifted off in acetone. The chips were characterized through scanning electron microscopy on a FEI Nova 600 Nanolab Dual-Beam FIB system, using a voltage of 18 kV and a through the lens (TLD) detection.

UV/Vis/IR extinction curves   Nanotriangle extinction spectra were measured as described by Peyskens et al. in the supplementary information of [26]. Light from an NKT EXR-4 supercontinuum source is filtered through a near-IR transmitting filter and coupled in a fiber. This fiber is plugged into a fiber to free-space U-bench (Thorlabs) consisting of 3 parts: an achromatic fiber collimator which converts the fiberized light to a free-space beam, a free-space broadband polarizer which polarizes the unpolarized light into a TE-beam and an aspheric lens used to focus the free-space beam on the input facet of the chip. At the output facet a lensed fiber is used to capture the transmitted light. This lensed fiber guides the light into an optical spectrum analyzer (Advantest Q8381). Extinction spectra of the nanotriangle-covered waveguides were calculated relative to the transmission of a reference waveguide:

$$E(\lambda) = 10 \log_{10}\left[\frac{T(\lambda)^{ref}}{T(\lambda)^{NSL}}\right]$$

pNTP Chip labeling   Chips were first cleaned with acetone, isopropanol and water and dried under a stream of nitrogen. Next, a short oxygen plasma (PVA-TEPLA GIGAbatch 310 M, 6000 sccm O_2, 600 W, 750 mTorr, 120 s) was used to further remove organic contaminants and render the surface hydrophilic. Immediately after, the chips were immersed for three hours in a 1 mM solution of 4-nitrothiophenol (pNTP, sigma N27209) in ethanol. After incubation, the labeled chips were thoroughly rinsed with ethanol and water to remove excessive pNTP molecules and again dried under a stream of nitrogen. Subsequently the chips were cleaved to allow for end-fire coupling. Three different chips were measured, in all cases the SERS spectra were acquired within 3 days after labeling.

Surface-enhanced Raman spectra   All Raman spectra were acquired on a WITec Alpha 300 R+ confocal Raman microscope (see also chapter 2.2) equipped with a 785 nm diode laser (Toptica, XTRA II) and a spectrometer using 300 lpmm grating diffracting the light onto a -70 °C cooled CCD camera (Andor iDus 401 BR-DD), read using a 0.033 MHz horizontal shift and 16.25 μs vertical shift speed. figure 4.11b shows a sketch of the setup. All nanotriangle-SERS spectra were measured with a laser power of 250 μW at the entrance facet of the microscope objective, and the polarization of the pump beam was set to

TE using a half-wave plate. Note that a low irradiance is necessary to avoid the photoin-duced reduction of pNTP into dimercaptoazobenzene [32] (see chapter 2.3.2). We observed this from a change in relative strength of the $1339\,cm^{-1}$ and $1080\,cm^{-1}$ peaks when increasing the power above $500\,\mu W$, both for waveguide- and free-space coupling. Stokes scattered light is collected in a $100\,\mu m$ core multimode fiber, simultaneously functioning as confocal pinhole, for both waveguide and free-space excitation. Free-space excited spectra were acquired through a *Zeiss 100x/0.9 EC Epiplan NEOFLUAR; ∞/0* objective across the waveguide with a spatial resolution of $250\,nm$ and an integration time of 0.23 s per pixels. Next, the average spectrum is calculated over the first $2.5\,\mu m$ of nanotriangles on the waveguide, being the part of the waveguide that contributes to 95% of the signal. In the waveguide-excited case, the light was end-fire coupled into the chip using a *Nikon 40x/0.6 S Plan Fluor ELWD DIC N1; ∞/0-2.0* objective. Stokes scattered light was collected in reflection through the same objective. These spectra were acquired over 100 averages at an 0.23 s integration time.

Waveguide-excited SERS spectra of the bowtie-antennas patterned on a $700\,nm \times 220\,nm$ single mode SiN waveguide were acquired using a 20 averages, a 1 s integration time and 0.5 mW input power. The SERS signal was found to saturate for five or more bowties on the waveguide. Free-space spectra were acquired from a single bowtie using the 100x/0.9 objective, with the polarization aligned to the long axis of the bowties.

Coupling losses   The efficiency of coupling the pump laser and Stokes light respectively in- and out of the chip was quantified in a transmission measurement on the WITec Alpha 300 R microscope, where two identical objectives *Nikon 40x/0.6 S Plan Fluor ELWD DIC N1; ∞/0-2.0* are placed on both edges of the end-fire coupled chip (figure 4.15). A total transmission loss at 785 nm of $6.2\pm0.23\,dB$ was measured over 6 different waveguides. We neglect propagation losses in the $2\,mm$ long waveguides. Collecting Stokes scattering in transmission is more efficient than in reflection for waveguides with negligible loss. This is because both paths can be independently aligned for respectively the excitation wavelength of 785 nm and Stokes emission at 877 nm. In reflection, chromatic aberrations of the objective inhibit an optimal alignment. An additional loss of $1.8 \pm 0.48\,dB$ is taken into account to compensate for the difference in Raman intensity at a Stokes shift at $1339\,cm^{-1}$ when collected in reflection as compared to transmission. This brings the total coupling loss to $8 \pm 0.71\,dB$.
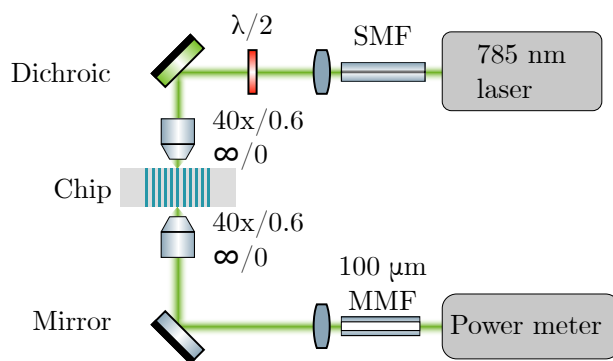

Figure 4.15 Transmission setup on the Raman microscope for measuring end-fire in- and out coupling losses at 785 nm

Quantification of enhancement factor SSEF   The effective height of the confocal volume H_{eff} was determined from an axial scan over a TiO_2 on CaF sample, using a $200\,\mu$m multimode fiber as a pinhole:

$$H_{eff} = \int \frac{\mu_\perp(z)}{\mu_0} dz$$

Here, μ_0 and $\mu_\perp(z)$ are respectively the Raman intensity in focus and at a distance z from the focal plane. The surface area of a single nanotriangle (A_m) covered by gold-binding molecules is calculated from SEM images. The shape of the nanotriangle is approximated as a triangular-based pyramid with a $150\,$nm base and $75\,$nm height.

B. Waveguide-based CO_2 sensing

PECVD SiN Chips   Waveguide-based CO_2 measurements were done through 4 cm long spirals of 220 nm thick PECVD SiN slotted waveguides with a 350 nm ridge width and 150 nm gap width. These waveguides were fabricated on 200 mm wafers by imec in the 'BioSin3' run and were designed by A. Dhakal. After polishing the facets to enable end-fire coupling, chips were wet cleaned in acetone, isopropanol and water and dry-cleaned in an oxygen plasma.

Raman spectra   The same Raman microscope as the one for acquiring SERS spectra was used, see above. The measurement volume was enclosed in a stage-top incubation chamber (OKOlab, custom build) with a CO_2 influx of 0.1 l/min. A 1 liter gas bottle (Sigma 364592-1L-EU) was connected to the chamber for the $^{13}CO_2$ measurements. A *Zeiss 100x/0.9 EC Epiplan NEOFLUAR; ∞/0* objective was used both for acquiring free-space CO_2 spectra and end-fire coupling TE polarized light the waveguides. All spectra were acquired with a 1 s integration time over 300 averages. The background of the waveguide-collected CO_2 spectra was removed two steps. First, a reference spectrum of the same waveguide in air was subtracted. Next, a 9th order polynomial fit was applied to flatten the background.

Coupling losses   Optical losses when end-fire coupling in- and out of the 700 nm wide rib-tapered SiN slot waveguides were characterized as described above. An additional correction factor for exciting and collecting through the 100x/0.9 objective was included from two additional transmission measurements with a 40x/0.6 collection and 100x/0.9 excitation objective and vice versa. This slightly more complicated scheme was used because we don't have two identical 100x/0.9 objectives. Based on earlier measurements, we use a waveguide loss of 3 dB/cm at 785 nm. The resulting coupling loss is 7 ± 1dB.

References

[1] Katrien De Vos, Irene Bartolozzi, Etienne Schacht, Peter Bienstman, and Roel Baets *Silicon-on-Insulator microring resonator for sensitive and label-free biosensing* Optics Express, 15(12):7610–7615, 2007.

[2] E Ryckeboer, R Bockstaele, M Vanslembrouck, and R Baets *Glucose sensing by waveguide-based absorption spectroscopy on a silicon chip.* Biomedical Optics Express, 5(5):1636–48, 2014.

[3] A. Z. Subramanian, P. Neutens, A. Dhakal, R. Jansen, T. Claes, X. Rottenberg, F. Peyskens, S. Selvaraja, P. Helin, B. Dubois, K. Leyssens, S. Severi, P. Deshpande, R. Baets, and P. Van Dorpe *Low-Loss Singlemode PECVD silicon nitride photonic wire waveguides for 532-900 nm wavelength window fabricated within a CMOS pilot line* IEEE Photonics Journal, 5(6):2202809, 2013.

[4] Eva Ryckeboer *Spectroscopic Detection of Glucose with a Silicon Photonic Integrated Circuit* Ghent University, 2014.

[5] Daan Martens, Ananth Z. Subramanian, Shibnath Pathak, Michael Vanslembrouck, Peter Bienstman, Wim Bogaerts, and Roel G. Baets *Compact silicon nitride arrayed waveguide gratings for very near-infrared wavelengths* IEEE Photonics Technology Letters, 27(2):137–140, 2015.

[6] Xiaomin Nie, Eva Ryckeboer, Gunther Roelkens, and Roel Baets *Novel Concept for a Broadband Co-propagative Stationary Fourier Transform Spectrometer Integrated on a SiN Waveguide Platform* CLEO 2016, pages 4–5, 2016.

[7] Emanuel P. Haglund, Sulakshna Kumari, Petter Westbergh, Johan S. Gustavsson, Roel G. Baets, Gunther Roelkens, and Anders Larsson *20-Gb/s Modulation of Silicon-Integrated Short-Wavelength Hybrid-Cavity VCSELs* IEEE Photonics Technology Letters, 28(8):856–859, 2016.

[8] Ananth Z Subramanian, Eva Ryckeboer, Ashim Dhakal, Frédéric Peyskens, Aditya Malik, Bart Kuyken, Haolan Zhao, Shibnath Pathak, Alfonso Ruocco, Andreas De Groote, Pieter Wuytens, Daan Martens, Francois Leo, Weiqiang Xie, Utsav Deepak Dave, Muhammad Muneeb, Pol Van Dorpe, Joris Van Campenhout, Wim Bogaerts, Peter Bienstman, Nicolas Le Thomas, Dries Van Thourhout, Zeger Hens, Gunther Roelkens, and Roel Baets *Silicon and silicon nitride photonic circuits for spectroscopic sensing on-a-chip* Photonics Research, 3(5):47–59, 2015.

[9] Md. Mahmud-Ul-Hasan, Pieter Neutens, Rita Vos, Liesbet Lagae, and Pol Van Dorpe *Suppression of Bulk Fluorescence Noise by Combining Waveguide-Based Near-Field Excitation and Collection* ACS Photonics, 4(3):495–500, mar 2017.

[10] A. Dhakal, A. Z. Subramanian, P. C. Wuytens, F. Peyskens, N. Le Thomas, and R. Baets *Evanescent excitation and collection of spontaneous Raman spectra using silicon nitride nanophotonic waveguides* Optics Letters, 39(13):4025–4028, 2014.

[11] Ashim Dhakal, Ali Raza, Frédéric Peyskens, Ananth Z Subramanian, Stéphane Clemmen, Nicolas Le Thomas, and Roel Baets *Efficiency of evanescent excitation and collection of spontaneous Raman scattering near high index contrast channel waveguides.* Optics express, 23(21):27391–404, 2015.

[12] Xiaomin Nie, Eva Ryckeboer, Gunther Roelkens, and Roel Baets *CMOS-compatible broadband co-propagative stationary Fourier transform spectrometer integrated on a silicon nitride photonics platform* Optics Express, 25(8):A409, 2017.

[13] Ashim Dhakal *Nanophotonic Waveguide Enhanced Raman Spectroscopy* Ghent University, Ghent, 2016.

[14] T H Stievater, S A Holmstrom, D A Kozak, R A Mcgill, M W Pruessner, N Tyndall, W S Rabinovich, and J B Khurgin *Trace-Gas Raman Spectroscopy Using Functionalized Waveguides* Optica, 3(8):891–6, 2016.

[15] Ashim Dhakal, Pieter C. Wuytens, Frédéric Peyskens, Karolien Jans, Nicolas Le Thomas, and Roel Baets *Nanophotonic Waveguide Enhanced Raman Spectroscopy of Biological Submonolayers* ACS Photonics, 3(11):2141–49, 2016.

[16] Shana O. Kelley, Chad A. Mirkin, David R. Walt, Rustem F. Ismagilov, Mehmet Toner, and Edward H. Sargent *Advancing the speed, sensitivity and accuracy of biomolecular detection using multi-length-scale engineering* Nature Nanotechnology, 9(12):969–980, 2014.

[17] Christopher C. Evans, Chengyu Liu, and Jin Suntivich *TiO2 Nanophotonic Sensors for Efficient Integrated Evanescent Raman Spectroscopy* ACS Photonics, 3(9):1662–1669, 2016.

[18] Ashim Dhakal, Pieter Wuytens, Ali Raza, Nicolas Le Thomas, and Roel Baets *Silicon Nitride Background in Nanophotonic Waveguide Enhanced Raman Spectroscopy* Materials, 10(2):140, 2017.

[19] Hendrik Rojegard *Trends in Low-Cost NDIR Gas Sensing*, 2013.

[20] EEC Council *Directive 91/322/EEC* Official Journal of the European Communities, 177(24):22–24, 2001.

[21] Wenbin Zhang, Hao Liu, Chenggong Sun, Trevor C. Drage, and Colin E. Snape *Capturing CO2 from ambient air using a polyethyleneimine-silica adsorbent in fluidized beds* Chemical Engineering Science, 116:306–316, 2014.

[22] Zilong Wang, Michalis N. Zervas, Philip N. Bartlett, and James S. Wilkinson *Surface and waveguide collection of Raman emission in waveguide-enhanced Raman spectroscopy* Optics Letters, 41(17):4146–4149, 2016.

[23] Sebastian Schlücker *Surface-enhanced raman spectroscopy: Concepts and chemical applications* Angewandte Chemie - International Edition, 53(19):4756–4795, 2014.

[24] Alba Espinosa-Soria, Amadeu Griol, and Alejandro Martínez *Experimental measurement of plasmonic nanostructures embedded in silicon waveguide gaps* Optics Express, 24(9):9592–601, 2016.

[25] Felipe Bernal Arango, Andrej Kwadrin, and A Femius Koenderink *Plasmonic Antennas Hybridized with Dielectric Waveguides* ACS Nano, 6(11):10156–10167, 2012.

[26] Frédéric Peyskens, Ashim Dhakal, Pol Van Dorpe, Nicolas Le Thomas, and Roel Baets *Surface Enhanced Raman Spectroscopy Using a Single Mode Nanophotonic-Plasmonic Platform* ACS Photonics, 3(1):102–108, 2016.

[27] Maysamreza Chamanzar, Zhixuan Xia, Siva Yegnanarayanan, and Ali Adibi *Hybrid integrated plasmonic-photonic waveguides for on-chip localized surface plasmon resonance (LSPR) sensing and spectroscopy.* Optics Express, 21(26):32086–98, 2013.

[28] Philip Measor, Leo Seballos, Dongliang Yin, Jin Z. Zhang, Evan J. Lunt, Aaron R. Hawkins, and Holger Schmidt *On-chip surface-enhanced Raman scattering detection using integrated liquid-core waveguides* Applied Physics Letters, 90(21):1–4, 2007.

[29] Lingbo Kong, Changwon Lee, Christopher M. Earhart, Bernardo Cordovez, and James W. Chan *A nanotweezer system for evanescent wave excited surface enhanced Raman spectroscopy (SERS) of single nanoparticles* Optics Express, 23(5):6793, 2015.

[30] Shiyun Lin, Wenqi Zhu, Yuhang Jin, and Kenneth B Crozier *Surface Enhanced Raman Scattering with Ag Nanoparticles Optically Trapped by a Photonic Crystal Cavity.* Nano Lett., 13(2):559–63, 2013.

[31] Traci R Jensen, Michelle Duval Malinsky, Christy L Haynes, and Richard P Van Duyne *Nanosphere Lithography : Tunable Localized Surface Plasmon Resonance Spectra of Silver Nanoparticles* Journal of Physical Chemistry B, 104(May):10549–10556, nov 2000.

[32] Mohammadali Tabatabaei, Alexandre Sangar, Nastaran Kazemi-Sanjani, Philippe Torchio, Alexandre Merlen, and Francois Lagugné-Labarthet *Optical Properties of Silver and Gold Tetrahedral Nanopyramid Arrays Prepared by Nanosphere Lithography* The Journal of Physical Chemistry C, 117:14778–86, 2013.

[33] Martin Moskovits *Persistent misconceptions regarding SERS* Physical Chemistry Chemical Physics, 15(15):5301, 2013.

[34] Frédéric Peyskens, Ananth Z. Subramanian, Pieter Neutens, Ashim Dhakal, Pol Van Dorpe, Nicolas Le Thomas, and Roel Baets *Bright and dark plasmon resonances of nanoplasmonic antennas evanescently coupled with a silicon nitride waveguide* Optics Express, 23(3):3088–101, 2015.

[35] E.C. Le Ru, M Meyer, and P.G. Etchegoin *Surface Enhanced Raman Scattering Enhancement Factors: A Comprehensive Study* Journal of Physical Chemistry C, 111(37):13794–13803, 2007.

[36] L. Baia, M. Baia, J. Popp, and S. Astilean *Gold films deposited over regular arrays of polystyrene nanospheres as highly effective SERS substrates from visible to NIR* Journal of Physical Chemistry B, 110(47):23982–23986, nov 2006.

[37] Pieter C Wuytens, Ananth Z Subramanian, Winnok H De Vos, Andre G Skirtach, and Roel Baets *Gold nanodome-patterned microchips for intracellular surface-enhanced Raman spectroscopy* The Analyst, 140(24):8080–8087, 2015.

5

GOLD NANODOME-PATTERNED MICROCHIPS FOR INTRACELLULAR SERS

While top-down substrates for surface-enhanced Raman spectroscopy (SERS) offer outstanding control and reproducibility of the gold nanopatterns and their related localized surface plasmon resonance, intracellular SERS experiments heavily rely on gold nanoparticles. These nanoparticles often result in varying and uncontrollable enhancement factors. Here we demonstrate how micron-sized chips with a gold nanodome SERS pattern can be used for intracellular sensing. By bringing top-down fabricated SERS substrates to the intracellular world, we set an important step towards time-dependent and quantitative intracellular SERS. In particular, we discuss the following issues:

1. *How to fabricate millions of 'quasi-colloidal' gold-nanodome patterned microchips?*

2. *Are these microchips ingested by cells and what is their influence on cell viability?*

3. *Can we detect the presence of extraneous molecules in the cell through the SERS-signals of these microchips?*

5.1   Introduction

A number of groups have recently demonstrated how nanophotonic technologies can provide solutions for tagging cells [1, 2] or probing intracellular parameters like pressure changes [3] and protein interactions [4]. Here, we fabricate a new type of intracellular nanophotonic microchip for surface-enhanced Raman scattering. As discussed in chapter 2, Raman scattering suffers from the inherently low Raman cross section of most molecules. This especially limiting for live-cell measurements, which require a limited laser power, short integration time and Raman excitation in the near infrared therapeutic window [5] to limit photo-damage, resulting in extremely low signals. Surface-enhanced Raman spectroscopy (SERS) offers a promising solution to this problem. *Conditio sine qua non* for intracellular SERS is a non-invasive introduction of gold nanostructures inside living cells [6, 7]. The first demonstration of intracellular SERS in the early nineties [8] made use of colloidal silver nanoparticles, later to be replaced by the more chemically inert gold nanoparticles [9] (AuNP) or -nanorods [10]. Plasmonic hot spots created in the gaps and crevices of aggregated clusters of these nanoparticles offer a strong Raman enhancement, which is why to date AuNP (and their aggregates) have remained the most important workhorse for intracellular SERS [6, 11]. Amongst others, AuNP-assisted SERS has been used to distinguish and classify various cell types on the basis of their biochemical signatures [12, 13], to study pathways like endocytosis [14] or apoptosis [15], for a real-time and label-free monitoring of extraneous molecules [16, 17] or for probing chemical parameters like pH [11, 18, 19] or redox potentials [20]. Despite their strong enhancement and potentially limited cytotoxicity [21, 22], colloidal nanoparticles often affect reproducibility due to their spatio-temporal dynamics. These result in clustering and a non-uniform distribution of these nanoparticles. This leads to enhancement factors which are unpredictable in space and time, thereby restricting quantitative or time-dependent intracellular SERS experiments. Probes with a predefined metal configuration have been designed to solve this problem, either in the form of nanopipettes pierced through the cell membrane during measurement [7, 23–25] or as micron-sized beads coated with silver [26]- and gold nanoparticles [27, 28] which can be entirely engulfed by cells without compromising cell viability [26, 28]. Although the nanopipettes solve the problem of variable gold nanostructures during measurement and coated microbeads allow to do this without a permanent incision of the cell membrane, these approaches still rely on the self-assembly of colloidal

---

[1]Laboratory of Cell Biology and Histology, Dept. Veterinary Sciences, University of Antwerp

gold nanoparticles. This inhibits control on the position and amount of SERS hot spots on the probes, which inevitably leads to a variability between different probes. In contrast, a wide variety of (extracellular) SERS substrates have been developed using top-down fabrication techniques [29] like electron-beam- [30, 31], deep-UV- [32] or nanosphere- lithography [33–36], where an accurate control of the shape and position of nanostructures have resulted in reproducible and tunable enhancements.

In this chapter, we develop intracellular SERS probes based on the gold nanodome SERS substrate described in chapter 3. First, we fabricate micron-sized chips with a uniform, reproducible gold nanopattern. Next, we show the cellular uptake of these microchips. Normal cell mitosis and cell viability assays give a preliminary indication of the low cytotoxicity of the microchips. Finally, we detect the intracellular SERS spectrum of extraneously added molecules in live cells as a proof-of-concept experiment. To the best of our knowledge, this approach demonstrates for the first time the possibility of using top-down SERS substrate fabrication techniques for intracellular sensing, thereby providing a predefined and reproducible gold nanopattern. Taking out the variability inherent to nanoparticle-based measurement, the use of top-down deposited SERS substrates for intracellular sensing takes a step towards reproducible SERS experiments in cells or tissue. Furthermore, the traceability and potentially low cytotoxicity of micron sized structures can provide an additional advantage in specific applications like a localized detection in tissue or a targeted delivery.

At the time the experiments discussed in this chapter were conducted, the nanodome-fabrication was not yet fully optimized. Therefore the SSEF of the nanodome substrate microchips was approximately ten times lower as compared to that of the nanodomes measured in chapters 3 and 6. The main difference is the use of evaporated Au for nanodome fabrication in this chapter. As discussed in chapter 3.3.3, Au sputtering is preferred over evaporation to achieve a reduced gold roughness and more controllable gap dimension.

5.2 Fabrication and characterisation of the SERS microchips

We adapted the nanosphere-lithography (NSL) based gold nanodome-fabrication process discussed in chapter 3.3 to obtain micron-sized, gold nanodome patterned microdisks freely dispersed in water. Remember that this self-assembly based lithographic technique was chosen because it allows for a relatively cheap, fast and reproducible nanopatterning [33]. Figure 5.1a schematically shows the most important fabrication steps, described in detail in the methods section. The first three steps are identical to the nanodome substrate fabrication described earlier.

We start from a thin film of silicon nitride (SiN) deposited on top of a 4" silicon wafer, spincoat a monolayer of hexagonally-close packed (HCP) polystyrene beads on top and etch a periodic pattern of nanodomes into the SiN substrate using a two-step reactive ion etch: first a more chemical O_2 etch to thin down the beads followed by a more physical CF_4H_2 etch to pattern the SiN. Subsequently 6 µm disks are defined by UV contact lithography. A Ni adhesion layer and 200 nm Au layer is then evaporated on the microdisk patterned nanodome surface. Finally, the chips are released from the underlying silicon surface with a potassium-hydroxide wet etch. The entire chip is centrifuged during etching to ensure an efficient collection of released microchips. Figure 5.1b shows a tilted view of such a nanopatterned microchip. Note that the size and shape of the microchips is fully controllable and only limited by the resolution of the UV-lithography system. Hence, microdisks with a diameter down to 1 µm can easily be fabricated in an identical way. Approximately three million SERS microchips are obtained from a $2, cm^2$ substrate, which provides a sufficient supply for intracellular experiments. A dried cluster containing a few thousand of these chips is shown in figure 5.1d. While ideally all these microchips are identical, in reality the reproducibility of the gold nanodome pattern is limited by the uniformity of the layer of spin-coated polystyrene beads. Next to a hexagonally close-packed (HCP) monolayer, there are also areas with multi-layers and packing defects. We currently achieve a 80-90 % HCP-monolayer coverage (figure 3.27 on page 3-30). To achieve a 100 % reproducibility, the use of self-assembling monolayers has to be avoided and techniques like e-beam-, deep-UV- or nano-imprint lithography should be used for patterning gold nanostructures.

Note that a similar fabrication flow can be used for fabricating microchips with almost any gold nanostructure. For example, figure 5.2 illustrates the fabrication of a nanotriangle-patterned SiN microdisk, also fabricated using nanosphere-lithography. Compared to the nanodomes, these have a lower SSEF (see table 3.2) but offer more accessible hot spots and an optically transparent substrate. Because of these different properties, the choice of a particular gold nanopattern can be application-inspired.

In order to work in the wavelength window that induces minimal photo-damage to biological samples, the geometry of the nanodome substrates was tuned for an optimal enhancement when exciting at a wavelength of 785 nm in water, as described in chapter 3.4.3. The spectral position of the plasmon resonance was characterized through UV-Vis reflection spectroscopy. Figure 5.3(a) shows the reflectance spectra of nanodome substrates characterized both in air (top) and water (bottom). The reflectance spectra redshift with an increasing gap size ($|g|$, figure 5.3(b)) in between the nanodomes. While an increasing gap size should give a blueshift of the resonance because of decoupled modes (see chapter 3.2), it is the decrease in effective height h_0 (in figure 3.18 on 3-21) that redshifts the resonance here, again a consequence of the evaporated rather than sputtered gold. As expected, the reflectance minima experience a strong red-shift (150-200 nm) in water, due to
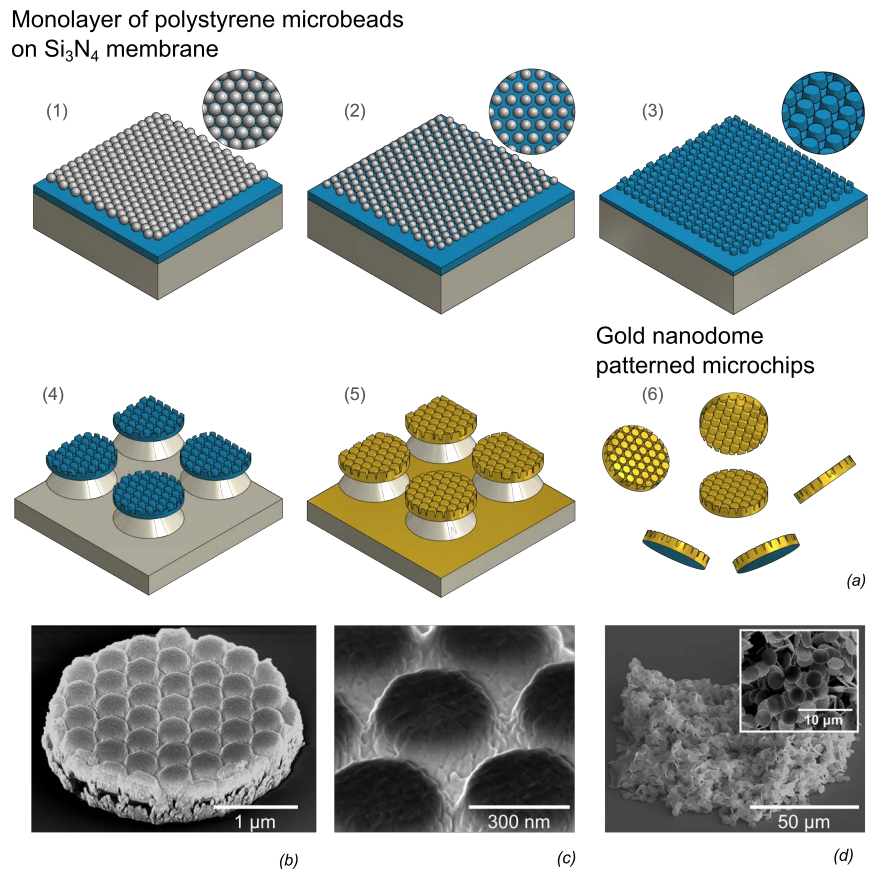
Monolayer of polystyrene microbeads
on Si$_3$N$_4$ membrane

Gold nanodome
patterned microchips

Figure 5.1 (a1) A nanodome pattern is created starting from a spincoated monolayer of 450 nm polystyrene beads on a Si$_3$N$_4$ / Si stack. The polystyrene beads are etched in the underlying SiN layer in a two step RIE-process (a2-a3), followed by removal of the beads, patterning of individual disks (a4) and gold deposition (a5). Finally the microdisks are underetched (a6). (b) Tilted SEM view showing a 3 µm diameter nanodome-patterned microdisk and (c) a close up of the metal surface. (d) Up to three million microchips are obtained from one chip, of which a few thousand can be seen in this cluster.
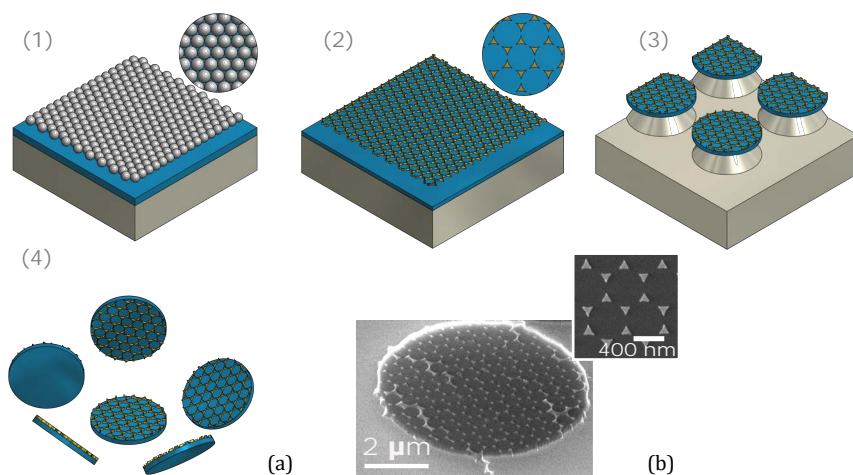
Figure 5.2 (a)Fabrication of nanotriangle coated dielectric microdisks through nanosphere lithography for the fabrication of a nanotriangle pattern (1-2), contact lithography for the definition of individual chips (3) and potassium hydroxide wet etching for release from underlying substrate (4). (b) Tilted SEM image of a nanotriangle-patterned SiN microchip

the higher refractive index of the surrounding medium. These findings correspond well with the characterization by Wu et al. [37] on nano-imprinted nanodomes. The spectral position of the pump and Stokes light, shaded region in 5.3(a), shows a good overlap with the reflectance minimum for the substrates with a 5-15 nm gap size in water. The water-environment (n=1.33) quite accurately represents the plasmonic properties inside cells (n=1.35-1.38 [38]). To compare the SERS enhancement amongst the different gap sizes, the substrates were coated with a para-nitrothiophenol (pNTP) monolayer [36]. Figure 5.3(c) shows the average spectra obtained from the monolayer-coated nanodome substrates with varying gap sizes. As expected, the substrates with a 5-15 nm gap show the strongest enhancement. A smaller gap size results in touching nanodomes while larger gap sizes reduce the coupling of the structures, both effects resulting in a reduced enhancement.

5.3 Cellular uptake of microchips and viability

An efficient uptake by cells is crucial when using microchips for intracellular sensing. Several routes for the intracellular delivery of micron-sized objects have been shown in the field of microcapsule-based drug delivery [39], like micro-injection and electroporation [27, 40]. In contrast to these 'forced' uptake methods, it has also been shown that cells can spontaneously engulf micron-sized objects [41]. We frequently observed the spontaneous uptake of the microchips by Normal Human Dermal Fibroblasts (NHDF) as well as HeLa cells. Seeding cells and microchips in equal concentrations 24 hours prior to Raman measurements typically results in roughly 40 % of cells with incorporated microchips (Table 5.1). The intracellular
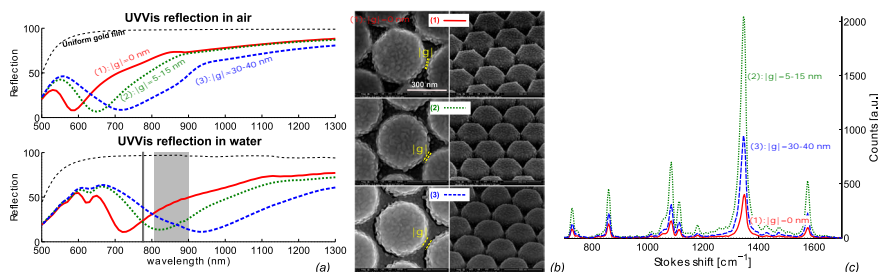
Figure 5.3 The properties of the nanodome substrates are strongly dependent on the nanometer-sized gap ($|g|$) in between nanodomes. (a) The UV-Vis reflection blueshifts with decreasing gap-size. In water (a, bottom), UV-Vis reflection spectra indicate that the plasmon resonance for a 5-15 nm gap size is ideally positioned for exciting Raman spectra at 785 nm, as can be seen from the gray-shaded pump and Stokes wavelengths. (b) SEM images of the corresponding substrates show a variation from touching nanodomes to a 30-40 nm gap in top and tilted views. (c) The 5-15 nm gap substrate also shows the strongest enhancement for a monolayer of 4-nitrothiophenol molecules bound to the gold surface.

localization of the microchips is verified by confocal microscopy (figure 5.4) of NHDF cells labeled with the fluorescently tagged lectin, WGA-AF488, that selectively binds glycans at the extracellular side of the plasma membrane. Orthogonal views (figure 5.4(a)) as well as 3D renderings (figure 5.4(b)), prove that the microchips are indeed within the cytoplasm of the cell.

In order to assess cell viability, the microchips were incubated with a cell culture of HeLa-H2B cells and monitored overnight by confocal time-lapse microscopy. The montage in figure 5.4(c) shows two cells, one with a single microchip and another with multiple microchips incorporated, undergoing mitosis. Note the redistribution of microchips among daughter cells. Cell division was frequently observed, while there were no significant differences in the fraction of divided cells and mitotic time span when comparing cells with and without microchips (Table 5.1) over a population of respectively 51 and 121 cells. This data indicates the low impact of the microchips on cell viability. An important characteristic of our planar microchips is that they consume a smaller portion of the cell-volume when compared to nanoparticle-coated microbeads [26, 27], while maximizing the surface/volume ratio available for SERS-detection. For example, a 5 μm x 200 nm disk consumes roughly 0.15% of the volume of a typical HeLa cell [42], while a 5 μm bead would occupy a volume of 2.5%.

Table 5.1: Mitosis of HeLa-H2B cells, starting 24 h after seeding cells with microchips. No significant difference is found between mitosis of cells with and without microchips

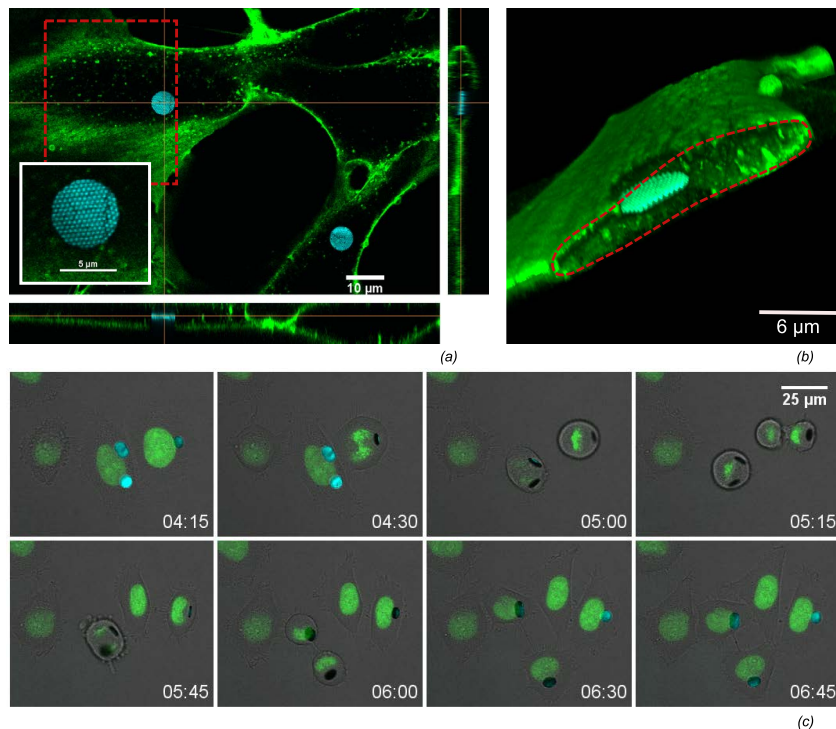|	Cells with chip	Cells without chip
Number of cells	51	121
Fraction of divided cells (8 h)	0.37	0.36
Mitotic time span	64±18 min	61±17 min

(a)

(b)

(c)

Figure 5.4 (a) The intracellular uptake in NHDF cells is confirmed by confocal fluorescence microscopy. A cross section view shows a highly reflective microchip surrounded by the green labeled membrane. The 450 nm-periodic nanodome pattern on the chip can be seen from the high-resolution picture in the inset. (b) A 3D volume rendering (using alpha blending) from the confocal slices makes the intracellular localization more clear. The volume rendering was sliced along the red dashed area in (a). (c) HeLa cells with a fluorescent labeled nucleus were followed in time to visualize mitosis of cells containing microchips (see also table 5.1), where the nucleus is green labeled and the cell boundary is visible on the overlayed transmission image.

To further investigate the influence of the microchips on cell viability, we used a *PrestoBlue*[TM] assay. The PrestoBlue reagent contains resazurin, a blue-colored, non-fluorescent, cell-permeable compound. Mitochondrial activity in the cell reduces resazurin into resorufin, a red fluorescent ($\lambda_{ex} = 560$ nm, $\lambda_{em} = 590$ nm) molecule [43]. Thus the fluorescent intensity allows for quantifying the total mitochondrial activity of a cell population, a measure for its viability or changes in metabolic states. For this purpose, we seeded NHDF cells and microchips at a ratio of 0, 2 and 4 microchips per cell and ran a PrestoBlue assay after 1, 2, 3 and 7 days of incubation. The number of cells in each well of a 96 well plate was chosen sufficiently low such that after incubation the fluorescence intensity is linear with the number of cells (see methods, figure 5.9). Figure 5.5 shows the results of this experiment. We do not observe a significant difference in viability when the chips are incubated with microchips up to a 4/1 ratio after 1-3 days of incubation. There

may be an influence after 7 days, tests with higher concentrations are required to confirm this trend.
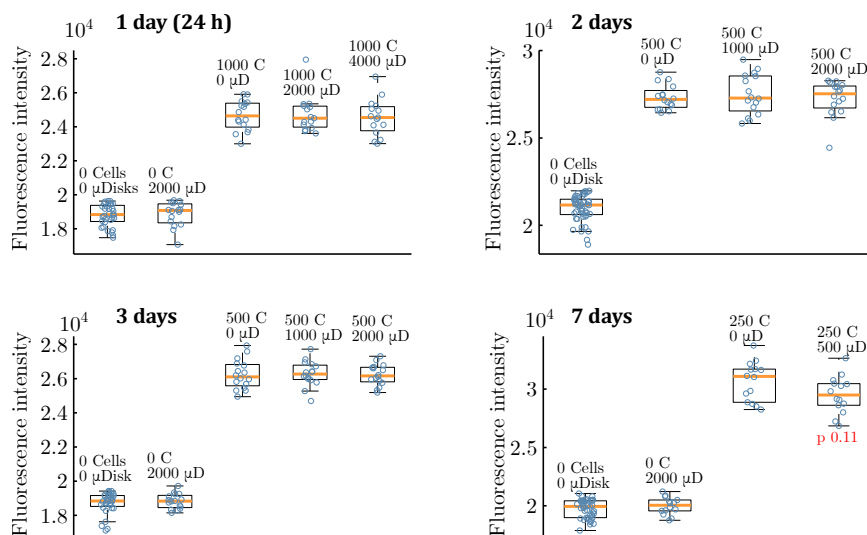

Figure 5.5 Cell viability of NHDF cells incubated with and without nanodome-microchips quantified from the reducing power of the cell population using a *PrestoBlue*^{TM} assay. Significance in the 7-days incubation graph was calculated with a Kruskal-Wallis test. Number of cells and beads refer to those seeded at day 0.

5.4   Intracellular label-free SERS

A promising application of intracellular SERS is the detection of extraneously delivered molecules [16, 17, 44]. As a proof-of-concept experiment, we use the nanodome-patterned microchips for an intracellular detection of the model-molecule rhodamine 6G (R6G). The microchips are added to the cell culture 24 hours prior to the experiment, after which a large fraction of them was internalized by NHDF cells. The microchip-containing cells are imaged on an inverted confocal Raman microscope. Subsequently, a 2 µM solution of R6G was added to the cell culture and detected in the cell. Both the intracellular localization of the microchips as the R6G molecules is confirmed through respectively confocal reflection and confocal fluorescence microscopy (figure 5.6(a)). On this same cell, SERS spectra are acquired from the area highlighted by the red box in 5.6(b). The integrated intensity of the Stokes scattered light shows that, as expected, only Raman signals are observed on top of the microchips (inset of 5.6(b)). On several positions on the microchips the SERS spectrum of R6G is detected, highlighted by integrating the $1365\,\mathrm{cm}^{-1}$ R6G-peak (green dots in inset 5.6(b)). Single spectra from this area are plotted in figure 5.6(c), showing a good correspondence of the R6G SERS spectrum with its reference spectrum. This undoubtedly demonstrates the label-free

intracellular detection of these molecules. Furthermore an exemplary spectrum from a different position is shown, containing peaks from other molecules present on the gold surface. This is probably originating from adsorbed proteins during or after uptake of the microchip.

Although the intracellular detection of R6G may be of limited importance from a biological point of view, this result indicates the potential of the microchips in applications such as a label-free monitoring of intracellular drug delivery [16, 17, 45]. Also, binding reporter molecules to the chips can allow indirect probing of cellular parameters like pH [26] or reactive oxygen [20]. Finally, functionalizing the surface with a peptide substrate may enable stable, single-cell, label-free monitoring of enzymatic activity [46]. The focus of this work is on intracellular sensing, but reproducible and traceable SERS microchips can also be promising for the detection of biomolecules in other environments such as tissues or fluids.
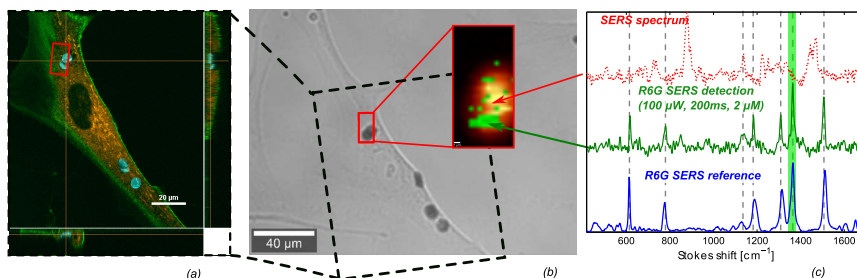

Figure 5.6 Label-free intracellular detection of R6G. (a) Confocal fluorescence scan of a single cell with several nanodome-patterned microchips show the intracellular localization of the microchips, as well as the uptake and inhomogeneous distribution of R6G in the cell. R6G fluorescence is shown in red, 448 nm reflection on the disk surface in cyan and the WGA-448 labeled cell membrane in green. (b) Transmission image of the same cell, where SERS spectra are mapped over the region marked with a red square. The inset shows the integrated number of counts in the 400-1700 cm^{-1} region (graded red-yellow), on top of which the presence of the 1365 cm^{-1} R6G-peak is highlighted in green, which corresponds to the green shaded area in (c). (c) SERS spectra on different positions of the microchip show the intracellular SERS detection of R6G (middle, green) and the R6G reference SERS spectrum (bottom,blue), while other positions show the presence of peaks related to other molecules adsorbed on the microchip (dotted red,top). Spectra are normalized and offset for clarity.

5.5 Localization of the microchips in the cell

Identical nanostructured chips with a predefined enhancement, such as used in these experiments, should in principle enable quantitative SERS experiments. However, there are a number of additional complications related to intracellular sensing with nano- or microparticles. Apart from the uptake itself, the location of the microchip in the cell is of importance for the applicability of the chip for intracellular sensing. Although a few papers report on the free localization of micro-particles

in the cytosol [3, 47, 48], most research on the uptake and localization of micro-particles indicates that these structures are located in phagosomes, or lysosomes in a later stage [41, 49]. As a consequence, a lipid bilayer possibly isolates the particles from the cytosol. This lipid membrane may complicate a sensitive detection of processes and molecules in the cytosol. The presence of such a lipid membrane would not inhibit the detection of R6G, as this molecule easily penetrates through membranes. In order to investigate whether the microchips are freely available in the cytosol or surrounded by a lipid membrane, we checked for co-localization of the microchips with the fluorescent dyes *Lysotracker Red DND-99*, which selectively accumulates in acidic cellular compartments, and *Vybrant DiI*, a lipophilic membrane stain which labels all intracellular lipid vesicles. We did not observe a clear co-localization of the microchips with these dyes under confocal fluorescence microscopy (figures 5.7 and 5.8). These experiments suggests that the microchips are neither in lysosomes nor in other lipid vesicles. However, these results are not conclusive and it is quite unlikely for the microdisks to be able to escape from a surround vesicle after uptake. Further experiments are needed to determine the exact intracellular location of the microchips, most importantly transmission-electron microscopy images of incubated microchips.

An additional problem lies in the adsorption of a protein corona on nano- and microparticles before, during and after their cellular uptake [50]. This protein corona forms an extra barrier for molecules to reach the plasmonic hot spots from the SERS substrates. Further research is needed to identify potential solutions to the aforementioned problems.
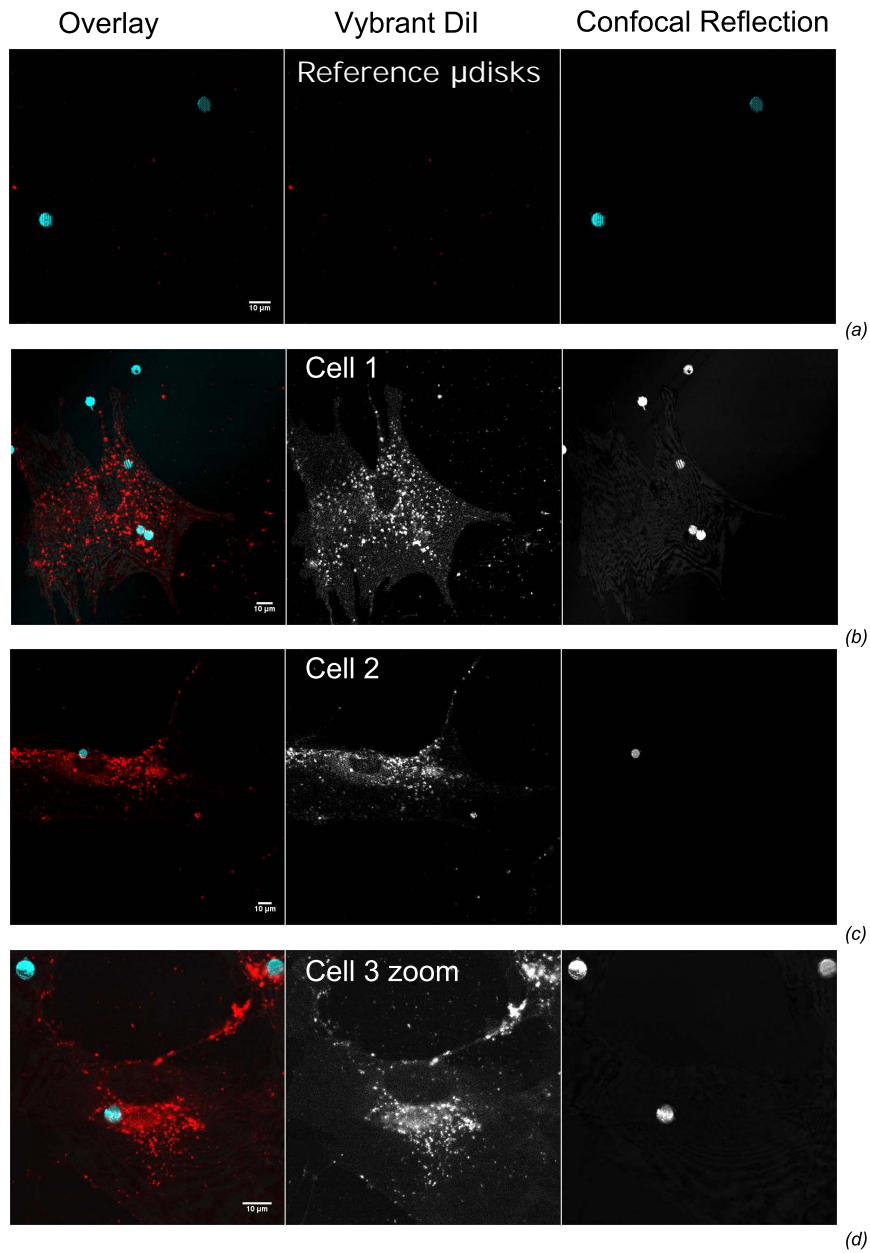
Figure 5.7 Staining NHDF cells containing microchips with the lipophilic dye *Vibrant DiI* does not indicate co-localization of the microchips (cyan) with lipid (red) membranes. (a) Reference measurement with only microchips and Vybrant DiI. (b-c) Cells with microchips and (d) zoomed image of a cell containing a microchip.
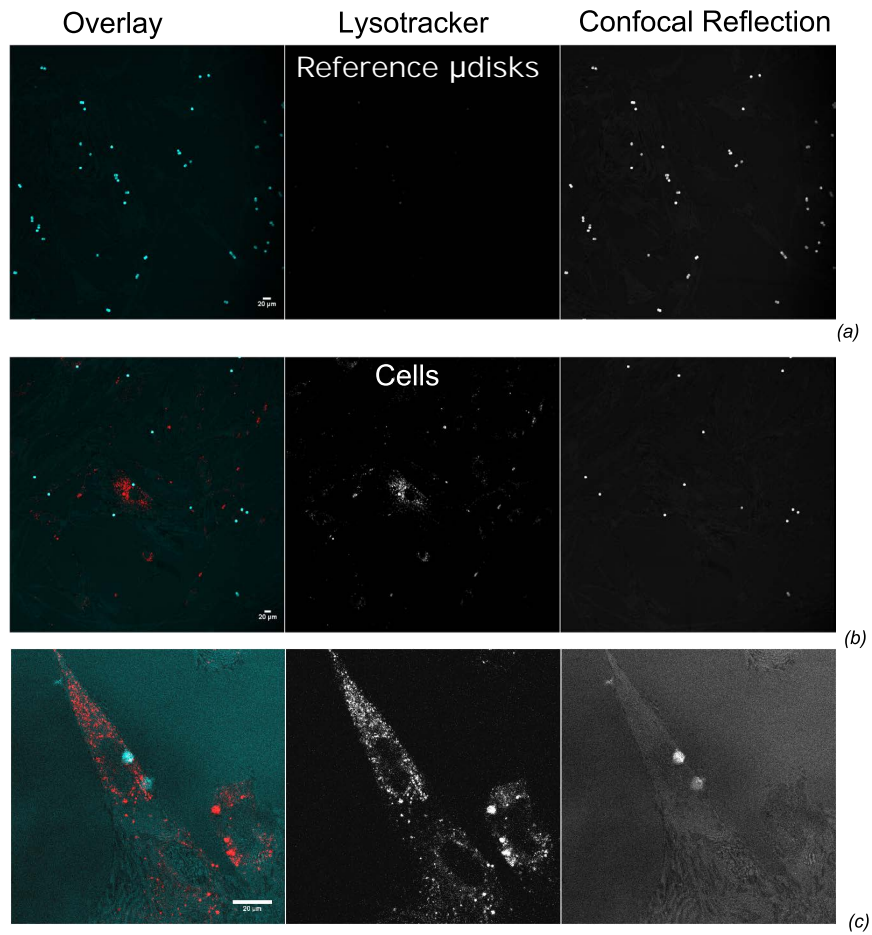
Figure 5.8 Staining acidic compartments of NHDF cells with *Lysotracker Red DND-99* does not indicate co-localization of the microchips (cyan) with lipid acid compartments like lysosomes (red). (a) Reference measurement with only microchips and Lysotracker. (b) Cells with microchips (c) Zoomed image of a cell containing a microchip.

5.6   Conclusions and perspectives

Gold nanopatterned microchips allow to bring the world of uniform, reproducible SERS substrates to intracellular applications. For this purpose, we have developed a fabrication scheme to produce 'quasi-colloidal' microdisks with a gold-nanodome pattern. We demonstrated the intracellular uptake of these microchips and indicated their low cytotoxicity from a cell viability assay and normal mitosis statistics of cells with incorporated microchips. In a proof-of-concept application, extraneously added molecules were detected by their SERS spectrum in the cell. This was verified by confocal fluorescence microscopy. In contrast to existing approaches like colloidal gold nanoparticles, our chips offer a controllable SERS enhancement as they are not subject to aggregation and offer a predefined gold nanopattern. Furthermore the planar shape leads to a reduced volume in the cell as compared to nanoparticle-coated microbeads, while retaining the traceability of a micron-sized structure. Although the experiments presented in this paper do not yet surpass results that have been achieved using colloidal gold nanoparticles, our new approach of using top-down fabricated nanopatterns for intracellular sensing does offer opportunities for a wide variety of SERS substrates to be used for this purpose. These may further improve the enhancement, uniformity and reproducibility of the intracellular microchips. In fact, repeating the experiment with the currently optimized nanodome substrate would readily increase the enhancement factor by an order of magnitude.

However, absorption of molecules on the SERS substrate severely complicates a label-free, quantitative sensing. Also, we have little control over the intracellular location and environment of the SERS microdisk. Upon intracellular uptake, the disk is likely to be encapsulated by a vesicle. In this case, the surrounding bi-lipid membrane inhibits a sensitive sensing of processes in the cytosol.

Materials and Methods

Fabrication of nanodome-patterned microchips   *Here, we describe the fabrication of nanodome-patterned chips exactly as used for the experiments in this chapter. Please check 3.3 for an optimized fabrication scheme for the nanodome SERS substrate.* A layer of 200 nm SiN was deposited on a 4" (100) Si wafer through plasma-enhanced chemical vapor deposition (Advanced Vacuum Vision 310-PECVD), out of which 2 cm x 2 cm pieces were cleaved for further processing. Next, a 5 w/v% colloidal solution of mono-disperse 448 nm ($\pm$3%) polystyrene beads in water (Microparticles GmbH) was densified to 15 w/v% by centrifugation for 15 minutes at 4300 g. This solution was re-suspended in a Triton-X (Sigma):Methanol (Sigma) solution (1:400). The final ratio of H_2O to Triton-X:Methanol was 1/2, again resulting in a 5 w/v% solution. Possible clusters formed upon centrifugation were broken by sonication in an ultrasonic bath for 20 minutes. Prior to spin-coating, the SiN/Si substrates were rendered hydrophilic in an O_2 plasma for 30 minutes (PVA-TEPLA GIGAbatch 310 M, 6000 sccm O_2, 600 W, 750 mTorr)). Next, a monolayer of polystyrene beads was formed by spin coating 50 µl of the polystyrene-beads solution

on a 4 cm^2 chip at approximately 1400 rpm for 40 seconds with an acceleration of 648 rpm/s. In a second spin coating step, excess polystyrene beads at the edges were spun off at 4000 rpm for 40 seconds. After visual inspection of the monolayer coverage, spin speed and acceleration were slightly adjusted to improve the monolayer quality of subsequent chips [51, 52]. Five different samples with polystyrene beads were thinned down in an O$_2$ plasma for respectively 30, 35, 40, 45 and 50 seconds (Advanced Vacuum Vision 320-RIE, 50 sccm O$_2$, 75 W, 100 mTorr), where the exact time defined the final gap size in between the nanodomes . Next, the pattern was transferred into the SiN layer by a highly anisotropic reactive-ion etch (80 sccm CF$_4$ / 3 sccm H$_2$, 210 W, 20 mT, 160 s). Specific details on the anisotropic etching of SiN can be found in [53]. Afterwards, partially-etched beads were washed off in an ultrasonic bath with ethanol, although dichloromethane (carcinogenic, Sigma) was sometimes required for a complete removal of the PS beads. Subsequently, 6 μm disks were patterned through contact-lithography (resist: AZ400-K, positive, Microchemicals) and etched into the SiN layer by the same anisotropic CF$_4$ H$_2$ etch for 350 s followed by an isotropic under-etch of the Si substrate (80 sccm SF$_6$ / 3 sccm H$_2$, 210 W, 20 mTorr, 160 s). Next, the chips were cleaned in acetone and isopropanol, followed by a O$_2$ plasma for 30 minutes (PVA-TEPLA GIGAbatch 310 M, 6000 sccm O$_2$, 600 W, 750 mTorr)) in order to remove photo-resist and other organic contaminants. This under-etch is required to enable the lift-off of the microchips after the subsequent evaporation of a 2-5 nm Ni + 200 nm Au layer. The patterned chips were further cleaved into 1 cm x 2 cm pieces and inserted into a 2 ml centrifugation tube (Eppendorf) to which a 30 w/v% potassium-hydroxide (*KOH*, VWR)/water solution was added at 70 °C to under-etch the Si substrate. After 300 seconds of etching, the tube was cooled for two minutes in a cold water bath at 5 °C. Finally the released microchips were sedimented in the tube by centrifugation for 6 minutes at 2300 g. The remaining KOH-etchant was washed out with water in at least five centrifugation steps. The colloidal microchip solution was stored at 4 °C.

UV-Vis characterization   UV/Vis spectra were acquired on a PerkinElmer Lambda 950 UV/Vis spectrometer. The nanodome substrates, which are not transparent, were characterized in specular reflection under an 8° angle with a 4 mm x 4 mm spot size and a 10 nm resolution in the 600-1200 nm wavelength range. A 150 nm uniform gold film on a 200 nm SiN/Si substrate was used as reference. Reflection spectra in water were acquired by squeezing a drop of water in between the substrate and a 170 μm microscope slide.

Cell Culture and Reagents   Normal Human Dermal Fibroblast (NHDF, PromoCell), HeLa cells (ATCC) and HeLa-H2B cells (a kind gift from Prof. Manders, UvA, The Netherlands) were cultured in Advanced Dulbecco's Modified Eagle's Medium (GIBCO-Life Technologies 12491-015) supplemented with 2% fetal bovine serum (GIBCO-Life Technologies 10500-056) and 1 % penicillin-streptomycin-L-glutamine (GIBCO-Life Technologies 10378-016), and grown in culture flasks in an incubator at 37 °C and 5% CO_2. HeLa-H2B is a transgenic HeLa derivative, stably expressing the DNA binding histone protein H2B fused with a green fluorescent protein (GFP). One day before Raman or fluorescence imaging, cells were seeded on a 35 mm gridded glass-bottom dish (MatTek). Prior to imaging, cells were washed three times with Hanks Balanced Salt Solution (HBSS, GIBCO-Life Technologies 14025-050) and imaged in HBSS supplemented with 25 mM HEPES. For the 12 h monitoring of cell division, pure HBSS was added.
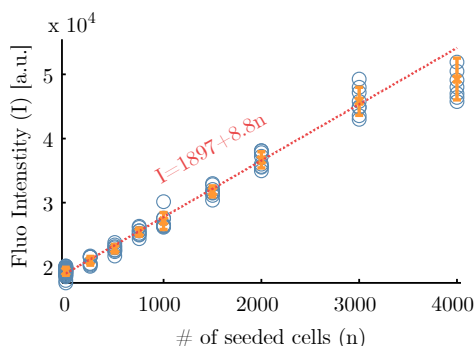
Figure 5.9 The fluorescent intensity of a *PrestoBlue*^{TM} assay in a 96-well plate increases linearly with the number of seeded cells for up to 3000 NHDF cells per well, measured 24 hours after seeding the specified number of cells.

Cell Viability Assay   NHDF Cells were seeded with microchips in 96-well plates (Greiner Bio-One 96-Well µClear, 655 095) and cultured as described above. Cells were grown in 200 µl buffer per well, with at least 16 repetitions per condition. Seeding locations of equal conditions were distributed over the plate as to avoid biased measurements. Prior to seeding, the concentration of cells and microchips was quantified using a counting chamber (Bürker-Türk). The medium was replaced by a 100 µl of a 1/10 PrestoBlue (Invitrogen A1362) / medium solution and incubated for 90 minutes. Next, the fluorescence was read using a TeCan Infinite Pro platereader in a top-read fluorescent mode using an excitation wavelength of 560 ± 5 nm and detection wavelength of 590 ± 10 nm. As a negative control, 2000 mirochips were added to 16 wells containing only this mixture. No contribution of these microchips to the fluorescent signal was observed.

Prior to testing cell viability, the linear range of the assay was determined from seeding increasing an number of cells per well. Figure 5.9 shows that there should be no more than 3000 cells per well. In the cell viability assay, the number of seeded cells was adapted to be within this range at the end of the incubation period, with an estimated 48 hours population doubling time.

Confocal fluorescence microscopy   Image acquisition was done using a Nikon A1r confocal microscope (Nikon Instruments, Apris, France), mounted on a Nikon Ti body and equipped with a 60x Plan Apo oil immersion objective (Numerical Aperture 1.4). For visualizing the nanodome microchips we took advantage of their strongly reflective gold layer, ideal for reflectance detection. The intracellular localization of the microchips was verified by labeling the cell membrane with a 10 µg/ml solution of Wheat Germ Agglutinin, Alexa Fluor 488 Conjugate (WGA-AF488, Life Technologies) dissolved in PBS. A single 488 nm Ar laser line was used to simultaneously acquire confocal fluorescence, transmission and reflectance signals. Using an 80/20 beam splitter, microchip reflectance was captured through a 488/20 nm band pass filter and WGA-AF488 fluorescence was detected through a 525/50 nm band pass filter. For live cell imaging, the microscope incubator was equilibrated at 36.5 °C, while a dedicated stage holder was used for maintaining 5% CO_2. and 90% relative humidity. To minimize photo-damage during time-lapse acquisitions, laser power was kept low ($\leq 2\%$) and temporal sampling was reduced to a minimum (15 min intervals). Image representation and annotation was performed using Nikon NIS Elements

software and Fiji open source freeware (http://fiji.sc).

Co-localization of the microchips with lipid vesicles was investigated using two different fluorescent dyes, Vybrant DiI (Molecular Probes) and Lysotracker Red DND-99 (Life Technologies). In this experiment, NHDF cells were incubated with microchips in a 96-well plate Greiner Bio-One 96-Well µClear, 655 095) for 24 hours and subsequently washed and stained according to the protocol from the supplier. Images were acquired with a Nikon CFI Plan Apo VC 20x objective (NA 0.75), except for figures 5.7(d) and 5.8(c), where a Nikon CFI Plan Apo VC 60xWI (NA 1.2) objective was used.

SERS experiments   Raman experiments were conducted on a WITec Alpha300R+ confocal Raman microscope equipped with a 785 nm excitation diode laser (Toptica) and an UHTS 300 spectrometer with a -60 °C cooled CCD camera (ANDOR iDus 401 BR-DD). To compare the enhancement across different substrates, they were immersed overnight in a 1 mM solution of para-nitrothiophenol (pNTP, Sigma), thoroughly rinsed with ethanol and dried with a nitrogen air gun. The substrates were immersed in a plastic dish with Mili-Q water. SERS spectra were collected with an upright low NA objective (Nikon PlanFluor 10x/0.3), resulting in a beam diameter of approximately 4 µm (characterized by scanning laterally over a Si edge). Spectra were acquired with a laser power of approximately 1 mW on sample and a 0.12 s integration time. 400 different spectra were collected in a 20 µm x 20 µm square, the average spectra and the 2σ interval is shown in figure 5.3(e). We did not observe significant changes in the pNTP spectra resulting form the laser illumination at this power. The enhancement of the different substrates was compared by integrating the intensity of the cm^{-1} peak from 1313 cm^{-1} to 1373 cm^{-1} after subtraction of the background. The relative standard deviation of the signal along the substrate was calculated by acquiring a total of 1600 spectra over an area of 1600 μm^2 and dividing the standard deviation of the integrated peak intensity by the mean integrated peak intensity.

For live cell SERS experiments, the microscope was used in inverted mode. Cells were cultured on a gridded glass-bottom dish (MatTek), which allowed correlation of Raman and fluorescence signals of the same cell on different microscopes. Cells were kept at 36.5 °C during experiments. Raman spectra were collected with a Nikon PlanFluor 20x/0.5 objective at a laser power of approximately 100 µW on sample with a 0.1 s integration time. Cells were imaged in HBSS, which was replaced by a 2 µM Rhodamine 6G (Sigma) solution in HBSS for intracellular R6G detection. The reference R6G spectrum was recorded on a nanodome SERS surface with a 10 µM R6G concentration in water and 2 s integration time over 25 averages and a laser power of approximately 1 mW. Spectra were processed using *Project FOUR* (WITec GmbH) to remove cosmic rays and the MATLAB package *COBRA* [54] to subtract the SERS background with a polynomial and wavelet-based fit.

References

[1] S. Durán, S. Novo, M. Duch, R. Gómez-Martínez, M. Fernández-Regúlez, A. San Paulo, C. Nogués, J. Esteve, E. Ibañez, and J. A. Plaza *Silicon-nanowire based attachment of silicon chips for mouse embryo labelling.* Lab on a Chip, 15(6):1508–14, 2015.

[2] Marcel Schubert, Anja Steude, Philipp Liehm, Nils M Kronenberg, Markus Karl, Elaine C. Campbell, Simon J. Powis, and Malte Gather *Lasing within live cells containing intracellular optical micro-resonators for barcode-type cell tagging and tracking* Nano Letters, 2015.

[3] Rodrigo Gómez-Martínez, Alberto M. Hernández-Pinto, Marta Duch, Patricia Vázquez, Kirill Zinoviev, Enrique J. de la Rosa, Jaume Esteve, Teresa Suárez, and José A. Plaza *Silicon chips*

detect intracellular pressure changes in living cells Nature Nanotechnology, 8:517–521, jun 2013.

[4] Gary Shambat, Sri-Rajasekhar Kothapalli, J Provine, Tomas Sarmiento, James Harris, Sanjiv Sam Gambhir, and Jelena Vučković *Single-Cell Photonic Nanocavity Probes.* Nano letters, 13(11):4999–5005, feb 2013.

[5] Ralph Weissleder *A clearer vision for in vivo imaging.* Nature biotechnology, 19(4):316–317, 2001.

[6] Katherine A Willets *Surface-enhanced Raman scattering (SERS) for probing internal cellular structure and dynamics.* Analytical and bioanalytical chemistry, 394(1):85–94, may 2009.

[7] Elina a. Vitol, Zulfiya Orynbayeva, Gary Friedman, and Yury Gogotsi *Nanoprobes for intracellular and single cell surface-enhanced Raman spectroscopy (SERS)* Journal of Raman Spectroscopy, 43(7):817–27, jul 2012.

[8] I.R. Nabiev, H. Morjani, and M. Manfait *Selective analysis of antitumor drug interaction with living cancer cells as probed by surface-enhanced Raman spectroscopy* European Biophysics Journal, 19:311–16, 1991.

[9] Katrin Kneipp, Abigail S. Haka, Harald Kneipp, Kamran Badizadegan, Noriko Yoshizawa, Charles Boone, Karen E. Shafer-Peltier, Jason T. Motz, Ramachandra R Dasari, and Michael S Feld *Surface-Enhanced Raman Spectroscopy in Single Living Cells Using Gold Nanoparticles* Applied Spectroscopy, 56(2):150–54, 2002.

[10] Sudipto Pal, Laura E Depero, and Ivano Alessandri *Using aggregates of gold nanorods in SER(R)S experiments: an empirical evaluation of some critical aspects.* Nanotechnology, 21(42):425701, 2010.

[11] Janina Kneipp, Harald Kneipp, Burghardt Wittig, and Katrin Kneipp *Novel optical nanosensors for probing and imaging live cells* Nanomedicine, 6(2):214–226, 2010.

[12] Anna Huefner, WL Kuan, RA Barker, and Sumeet Mahajan *Intracellular SERS nanoprobes for distinction of different neuronal cell types* Nano letters, 13:2463–70, 2013.

[13] S. Cinta Pinzaru, Andronie. L.M., I. Domsa, O. Cozar, and Simion Astilean *Bridging biomolecules with nanoparticles: surface-enhanced Raman scattering from colon carcinoma and normal tissue* Journal of Raman Spectroscopy, 39(February):331–32, 2008.

[14] Anna Huefner, Dedy Septiadi, Bodo D Wilts, Imran I Patel, Wei-Li Kuan, Alexandra Fragniere, Roger A. Barker, and Sumeet Mahajan *Gold nanoparticles explore cells: cellular uptake and their use as intracellular probes.* Methods, 68(2):354–63, jul 2014.

[15] Lauren A Austin, Bin Kang, and Mostafa A El-Sayed *A new nanotechnology technique for determining drug efficacy using targeted plasmonically enhanced single cell imaging spectroscopy.* Journal of the American Chemical Society, 135(12):4688–91, mar 2013.

[16] Kwang-Su Ock, Erdene Ochir Ganbold, Jin Park, Keunchang Cho, Sang-Woo Joo, and So Yeong Lee *Label-free Raman spectroscopy for accessing intracellular anticancer drug release on gold nanoparticles.* The Analyst, 137(12):2852–9, jun 2012.

[17] Jie Huang, Cheng Zong, He Shen, Yuhua Cao, Bin Ren, and Zhijun Zhang *Tracking the intracellular drug release from graphene oxide using surface-enhanced Raman spectroscopy.* Nanoscale, 5(21):10591–8, nov 2013.

[18] Stefan Bálint, Satish Rao, Mónica Marro Sánchez, Pavol Miskovský, and Dmitri Petrov *Monitoring of local pH in photodynamic therapy-treated live cancer cells using surface-enhanced Raman scattering probes* Journal of Raman Spectroscopy, 2011(January):1215–21, 2011.

[19] Sandra W. Bishnoi, Christopher J. Rozell, Carly S. Levin, Muhammed K. Gheith, Bruce R. Johnson, Don H. Johnson, and Naomi J. Halas *All-optical nanoscale pH meter* Nano Letters, 6:1687–1692, 2006.

[20] Craig A R Auchinvole, Patricia Richardson, Catherine McGuinnes, Venkatesh Mallikarjun, Ken Donaldson, Hamish McNab, and Colin J Campbell *Monitoring intracellular redox potential changes using SERS nanosensors.* ACS nano, 6(1):888–96, jan 2012.

[21] Stefaan J Soenen, Bella Manshian, Toke Thiron, Maria Cornelissen, Frank Vanhaecke, Shareen Doak, Wolfgang J Parak, Stefaan De Smedt, and Kevin Braeckmans *Cytotoxic Effects of Gold Nanoparticles : A Multiparametric Study* ACS Nano, 6(7):5767–83, jun 2012.

[22] Yu Pan, Sabine Neuss, Annika Leifert, Monika Fischler, Fei Wen, Ulrich Simon, Günter Schmid, Wolfgang Brandau, and Willi Jahnen-Dechent *Size-dependent cytotoxicity of gold nanoparticles* Small, 3(11):1941–1949, 2007.

[23] Jonathan P. Scaffidi, Molly K. Gregas, Victoria Seewaldt, and Tuan Vo-Dinh *SERS-based plasmonic nanobiosensing in single living cells* Analytical and Bioanalytical Chemistry, 393:1135–41, 2009.

[24] Jun Jie Niu, Michael G Schrlau, Gary Friedman, and Yury Gogotsi *Carbon nanotube-tipped endoscope for in situ intracellular surface-enhanced raman spectroscopy* Small, 7:540–545, 2011.

[25] Gang Lu, Herlinde De Keersmaecker, Liang Su, Bart Kenens, Susana Rocha, Eduard Fron, Chang Chen, Pol Van Dorpe, Hideaki Mizuno, Johan Hofkens, James a. Hutchison, and Hiroshi Uji-i *Live-Cell SERS Endoscopy Using Plasmonic Nanowire Waveguides* Advanced Materials, pages 5124–5128, may 2014.

[26] Stefan Bálint, Satish Rao, Mónica Marro Sánchez, Veronika Huntosová, Pavol Miskovský, and Dmitri Petrov *Diffusion and cellular uptake of drugs in live cells studied with surface-enhanced Raman scattering probes.* Journal of Biomedical Optics, 15(2):027005(1–7), 2010.

[27] Alexey Yashchenok, Admir Masic, Dmitry Gorin, Bong Sup Shim, Nicholas A Kotov, Peter Fratzl, Helmuth Möhwald, and Andre Skirtach *Nanoengineered colloidal probes for Raman-based detection of biomolecules inside living cells.* Small, 9(3):351–6, feb 2013.

[28] P. C. Wuytens, Al. M. Yashchenok, A. Z. Subramanian, A. G. Skirtach, and R Baets *Gold Nanoparticle Coated Silicon Nitride chips for Intracellular Surface-Enhanced Raman Spectroscopy* In CLEO, volume STh4H.7, 2014.

[29] Juan J. Giner-Casares and Luis M. Liz-Marzán *Plasmonic nanoparticles in 2D for biological applications: Toward active multipurpose platforms* Nano Today, 9(3):365–377, 2014.

[30] Uwe Huebner, Karina Weber, Dana Cialla, Robert Haehle, Henrik Schneidewind, Matthias Zeisberger, Roland Mattheis, Hans-Georg Meyer, and Juergen Popp *Microfabricated polymer-substrates for SERS* Microelectronic Engineering, 98:444–47, oct 2012.

[31] Frédéric Peyskens, Ananth Z. Subramanian, Pieter Neutens, Ashim Dhakal, Pol Van Dorpe, Nicolas Le Thomas, and Roel Baets *Bright and dark plasmon resonances of nanoplasmonic antennas evanescently coupled with a silicon nitride waveguide* Optics Express, 23(3):3088–101, 2015.

[32] Jiaqi Li, Chang Chen, Hilde Jans, Xiumei Xu, Niels Verellen, Ingrid Vos, Yasuaki Okumura, Victor V. Moshchalkov, Liesbet Lagae, and Pol Van Dorpe *300 mm Wafer-Level , Ultra-Dense Arrays of Au- Capped Nanopillars with sub-10 nm Gaps as Reliable SERS Substrates* Nanoscale, 6:12391–96, 2014.

[33] John C. Hulteen and Richard P. Van Duyne *Nanosphere lithography: A materials general fabrication process for periodic particle array surfaces* Journal of Vacuum Science & Technology A: Vacuum, Surfaces, and Films, 13(3):1553–8, may 1995.

[34] Douglas A Stuart, Chanda Ranjit Yonzon, Xiaoyu Zhang, Olga Lyandres, Nilam C Shah, Matthew R Glucksberg, Joseph T Walsh, and Richard P Van Duyne *Glucose sensing using near-infrared surface-enhanced Raman spectroscopy: gold surfaces, 10-day stability, and improved accuracy.* Analytical Chemistry, 77(13):4013–9, jul 2005.

[35] Cosmin Farcau and Simion Astilean *Mapping the SERS Efficiency and Hot-Spots Localization on Gold Film over Nanospheres Substrates* The Journal of Physical Chemistry C, 114(27):11717–22, jul 2010.

[36] Mohammadali Tabatabaei, Alexandre Sangar, Nastaran Kazemi-Sanjani, Philippe Torchio, Alexandre Merlen, and Francois Lagugné-Labarthet *Optical Properties of Silver and Gold Tetrahedral Nanopyramid Arrays Prepared by Nanosphere Lithography* The Journal of Physical Chemistry C, 117:14778–86, 2013.

[37] Hsin-Yu Wu, Charles J Choi, and Brian T Cunningham *Plasmonic nanogap-enhanced Raman scattering using a resonant nanodome array.* Small, 8(18):2878–85, sep 2012.

[38] J Beuthan, O Minet, J Helfmann, M Herrig, and G Müller *The spatial variation of the refractive index in biological cells.* Physics in medicine and biology, 41(3):369–382, 1996.

[39] Pieter Wuytens, Bogdan Parakhonskiy, Alexey Yashchenok, Mathias Winterhalter, and Andre Skirtach *Pharmacological aspects of release from microcapsules from polymeric multilayers to lipid membranes* Current Opinion in Pharmacology, 18:129–40, 2014.

[40] Raghavendra Palankar, André G Skirtach, Oliver Kreft, Matthieu Bédard, Malgorzata Garstka, Keith Gould, Helmuth Möhwald, Gleb B Sukhorukov, Matthias Winterhalter, and Sebastian Springer *Controlled intracellular release of peptides from microcapsules enhances antigen presentation on MHC class I molecules.* Small, 5(19):2168–76, oct 2009.

[41] Alumdena Muñoz Javier, Oliver Kreft, Maximilian Semmling, Susanne Kempter, Andre G. Skirtach, Oliver T. Bruns, Pablo del Pino, Mathieu F. Bedard, Joachim Rädler, Josef Käs, Christian Plank, Gleb B. Sukhorukov, and Wolfgang J. Parak *Uptake of Colloidal Polyelectrolyte-Coated Particles and Polyelectrolyte Multilayer Capsules by Living Cells* Advanced Materials, 20(22):4281–7, nov 2008.

[42] L. Zhao, C.D. Kroenke, J. Song, D. Piwnica-Worms, J.J.H. Ackerman, and J. J. Neil *Intracellular water-specific MR of microbead-adherent cells: The HeLa cell intracellular water exchange lifetime.* NMR in Biomedicine, 21:159–164, 2008.

[43] Invitrogen *PrestoBlue Cell Viability Reagent Documentation* Technical Report 1, Invitrogen, 2010.

[44] Elina A Vitol, Zulfiya Orynbayeva, Michael J Bouchard, Jane Azizkhan-clifford, Gary Friedman, and Yury Gogotsi *In Situ Intracellular Spectroscopy with Surface Enhanced Raman Spectroscopy (SERS)-Enabled Nanopipettes* ACS nano, 3(11):3529–36, 2009.

[45] Jing Yang, Yiping Cui, Shenfei Zong, Ruohu Zhang, Chunyuan Song, and Zhuyuan Wang *Tracking multiplex drugs and their dynamics in living cells using the label-free surface-enhanced Raman scattering technique.* Molecular pharmaceutics, 9(4):842–9, apr 2012.

[46] Gang L Liu, Yazmin T Rosa-Bauza, Cleo M Salisbury, Charles Craik, Jonathan a Ellman, Fanqing Frank Chen, and Luke P Lee *Peptide-nanoparticle hybrid SERS probes for optical detection of protease activity.* Journal of nanoscience and nanotechnology, 7(7):2323–2330, 2007.

[47] Uta Reibetanz, Claudia Claus, Elke Typlt, Jörg Hofmann, and Edwin Donath *Defoliation and plasmid delivery with layer-by-layer coated colloids* Macromolecular Bioscience, 6:153–160, 2006.

[48] Deborah Studer, Raghavendra Palankar, Matthieu Bédard, Mathias Winterhalter, and Sebastian Springer *Retrieval of a metabolite from cells with polyelectrolyte microcapsules* Small, 6(21):2412–19, 2010.

[49] Stefaan De Koker, Richard Hoogenboom, and Bruno G. De Geest *Polymeric multilayer capsules for drug delivery* Chemical Society Reviews, 41(7):2867, 2012.

[50] Marco P Monopoli, Christoffer Aberg, Anna Salvati, and Kenneth a Dawson *Biomolecular coronas provide the biological identity of nanosized materials.* Nature nanotechnology, 7(12):779–86, dec 2012.

[51] Jian Chen, Peitao Dong, Di Di, Chaoguang Wang, Haoxu Wang, Junfeng Wang, and Xuezhong Wu *Controllable fabrication of 2D colloidal-crystal films with polystyrene nanospheres of various diameters by spin-coating* Applied Surface Science, 270:6–15, apr 2013.

[52] Pierre Colson, Rudi Cloots, and Catherine Henrist *Experimental design applied to spin coating of 2D colloidal crystal masks: a relevant method?* Langmuir, 27(21):12800–6, nov 2011.

[53] Weiqiang Xie, Yunpeng Zhu, Tangi Aubert, Steven Verstuyft, Zeger Hens, and Dries Van Thourhout *Low-loss silicon nitride waveguide hybridly integrated with colloidal quantum dots* Optics Express, 23(9):12152, 2015.

[54] C M Galloway, E C Le Ru, and P G Etchegoin *An iterative algorithm for background removal in spectroscopy by wavelet transforms.* Applied spectroscopy, 63(12):1370–6, dec 2009.

6

SERS-BASED MONITORING OF PROTEASE ACTIVITY

Proteases, enzymes catalyzing the hydrolysis of peptide bonds, play a crucial role in the modification of proteins as well as their breakdown into constituent amino acids. Proteases are also of vital importance in numerous signaling pathways [1]. A sensitive and quantitative analysis of protease activity is of critical importance for, amongst others, medical diagnostics [2], drug development [1–3] and single cell analysis [4, 5]. As over 500 different genes encoding for proteases have been identified in the human genome, there is large interest in a detection technology that allows for a selective, sensitive and multiplexed measurement of protease activity. Surface-enhanced Raman scattering provides a promising candidate: peptides and plasmonic hotspots have a similar size while Raman fingerprints hold large potential for spectral multiplexing. In this chapter we investigate the use of the nanodome platform for monitoring protease activity through peptide hydrolysis. In particular, we provide a (partial) answer to the following questions:

1. *Are peptide monolayers detectable on the nanodome SERS platform?*

2. *Can we monitor protease activity through the spectrum of these peptides?*

3. *Is this technology suited for a single-cell analysis of inflammasome activation?*

4. *Can SiN waveguides with plasmonic antennas be used for an on-chip detection of protease-activity?*

6.1 Introduction

6.1.1 Established methods for monitoring protease activity

Proteases act by cleaving peptide bonds through hydrolysis. In many cases, the easiest way for quantifying protease activity is through the detection of cleaved peptides that are specific substrates[4] for that protease. An alternative approach is to directly detect the activated protease itself. We will briefly discuss the principle, advantages and drawbacks of the most common methods for monitoring protease activity. For a more elaborate overview, we refer the reader to specialized literature on this matter [6–8].

Protease activity detected through substrate cleavage

Colorimetric Assays   Many different technologies exist for detecting substrate cleavage, most of them are variations on the same principle. A synthetic peptide is fabricated containing two parts: a recognition sequence that makes the peptide a substrate for a specific enzyme (e.g. -YVAD for caspase-1 and -R for trypsin) and a reporter molecule that will be detectable after cleavage. In many commercial assays, this readout is based on colorimetric changes. Here, the reporter molecule is a chromophore that absorbs a specific wavelength when cleaved-off (figure 6.1). Para-nitroaniline (pNA) is often used, because it can easily be conjugated to the carboxyl-terminal of a peptide. When released, free pNA will absorb light around 405 nm. These kind of colorimetric assays are often used because they have an easy experimental procedure and can be done using standard equipment. However, the sensitivity of the assay is limited. In our experiments using a *Tecan Infinite 200 PRO* platereader, we measured a detection limit of approximately $1\,\mu$M in a volume of $100\,\mu$l, corresponding to a total amount of 100 pmol pNA. In this work, we used pNA-based colorimetric assays for measuring trypsin activity and the functioning of inhibitors on some of the substrates described in table 6.1.

---

[1]Department of Internal Medicine (UGent) and Inflammation Research Center (VIB)

[2]Department of Biochemistry (UGent) and Center for Medical Biotechnology (VIB)

[3]Antelope Diagnostics and Center for Nano- and BioPhotonics

[4]The term substrate is confusing in the context of SERS for protease sensing. During protease activity, a substrate is the material upon which the protease acts. Here, this is the peptide chain that is converted from substrate into products upon digestion by the protease. In the field of SERS, a substrate refers to the nanostructured surface that provides a localized surface-plasmon resonance responsible for the Raman enhancement. In this paper, the word substrate is used for the peptide chain. We refer to the nanostructured surface as a SERS platform.

Fluorescent Assays Using fluorophores instead of chromophores significantly increases the sensitivity of the assay. 7-Amino-4-methyl coumarin (AMC) or 7-amino-4-trifluoromethyl coumarin (AFC) are frequently used. These can be bound to the carboxyl side chain of aspartic acid and will only become fluorescent when cleaved off as a free molecule (figure 6.1b). Using the same platereader as before, the detection limit for the fluorescent -AMC molecule was below $10\,\text{nM}$. We use -AMC functionalized peptides both as SERS- and fluorescent probes for measuring caspase-1 activity, as described in section 6.4.2 and figure 6.17. The use of this fluorophore is limited to proteases cleaving C-terminal of aspartic acid in the *asp-AMC* complex. Furthermore, the presence of non-natural molecules like AMC or pNA in P_1' positions can result in sub-optimal cleavage sites for many proteases.

Long range resonance energy transfer mechanisms provide a solution: they allow to introduce a number of amino acids in between the two actors involved in the energy transfer. Figure 6.1(c) depicts such as a process in which 2-aminobenzoic acid (Abz) and 3-nitrotyrosine ($\text{Tyr}(\text{NO}_2)$) are used as the fluorescent donor and acceptor [9]. The fluorescence of Abz is quenched until cleavage of the intermediate peptide increases the distance between Abz and $\text{Tyr}(\text{NO}_2)$. At a separation distance of 2 nm, corresponding to approximately 7 amino acids, the fluorescence is quenched to 0.3% of the cleaved product [10]. Multiple variations on this theme using fluorescence resonance energy transfer (FRET) exist [4, 6].

Luminescent Assays Luminescent probes can offer a superior sensitivity over fluorescent assays. Many fluorescent labels are strong scatterers, but the sensitivity of the assay is limited by the fluorescent background of other molecules. In contrast, luminescent molecules do not require external illumination for their excitation. As a consequence, they can be detected with zero background signal. Figure 6.1 (d) shows the concept. First, the protease releases aminoluciferin from a specific substrate. Next, luciferase will render the free aminoluciferin into a glowing molecule whose luminescence can last over several hours.

Liquid Chromatography and Mass-spectrometry Liquid chromatography can be used to separate cleaved products form the enzyme substrates based on their physical properties such as mass or charge. Unlike the techniques described in figure 6.2, there is no need for labels. As described in section 6.3.1, we used reverse phase high-performance liquid chromatography (RP-HPLC) as a reference method for measuring trypsin and endoproteinase Glu-C on our synthetic peptides. In short, the peptide fragments are separated based on their affinity for hydrophobic silica beads. A gradient of increasing acetonitrile concentration result in the elution of more hydrophobic fragments. The presence of protein fragments in the eluted phase is then quantified through UV-absorption spectroscopy. Each protein fragment will have a characteristic retention time, which is higher for longer and more hydrophobic fragments. These fragments are subsequently identified through their molecular weight using mass spectrometry. For example, figure 6.5(a2) on page 6-14 shows the different eluted fractions and their molecular weights for the

CALNNYGGGGVRGNF peptide before and after trypsin digestion.

In comparison to the fluorescent or colorimetric assays, HPLC/mass-spec experiments are resource-, time- and infrastructure- intensive. Furthermore, the proteolysis can not be followed in real time. For example, in our experiments using routine lab equipment, checking the activity of a protease on a substrate using a 3-step HPLC (before, midway and end of digestion) required about three hours of chromatography time with a sample consumption of 100 μg peptide and 1-3 ug of protease per step. For comparison, a real-time fluorescent measurement took less than 30 minutes and a 20 times lower sample consumption. Furthermore, the use of multi-well plates in the fluorescent assay allows to acquire the full enzyme-substrate kinetics in one experiment.
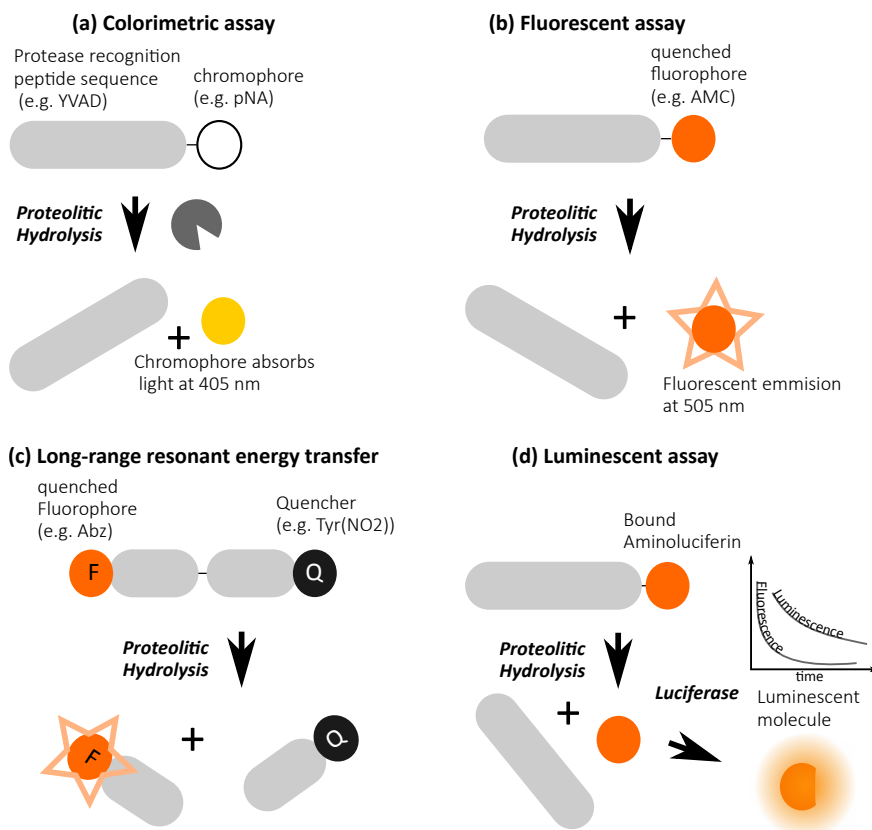
Figure 6.1 Protease activity detected through substrate cleavage using different types of reporter molecules for an optical readout. Many variations on these themes are commercially available.

An important advantage of detection through substrate cleavage is that only activated proteases contribute to the signal. The discrimination between proteases in their active and non-active form is often difficult using a direct detection based on

the physical or chemical properties of the protease. Also, live-cell and even in-vivo activity detection are possible using cell permeable substrates. On the other hand, substrate cleavage by other proteases than the one of interest is often an issue with experiments in a more complex environment. A peptide can be a substrate for multiple proteolytic enzymes who, apart from both cleaving this particular substrate, may have entirely different functionalities. For example, it was found that granzyme B cleaves many caspase substrates [11]. Overlapping substrate specificities is less of a problem using a direct detection the protease instead of their cleaved products.

Direct detection of activated proteases
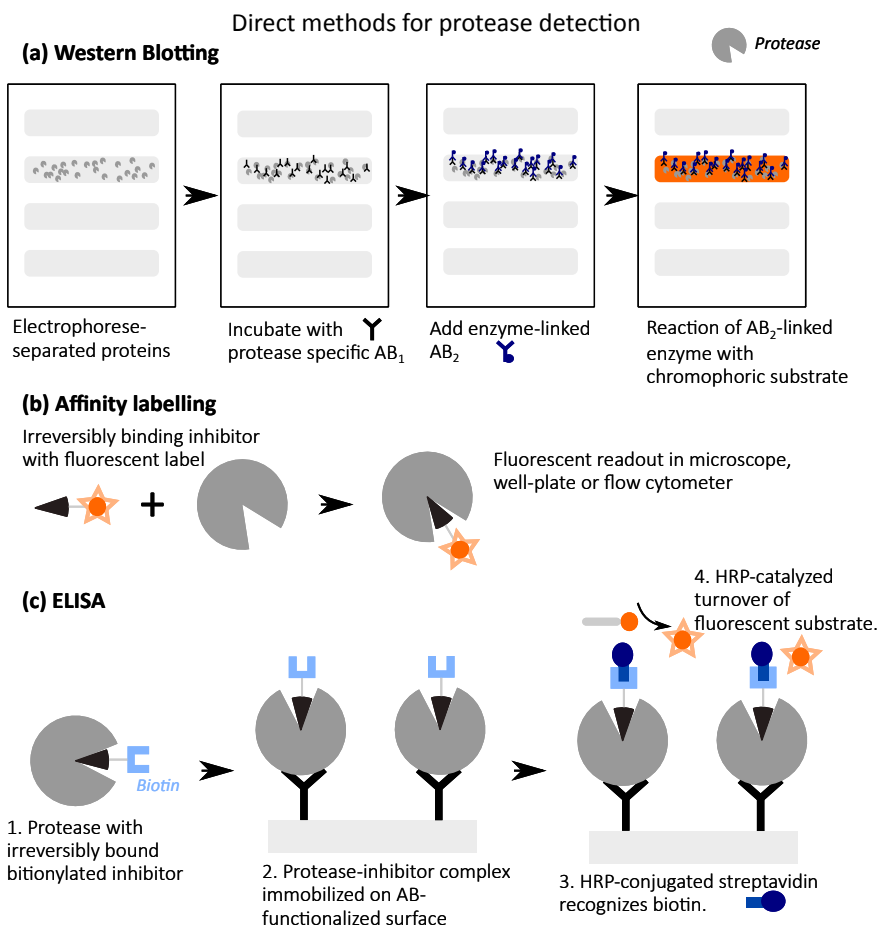
Figure 6.2 Direct methods for detecting protease activity.

Western Blotting   In western Blotting (WB), proteins and fragmented proteins are first separated by size using gel electrophoresis and subsequently blotted on a porous membrane (figure 6.2a). Next, specific antibodies (AB_1) for the desired protein are added. Then a second set of antibodies AB_2 binds to the bound AB_1. AB_2 is linked to an enzyme that catalyzes a chromatic reaction on a substrate that is added in a final step. This colored substrate marks the band of the protein [8]. Because WB directly detects the protease instead of its activity, it is often not able to distinguish between the amount of expressed proteases and their actual activity. There do exist a number antibodies (AB_1) that only recognize activated proteases [7]. However, WB is still labor intensive, only semi-quantitative and not applicable to in-vitro or in-vivo measurements.

Affinity binding and ELISA   An emerging method for the detection of activated proteases is the use of so-called activity-based probes (ABP) [12]. A specific inhibitor bounds covalently and irreversibly to the protease (figure 6.2b) using protease-specific chemical interactions. This inhibitor is tagged with a recognition molecule, such as a fluorescent label or a biotin for streptavidin binding. After washout, the presence of activated enzymes can quantified by detecting the presence of this label. A similar principle to the ABP can be used in combination with ELISA, as depicted in figure 6.2c. Here, active proteases are tagged and immobilized on an antibody-functionalized surface and detected through the turnover of a fluorescent substrate by a secondary bound enzyme such as horseradish peroxidase (HRP).

6.1.2   Emerging technologies for monitoring protease activity

A complete overview of the myriad of newly proposed concepts for detecting protease activity, including activity based probes [12, 13], enzyme responsive materials [14] and magnetic resonance sensors [6], is outside the scope of this text. We limit ourselves to highlighting a number of methods that combine nanotechnology with optical readouts for measuring protease activity through substrate cleavage [6, 7, 15, 16], as they are the nearest competitors for the new approach we will introduce in this chapter.

Nanoparticle-based sensors   Gold nanoparticles can be easily synthesized and are considered to be biocompatible because gold is an inert material. As a consequence, gold nanoparticles (Au-NPs) have become a popular platform for developing protease-activity sensing technologies in the last decade [6, 16]. Three mutually related optical characteristics make them attractive: their localized surface plasmon resonance (LSPR), broadband fluorescent quenching and the field enhancement close to the gold surface. LSPR-based activity sensing makes use of the clustering [17] or de-clustering [18] of gold nanoparticles upon peptide cleavage. For example, a group of nanoparticles can be clustered together using a peptide with gold-biding cysteine at both ends. Upon cleavage, the distance between

the nanoparticles increases which results in a blueshift of the LSPR-absorption. Au-NPs can also be used as a fluorescent quencher, where the fluorescence of a molecule is restored when it is cleaved off the nanoparticle [19]. In contrast to quenching based a FRET molecule as shown in figure 6.1, the spectral range of the quenching by Au-NPs is much broader. By quenching different fluorescent labels across the 450-750 nm wavelength range, a single Au-NP can simultaneously detect the activity of multiple proteases [7]. However, the broad fluorescent emission spectrum of these labels still limits multiplexing. Fluorescence assays are being further improved by replacing conventional fluorophores with quantum dots (QDs) [20]. These can have a higher quantum efficiency, longer fluorescent lifetime and more narrow emission spectrum.

SERS In contrast to fluorescent or colorimetric assays, the specificity of Raman fingerprints enables highly spectrally multiplexed measurements [21]. Surface-enhanced Raman scattering (SERS) provides a promising technology for sensitive and selective detection of peptide bond hydrolysis because the nanometer-sized peptides match well with the typical size of a plasmonic hot-spot. Not surprisingly, a number of studies reported on detection of protease activity based on (SERS) [18, 22–25] and surface-enhanced resonance Raman scattering (SERRS) [26–28]. These include indirect sensing methods based on clustering [25] and anti-clustering [18] of nanoparticles upon cleavage, and direct detection methods based on the appearance [28] and disappearance [22, 23] of the spectra from strong Raman scatterers used as SERS labels. These studies demonstrate the ability for detecting protease activities at single-cell concentrations levels in sub-nL volumes [18, 23, 26].

In the following two sections, we present a novel and generic SERS-based method for the detection of protease activities through peptide hydrolysis using only natural amino acids. We use the inherent SERS fingerprint of aromatic amino acids [29, 30] in our peptides, which eliminates the use of fluorescent- or SERS-labels. As a consequence, the peptide design is easily adjustable towards a specific substrate for different proteases. These peptides form a self-assembled monolayer [31] on a gold-nanodome patterned SERS platform, with distinguishable vibrational spectra both before and after the cleavage site. This enables discriminating specific protease cleavage from ligand exchange [19, 32]. We take a stepwise approach to prove that the changes in SERS spectra upon peptide hydrolysis indeed originate from substrate cleavage. First, Raman spectra of the pure peptide are compared to SERS spectra acquired on the nanodome surface. Peaks are attributed to known vibrations in literature and to own experimental data. Next, we investigate the SERS spectra of the cleaved products separated by RP-HPLC after incubating specific substrates with the serine proteases trypsin and endoproteinase Glu-C. We also verify that the peptides are bound to the nanodome gold surface through an amine-terminal cysteine, correctly presenting the cleavage site away from the solid interface. Finally, we demonstrate digestion of a surface-bound trypsin substrate and

follow this reaction in real-time through continuous changes in the SERS spectra.

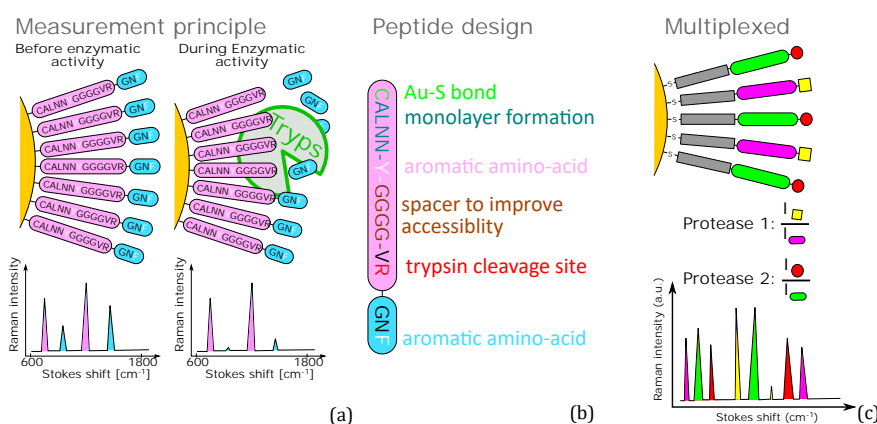## 6.2   Functionalization of gold nanodomes with peptides

Figure 6.3 (a) A gold-bound peptide substrate provides a SERS fingerprint with distinctive peaks from amino acids on both sides of the cleavage site. After protease hydrolysis, the non-bound product diffuses away and its Raman peaks disappear. (b) The peptide substrate designed for trypsin hydrolysis, which cleaves C-terminal to arginine (R) residues. (c) Concept of a multiplexed measurement of the activity of two different proteases based on peptide substrates with different SERS peaks.

6.2.1   Peptide substrate design

Figure 6.3a conceptually sketches the measurement principle. A monolayer of peptides containing a specific cleavage site is bound to a gold nanostructure. This monolayer provides a SERS signature from amino acids both before and after the cleavage site. After protease digestion, the part of the SERS spectrum originating from the cleaved-off, non-surface bound product decreases, while the products attached to the gold surface provide the same signal. Although the measurement principle is fairly straightforward, a correct design of the peptide is crucial for efficient protease digestion and sensitive SERS detection. The design and fabrication of suitable peptide substrates was not achieved overnight. All peptide designs fabricated and tested in this work are summarized in table 6.1. The peptides should form a stable monolayer on a gold surface, provide an accessible cleavage site and include strong SERS scatterers. Furthermore, the total length of the molecule must remain limited to a few nanometers because of decreasing SERS signal with increasing distance [33, 34]. Figure 6.3b shows the proposed peptide in more detail, designed as a specific substrate for trypsin digestion. From amine- to carboxyl-terminus, it starts with the pentapeptide CALNN [19, 31, 32, 34]. In this part, the cysteine (C) ensures a covalent sulfur-gold bond [35]. The hydrophobic amino

Table 6.1: Different peptide substrates and matrix molecules used in this work. Aromatic compounds are highlighted in bold, the * represents the gold-binding side and | shows the cleavage site for the specified protease. Raman and SERS spectra of all these molecules are given in appendix XX. Amino-acids are written from amino to carboxyl-terminus. See figures A.19, A.17, A.18 and A.20 for the Raman spectra of all the molecules in this table.

Substrate	Supplier	Comments
Caspase-1		
YVAD| **G**C*	Caslo	(-) No aromatic reporter in remaining product *GC*
YVAD|**GFC***	Caslo	(+) Aromatic amino acids in both products
		(-) C-terminal *Cys* based S-Au bond prone to reduction
		(-) Short distance Au to cleavage site gives steric hindrance
YVAD|**GF**-PEG$_4$-Alk$_{11}$Thiol*	In-house	(++) Well protected S-Au bond by SAM
(abbrev = YVADGFpAt)		(-) Difficult to test caspase-1 activity in solution
		(-) Complex synthesis
*C**F**GGGGG**Y**VAD|**amc**	Eurogentec	(+) Cas-1 active in solution from fluorescent (*-amc*) assay
		(-) Unprotected S-Au bond prone to reduction
*SH.(CH$_2$)$_5$CO-**F**-γaba-**Y**VAD|**amc**	In-house	(+) Cas-1 active in solution
(abbrev = mFγYVAD.amc)		(+) Partially protected S-Au bond
Trypsin		
*C**G**F**VR|**pna**	BioMatik	(+) Trypsin active in solution from absorption (*-pna*) assay
		(-) Short distance Au to cleavage site gives steric hindrance
*SH(CH$_2$)$_5$CO-**Y**-γaba-NNR|**F**D	In-house	(- -) No trypsin activity in solution
*SH(CH$_2$)$_5$CO-**Y**GGNNR|**F**H	In-house	(-) Poor trypsin activity in solution
*CALNN**Y**GGGGVR|**GN**F	In-house	(+) Partially protected S-Au bond by SAM
		(+) Trypsin active in solution
		(++) Trypsin active on gold-bound substrate
*AcCGGGGGG**F**GVR|**pna**	Caslo	(+) Trypsin active in solution
		(+) Increased SERS signal
		(-) Unprotected S-Au bond
		Ongoing experiments
Endoproteinase Glu-C		
*SH(CH$_2$)$_5$CO-**Y**-γaba-NNE|**S**WD	In-house	(-) Poor endoproteinase Glu-C activity in solution
*CALNN**Y**GGGGNNE|**S**WH	In-house	(+) Partially protected S-Au bond by SAM
		(+) Endoproteinase Glu-C active in solution
		Ongoing experiments
Matrix Molecules		
*SHCH$_2$(CH$_2$)$_6$CH$_2$	Sigma	Spacer molecule for AlkThiol or SH(CH$_2$)$_5$ molecules
*CALNN.CONH$_2$	In-house	Spacer molecule for CALNN-... substrates

acids alanine (A) and leucine (L) help to form a self-assembled monolayer, followed by a double hydrophilic asparagine (N) to ensure a good solubility [31]. CALNN is followed by tyrosine (Y), an aromatic amino acid that serves as a first SERS reporter. If present, its SERS signature confirms that the **CALNNY** fraction is still bound to the gold surface, meaning that there has not been any ligand exchange [36], desorption or non-specific cleavage in this part. Next, a stretch of glycines (**GGGG**) is included, small amino acids that form a flexible chain to improve the accessibility of proteases to the cleavage site. We experimentally found that the presence of this additional spacer is crucial for trypsin activity on surface-bound peptides. These glycines are followed by **VR** being respectively the P_2 and P_1 subsite for trypsin. It is well known that trypsin cleaves at the carboxyl side of arginine (R) and lysine (K) [37]. The hydrophobic valine (V) in a P_2 position further increases the efficiency of the catalysis [38]. The cleavage site is followed by a **GNF** sequence. The small glycine at P'_1 ensures a good accessibility

of trypsin to the cleavage site, the hydrophilic asparagine helps the solubility of the end-fraction of the peptide and, finally, the second aromatic amino acid phenylalanine (F) functions as a second SERS reporter. As a consequence, for this specific substrate the intensity of F-related peaks divided by that of Y-related peaks in the SERS spectrum (I_F/I_Y) gives a metric for cleavage and diffusion of the -GNF fraction.

Table 6.2: Peak assignment of Raman and SERS spectra of the CALNNYGGGGVRGNF peptide. The Raman spectrum of the short peptide CALNN was measured separately (figureA.20). SERS peaks marked in bold will selectively decrease upon trypsin activity. Peaks in italic originate from peptide backbone vibrations.

Raman (cm^{-1})	SERS (cm^{-1})	Origin	Raman	SERS	Origin
621	618	F [29]	1126	1124	G [39], CALNN
642	-	Y [29], CALNN	1176	1178	Y [39]
723	730	CALNN	1207	1206	F [29]
834	829	Y [29]	*1229*	*1240*	*Amide IIIβ* [40]
853	860	Y [29], A [39]	1325	1330	G [39]
898	889	G [39]	1429	1426	CALNN
957	948	CALNN	-	1448	G [39]
1003	**1003**	F [29, 39]	1607	1603	CALNN
1031	1030	F [29, 39],CALNN	*1674*	*1677*	*Amide I* [39]

An analogous peptide substrate for a different protease was fabricated by adjusting the specific cleavage site. Placing the amino acids **NNE-** in the $P_3 - P_1$ and **-SWH** in $P_1' - P_3'$ positions (figure 6.5(b1)) makes the substrate suited for hydrolysis by endoproteinase Glu-C, which cleaves peptide bonds C-terminal to glutamic acid (E) residues [9]. Tryptophan (W) serves here as an aromatic reporter in the cleaved-off fraction, resulting in a different SERS spectrum that allows using I_W/I_Y as a metric for endoproteinase Glu-C digestion. Thus, the generic design of the peptide substrate provides the ability to use this technology in different applications, and has the potential for simultaneously monitoring the activity of different proteases on different substrates. In future, non-natural aromatic amino acids could be added to the peptide sequence to widen the multiplexing possibilities.

6.2.2 The nanodome SERS platform as a compromise between accessibility and enhancement

For most applications, the ideal SERS platform provides a strong, uniform field-enhancement and has good batch to batch reproducibility. For the specific case of a sensitive and quantitative monitoring of protease activity, the field enhancement has to stretch a few nanometers from the gold surface and the hotspots have to be accessible. The latter is of crucial importance, as most proteases have a molecular weight of 20-50 kDa, roughly corresponding to a Stokes radius of 2-3 nm [42]. One can easily imagine that a peptide substrate located in a sub-5 nm wide hotspot is inaccessible for a trypsin (23 kDa) or endoproteinase Glu-C (27.7 kDa) molecule. Fortunately, pore sizes starting from 10 nm are accessible

Table 6.3: Peak assignment for the CALNNYGGGGNNESWH peptide for endoproteinase Glu-C digestion. SERS peaks marked in bold will selectively decrease upon endoproteinase Glu-C activity. Peaks in italic originate from peptide backbone vibrations.

Raman (cm^{-1})	SERS (cm^{-1})	Origin	Raman	SERS	Origin
642	642	Y [29], CALNN	-	1118	W [39]
723	-	CALNN	1176	1177	Y [39]
758	**754**	W [29, 39, 41]	1232	1235	W [39], *Amide IIIβ* [40]
832	-	Y [29],	1257	-	W [39], H [39]
852	-	Y [29], A [39]	**1361**	**1356**	W [29, 39, 41]
-	868	?	1430	1423	CALNN, W [39]
879	-	W [29, 39, 41]	-	1535	?
893	-	G [39]	1552	-	W [29, 39, 41]
-	999	?	-	1602	CALNN
1012	-	W [29, 39]	1618	-	W [39],G [39],CALNN
1030	1027	CALNN	*1672*	*1674*	*Amide I* [39]

to enzymes in this size range [43]. The requirements described above are to a certain degree contradictory Isolated nanostructures such as nanorods or nanotriangles provide optimal accessibility, but exhibit a low enhancement factor and a stronger distance-dependence as compared to coupled geometries. On the other hand, superior surface-enhancement is achieved in coupled nanostructures with a sub-5 nm, poorly accessible gap [44]. To address these concerns, we fabricated gold-nanodome structures with a gap (g) of 10-15 nm as described in detail in chapter 3. The nandome fabrication method provides ample chips with a strong and uniform enhancement factor at a reasonable cost and effort, avoiding the use of e-beam lithography. The localized surface-plasmon resonance of these structures was optimized through UV-Vis reflection and SERS measurements for an optimal enhancement with a 785 nm Raman pump laser and $600\ \mathrm{cm}^{-1}$ to $1700\ \mathrm{cm}^{-1}$ Stokes shifts in a water environment. Figure 6.4a shows the resulting geometry with a gap width (g) of 12 ± 2 nm and a height (h) of 53 ± 4 nm. We experimentally measured a SERS substrate enhancement factor (SSEF [45]) of $1 \pm 0.2 \cdot 10^6$ for the chips used in this manuscript. The coefficient of variation (σ/μ) on the SERS signal across a single chip is 6-7%. For comparison, we measured a maximum SSEF of $9.8 \cdot 10^6$ in nanodome structures with a gap width of approximately 5 nm, unlikely to have a good accessibility of the peptide substrate in the hotspots. Note that SSEF, defined in chapter 3.4.1 is a figure for the surface-enhancement per molecule averaged across the gold surface. The surface area of the hotspots accounts for approximately 10-15% of the total gold surface area, calculated from the SEM images in Figure 3a. Thus, for molecules in this region, the SERS hotspot enhancement factor (SHEF) is in the order of 10^7, which is in correspondence with the 3D FDTD simulated electric field profile (Figure 6.4b) in a $|E|^4$ approximation. These field profiles also show that the LSPR stretches across the full width of the gap. Assuming a loading density of 2 peptides/nm^2 [34, 36] there are roughly 10^4 peptides per hotspot.
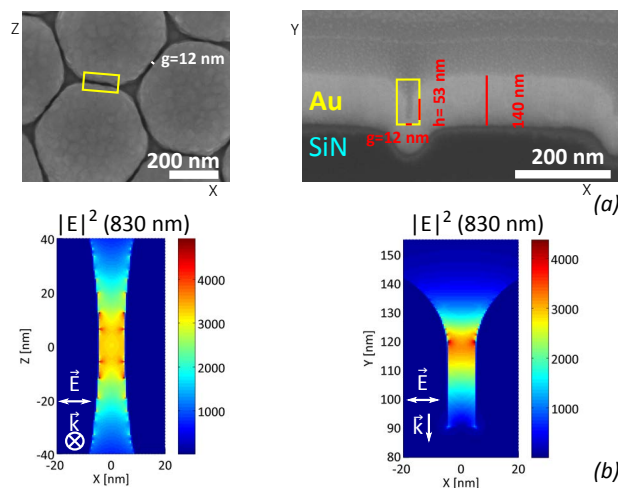
Figure 6.4 (a) Top-down and cross-section SEM images for a nanodome-pattern chip with a 12 nm wide (g) and 53 nm high (h) inter-dome gap. (b) Corresponding $|E|^2$ field distributions for this geometry at resonance wavelength simulated through 3D FDTD, showing that the localized surface plasmonic resonance is confined to the inter-dome gap region. The field distributions are plotted over the region corresponding to the yellow rectangles.

6.3 SERS-based detection of trypsin and endoproteinase Glu-C activity

Figures 6.5a1 and 6.5b1 compares the normal Raman spectra to the SERS spectra of respectively CALNNYGGGGVRGNF (trypsin substrate) and CALNNYGGG-GNNESWH (endoproteinase Glu-C substrate) peptides labeled on a nanodome platform. Their respective Raman bands are identified in table 6.2 and table 6.3 based on SERS [29, 30] and Raman [39, 41] spectra of amino acids reported in literature and on own measurements of the peptide CALNN. We are particularly interested in peaks selective for the peptide products that are either cleaved off or remain on the surface. These include the 1003 cm^{-1} symmetric bending mode of phenylalanine (F) versus the 833 cm^{-1} in-plane and 853 cm^{-1} out-of-plane ring breathing modes of tyrosine (Y), and the symmetric benzene/pyrrole in-phase breathing mode of tryptophan (W) at 760 cm^{-1} [29].

6.3.1 Protease-mediated peptide hydrolysis in solution

Hydrolysis of bulk peptides observed through SERS spectra of HPLC separated fractions

As a first step, we monitored the activity of the protease on the substrate in solution. RP-HPLC was used to separate the substrate form the digestion products, which are subsequently labeled on a nanodome platform. From the difference

spectrum, we derive the characteristic peaks of the cleaved-off and remaining fractions. Figure 6.5a2-a4 depicts the results of this experiment for trypsin and its CALNNYGGGGVRGNF ($100\,\mu\mathrm{g/ml}$) substrate. The peptide was incubated with trypsin ($3.3\,\mu\mathrm{g/ml}$) at a 1/30 (w/w) ratio in a 50 mM ammonium-bicarbonate (pH 7.8) buffer in water, and separated with RP-HPLC (figure 6.5a2) after 0, 30 and 90 minutes of incubation. The RP-HPLC-separated peptides and their fragments were identified using matrix assisted laser desorption/ionisation time-of-flight (MALDI-TOF) mass spectrometry. Prior to adding trypsin, we found two fractions; one corresponding to an uncleaved monomer and the other to an uncleaved dimer. The dimer formation is a consequence of the oxidation of the cysteine thiol groups upon which a disulfide bond is formed between two peptides. The substrate was almost fully digested after 30 minutes and transformed into cleaved monomer, single cleaved dimer and double cleaved dimer fractions. After 90 minutes, the peptides were found to be fully cleaved. Subsequently, we labeled nanodome chips with cleaved and uncleaved fractions. The resulting SERS spectra (Figure 6.5a3-a4 [5]) show a full disappearance of the 1003 $\mathrm{cm^{-1}}$ peak in the cleaved fraction. Furthermore, the peaks at 618 $\mathrm{cm^{-1}}$, 1030 $\mathrm{cm^{-1}}$ and 1207 $\mathrm{cm^{-1}}$ show a partial decrease, although their signal to noise ratio is low. All these peaks correspond to those attributed to phenylalanine (Table 1). From this experiment, we conclude that the ratio between the 1003 $\mathrm{cm^{-1}}$ peak and the 829-860 $\mathrm{cm^{-1}}$ peaks ($I_{1003}/I_{829-860}$) provides a correct metric for I_F/I_Y, the cleavage of the substrate by trypsin.

Figure 6.5(b2-b4) describes an analogous experiment for endoproteinase Glu-C ($3.3\,\mu\mathrm{g/ml}$) and its CALNNYGGGGNNESWH ($100\,\mu\mathrm{g/ml}$) substrate. Peptide digestion was slightly less efficient, with almost full conversion of substrate to products only after 4 hours of incubation. Because of the large adsorption of tryptophan at 270 nm and its strong interaction with the RP-HPLC resin, the SWH product is also visible as a separate fraction. After binding the cleaved peptide and uncleaved dimer to nanodome chips, we observed a disappearance of the 754 $\mathrm{cm^{-1}}$ and 1356 $\mathrm{cm^{-1}}$ peaks upon cleavage, as well as a reduction of the contributions at 999, 1118 and 1531 $\mathrm{cm^{-1}}$ peaks. These changes correspond to the peak assignments shown in table 6.3, but more experiments are needed for an improved peak assignment of the CALNNYGGGGNNESWH substrate.

---

[5]The appearance of some new peaks the fractions in figure 6.5(a3-b3) compared to the spectra acquired in figure 6.5a1-b1 is attributed to unknown sources of contamination during the HPLC separation. For example, the newly appearing peaks in the cleaved fraction CALNNYGGGGVR at 747, 1540 and 1603 $\mathrm{cm^{-1}}$ did not appear in other experiments on this peptide.
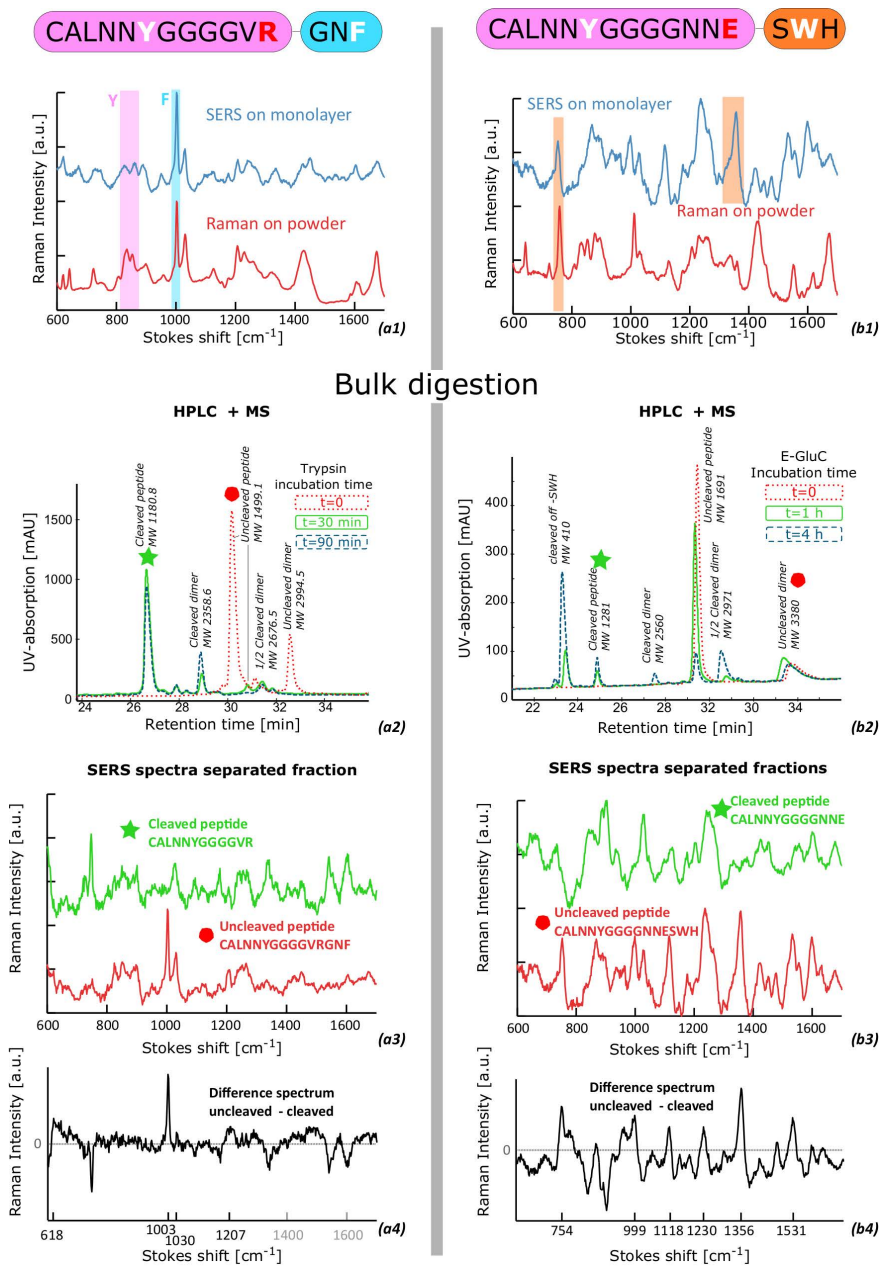
Figure 6.5 (a1) Raman and SERS spectra of the CALNNYGGGGVRGNF trypsin substrate show characteristic tyrosine and phenylalanine peaks. (a2) RP-HPLC was performed after incubation of this peptide with trypsin and eluting peaks were analysed by mass spectrometry which shows almost full digestion of after 30 minutes of incubation with trypsin. (a3) SERS spectra of RP-HPLC separated fractions and their difference spectra (a4) confirm the full disappearance of F-related peaks upon trypsin digestion. (b1) Raman and SERS spectra of the CALNNYGGGGNNESWH endoproteinase Glu-C substrate with characteristic tryptophan peaks. (b2) RP-HPLC and mass spectrometry analysis after incubation with endoproteinase Glu-C show an almost complete digestion after 4 hours of incubation. (b3-b4) SERS spectra and difference spectrum of the RP-HPLC separated fractions show the disappearance of tryptophan-related peaks after cleavage.

Hydrolysis of unbound peptides observed through SERS spectra of a non-separated mixture

Apart from a thiol-gold interaction, N-terminal primary amines can also lead to a charge-based adsorption on metal surfaces [46]. This effect may be additive in the case of cysteine, but could lead to the adsorption of unwanted amino acids on the gold surface. In a second set of in-solution experiments, we ran a similar trypsin CALNNYGGGGVRGNF assay without separating the fractions by RP-HPLC (figure 6.6). One nanodome chip was labeled with a reference solution of the peptide ($100\,\mu g/ml$), another with a solution of peptide ($100\,\mu g/ml$) and trypsin ($3.3\,\mu g/ml$) after 2 hours of incubation. The lack of a phenylalanine peak at $1003\ \mathrm{cm}^{-1}$ in the trypsin-incubated solution confirms that the peptide had been fully digested and that the products bind the surface through the thiol side-chain on the cysteine, but not through charge-based adsorption of the free amino group on the GNF cleaved off product. Furthermore, the SERS and difference SERS-spectra shown in figure 6.6 confirm the findings of the RP-HPLC experiment in figure 6.5a.
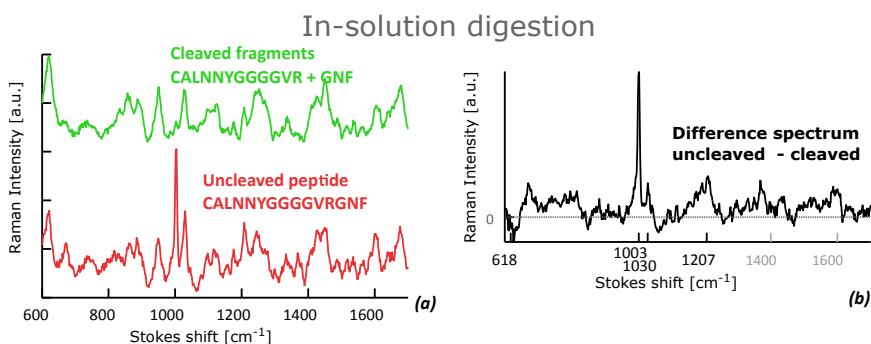
Figure 6.6 SERS spectra of a peptide solution before (red) and after (green) trypsin incubation prove that the binding of the peptide to the chip gold surface happens via the side-chain of the N-terminal cysteine through a gold-sulfur bond, but not via the free amine part of the GNF product. (b) The difference spectrum before and after cleavage agrees with the difference between the RP-HPLC separated uncleaved and cleaved fractions shown in 6.5.

6.3.2   Trypsin hydrolysis of gold-nanodome bound peptides

In a third experimental setup, three CALNNYGGGGVRGNF labeled nanodome chips were incubated in a buffer without trypsin, with trypsin and with trypsin plus an ovomucoid inhibitor for 45 minutes (figure 6.7). The chip incubated with trypsin plus inhibitor shows a SERS spectrum resembling that of the reference chip, suggesting full blockade of tryptic cleavage by the ovomucoid inhibitor. On the chip with trypsin only, the surface bound peptides are cleaved, resulting in a decrease of $I_{1003}/I_{829-860}$ by 40-48%. A full disappearance of the GNF finger-print was never observed, at most $I_{1003}/I_{829-860}$ decreased by 53% over all our experiments. We consider two possible origins for the remaining signal at 1003

cm^{-1}. One is a partial re-adsorption of the GNF products on the gold surface; the tripeptides that do not diffuse out of the hotspot region will continue contributing to the SERS spectrum. However, the experiment in figure 6.6 suggests this is not the case. More likely, the remaining signal originates from peptides that are not accessible to the protease due to steric hindrance. This can be a result of a too dense monolayer of peptides [19, 23] or inaccessible parts of the nanodome geometry. Especially in the latter case, the inaccessible peptides are probably located in the nanodome gaps and will contribute disproportionately strong to the SERS signal. Thus, it is plausible that significantly more than 53% of the protease-accessible peptides has been cleaved. The difference spectrum in figure 6.7c shows exactly the same features as those observed upon bulk digestion followed by SERS labeling in figure 6.5a4 and figure 6.6c. Furthermore, we did not observe significant differences in the absolute strength of the CALNNYGGGGVR fingerprint, which shows that ligand exchange was limited in this assay. Ligand exchange is more prominent in a reducing environment, in which a reduction the gold-sulfur bond results in a detachment of the peptides. These reductive environments are present in cells and of particular importance for the activation of cysteine proteases, as discussed in section 6.4. While the normalization to the trypsin peaks at 833-853 cm^{-1} is not strictly necessary in this case, it does provide an inherent correction for differences in acquisition parameters such as laser power or focus drift as well as limited variations across the SERS platform.
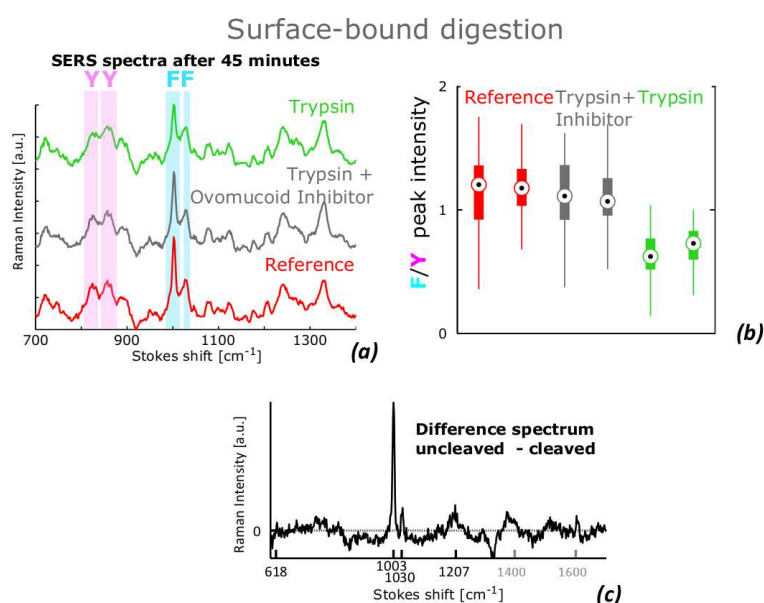
Figure 6.7 Trypsin cleavage of surface-bound CALNNYGGGGVRGNF peptides. (a) SERS spectra with the characteristic tyrosine and phenylalanine peaks highlighted in blue and pink. (b) Relative intensity of the highlighted peaks (I_F/I_Y), showing peptide cleavage in the presence of trypsin which is blocked when an ovomucoid (Type II-O) inhibitor is added. (c) Difference spectrum between the sample with and without trypsin, which agrees well with the results of the bulk digestion.

Real time observation of trypsin activity

Finally, CALNNYGGGGVRGNF labeled chips were incubated with trypsin under the Raman microscope for a real-time acquisition of SERS spectra. Figure 6.8a shows the evolution of these spectra before and after trypsin addition. A new spectrum was acquired every 2-3 minutes with an integration time of 100 seconds. A relative decrease of I_{1003} versus the peaks at 829, 860, 948, 1248, 1330, 1603 and 1677 cm^{-1} is visible within the first minutes after adding $0.2\,\mu\mathrm{g/ml}$ trypsin (8.6 nM) to a total volume of 1 ml (8.6 pmol), in agreement with table 6.2 and the earlier experiments described in this work. SERS spectra after 2 minutes and 30 minutes of trypsin incubation show a further reduction of I_{1003} and I_{1206} with increasing incubation time (figure 6.8b). The fast decrease of $I_{1003}/I_{829-860}$ in the first minutes after trypsin addition demonstrate that at trypsin concentrations ranging from 1 to $0.2\,\mu\mathrm{g/ml}$, most of the accessible substrate was cleaved within the timespan of the first measurement (figure 6.8c). The curves of $I_{1003}/I_{829-860}$ versus time qualitatively agrees to the kinetics of enzymatic reactions on self-assembled monolayers [47]. More measurements are required to accurately determine the trypsin detection limit and on-chip enzyme kinetics, especially in the first minutes after trypsin incubation. In the near future, we hope to demonstrate the similar data for endoproteinase Glu-C and its substrate, as well as a multiplexed assay for both trypsin and endoproteinase Glu-C. Currently, our assay allows for a sampling speed of 1-2 minutes. We expect this can be improved in future to approximately 10 seconds, which would put us in a good position detecting protease activation in single-cells, typically happening over timescales of several minutes [4, 48].
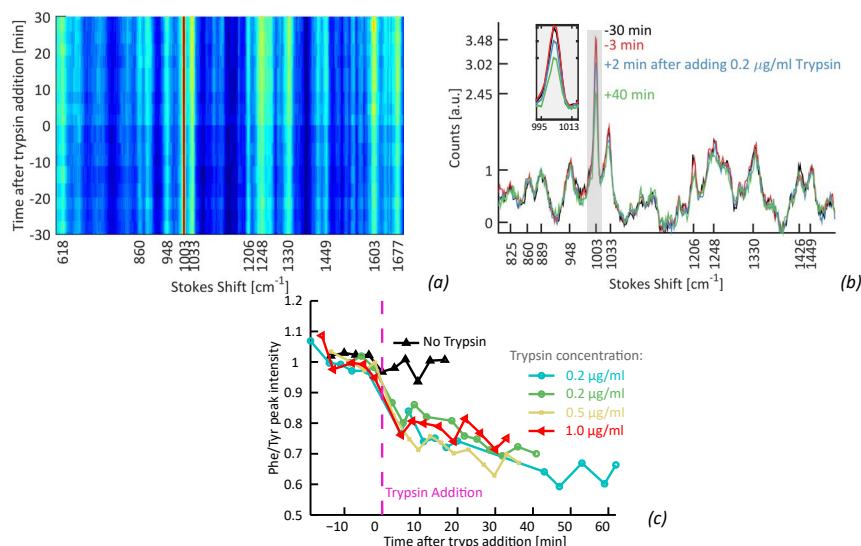
Figure 6.8 Real-time trypsin digestion of gold-nanodome bound peptides. (a) Evolution of SERS spectra before and after trypsin addition, scaled for equal 1003 cm^{-1} intensity. This shows a relative increase of CALNNYGGGGVR-related peaks at 829, 860, 948, 1248, 1330, 1603 and 1677 cm^{-1} versus the 1003 cm^{-1} phenylalanine peak upon trypsin addition (t=0). (b) SERS spectra at individual time points, the inset zooms in on the cm^{-1} F-peak. (c) Time evolution of I_F/I_Y, characterized by $I_{1003}/I_{829-860}$ and measured in four different experiments, all showing a fast cleavage within the first minutes after trypsin addition.

6.4 Towards a single-cell monitoring of inflammasome activation

6.4.1 Motivation

Our current knowledge of cell-related processes is largely based on population-level studies, using bulk methods such as immune-assays and mass spectrometry. However, in recent years it was demonstrated how the behavior of a single cell can significantly differ from the average response of a population. For example, genetically identical cells can show different responses to the same drug because of variable epigenetic regulation at the single-cell level in the cell population [5, 49]. An understanding of cell dynamics at the single-cell level was shown to enable a better understanding of biological systems and can also provide an improved insight to cellular drug response. A high degree of heterogeneity in single-cell dynamics was observed in different processes related to cancer-drug induced cell death responses and cellular immunity [4, 50, 51]. In particular, all-or-none activation of NF-κB [51] and caspase-1 (cas-1) under different external stimuli [4] have been reported in the context of immune signaling. These examples illustrate the importance of considering single-cell dynamics for the analysis of immune responses in inflammasome-associated infections and inflammatory diseases. Es-

tablished assays like western blotting and ELISA are not up to the big challenges presented by single-cell analysis, mainly because of the limiting sensitivity of these bulk methodologies for the local detection of a small amount of protein in a very complex biological environment. Single-cell monitoring of inflammasome activation has only very recently been reported [4], but the technological approach used in the cited work is not amenable to monitoring inflammasome activation in physiologically relevant samples from patients and/or in vivo mouse disease models because it relies on the ectopic expression of fluorescent labeled fusion proteins. Therefore, the development of non-fluorescent single-cell detection methods for inflammasome activation at the endogenous level offers tremendous opportunity in biomedical and clinical research. At the same time, these single-cell approaches hold promise for delivering meaningful biomedical insight starting from limiting amounts of precious clinical samples. Without doubt, there is a strong interest in a technology that allows for a highly multiplexed detection of inflammasome-associated cellular processes on a single cell basis.
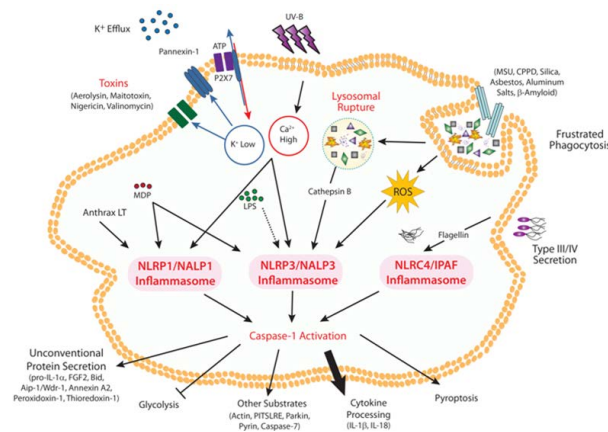
Figure 6.9 Inflammasome activation in the context of infection or chronic inflammation converges on the activation of the inflammatory protease caspase-1. This leads to proteolytic conversion and extracellular release of the highly inflammatory cytokines interleukin-1 and interleukin-18 *(image from www.adipogen.com/inflammasomes/)*

The central biological response on which inflammasome activation in the context of infection or chronic inflammation converges is activation of the inflammatory protease caspase-1. Caspase-1 is part of the family of cysteine-dependent aspartate-directed proteases. Its activation leads to the proteolytic conversion and extracellular release of the highly inflammatory cytokines interleukin-1 and interleukin-18 [7, 52] (figure 6.9). Monitoring the activity of caspase-1 in the close vicinity of single cells is especially relevant with regard to pathological processes related to inflammation, since immune cells secrete a multitude of inflammatory factors and express a large functional heterogeneity.

In this section, we describe our progress towards monitoring the activity of externally added and activated caspase-1 through the SERS spectrum of nanodome-bound peptides. Although we have made significant advances, we have not unambiguously demonstrated a detection of caspase-1 activity. Note that the experiments in this section were performed prior to taking a step back to trypsin in order to simplify the problem. Based on the current knowledge and expertise from the trypsin-assay, we believe to be in a better shape for tackling the challenges related to caspase-1 activity detection in the future.

6.4.2 Specific substrate design for caspase-1 activity

In comparison to the serine proteases trypsin and endoproteinase Glu-C described before, detecting caspase-1 activity poses some additional difficulties. From a practical viewpoint, caspase-1 is a far more expensive and less accessible enzyme. This implies that standard RP-HPLC experiments for checking the activity of the protease on a specific substrate are difficult, because they require large amounts of peptide substrate and protease. But most importantly, caspase-1 is a cysteine proteases. Its activation hence requires a reductive environment, which may at the same time reduce the gold-sulfur bond that links the peptide to the SERS structure. These complications explain our struggle with finding a good substrate for gold-bound caspase-1 cleavage, as explained below (summarized in table 6.1)

P.1 : YVADGFC
Caspase-1 cleaves at the carboxyl-terminal of aspartic acid, with ideally YVAD- or WEHD- in P_4-P_1 positions. Hence, a straightforward peptide substrate is YVADGFC (figure 6.10), including the aromatics Y and F before and after the cleavage site, as well as a C-terminal cysteine for gold binding through its thiol side chain[6]. The reducing environment required for the activation of caspase-1 is typically achieved by adding a milimolar concentration of dithiothreitol (DTT). Unfortunately, a 1-5 mM DTT concentration quickly reduced the gold-thiol bond, resulting in a fast detachment of YVADGFC from the gold surface. This release is visible from a strong decrease in the overall intensity of the SERS spectra in figure 6.11.

There are two possible solutions to this problem. The first solution is to change the binding chemistry to a different, non sulfur-gold, interaction [53]. Charge-based interactions such as the adsorption of a free amino-group are a poor alternative. They are much weaker than the covalent gold-sulfur bond [35] and will therefore be very sensitive to ligand exchange. A better option could be the introduction of a free carboxyl or amine group on the surface using for example (3-aminopropyl)triethoxysilane (APTES) [54]. Because these reactions require free oxide groups, a thin shell of dielectric is needed on top of the gold layer. These kind of shells have been used earlier for stabilizing nanoparticles [55]. In principle, it is feasible to deposit a nm-thick shell of SiO_2 using plasma-enhanced

---

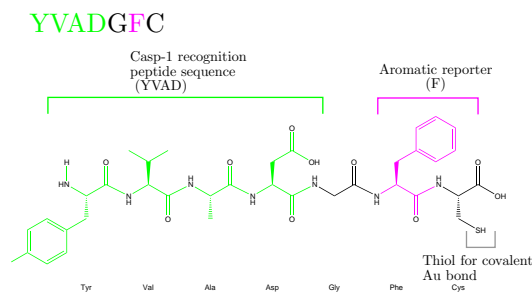[6]In retrospect, there are multiple issues with this peptide design, see table 6.1

Figure 6.10 Chemical structure of the YVADGFC peptide, which binds on a gold surface through the thiol group of a C-terminal cysteine. This configuration offers little protection against reduction of the Au-cysteine bond: their is no additional charge-based adsorption through a free amino-group, neither is there a hydrophobic SAM layer protecting the S-Au bond from the reductive environment.
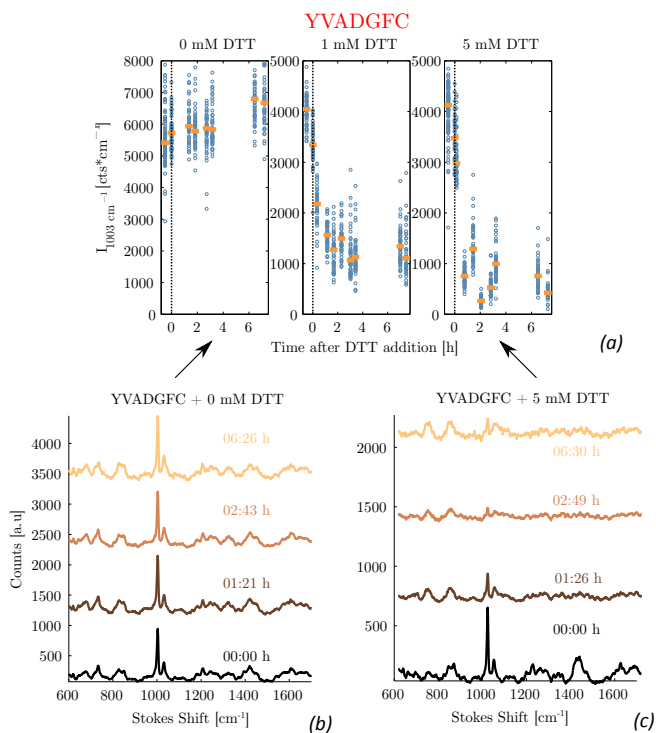

Figure 6.11 Effect of the reducing agent dithiothreitol (DTT) on a gold-bound layer of YVADGFC. (a) The fast decrease of the peak intensity at 1003 cm^{-1} (F) for 1 and 5 mM of DTT is a consequence of a detachment of the YVADGFC peptides due to reduction of the Au-S bond. (b) When no DTT is present, SERS spectra are stable over at least 6 hours. (c) 5 mM DTT leads to a strong decrease of the SERS signal within the first hour.

chemical vapor deposition (PECVD) or atomic layer deposition (ALD). Because this additional material will also influence the plasmonic resonance and size of the

gap, this would require a re-optimization of the fabrication process. Furthermore this chemistry is experimentally far more complex than the straightforward gold-sulfur bond. For these reasons we decided to stick with the gold-sulfur interaction. Nevertheless, alternative chemistries could provide a superior resistance to reductive environments.

The second solution is to protect the gold-sulfur interface through the formation of a self-assembled monolayer (SAM) [56]. We discuss two peptide substrates that include such a protective layer

P.2 : $\mathbf{YVADGF - PEG_4 - undecanethiol}$ *(YVADGFpAt)*

The long alkanethiol chain in the substrate presented in figure 6.12 forms highly stable SAM's, according to a principle similar to that in the CALNN- peptides used before. The sulfur forms a semi-covalent bond with the gold surface, and the hydrophobic C_{11} chains align with each other to minimize surface energy. As such, they form a densely packed monolayer with a grafting density of up to 5.7 molecules per nm^2 [57, 58]. Next, the polar polyethylene glycol (PEG$_4$) chain ensures a good wetting of the surface from which the sequence of amino-acids starts. Furthermore, the PEG layer inhibits non-specific binding of proteins [59]. This will be of importance in the complex environment of cells or biofluids. In short, a stable hydrophobic shell is formed that should prevent the reductive environment, i.e. the DTT molecules, from reaching the gold surface. SERS spectra acquired under 1-5 mM DTT concentrations for up to 7 hours (figure 6.13) show that a gold-nanodome bound layer of YVADGFpAt molecules is indeed significantly more stable than the YVADGFC monolayers in figure 6.11. Figure 6.14 compares SERS spectra acquired after 16 hours of incubation with different DTT concentrations in more detail, showing very little influence of the 1 mM concentration. These long incubation times are excessive, the relevant time-scale for monitoring caspase activity in a cell environment is within tens of minutes [4]. From this data, we conclude that the PEG-alkanethiol SAM layer provides sufficient protection against a reduction of the gold-sulfur bond.

However, we have not been able to observe the cleavage of this YVADGFpAt molecule through its SERS spectrum. Most likely, the short distance between the cleavage site at the C-terminal of aspartic acid the inert PEG-layer sterically hinders the caspase-1 activity. Neither could we test its activity on this substrate in solution, RP-HPLC requires a too large amount of the peptide and there is no built-in label for a colorimetric or fluorescent assay.

P.3 : $\mathbf{Meraptohexanoic\,acid.F.\gamma Aminobutyric\,acid.YVAD - amc}$ *(mFγYVAD.amc)*

Figure 6.15 shows the full chemical structure of this substrate. YVAD-amc is a commercially available reference substrate for monitoring caspase-1 activity in a fluorescence assay. The quenched aminomethyl coumarin (amc[7]) group becomes fluorescent ($\lambda_{ex} = 340 - 360\,nm$, $\lambda_{em} = 440 - 460\,nm$) upon hy-

---

[7]Lower case to avoid confusion with the amino acid notation

drolysis (see methods, figure 6.30 on page 6-46). To ensure a good activity of caspase-1 on a gold-bound peptide substrate, we use this exact sequence and couple it to a thiol-based SAM. The synthesis of -amc functionalized peptides is relatively easy: the amine-group of amc can be coupled to the carboxyl side-chain of aspartic acid. A $SH(CH_2))_5CO.F.NH_2(CH_2)_3COO^-$ tail is coupled to this $-YVAD.amc$ sequence. This tail is a compromise between ease of fabrication and monolayer stability. It can be added during on-bead synthesis in three steps using only commercially available products, first coupling gamma-aminobutyric acid (γ aba, $NH_2(CH_2)_3CO$) as a flexible spacer molecule which increases the distance between the cleavage site and the gold surface. Second, the aromatic amino acid F is added, this time as a SERS reporter on the gold-side of the cleavage site. Finally 6-mercaptohexanoic acid ($SH(CH_2))_5CO$) is coupled to fulfill a similar role to the 11-alkanethiol chain discussed above. Despite the shorter alkane-chain and lack of a PEG-layer, we still observe a reasonable resistivity of the gold bond to a 1 mM DTT concentration (figure 6.16). However, not unexpected, the stability of this substrate layer is less stable than a PEG-alkanethiol SAM, especially under higher DTT concentrations (figure 6.16c).
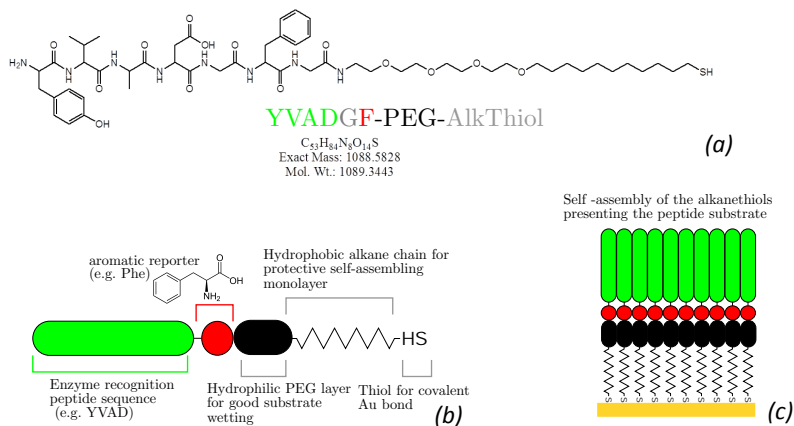
Figure 6.12 (a-b)Chemical structure of the YVADGFpAt substrate for caspase-1 activity. (c) The hydrophobic alkanethiol chains in the YVADGFpAt molecules form a densely-packed self assembling monolayer, thereby creating a hydrophobic shell which protects the Au-S bond from reduction.
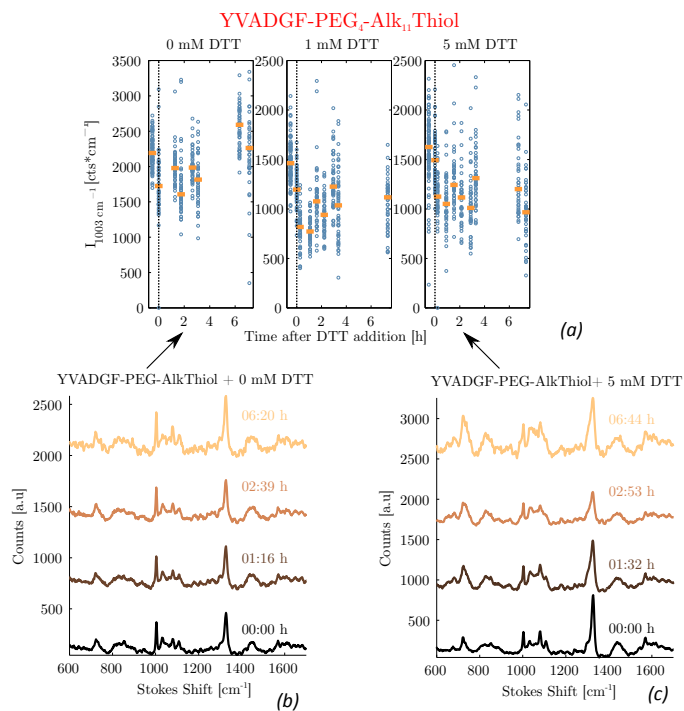
Figure 6.13 DTT has a limited influence on a YVADGFpAt monolayer on a gold nanodome SERS surface. (a) Integrated intensity of the 1003 cm^{-1} Phe peak for different DTT concentrations. (b) SERS spectra after 0 to 6 hours without DTT (c) SERS spectra after 0 to 6 hours with a 5 mM DTT concentration. (The spectra in this experiment suffer from a contamination of the nanodome chips with, most likely, pNTP. The experiment was repeated in figure 6.14)
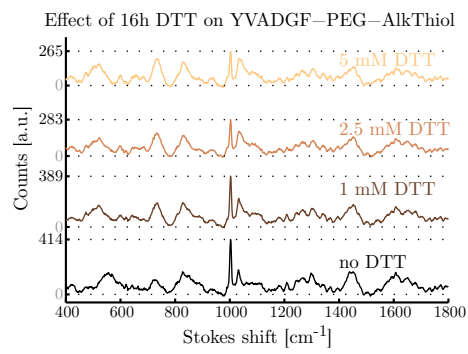
Figure 6.14 Effect of 16 hours incubation with different concentrations of DTT on the SERS spectrum of a YVADGFpAt self-assembled monolayer on a nanodome surface.
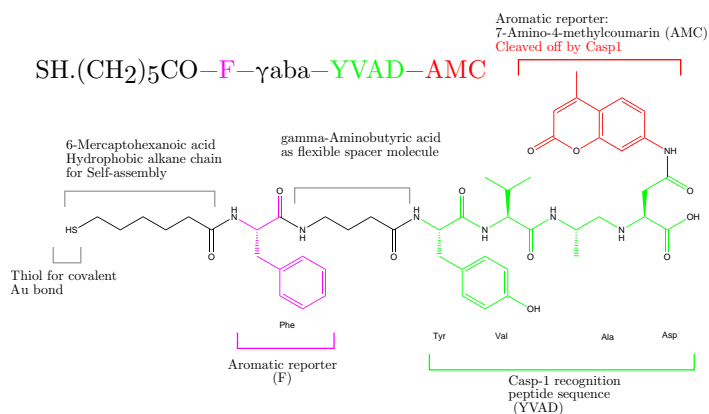
Figure 6.15 Chemical structure of the mFγYVAD.amc synthetic peptide used for caspase 1 digestion. Similar to the alkanethiol chain, the peptide has a hydrophobic tail for protecting the gold-thiol bond against reduction. This peptide can be entirely fabricated using on-bead synthesis.
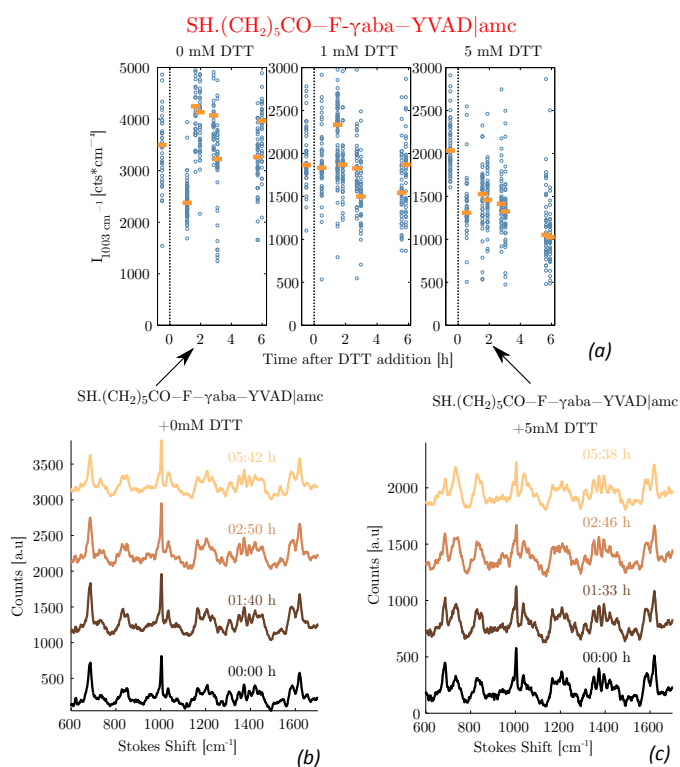
Figure 6.16 The mFγYVAD.amc monolayer on a gold nanodome SERS substrate looks reasonably stable under a 1 mM DTT concentration. (a) Integrated intensity of the 1003 cm^{-1} Phe peak for different DTT concentrations. (b) SERS spectra after 0 to 6 hours without DTT (c) SERS spectra after 0 to 6 hours with a 5 mM DTT concentration.

6.4.3 In-solution caspase-1 activity on mFγYVAD.amc

The activity of caspase-1 on different substrates is measured in solution through the fluorescence of a cleaved-off -amc group. Ac-YVAD-amc is used as a commercially available positive control. From the linear increase in fluorescence with time in the first hour (figure 6.17a), we determine a cleavage rate of 0.53 ± 0.1 $pmol/(min \cdot \mu g_{cas-1})$ on Ac-YVAD-amc and 0.28 ± 0.05 pmol/$(\min \cdot \mu g)$ on mFγYVAD.amc (figure 6.17b). Hence the decrease in activity due to the hydrophobic tail is limited. Interestingly, lowering the DTT concentration from 5 mM to 1 mM during caspase-1 activation has only a small effect on the cleavage rate, which is still at 0.24 ± 0.015 pmol/$(\min \cdot \mu g)$ for the mFγYVAD.amc substrate. Note that the actual concentration of DTT in the assay is lower than this 1 mM value, because it is partially consumed by the activation of caspase-1. Given that mFγYVAD.amc is well cleaved by caspase-1 in a 1 mM DTT environment and the gold-sulfur bond is reasonably stable over one hour under this conditions (figure 6.16), it is a viable candidate for gold-bound caspase-1 hydrolysis.

(a) **(b)**
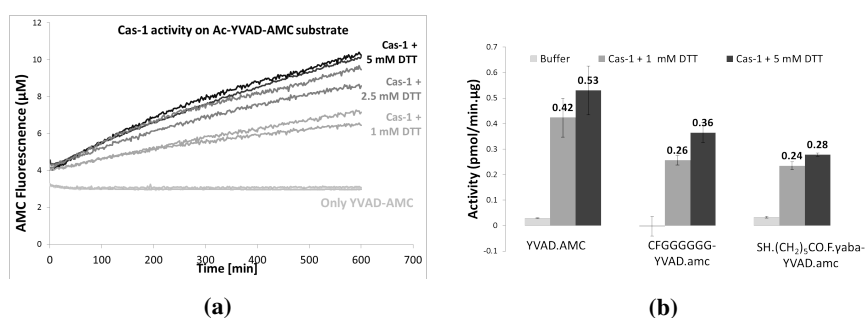
Figure 6.17 Activity of caspase-1 for different DTT concentrations on various substrates quantified in a bulk fluorescent assay. (a) Increase of fluorescence marks hydrolysis through the release of a -AMC fraction. (b) Activity calculated from the linear slope at the start of the reaction.

We take a closer look at three different characteristics of the mFγYVAD.amc: (1) The origin of its SERS and Raman spectrum, (2) the kinetics of in-solution caspase-1 mediated hydrolysis of this substrate and (3) the estimated number of molecules bound to a chip[8].

Raman and SERS spectra of mFγYVAD.amc Ideally, the difference spectrum between cleaved and uncleaved mFγYVAD.amc would be determined from an in-solution assay followed by on-chip labeling, such as done for the trypsin and endoproteinase Glu-C substrates in section 6.3.1. However, the presence of DTT complicates this experiments because it hinders the formation of Au-S bonds. We could not find suitable concentrations for enzyme, DTT and substrate that would allow the formation of a monolayer layer of fully digested mFγYVAD peptide

---

[8]Be aware that the values reported may vary significantly (a factor 2 is reasonable) with experimental conditions, such as the age of the caspase-1 and exact weight of the enzyme and protease.

products. Neither did we have any success using the serine protease granzyme B, which is known to cleave many caspase substrates [11], as an alternative enzyme. Therefore, we have to rely on the SERS and Raman spectra in figure 6.18 and the corresponding peak attribution in table 6.4 for determining the -amc peaks that should decrease upon peptide digestion. From this data, we find that for example I_{1619}/I_{1003} and I_{1372}/I_{1003} can provide a metric for caspase-1 activity on surface-bound peptides.

Table 6.4: Peak assignment for the mFγYVAD.amc peptide for caspase-1 digestion. amc-Peaks are attributed from a measured Raman spectrum of pure -amc (figure A.2) and different -amc conjugated peptides (figure A.19). Peaks marked with amc* are only present in bound -amc. A decrease of SERS peaks marked are used for detecting caspase-1 cleavage.

Raman (cm^{-1})	SERS (cm^{-1})	Origin	Raman	SERS	Origin
441	443	amc	1168	1166	amc
524	525	amc	1202	1206	F [29, 39]
580	582	amc	1226	1230	amc
621	621	F [29]	1310	1310	amc*
644	643	Y [29]	1348	1349	amc*
687	687	amc	**1370**	**1372**	amc
827	831	Y [29, 39]	1392	1395	amc
853	848	Y [29, 39]	1581	1585	amc*
1003	1003	F [29, 39]	**1620**	**1619**	amc
1033	1034	F [29, 39]			
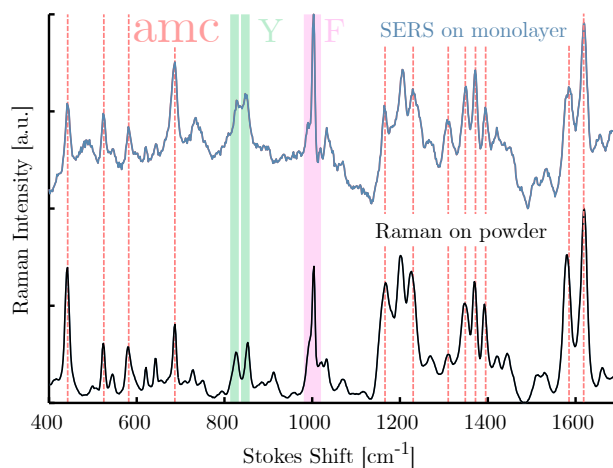
Figure 6.18 Normal Raman and SERS spectra of the mFγYVAD.amc peptide, a specific substrate for caspase-1. We use amc as a SERS label for monitoring cleavage through the peaks marked with a dashed red line.

Kinetics of caspase-1 mediated mFγYVAD.amc hydrolysis   The kinetics of a single-substrate reaction follows the well known Michaelis-Menten equation, linking the initial reaction rate v_0 to the substrate concentration $[S]$, the Michaelis

constant of a specific substrate-enzyme mechanism K_m and the maximum enzyme turnover rate v_{max}:

$$v_0 = \frac{v_{max}[S]}{K_m + [S]} \tag{6.1}$$

From the linear increase of fluorescence with time, we can calculate v_0 for different substrate concentrations. Next, the characteristic values K_m and v_{max} can be retrieved from a Lineweaver-Burk plot:

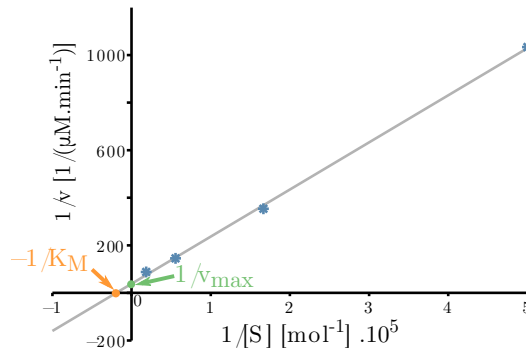$$\frac{1}{v_0} = \frac{K_m}{v_{max} \cdot [S]} + \frac{1}{v_{max}} \tag{6.2}$$

Figure 6.19 Lineweaver-Burk plot for the mFγYVAD.amc substrate. From this data, we find $K_m = 52\,\mu\text{M}$ and $v_{max} = 0.73\,\text{pmol}/(\text{min} \cdot \mu\text{g})$

Figure 6.19 shows equation 6.2 for a caspase-1 concentration of 36 µg/ml in a 50 µl assay buffer (see methods) supplemented with 10 mM DTT. We find a K_m of 52 µM and v_{max} of $0.73\,\text{pmol}/(\text{min} \cdot \mu\text{g})$.

mFγYVAD.amc grafting density on gold nanodomes   We use enzyme kinetics from equation (6.2) to estimate the number of bound *(mFγYVAD.amc)* molecules on an 8 mm^2 nanodome chip. After overnight labeling, a functionalized chip is incubated in an excessive DTT concentration to release the peptides from the gold surface. From the SERS spectra shown in figure 6.20a, we see that the signal of *F* and *amc* (table 6.4) is almost completely gone after 7 hours of incubation in 20 mM DTT. Next, the supernatant of this chip is used in a fluorescent assay with identical conditions to those used for determining K_m and v_{max} (figure 6.20b). From the initial reaction rate v_0 of 0.007 $\text{pmol}/(\text{min}.\mu\text{g})$, we find a substrate concentration $[S_{chip}]$ of 0.48 µM, corresponding to a total amount of 24 pmol of previously bound substrate molecules on the chip.

$$[S] = \frac{v_0 K_m}{v_{max} - v_0} \tag{6.3}$$

The total surface area of the nanodome-patterned chip equals $8 \times 1.6 = 12.8 \, mm^2$. The factor 1.6 is the ratio of the surface area of the patterned geometry over the projected area, see chapter 3.4.1. Thus we find a grafting density of approximately 2 molecules per nm^2. It is likely that this experiment underestimates the substrate concentration, a number of peptides may have degraded or clustered over the 7 hours incubation time, and some of them will have remained on the chip surface, as indicated by the remaining SERS signal in figure 6.20a. Nevertheless, a labeling density of $2/nm^2$ is in reasonable agreement with other experimental values reported in literature. Duchesne et al. report a grafting density of $2.4/nm^2$ for a monolayer of the pentapeptide CALNN. Caldwell et al. [60] report a nearest neighboring distance of $0.45 \, nm$ for azobenzene-undecanethiol layers on gold, corresponding to a grafting density of $5.7/nm^2$. Their higher value is expected because alkanethiol-chains with a long methyl-chain, such as the undecanethiol used here, are known to form a tightly hexagonally packed layer. Therefore they are better resistant to DTT-induced reduction of the gold-sulfur bond, as we also reported in figure 6.14. From this experiment we conclude that the *(mFγYVAD.amc)* forms a close-to-monolayer coverage on the nanodome surface.
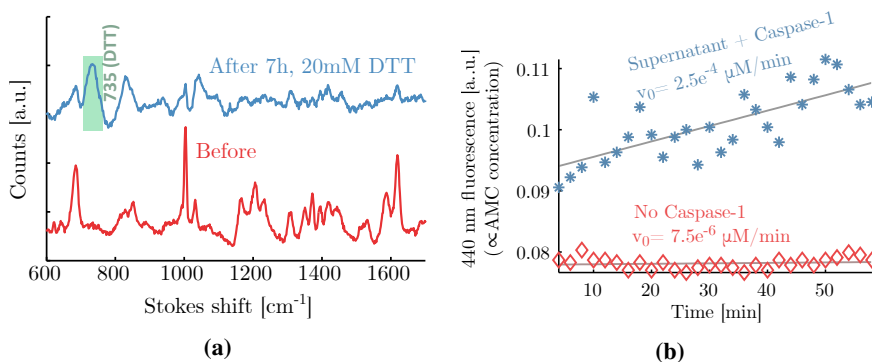
Figure 6.20 A grafting density of $2/nm^2$ is estimated from a fluorescent assay on the supernatant of a DTT-released monolayer of mFγYVAD.amc. (a) SERS spectra before and after incubating a 8 mm^2 chip in 20 mM DTT for 7 hours. The mFγYVAD.amc signal has largely disappeared while DTT-related peaks appear. (b) Fluorescence assay on supernatant of the chip, resulting in a v_0 of $2.5 \cdot 10^{-4} \, \mu M/min$, corresponds to a concentration of $0.007 \, pmol/(min \cdot \mu g)$.

6.4.4   On-chip caspase-1 activity, an unsolved mystery?

Our results on caspase-1 activity on nanodome-bound mFγYVAD.amc substrate are to some degree contradictory and to date not fully understood. Figures 6.21 and 6.22 summarize the effect of four different incubation conditions on the SERS spectrum of a gold nanodome-bound mFγYVAD.amc substrate: the addition of (a) 1 mM DTT, (b) caspase-1 activated in 1 mM DTT (c) a mutant, non functional caspase-1 in 1 mM DTT and (d) caspase-1 activated in 1 mM DTT but blocked by a YVAD-cmk inhibitor.

The evolution of SERS spectra with time under different conditions is shown in figure 6.21. All these spectra scaled for equal intensity of the 1003 cm^{-1} Phe peak, which for this substrate provides a selective signal from the product remaining on the gold surface after caspase-1 hydrolysis. Peptide cleavage should result in a decrease of the peaks originating from -amc, such as those at 442, 1372 and 1619 cm^{-1}, as listed in table 6.4. Hence I_{442}/I_{1003}, I_{1372}/I_{1003} and I_{1619}/I_{1003} are metrics for selective cleavage. These ratios are plotted versus incubation time in figure 6.22. When solely adding 1 mM DTT (figures 6.21(a) and dashed lines in 6.22(a)) the SERS intensity gradually decreases, but we observe no significant difference in amc/Phe peak strength. The most prominent changes at 504 cm^{-1} and 735 cm^{-1} originate from DTT [61], indicating adsorption of this molecule on the gold surface. Most probably, the changes at 1033 cm^{-1} and 830 cm^{-1} are also DTT-related, as these were also observed at high DTT concentrations with the mFγYVAD.amc and YVADGF-PEG-AlkThiol substrates, see respectively figures 6.20a and 6.14. The addition of activated caspase-1 in an excess concentration of 300 μg/ml, pre-activated in a 1 mM DTT buffer repeatedly resulted in a decrease of I_{1372}/I_{1003} and I_{1619}/I_{1003} (figure 6.21(a) and solid lines in figure 6.22 (a,b,d)). These changes happen within the first tens of minutes after adding the protease, indicating an immediate partial digestion of the surface-bound substrate. Similar to our observations with on-chip trypsin digestion, I_{amc}/I_F drops to roughly 50 % of the original value. Again, the remaining signal is most probably due to inaccessible peptides. Note that a molecular weight of 45 kDa, caspase-1 is even bigger than the 23.3 kDa heavy trypsin.

Remarkably, a similar trend was observed when adding an inactivated mutant caspase-1 (300 μg/ml) (figures 6.21(c) and 6.22 (b,c)) . While, as expected, the mutant caspase did not show any activity in a fluorescent assay on the same substrate in solution. We get a similar results when using the normal caspase-1 with a YVAD-cmk (20 μM) inhibitor. After pre-incubating the caspase with this inhibitor for 30 minutes, there was no activity observed in a fluorescent assay in solution. However, we saw the same trend in the SERS spectra when adding caspase-1 with and without inhibitor (figures 6.21(d) and 6.22 (d)). We have no satisfying explanation for this behavior. Following causes are unlikely:

1. The buffer in which the caspase-1 is dissolved, containing 20 mM Tris-HCL (pH 7.5), 10 % glycerol, 0.3 M NaCl, 1 mM glutathion, 0.25 M imidazole and a protease-inhibitor cocktail tablet (Roche) in a 20 ml volume: no changes were observed when adding this buffer.

2. A remaining activity of a low number of caspase-1 molecules: the SERS assay was not sensitive to a low caspase-1 concentration

Further research is needed to understand this behavior. A number of plausible causes are:

1. Cleavage by other proteases coming through the caspase-1 purification process. When the peptide sequence is cleaved at a different position for the

carboxyl-terminal of *D*, the -amc group will remain quenched. This can be tested by denaturing all possible peptides by boiling the solution.

2. Non-specific adsorption of proteases on the peptide-labeled gold surface. This can lead to a conformational change of the peptide substrate, which may result in spectral changes. This can be partially tested by checking the influence of other proteins, for example bovine serum albumin or dextran.
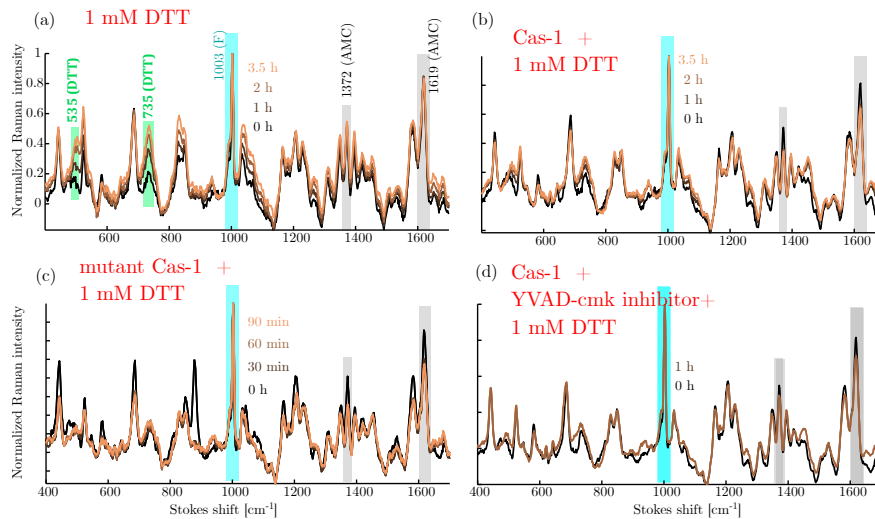
Figure 6.21 Influence of caspase-1 and 1 mM DTT on the SERS spectra of a nanodome-bound mFγYVAD.amc. All spectra are normalized to the $1003\,\mathrm{cm}^{-1}$ F peak, blue shaded.
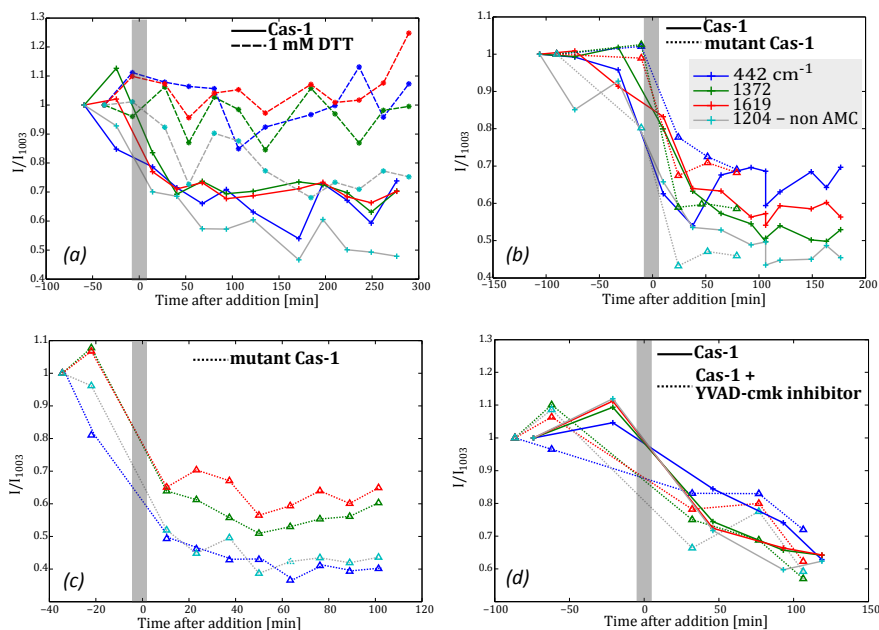
Figure 6.22 Change of the relative intensity of peaks related to I_{amc}/I_F shown in figure 6.21 under different conditions, all using the gold-nanodome bound mFγYVAD.amc substrate in a buffer solution supplemented with 1 mM DTT.

6.4.5   Perspectives for single-cell sensing

Obviously a large number of challenges have to be tackled to evolve from the currently ambiguous caspase-1 activity detection to a single-cell activity measurement. Nevertheless, it is interesting to outline our strategy towards this end. In contrast to the experiments on intracellular label-free SERS probes described in chapter 5, we plan to monitor inflammasome activity in the close vicinity of a single cell rather than inside it for two reasons. First, one of the major problems in using microparticles for intracellular sensing is the intracellular trafficking pathway of these particles. One can expect that these particles are taken up via phagocytic pathways hampering them to contact and hence sense relevant biochemical processes, which take place in the cytosol. Hence these particles should be either released from the phagocytic compartments, for example using photodynamic treatment or a laser-induced release from capsules [62], or introduced directly into the cytosol via poration techniques such as electro or sonoporation or via micro-injection. Although not impossible, this remains difficult with microparticles. Second, the introduction of exotic nano- or microparticles would drastically complicates working with physiologically relevant samples or in-vivo mouse models.
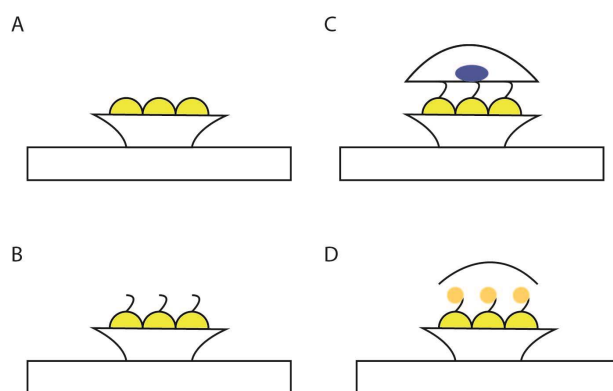
Figure 6.23 (a) Sensor consisting of a gold-nanodome patterned silicon chip b) the sensors are functionalized with proteins that are substrates for specific enzymatic reactions c) cells can be grown on top of the sensors, d) upon a specific stimulus the cell releases its content (pyroptosis) and specific enzymatic activity can be measured on a single cell level.

Protease activity in the vicinity of a single cell is especially relevant when investigating pathological processes related to inflammation. Caspase-1 activation leads to pyroptosis, a specific inflammatory form of programmed cell death that occurs most frequently upon infection with intracellular pathogens. As depicted in figure 6.23, individual cells will be grown on a gold-nanodome patterned chip which is functionalized with a specific peptide substrate. After the inflammatory trigger, pyroptosis makes the cell release its contents and the activated proteases

such as caspase-1 will act on the nearby peptide substrate. More specifically, the endogenous levels of caspase-1 expressed by immune cells will be activated using well-established inflammasome triggers. Lipopolysaccharide (LPS) and nigericin-stimulation will be used to activate caspase-1 through the NLRP3 inflammasome. Anthrax lethal toxin activates the NLRP1b inflammasome and intracellular flag-ellin will stimulate caspase-1 activation by the NLRC4 inflammasome (figure 6.9). Consequent to caspase-1 activation, these stimuli lead to inflammasome-induced cell membrane permeabilization and the secretion of enzymatically active caspase-1 in the extracellular environment [52]. Along with caspase-1, pyroptotic cells secrete a multitude of other enzymes, including active caspase-3/7, 8 and 11 [63–65]. SERS holds the potential for monitoring the activity of these related proteases in a multiplexed fashion using selective substrates for each caspase (DEVD for caspase-3/7, IETD for caspase-8 and WEHD for caspase-11).
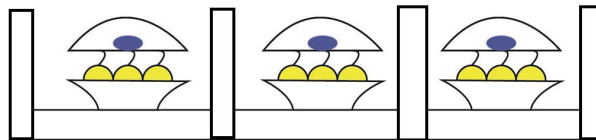
Figure 6.24 Chip with multiple SERS-wells for single-cell monitoring. The walls should limit diffusion in between single cells. The size of a well should be roughly 20x20x20 μm^3
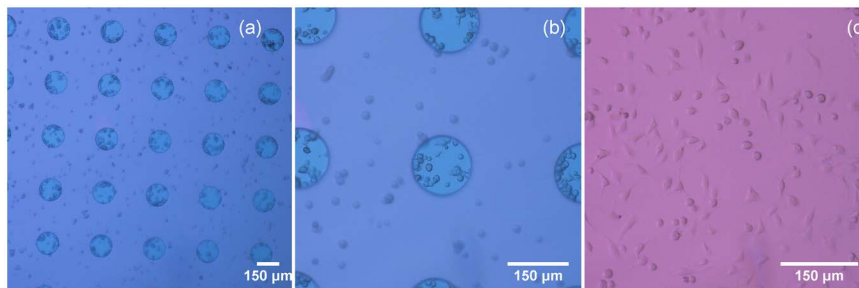
Figure 6.25 Pattern of *SU-8 50* wells with a 150 μm diameter and 40, μm height are a first attempt towards a single cell substrate. (a-b) SiN chip patterned with SU-8 wells, seeded with macrophage cells. (c) Nanodome substrate with the same cell type, indicating a good adherence of the cells on the nanopatterned substrate.

When monitoring the release of activated proteases from single cells, diffusion between different cells has to be limited such that the measurement on one cell is not influenced by its neighbors (figure 6.24). Single-cell culture is possible in microwells [66], where the walls in between different wells serve to prevent cell migration and diffusion of molecules between wells. Because the existing approaches for single-cell cultures are not compatible with the nanodome-coated chips, we created a custom microwell pattern on the nanodome-coated substrates using UV contact lithography. As depicted in figure 6.25(a,b), 40 μm high wells

were patterned in a UV-cured SU-8 polymer as a first attempt towards a single-cell platform. In preliminary experiments, we found a good adhesion of macrophage cells (differentiated from the bone marrow of mice) to the gold nanodome surface (figure 6.25c).

We make a back-of-the-envelope calculation to estimate the effect of inter-cellular protease diffusion on the measurement. Consider two wells, separated by 200 µm and each containing a single cell. The minimum volume occupied by a caspase-1 molecule with a molecular weight M_w of 45 g/mol is calculated from the specific density of proteins ρ_s (1.37 g/cm³) and Avogadro's number N_A:

$$V = \frac{M_w}{\rho_s N_A} = 54 \, \text{nm}^3 \tag{6.4}$$

Hence the minimal radius R_{min} of caspase-1 is 2.35 nm, under the assumption that it would be a perfectly spherical molecule. The Stokes radius R_s, which is the radius of a sphere with equal diffusion speed as the molecule, is about 1.2-1.3 times larger than R_{min} for most globular proteins [42]:

$$R_s = 1.3 \left(\frac{3V}{4\pi} \right)^{1/3} = 3.1 \, \text{nm} \tag{6.5}$$

The diffusion length L_D of a molecule in a given time t can be calculated from its diffusion coefficient D:

$$L_d = \sqrt{Dt} \tag{6.6}$$

This diffusion coefficient depends on R_s, the temperature T (300 K) and the viscosity of the medium ν at that temperature, which is $7.0 \cdot 10^{-4}$ Pa.s for water at 300 K.

$$D = \frac{kT}{6\pi\nu R_s} = 1.03 \cdot 10^{-6} \, \text{cm}^2\text{s}^{-1} \tag{6.7}$$

From equations 6.6 and 6.7, we find that the diffusion time for a caspase-1 molecule from one cell to another over a distance of 200 μm is approximately 400 seconds. Assuming a cell volume of roughly 2000 μm³, this distance also implies that the intracellular protease concentration has decreased by a factor $8 \cdot 10^3$. From these numbers, we conclude that a microwell array with a 200 μm period is largely sufficient for single-cell monitoring. In contrast, it would take less than one second for the protease to diffuse over a few micron from the cell to the nearby nanodome surface after pyroptosis.

6.5   Towards a lab-on-chip platform for protease activity

The concept of on-chip integrated single-cell sensing offers a number of distinct advantages. Most importantly, the heterogeneous behavior of cells stresses the need for simultaneously monitoring a high number of single cells, thereby linking single-cell behavior to population-averaged measurements. Single-cells on a platform such as described in figure 6.24 still require a confocal Raman microscope for a time-sequential readout. Therefore only a limited number of cells can be monitored in one experiment. An integrated photonics platform provides opportunities for a waveguide-based parallel readout of multiple cells. Furthermore an integrated silicon photonic platform allows for implementing various functions of traditional optical components on a single photonics chip, as described in chapter 4. This way bulky analysis methods can be miniaturized in a lab-on-chip fashion, thereby reducing both the size and cost of the required infrastructure, enabling point-of-care diagnosis. Finally, an integrated chip can be combined with microfluidics, which can greatly reduce sample consumption and can lead to single-cell treatment as well as single-cell analysis. Many of these advantages are also valuable for other applications of protease activity such as drug development.

In chapter 4.3 we discussed the integration of different kinds of plasmonic antennas on SiN waveguides. The experimental data on both e-beamed bowties and NSL-fabricated nanotriangles confirmed that the excitation and collection of SERS spectra through waveguides is at least as efficient compared to a microscope with a high NA objective. Thus it should be possible to transfer the results of gold-bound trypsin digestion to a waveguide platform. However, a significant improvement of the on-chip SNR is required. With a measured SERS substrate enhancement factor (SSEF) of $2.5 \cdot 10^5$, the weakly coupled nanotriangles have a much lower SERS signal as compared to the gold nanodomes (figure 4.14 on page 4-18). In addition, the background originating from the SiN waveguide further decreases the SNR.

In a proof-of-concept experiment, we measure the signal of a **C**F**GVR-pNA** peptide substrate on a gold nanotriangle-patterned waveguide. Compared to CALNN**Y**-GGGGVRGN**F** used in section 6.3.2 , this peptide provides a stronger SERS signal because of the shorter distance of Phe and pNA to the gold surface and the increased Raman cross section of pNA versus Tyr (see table 2.2 on page 2-12). As shown in figure 6.26a, the most prominent peaks of the CFGVR-pNA are just detectable in the waveguide excited- and collected SERS spectrum with a 100 s integration time. In contrast, this spectrum can be nicely resolved in a gold-nanodome, free space, SERS measurement.

The raw waveguide-collected SERS spectrum 6.26b shows that the SERS peaks are superimposed on the broad SiN and SERS background, which is modulated with a periodic ripple. This ripple most likely originates from modal interference
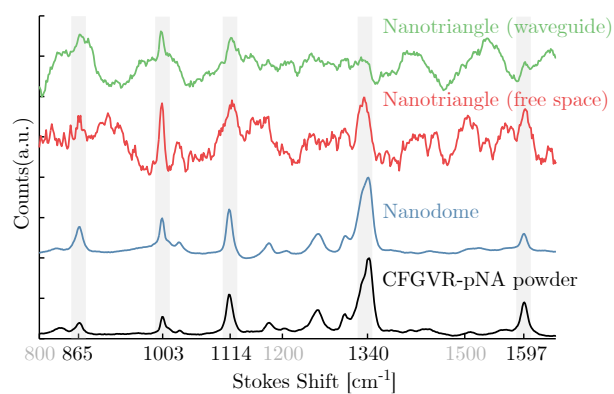
(a)
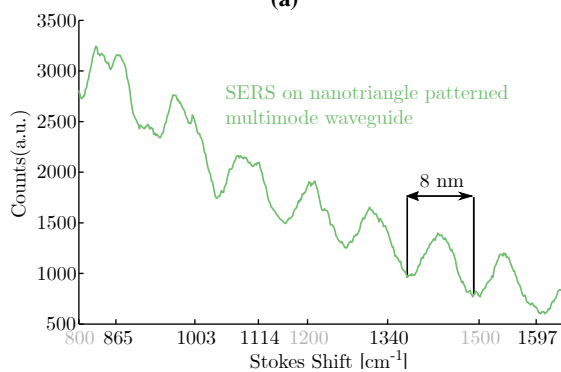
(b)

Figure 6.26 (a) Raman (black) and SERS spectra of the CFGVR-pNA peptide. The most prominent Raman bands, shaded in gray, are just detectable on waveguide-excited nanotriangles. Spectra are background subtracted, normalized and cascaded. The waveguide-excited spectrum represents the average over three different waveguides. (b) Raw SERS spectrum collect through a CFGVR-pNA labeled, gold nanotriangle functionalized SiN multimode waveguide with a 2.4 μm by 220 nm cross section.

between the region where the SERS signal is generated and the output facet of the waveguide. Consider two modes in a waveguide with length L, one propagating with effective index n_1^{eff} and one with $n_2^{eff} = n_1^{eff} + \delta n$. Destructive interference occurs if the optical path length difference between both modes equals:

$$\frac{2\pi \delta n L}{\lambda_s} = m\pi \qquad |m \in \mathbb{N}^+ \tag{6.8}$$

The next minimum occurs at and $\lambda_s + \delta\lambda$, destructive interference again implies:

$$\frac{2\pi \delta n L}{\lambda_s + \delta\lambda} = (m-2)\pi \tag{6.9}$$

Dividing (6.8) by (6.9), we find:

$$\frac{m}{m-2} = \frac{\lambda_s}{\lambda_s + \delta\lambda} \tag{6.10}$$

$$m = 2\left[1 - \frac{\lambda_s}{\lambda_s + \delta\lambda}\right]^{-1} \tag{6.11}$$

Combining (6.11) and (6.8) yields:

$$\delta n = \frac{m\lambda_s}{2L} \tag{6.12}$$

$$= \frac{\lambda_s^2 + \lambda_s\delta\lambda}{L\delta\lambda} \tag{6.13}$$

For a 1.2 μm wide and 220 nm high waveguide with a distance L of 1700 μm between the input facet and the nanotriangle stretch, the measured period of the ripple is 3.5 ± 0.5 nm at a Stokes wavelength of 910-930 nm. This corresponds to a δn of 0.145 ± 0.021. From a mode simulation, we indeed find two guided TE modes in this SiN waveguide ($n_{SiN} = 1.9$) on a SiO substrate ($n_{SiO=1.45}$) at 915 nm, with $n_1^{eff} = 1.570$ and $n_2^{eff} = 1.451$, corresponding to a δn of 0.119. The waveguides used for measuring the CFGVR-pNA spectrum in figure 6.26a are $2.2\,\mu m$ wide. Here, the period of the ripple is 8 ± 1 nm. The length L between the cleaved facet and the nanotriangle section is 1360 μm, thus from (6.13) the measured δn equals 0.078 ± 0.005. In this wider waveguide, there are three TE modes at 915 nm, with $n_1^{eff} = 1.599$, $n_2^{eff} = 1.568$, $n_3^{eff} = 1.514$. Figure 6.27 shows the field profiles of these modes. The periodicity of the ripple suggests a strong interference between mode 1 and mode 3, with a simulated δn of 0.085. In general, we observed that the ripple is stronger for waveguides in which a third mode exists.

The detection of peptide spectra through the waveguide is promising for future research. As compared to nanodomes, the nanotriangles are expected to offer an improved substrate accessibility for the enzymes, while minimizing the amount gold-bound peptide on positions that don't contribute to the SERS spectrum. Although the SNR of waveguide-collected SERS spectrum is very low in this experiment, it should be fairly easy to reduce the background signal. The ripple on
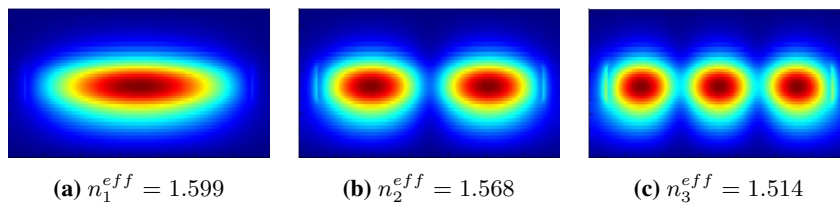
<div align="center">

(a) $n_1^{eff} = 1.599$ **(b)** $n_2^{eff} = 1.568$ **(c)** $n_3^{eff} = 1.514$

</div>

Figure 6.27 Three guided quasi-TE modes exist in the 2.4 μm by 220 nm SiN waveguide. (box size=2.8 μm by 1 μm)

the spectrum can be removed by reducing the waveguide dimensions to obtain a single TE-mode waveguide. The SiN background signal can be reduced by shortening the access waveguide or using integrated spectral filters around the SERS region. Also, a significant increase in signal to the level of the nanodome-surface is necessary. This is far from trivial, but we are currently exploring multiple ideas to improve the signal of the on-chip SERS platform.

6.6   Conclusion and perspectives

6.6.1   Conclusions

We successfully used SERS to monitor protease-catalyzed hydrolysis of a peptide made from just natural amino acids by using the Raman fingerprint of aromatic amino acids. By incorporating different aromatic amino acids on both sides of the protease cleavage-site, we obtain a ratiometric measurement for protease activity based on the relative intensity of different SERS bands. This method allows distinguishing protease activity from ligand-exchange, an issue that was often neglected in previously published assays. The peptide CALNNYGGGGVRGNF forms a stable monolayer of trypsin substrates on a gold-nanodome platform, whose plasmonic hotspots are accessible to proteases of 20-30 kDa. Real-time monitoring of trypsin activity on this gold-bound peptide shows immediate digestion within the first two minutes for a 8.6 nM concentration. We further demonstrate that an analogous peptide sequence CALNNYGGGGNNESWH provides a good substrate for endoproteinase Glu-C and identify the SERS spectra of both substrates and their products, thereby taking a first step towards a label-free multiplexed measurement of protease activity. We are working on a further quantification of the enzyme activity on gold-nanodome bound substrates for single and multiplexed protease activity. In summary, important advantages of the method presented in this chapter over existing techniques are the completely label-free measurements, the inherent control against ligand exchange and the use of a relatively easy and cheap nanosphere-lithography based SERS platform.

In principle, our detection method can be adapted towards a variety of different proteases. However, we observed difficulties with the stability of the peptide-gold chemistry when using serine proteases in a reductive environment. We showed

that self-assembling monolayers such as PEG-alkanethiol can be used to protect the gold-thiol bond, but have not yet unambiguously demonstrated a real-time, SERS-based measurement of capase-1 activity, the central protease involved in inflammasome activation.

Preliminary experiments show that the spectrum of a peptide monolayer can be detected using the nanotriangle-decorated SiN waveguides introduced in chapter 4.3, albeit with low signal-to-noise ratio. Provided that the latter can be drastically improved, this approach is promising for the future development of a miniature lab-on-a-chip for a multiplexed and parallelized detection of protease activity, for example in a single-cell context (see general perspectives, figure 7.2 on page 7-6).

The 8.6 nM concentration of trypsin used in this work is not among the lowest detectable protease concentrations reported. Although we have not yet fully studied the sensitivity of our assay, a detection limit in the pM range [23, 25] is unlikely in the current setup. Options to increase the sensitivity include reducing the substrate density using a matrix peptide [19] or selectively labeling the hotspots. Also, the assay presented in this work has not yet been tested in realistic in-vitro conditions, where non-specific cleavage or ligand exchange reductive environments may complicate the measurement. Possibly more stable monolayers using a double cysteine [32] or alkanethiol-PEG [56] chains will be required in these cases.

6.6.2 Challenges

We currently have insufficient understanding of a number of experimental observations. A better insight in the phenomena described below should allow for a further improvement of the SERS-based protease sensing.

A. Photodegradation of the SERS signal

We observed a degradation in the SERS signal of a peptide monolayer when exposing the same spot for a few minutes with an irradiance of approximately $0.4\,\mathrm{mW}\mu\mathrm{m}^{-2}$, as described in section 2.3.2 (figure 2.15 on page 2-29). We currently bypassed this problem by continuously moving the excitation laser over the nanodome surface. However, this induces an extra variability in the SERS signal. Furthermore, this trick is not possible when using a waveguide-based excitation and collection of the SERS signal. Currently, the SNR is too low to further reduce the irradiance.

B. Discrepancy in SERS intensity of peptides versus nitrothiophenol

The differential Raman cross sections of pNTP ($1.8 \times 10^{-29}\mathrm{cm}^2\mathrm{sr}^{-1}$ for the 1339 cm^{-1} peak, dissolved in ethanol) and, for example, CFGVR-**pNA** ($1.4 \times 10^{-29}\mathrm{cm}^2\mathrm{sr}^{-1}$ for the 1342 cm^{-1} peak, dissolved in DMSO) measured in liquid

are similar, as determined in chapter 2.1.3 (table 2.2 on 2-12). In contrast, the SERS signal of CFGVR-**pNA** on a nanodome or nanotriangle substrate is 10-100 times weaker. We identify three plausible explanations:

1. Change in cross section Raman cross sections were measured on dissolved molecules in a specific solvent. The differential cross section of specific modes can be different in a surface-bound monolayer. Possibly the signal of the peptide chain can be increased by changing the aromatic reporters to, for example, non natural aromatic amino-acids.

2. Grafting density The peptides could form a sub-monolayer coverage or, conversely, the pNTP molecules form a multilayer. This would lead to significantly different loading densities. However, the experiment described in figure 6.20b suggests a close-to-monolayer coverage. Also, the grafting densities reported in literature for similar molecules are within the same range: $5.7/\mathrm{nm}^2$ for azobenzene-undecanethiol layers on gold films [60], $2.4/\mathrm{nm}^2$ for CALNN [36] on Au NPs and $4.5/\mathrm{nm}^2$ for 4-aminobenzenthiol [67] on gold powder. Possibly the orientation of the molecules in this monolayer also plays a role.

3. Distance dependence The SERS enhancement reduces with increasing distance from the gold surface. This distance dependence is strongly influenced by the geometry of the SERS substrate. Ye et al. [58] found that increasing the length of an alkanethiol chain bound to Ag islands by 0.7 nm result in halving the SERS signal. For gap resonances in AgFON substrates, Masango et al. [33] report a drop of the signal to 20% at 0.7 nm and 7% at 3 nm distance from the Ag surface. While the 3D-FDTD simulated field profile of the nanodome geometry suggests only a limited distance dependence for narrower gaps (see for example figure 3.34c on page 3-41), it is difficult to predict the field enhancement at a sub-nm distance from the surface from a FDTD simulation. The nitrobenzene ring in pNTP is located very close to the gold surface, thus it may experience a stronger enhancement than the aromatics in the longer peptide chains. We have not studied the length of our surface-bound peptide layers in detail, but from literature we can estimate a length of 2-3 nm: the length of an undecanethiol chain is estimated to be 1-1.5 nm [57, 58] and the distance form the gold-surface to the carboxyl-terminal atom of the last N in CALNN was reported to be approximately 1.6 nm [34]. For pNTP, a monolayer thickness of 0.6 ± 0.2 nm has been measured and calculated [68].

C. Accessibility of the peptide substrate

We have demonstrated the cleavage of surface-bound peptides by trypsin, but the kinetics of the process are probably influenced by accessibility of the peptide substrate. With different proteases, this accessibility can also be different. Three factors can lead to steric hindrance for protease cleavage: the narrow dimensions of the plasmonic hotspot, the proximity of the gold surface to the cleavage site and

the high density of the peptide monolayer. The latter issue can be resolved by using spacer layers which reduce the grafting density of the enzyme substrate while retaining a stable monolayer [19, 23]. For example, the pentapeptide CALNN can be used to increase the distance between CALNNYGGGGVRGNF trypsin substrates, as sketched in figure 6.28. Obviously, a reduction in grafting density comes with a reduction in SERS signal, illustrated for an monolayer fabricated from different ratios of octanethiol/CFGVR-pNA in figure 6.29. Note that the octanethiol spacer layer used here is not ideal, to form a stable monolayer it should have a similar structure to gold-bound tail of the substrate.
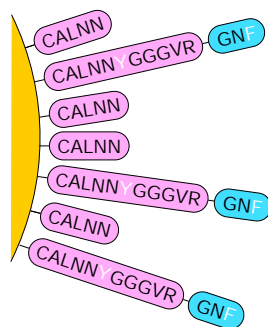
Figure 6.28 Including a spacer molecule can improve the accessibility of a surface-bound peptide substrate. For a stable self-assembling monolayer, both substrate and spacer should have the same structure, for example CALNN(CO-NH$_2$) and CALNNYGGGGVR-GNF.
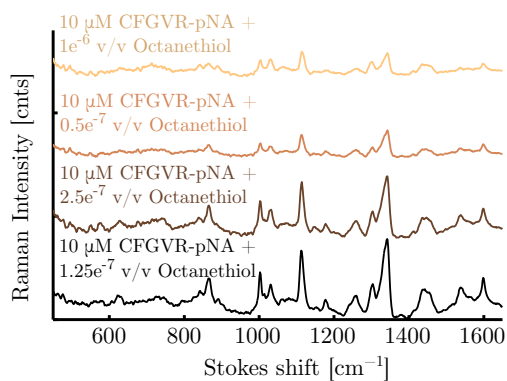
Figure 6.29 SERS spectra obtained from a nanodome sample labeled with 10 μM of CFGVR-pNA supplemented with increasing concentrations of octanethiol, a possible, non-ideal, spacer layer for this peptide.

Materials and Methods

Materials   7-Amino-4-methylcoumarin (amc, Sigma A9891), Acetone (VWR), Acetonitrile (Sigma), Ammonium bicarbonate (Sigma), Bovine Serum Albumin (Sigma), N-Benzoyl-DL-arginine 4-nitroanilide hydrochloride (L-BAPNA, Sigma B4875), Caspase-1 (purified product from Prof. M. Lamkanfi's lab), Caspase-1 (human recombinant active, Enzo ALX-201-056-U100), Dichloromethane (Sigma), Dimethylformamide (DMF, Sigma), Dithiothreitol, Endoproteinase Glu-C (Staphylococcus Aureus V-8 Protease, Thermofisher 20195 and Wako WEN 2475), Ethanol (Anhydrous, Sigma), Granzyme B (recombinant murine, Peprotech) , Hydrogen Peroxide (VWR), Isopropyl alcohol (VWR), Methanol (VWR), Mutant Caspase-1 (purified product from Prof. M. Lamkanfi's lab), para-nitroaniline (pNA, Sigma 185310), para-Nitrothiophenol (pNTP, Sigma N27209), Tris-base, Trypsin - Sequencing Grade Modified (Promega V5111), Protein inhibitor cocktail (PIC, Roche), monodisperse Polystyrene microbeads (microparticles GmbH, 448 nm), Sulfuric Acid (VWR), Ovomucoid (Type II-O) Trypsin inhibitor from chicken egg white (Sigma, T9253), YVAD-amc (Enzo, ALX-260-024-M005), YVAD-cmk caspase-1 inhibitor (Enzo ALX-260-028) and ZVAD-fmk caspase-1 inhibitor (Enzo ALX-260-020),

Finite Difference Time Domain Simulations   Lumerical FDTD solutions was used for simulating the field profile in the plasmonic hotspots. A total-field scattered-field source (TFSF) is incident on a gold nanodome dimer in water on a SiN/Si substrate with 224 nm radius and 10 nm gap width with anti-symmetric, PML and symmetric boundaries along respectively X, Y and Z. All geometrical parameters were set to match the data from the SEM top view and cross-section images to the best of our ability. The refractive indices are set as follows: $n_{SiN} = 2$, $n_{Au} =$ Johnson and Christy [69], n_{H_2O}=1.33.

Peptide synthesis[9]   The peptides were synthesized using standard solid-phase Fmoc chemistry on a SyroI (biotage) instrument. The synthesis was started on 25 µmol preloaded Fmoc-His(Trt) or Fmoc-Phe wang resin respectively (novabiochem). The amino acids were coupled in a 4-fold excess using HOBT/HBTU activation. The peptides were cleaved with TFA containing phenol, triisopropylsilane and 5% H_2O for 3 hours. The peptides were precipitated with tributylmethyl ether and recovered by centrifugation at 2000 g. The ether washing/ centrifugation step was repeated 3 times. The peptides were purified by a water/acetonitrile gradient elution on a RPC C18 column (Macherey-Nagel).
Alkanethiol-PEG chains were synthesize according to a protocol described in [56] and linked with a peptide in a post-synthesis reaction.

Peptide handling   Lyophilized peptides were aliquoted in vials of $0.5 \pm 0.1 \, \mu$g and flushed with Argon prior to storage at -20 °C. Because of the inaccuracy when weighing sub-mg powders, there is a 20 % error on all mentioned in-house peptide concentrations. On the day of usage, peptides were first dissolved to 100 µg/µl in DMF and further diluted to 100 µg/ml in either a 10% acetonitrile/water mixture for labeling or a 50 mM ammonium bicarbonate buffer (pH 7.8) for bulk digestion experiments. DMF was used rather than DMSO because the latter will oxidize the cysteine thiol-side chain. The necessary safety precautions should be taken when using DMF, and DMSO is preferable if cysteine oxidation

---

[9]Peptides were synthesized by Hans Demol, Dept. Of Biochemistry, UGent

is not an issue. Especially for the self-assembling peptides, long or even short-term storage in-solution is not advised as they will easily cluster or sediment.

Nanodome fabrication   Nanodome chips were fabricated as described in chapter 3. Chips were used up to a few months after fabrication, although we did notice an increase in contamination from the SERS spectra acquired on older, unlabeled chips.

Chip Labeling   Prior to labeling the chips with peptides, they were cleaved into pieces of a few mm^2 and cleaned by sonication in acetone, rinsed with isopropylalcohol and water and dried with under a stream of nitrogen. Next, remaining organic contaminants were removed in an O_2 plasma, which also renders the surface hydrophilic (120 s, PVA-TEPLA GIGAbatch 310 M, 6000 sccm O2, 600W, 750 mTorr). Immediately afterwards, the chips were immersed in separate wells of a polypropylene 96-well plate, using 100 μl of a 100 μg/ml peptide solution in 10% acetonitrile in water. After overnight incubation, the chips were rinsed excessively with deionized water. After labeling, the chips were stored in water, water with 10 % Acetonitrile or PBS, depending on the specific peptide. Drying out of the chips should be avoided. We have not done a systematic study on the stability of the monolayer with time. Until optimal storage conditions have been found, it is recommended to do all experiments within 48 hours after labeling. The use of any polystyrene-containing lab consumables (such as petri dishes and well plates) in combination with acetonitrile or DMF should be avoided. Polystyrene is not resistant to these solvents which results in a contamination of the chip surface with polystyrene. This is dramatic for our application: as a result of its identical aromatic ring (figure A.12), the Raman spectrum polystyrene interferes with that of phenylalanine. Likewise, polystyrene dishes in combination with low-NA objectives may contribute to a polystyrene background signal. Other often encountered contaminating SERS peaks have been traced back to 4-NTP (figure A.11) and R6G (figure A.14). Most common sources of this contamination are tweezers, glassware and, in particular, micropipettes. A two-step cleaning of the plasma chamber (10 min 111, 5 min O_2) is also recommended prior to exposing the nanodome surface, as traces of photoresist or other polymers in the chamber may settle on the chip surface.

Peptide assays   All enzymes were stored at -80 °C and aliquoted in single-use vials to limit the number of freeze-thaw cycles. Protease and peptide concentrations were used as below unless mentioned differently.
Trypsin All assays were done in a freshly prepared 50 mM ammonium-bicarbonate buffer (pH 7.8) at 37 °C. Trypsin was first incubated at 37 °C for 15 min prior to addition to the peptide substrate, ensuring immediate maximal enzyme activity. The effectivity of the ovomucoid trypsin inhibitor for blocking trypsin digestion was tested in a 405 nm absorption assay (Tecan Infinite 200 PRO) on the commercially available L-BAPNA trypsin substrate. We used an excessive inhibitor concentration of 100 μg/ml.
Endoproteinase GluC All assays were done in a freshly prepared 100 mM ammonium bicarbonate buffer (pH 7.8) at 37 °C. Endoproteinase GluC was first incubated at 37 °C for 15 min prior to addition to the peptide substrate, ensuring immediate maximal enzyme activity. The activity of this protease from two different commercial suppliers was tested (Staphylococcus aureus V-8 Protease, Thermofisher 20195 and Endoproteinase GluC sequencing grade, Wako, WEN 2475). Both had similar activity on the CALNNYGGGGNNESWH substrate (3 μg/ml protease, 100μg/ml substrate). We could not find a commercially available fluorescent or colorimetric substrate as positive control for this enzyme.

Caspase-1 All caspase-1 assays were done in a buffer consisting of 20 mM PIPES (pH 7.5), 100 mM NaCl, 1 mM EDTA, 0.1 % (w/v) CHAPS, 10 % sucrose. Caspase-1 ($20\,\mu g/ml$) and DTT (0.5-10 mM) were first pre-incubated for 15 minutes at 37 °C prior to adding the peptide substrate (typically 50 µM). In all experiments, a caspase-1 solution purified by prof. M. Lamkanfi's lab was used. Using a YVAD-amc substrate in a fluorescent assay, we found this caspase-1 to be much more active than a commercial product (Enzo Caspase-1 ALX–201-056-U100).

HPLC and mass spectrometry   After incubation for a specific time at 37 °C, 750 µl of a solution with 100 µg/ml substrate and 3.3 µg/ml trypsin or endoproteinase Glu-C in 50-100 mM ammoniumbicarbonate was injected in a C-18 reversed phase high-performance liquid chromatography column (Macherey-Nagel) and eluted by a water/acetonitrile gradient (kta Purifier, GE). The molecular weight of separated fractions was determined using matrix-assisted laser desorption/ionization time-of-flight mass spectrometry (Bruker MALDI-TOF).

Fluorescent and colorimetric assays   An assay based on the fluorescence of free -amc was used to quantify the activity of caspase-1 on the -amc terminated substrates in table 6.1. Experiments were done using a *Tecan Infinite 200 PRO platereader* in top-read mode with a $350 \pm 5\,nm$ excitation and $440 \pm 20\,nm$ emission filter. These excitation and emission filters were experimentally determined using a similar platereader (Prof. G. Smagghe's lab) equipped with a monochromator (figure 6.30).
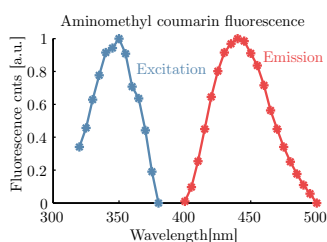
Figure 6.30 Measured excitation and emission profile of YVAD-amc.

Typically, 3 wells per condition of a 96-well flat bottom black PP plate (Greiner, M9685) were filled with a final volume of $50\,\mu l$ per well. The commercial caspase-1 substrate YVAD-amc was used as a positive control. We found a complete inhibition of capase-1 activity by the YVAD-cmk and zVAD-fmk inhibitors when pre-incubating the caspase-1 with DTT and inhibitor (10 µM). The platereader was calibrated with amc concentrations ranging from 0.05-500 µM to convert fluorescent intensity into a the concentration of free amc molecules (C_{amc}) in µM. For a 50 µl volume at different gain settings G in the linear regime (up to 8 µM) this becomes:

$$G_{50} : I_{fluo} = 2440 \times C_{amc} + 232$$

$$G_{35} : I_{fluo} = 190 \times C_{amc} + 28$$

$$G_{30} : I_{fluo} = 90 \times C_{amc} + 14$$

The same platereader was used for measuring the activity of trypsin on -pNA functionalized peptides. The absorption was measured through a 96 well flat bottom transparent PS plate (Greiner 655101) in a transmission (bottom) mode using a bandpass filter at 405 ± 5 nm. For a total volume of 100 µl, the concentration of free -pNA molecules C_{pNA} (µM) in function of the absorbance at 405 nm A_{405} equals:

$$A_{405} = 0.0016 \times C_{pNA} + 0.045$$

Raman microscopy   Spectra were acquired on a WITec Alpha 300 R+ confocal Raman microscope equipped with a -70 °C cooled CCD camera (Andor iDus 401 BR-DD) and a 785 nm diode laser (Toptica, XTRA II). Normal Raman spectra of the peptide powders were acquired using a Zeiss 100x/0.9 EC Epiplan NEOFLUAR; $\infty/0$ objective and a laser power of 100 mW, measured before the objective. All spectra were acquired using a 600 lpmm grating and a 100 µm diameter collection fiber. We used three different configurations for acquiring SERS spectra:

1. Zeiss 63x/1.0 W Plan Apochromat $\infty/0$ objective, taking 10x10 spectra in a 20 µm x 20 µm map with with a 0.2-2 mW laser power. For example used for the results on surface-bound and real-time trypsin digestion in figures 6.7 and 6.8.

2. Nikon 10x/0.3 PlanFluar $\infty/0.17$ objective, taking 7x7 spectra in a 50 µm x 50 µm map with a 3s integration time and a 1-3 mW laser power, for example used for finding the influence of DTT in figures 6.11, 6.13 and6.13.

3. Zeiss 20x/0.5 W N-Achroplan $\infty/0$ objective, taking 7x7 spectra in a 40 µm x 40 µm map with a 3s integration time and a 1-3 mW laser power

The choice of the objective was determined by multiple experimental parameters. These include the presence of solvents and the number of simultaneously measured conditions (both inhibiting the use of dipping objectives), the SNR of the SERS signal (higher signal and reduced background with higher NA objectives) and evaporation of the sample (inhibiting the use of dry objectives). The exact used laser power depends on the SSEF of the SERS substrate. The power was reduced for chips with a higher enhancement, as a strong plasmon resonance also induces faster photodegradation of the SERS signal. For real-time monitoring of enzymatic activity, the chip was placed in a metal petri dish filled with 1 ml buffer inside a stage-top incubator at 37 °C (Okolab). Because of signal degradation upon laser illumination, each trace is the median spectrum of a spatially distributed map with settings as described above. In the real-time assay, every next trace was mapped on a different location on the SERS platform. A limited amount of inhomogeneity across the gold nanodome area accounts for the variation in $I_{1003}/I_{829-860}$ visible in figure 6.8(c).

SERS data processing   Starting from the 10x10 individual spectra, WITec Project Four was used for removing cosmic rays. Next, the data was exported to Matlab and aberrant spectra were rejected using a variance-based filter, after which the background of each individual spectrum is subtracted using a high-pass filter. All SERS spectra plotted in this chapter are the median spectra of these data. Peak intensities were calculated by integrating the peaks at their respective positions and subtracting the background with a linear fit for the individual spectra. For example, the individual measurements points in figures 6.13, 6.11 and 6.16 are visualizations of these individual peak intensities.

References

[1] M Drag and G S Salvesen *Emerging principles in protease-based drug discovery* Nature Reviews: Drug Discovery, 9(9):690–701, 2010.

[2] B. Turk *Targeting proteases: successes, failures and future prospects* Nature Reviews. Drug Discovery, 5(9):785–799, 2006.

[3] Charles J Choi, Zhida Xu, Hsin-Yu Wu, Gang Logan Liu, and Brian T Cunningham *Surface-enhanced Raman nanodomes.* Nanotechnology, 21(41):415301, oct 2010.

[4] Ting Liu, Yoshifumi Yamaguchi, Yoshitaka Shirasaki, Koichi Shikada, Mai Yamagishi, Katsuaki Hoshino, Tsuneyasu Kaisho, Kiwamu Takemoto, Toshihiko Suzuki, Erina Kuranaga, Osamu Ohara, and Masayuki Miura *Single-Cell Imaging of Caspase-1 Dynamics Reveals an All-or-None Inflammasome Signaling Response* Cell Reports, 8(4):974–982, 2014.

[5] Meiye Wu and Anup K Sing *Single-Cell Protein Analysis* Current Opinion in Biotechnology, 23(1):83–88, 2012.

[6] Katharina Welser, Rosemary Adsley, Bernadette M Moore, Weng C Chan, Jonathan W Aylott, and C Chan *Protease sensing with nanoparticle based platforms.* The Analyst, 136(1):29–41, 2011.

[7] Dusica Maysinger and Eliza Hutter *Nanoparticle-based caspase sensors.* Nanomedicine, 10(3):483–501, 2015.

[8] H. Lodish, A. Berk, P. Matsudaira, C. Kaiser, M. Krieger, M. P. Scott, S. L Zipursky, and J. Darnell *Molecular Cell Biology* W. H. Freeman and Company, 5 edition, 2004.

[9] K Breddam and M Meldal *Substrate preferences of glutamic-acid-specific endopeptidases...* European Journal of Biochemistry, 206:103–107, 1992.

[10] Morten Meldal and Klaus Breddam *Anthranilamide and nitrotyrosine as a donor-acceptor pair in internally quenched fluorescent substrates for endopeptidases: Multicolumn peptide synthesis of enzyme substrates for subtilisin carlsberg and pepsin* Analytical Biochemistry, 195(1):141–147, 1991.

[11] Felipe Andrade, Sophie Roy, Donald Nicholson, Nancy Thornberry, Antony Rosen, and Livia Casciola-Rosen *Granzyme B directly and efficiently cleaves several downstream caspases substrates: Implications for CTL-induced apoptosis* Immunity, 8(4):451–460, 1998.

[12] Laura E Sanman and Matthew Bogyo *Activity-based profiling of proteases.* Annual review of biochemistry, 83:249–73, 2014.

[13] Sevnur Serim, Ute Haedke, and Steven H L Verhelst *Activity-Based Probes for the Study of Proteases: Recent Advances and Developments* ChemMedChem, 7(7):1146–1159, 2012.

[14] Mischa Zelzer, Simon J. Todd, Andrew R. Hirst, Tom O. McDonald, and Rein V. Ulijn *Enzyme responsive materials: design strategies and future developments* Biomater. Sci., 1(1):11–39, 2013.

[15] Young-Pil Kim and Hak Sung Kim *Nanoparticles for Use in Enzyme Assays* ChemBioChem, 17(4):275–282, 2016.

[16] Eliza Hutter and Dusica Maysinger *Gold-nanoparticle-based biosensors for detection of enzyme activity* Trends in Pharmacological Sciences, 34(9):497–507, 2013.

[17] Anming Tang, Bin Mei, Weijuan Wang, Wanglai Hu, Fang Li, Jun Zhou, Qing Yang, Hua Cui, Mian Wu, and Gaolin Liang *FITC-quencher based, caspase 3-activatable nanoprobes for effectively sensing caspase 3 in vitro and in cells* Nanoscale, 5(August):8963–8967, 2013.

[18] Lingxin Chen, Xiuli Fu, and Jinhua Li *Ultrasensitive surface-enhanced Raman scattering detection of trypsin based on anti-aggregation of 4-mercaptopyridine-functionalized silver nanoparticles: an optical sensing platform toward proteases.* Nanoscale, 5(13):5905–11, 2013.

[19] Paul Free, Christopher P Shaw, and Raphael Levy *PEGylation modulates the interfacial kinetics of proteases on peptide-capped gold nanoparticles* Chemical Communications, 33:5009–5011, 2009.

[20] Young Pil Kim, Young Hee Oh, Eunkeu Oh, Sungho Ko, Min Kyu Han, and Hak Sung Kim *Energy transfer-based multiplexed assay of proteases by using gold nanoparticle and quantum dot conjugates on a surface* Analytical Chemistry, 80(12):4634–4641, 2008.

[21] Yuming Lai, Shuqing Sun, Tao He, Sebastian Schlücker, and Yuling Wang *Raman-encoded microbeads for spectral multiplexing with SERS detection* RSC Advanced, 5:13762–13767, 2015.

[22] Gang L Liu, Yazmin T Rosa-Bauza, Cleo M Salisbury, Charles Craik, Jonathan a Ellman, Fanqing Frank Chen, and Luke P Lee *Peptide-nanoparticle hybrid SERS probes for optical detection of protease activity.* Journal of nanoscience and nanotechnology, 7(7):2323–2330, 2007.

[23] Cheng Sun, Kai Hung Su, Jason Valentine, Yazmin T. Rosa-Bauza, Jonathan A. Ellman, Omeed Elboudwarej, Bipasha Mukherjee, Charles S. Craik, Marc A. Shuman, Fanqing Frank Chen, and Xiang Zhang *Time-resolved single-step protease activity quantification using nanoplasmonic resonator sensors* ACS Nano, 4(2):978–984, 2010.

[24] Cuicui Fu, Weiqing Xu, Gang Chen, and Shuping Xu *'Switch-off' biosensing for chymotrypsin-catalyzed reaction by SPR-SERS spectroscopy.* The Analyst, 138(21):6282–6, 2013.

[25] Zitong Wu, Yifei Liu, Yizhen Liu, Huaming Xiao, Aiguo Shen, Xiaodong Zhou, and Jiming Hu *A simple and universal "turn-on" detection platform for proteases based on surface enhanced Raman scattering (SERS)* Biosensors and Bioelectronics, 65:375–381, 2015.

[26] Andrew Ingram, Louise Byers, Karen Faulds, Barry D. Moore, and Duncan Graham *SERRS-based enzymatic probes for the detection of protease activity* Journal of the American Chemical Society, 130(36):11846–11847, 2008.

[27] Iain A Larmour, Karen Faulds, and Duncan Graham *The past and future of enzyme measurements using enhanced Raman spectroscopy* Chemical Science, 1:151–160, 2010.

[28] Barry D Moore, Lorna Stevenson, Alan Watt, Sabine Flitsch, Nicolas J Turner, Chris Cassidy, and Duncan Graham *Rapid and ultra-sensitive determination of enzyme activities using surface-enhanced resonance Raman scattering.* Nature biotechnology, 22(9):1133–8, 2004.

[29] Fang Wei, Dongmao Zhang, Naomi J. Halas, and Jeffrey D. Hartgerink *Aromatic amino acids providing characteristic motifs in the raman and SERS spectroscopy of peptides* Journal of Physical Chemistry B, 112(30):9158–9164, 2008.

[30] Emma Jorgenson and Anatoli Ianoul *Biofunctionalization of Plasmonic Nanoparticles with Short Peptides Monitored by SERS* The Journal of Physical Chemistry B, 121:967–974, 2017.

[31] Raphaël Lévy, Nguyen T K Thanh, R. Christopher Doty, Irshad Hussain, Richard J. Nichols, David J. Schiffrin, Mathias Brust, and David G. Fernig *Rational and combinatorial design of peptide capping ligands for gold nanoparticles* Journal of the American Chemical Society, 126(32):10076–10084, 2004.

[32] Violaine See, Paul Free, Yann Cesbron, Paula Nativo, Umbreen Shaheen, Daniel J Rigden, David G Spiller, David G Fernig, Michael R H White, Ian A Prior, Mathias Brust, Brahim Lounis, and Raphael Levy *Cathepsin L Digestion of Nanobioconjugates upon Endocytosis* ACS Nano, 3(9):2461–2468, 2009.

[33] Sicelo S. Masango, Ryan A. Hackler, Nicolas Large, Anne Isabelle Henry, Michael O. McAnally, George C. Schatz, Peter C. Stair, and Richard P. Van Duyne *High-Resolution Distance Dependence Study of Surface-Enhanced Raman Scattering Enabled by Atomic Layer Deposition* Nano Letters, 16(7):4251–4259, 2016.

[34] Elena Colangelo, Qiubo Chen, Adam M Davidson, David Paramelle, Michael B Sullivan, Martin Volk, and Raphael Levy *Experimental and Computational Investigation of the Structure of Peptide Monolayers on Gold Nanoparticles* Langmuir, 33:438–449, 2017.

[35] Hannu Häkkinen *The gold sulfur interface at the nanoscale* Nature Chemistry, 4(6):443–455, 2012.

[36] Laurence Duchesne, Denis Gentili, Mauro Comes-Franchini, and David G. Fernig *Robust ligand shells for biological applications of gold nanoparticles* Langmuir, 24(23):13572–13580, 2008.

[37] Elien Vandermarliere, Michael Mueller, and Lennart Martens *Getting intimate with Trypsin, the leading protease in proteomics* Mass Spectrometry Reviews, 32:453–465, 2013.

[38] M Pozsgay, G Szabó, S Bajusz, R Simonsson, R Gáspár, and P Elödi *Investigation of the substrate-binding site of trypsin by the aid of tripeptidyl-p-nitroanilide substrates.* Eur. J. Biochem., 115(3):497–502, 1981.

[39] Joke De Gelder, Kris De Gussem, Peter Vandenabeele, and Luc Moens *Reference database of Raman spectra of biological molecules* Journal of Raman Spectroscopy, 38(April):1133–1147, 2007.

[40] Zanyar Movasaghi, Shazza Rehman, and Ihtesham U. Rehman *Raman Spectroscopy of Biological Tissues* Applied Spectroscopy Reviews, 42(5):493–541, 2007.

[41] Guangyong Zhu, Xian Zhu, Qi Fan, and Xueliang Wan *Raman spectra of amino acids and their aqueous solutions* Spectrochimica Acta - Part A: Molecular and Biomolecular Spectroscopy, 78(3):1187–1195, 2011.

[42] Harold P. Erickson *Size and shape of protein molecules at the nanometer level determined by sedimentation, gel filtration, and electron microscopy* Biological Procedures Online, 11(1):32–51, 2009.

[43] Lauren Bayne, Rein V. Ulijn, and Peter J. Halling *Effect of pore size on the performance of immobilised enzymes* Chem. Soc. Rev., 42:9000–9010, 2013.

[44] Eric C Le Ru and Pablo G Etchegoin *Principles of Surface-Enhanced Raman Spectroscopy and related plasmonic effects* Elsevier, Amsterdam, jan 2009.

[45] E.C. Le Ru, M Meyer, and P.G. Etchegoin *Surface Enhanced Raman Scattering Enhancement Factors: A Comprehensive Study* Journal of Physical Chemistry C, 111(37):13794–13803, 2007.

[46] Jingdong Zhang, Qijin Chi, Jens U Nielsen, Esben P Friis, Jens E T Andersen, and Jens Ulstrup *Two-Dimensional Cysteine and Cystine Cluster Networks on Au (111) Disclosed by Voltammetry and in Situ Scanning Tunneling* Langmuir, 16(18):7229–7237, 2000.

[47] Satish Nayak, Woon-seok Yeo, and Milan Mrksich *Determination of Kinetic Parameters for Interfacial Enzymatic Reactions on Self-Assembled Monolayers* Langmuir, 172(31):5578–5583, 2007.

[48] Kazuhiro Aoki, Yuji Kamioka, and Michiyuki Matsuda *Fluorescence resonance energy transfer imaging of cell signaling from in vitro to in vivo : Basis of biosensor construction, live imaging, and image processing* Development, Growth & Differentiation, 55(4):515–522, 2013.

[49] Karel Klepárník and František Foret *Recent advances in the development of single cell analysis-A review* Analytica Chimica Acta, 800:12–21, 2013.

[50] Chao Ma, Rong Fan, Habib Ahmad, Qihui Shi, Begonya Comin-Anduix, Thinle Chodon, Richard C Koya, Chao-Chao Liu, Gabriel a Kwong, Caius G Radu, Antoni Ribas, and James R Heath *A clinical microchip for evaluation of single immune cells reveals high functional heterogeneity in phenotypically similar T cells.* Nature medicine, 17(6):738–743, 2011.

[51] Sava Tay, Jacob J. Hughey, Timothy K. Lee, Tomasz Lipniacki, Stephen R. Quake, and Markus W. Covert *Single-cell NF-κB dynamics reveal digital activation and analogue information processing* Nature, 466(7303):267–271, 2010.

[52] Mohamed Lamkanfi and Vishva M. Dixit *Mechanisms and functions of inflammasomes* Cell, 157(5):1013–1022, 2014.

[53] R A Sperling and W J Parak *Surface modification, functionalization and bioconjugation of colloidal inorganic nanoparticles.* Philosophical transactions. Series A, Mathematical, physical, and engineering sciences, 368(1915):1333–1383, 2010.

[54] Ashim Dhakal, Pieter C. Wuytens, Frédéric Peyskens, Karolien Jans, Nicolas Le Thomas, and Roel Baets *Nanophotonic Waveguide Enhanced Raman Spectroscopy of Biological Submonolayers* ACS Photonics, 3(11):2141–49, 2016.

[55] Jian Feng Li, Yi Fan Huang, Yong Ding, Zhi Lin Yang, Song Bo Li, Xiao Shun Zhou, Feng Ru Fan, Wei Zhang, Zhi You Zhou, De Yin Wu, Bin Ren, Zhong Lin Wang, and Zhong Qun Tian *Shell-isolated nanoparticle-enhanced Raman spectroscopy* Nature, 464(7287):392–395, 2010.

[56] Ratmir Derda, Daniel J. Wherritt, and Laura L. Kiessling *Solid-phase synthesis of alkanethiols for the preparation of self-assembled monolayers* Langmuir, 23(22):11164–11167, 2007.

[57] Colin D Bain, E Barry Troughton, Yu Tai Tao, Joseph Evall, George M Whitesides, and Ralph G Nuzzo *Formation of monolayer films by the spontaneous assembly of organic thiols from solution onto gold* Journal of the American Chemical Society, 111(1):321–335, 1989.

[58] Qi Ye, Jianxin Fang, and Li Sun *Surface-Enhanced Raman Scattering from Functionalized Self-Assembled Monolayers. 2. Distance Dependence of Enhanced Raman Scattering from an Azobenzene Terminal Group* Journal of Physical Chemistry B, 101(41):8221–8224, 1997.

[59] Zheng and Huang Davidson *Ethylene glycol monolayer protected nanoparticles for liminating nonspecific binding with biological molecules* J Am Chem Soc, 125:7790–7791, 2003.

[60] W.B. Caldwell, D.J. Campbell, K. Chen, B.R. Herr, C. A. Mirkin, A. Malik, M.K. Durbin, P. Dutta, and K. G. Huang *A Highly Ordered Self-Assembled Monolayer Film of an Azobenzenealkanethiol on Au(111): Electrochemical Properties and Structural Characterization by Synchrotron in-Plane X-ray Diffraction, Atomic Force Microscopy, and Surface-Enhanced Raman Spectroscopy* J Am Chem Soc, 117(22):6071–6082, 1995.

[61] Horiba   *http://www.horiba.com/scientific/products/raman-spectroscopy/accessories/sers-substrates*, 2016.

[62] P. C. Wuytens, Al. M. Yashchenok, A. Z. Subramanian, A. G. Skirtach, and R Baets *Gold Nanoparticle Coated Silicon Nitride chips for Intracellular Surface-Enhanced Raman Spectroscopy* In CLEO, volume STh4H.7, 2014.

[63] Mohamed Lamkanfi, Thirumala-Devi Kanneganti, Petra Van Damme, Tom Vanden Berghe, Isabel Vanoverberghe, Joël Vandekerckhove, Peter Vandenabeele, Kris Gevaert, and Gabriel Núñez *Targeted peptidecentric proteomics reveals caspase-7 as a substrate of the caspase-1 inflammasomes.* Molecular & cellular proteomics : MCP, 7(12):2350–63, 2008.

[64] Nobuhiko Kayagaki, Søren Warming, Mohamed Lamkanfi, Lieselotte Vande Walle, Salina Louie, Jennifer Dong, Kim Newton, Yan Qu, Jinfeng Liu, Sherry Heldens, Juan Zhang, Wyne P. Lee, Merone Roose-Girma, and Vishva M. Dixit *Non-canonical inflammasome activation targets caspase-11* Nature, 479(7371):117–121, 2011.

[65] Prajwal Gurung, R. K. Subbarao Malireddi, Paras K. Anand, Dieter Demon, Lieselotte Vande Walle, Zhiping Liu, Peter Vogel, Mohamed Lamkanfi, and Thirumala Devi Kanneganti *Toll or interleukin-1 receptor (TIR) domain-containing adaptor inducing interferon-β (TRIF)-mediated caspase-11 protease production integrates toll-like receptor 4 (TLR4) protein- and Nlrp3 inflammasome-mediated host defense against enteropathogens* Journal of Biological Chemistry, 287(41):34474–34483, 2012.

[66] Jacqueline R. Rettig and Albert Folch *Large-Scale Single-Cell Trapping And Imaging Using Microwell Arrays* Analytical Chemistry, 77(17):5628–5634, 2005.

[67] Nobuyuki Mohri, Morimasa Inoue, Yoshifumi Arai, and Kenichi Yoshikawa *Kinetic Study on Monolayer Formation with 4-Aminobenzenethiol on a Gold Surface* Langmuir, 11(5):1612–1616, 1995.

[68] A Jakubowicz, H Jia, R M Wallace, and B E Gnade *Adsorption kinetics of p-nitrobenzenethiol self-assembled monolayers on a gold surface.* Langmuir, 21(3):950–955, 2005.

[69] P.B. Johnson and R.W. Christy *Optical Contstants of Noble Metal*, 1972.

7
CONCLUSIONS AND PERSPECTIVES

We summarize the most important achievements and future challenges for the two technology platforms and two biosensing applications developed during this PhD thesis, and finish with the most promising perspectives.

The first technological tool is the gold-nanodome SERS platform, designed for use in combination with Raman microscopes. This platform was used for the majority of the SERS experiments in this thesis, and with reason. We can fabricate 4" wafers fully patterned with nanodomes in one or two working days, at a €10-100 consumable cost. These nanodome-patterned wafers provide a large-scale SERS substrate with a SERS substrate averaged enhancement factor up to 10^7 and only 7% signal variation over a distance of several millimeters. The resulting gold surface is chemically and physically robust, and the characteristics of the LSPP resonance can be easily adjusted during the fabrication process. However, this nanodome platform can not be seen as a unique scientific advancement. In parallel with our development, alternative fabrication methods like deep-UV lithography [1] and nanoimprint lithography [2] have been published that can present comparable statistics. The nanodome platform was a very efficient tool for the applications developed in this thesis, but to a certain extent it may be interchangeable with other SERS substrates described in literature.

What's next? *Incremental improvements to this platform are possible. (1) Process optimization can improve the substrate uniformity and batch-to-batch reproducibility. Currently limiting factors are the quality of the spincoated monolayer of polystyrene beads and the accuracy with which we can deposit a 100 nm gold*

layer. (2) A further increase of the enhancement factor can possibly be achieved by slightly increasing the periodicity of the structure, which will result in an increased coupling between the localized and propagating surface plasmon polaritons. Apart from these, the nanodome platform has been throughly optimized and the expected gain in enhancement is limited. Arguably, under the boundary conditions of using a gold layer with a 785 nm pump laser and accessible hotspots, it will be hard to improve the total Stokes scattered power collected from a gold-bound monolayer by more than a factor 10.

The second technology platform is a hybrid combination of nanophotonic silicon nitride waveguides and gold nanotriangles. SERS spectra are excited and collected through the waveguide from a micrometer long stretch of nanotriangles patterned on the waveguide's top surface. This platform presents three important improvements over the prior platform developed in our group by Peyskens et al. [3], which exists of e-beam-written bowtie antennas on e-beam-written waveguides. First, it drastically simplifies the fabrication by replacing electron-beam lithography with nanosphere lithography. Second, the nanosphere lithography process allows to fabricate gold nanoantennas in a post-processing step on deep-UV lithography fabricated waveguides. This integration of nanoplasmonic antennas with a mature integrated photonics platform is a prerequisite for fully integrated spectroscopic sensors. Third, we measure a tenfold increase of the total waveguide collected Stokes scattering while the waveguide-to-waveguide variation of the SERS signal was not markedly different from the e-beam fabricated case. This increased enhancement is probably due to the sharply defined edges of the nanotriangles. The collected SERS signal through the waveguide is approximately equal to that using a free-space excitation and collection through a 0.9 NA objective on the same nanotriangles. The SSEF of these nanotriangles under free-space excitation is $2.5 \pm 1 \times 10^5$. This enhancement is in line with earlier reported values for these kind of structures. However, the signal to noise ratio in this platform is not even close to the performance of free-space SERS substrates like the nanodome pattern. The total collected Stokes scattered power from a monolayer of gold-bound molecules is more than 100 times lower and the SiN core of the waveguide increases the background signal.

***What's next?** The huge discrepancy in signal to noise ratio with state-of-the-art, free-space SERS substrates exclaims the potential for an improved on-chip SERS platform. A number of incremental improvements can be implemented with relative ease: (1) The fabrication of nanotriangles on single mode waveguides to remove the mulitmode-interference ripple. (2) A reduction of the plasmonic resonance damping due the Ti adhesion layer, either by replacing it with an organic molecule or minimizing its thickness. (3) A further optimization of the nanotriangle geometry for a maximal SSEF (4) A planarization of the SiN waveguide surface to improve the monolayer quality, thus reduce the waveguide-waveguide variation. However, increasing the sensitivity to the level of the best free-space SERS plat-*

forms will require more radical innovations. On the one hand, the shot noise has to be reduced by decreasing the background signal from the SiN waveguide (figure 7.1a). One option is to use a set of integrated filters. A high-pass or notch frequency filter right before the SERS-section to remove all the Stokes scattered light, followed by a low-pass frequency filter after the SERS section to suppress the pump wavelength, will limit the collection length to a few hundred micrometers. Another option is a 'confocal' detection scheme using Y splitters, as proposed in [4]. On the other hand, the SERS signal has to be increased by two orders of magnitude. This will require waveguide-integrated structures with reproducible sub-20 nm gaps. The wide variety of free-space SERS platforms described in literature provide a source of inspiration, but the challenge remains to convert these to a nanostructure that couples efficiently to a single-mode SiN waveguide and can be fabricated with scalable technology. We have multiple ideas towards this end, one approach is the integration of nanodome-like structures in a SiN waveguide (figure 7.1b).

I am convinced that further technological developments on this topic will lead to breakthrough applications currently limited to free-space SERS sensing.

(a) Reducing the SiN background signal: (1) 'Confocal' reflection measurement using a Y-splitter [4] (2) Integration of pump and Stokes filters

(b) Increasing the SERS enhancement: First trial to integrate nanodomes in SiN waveguides
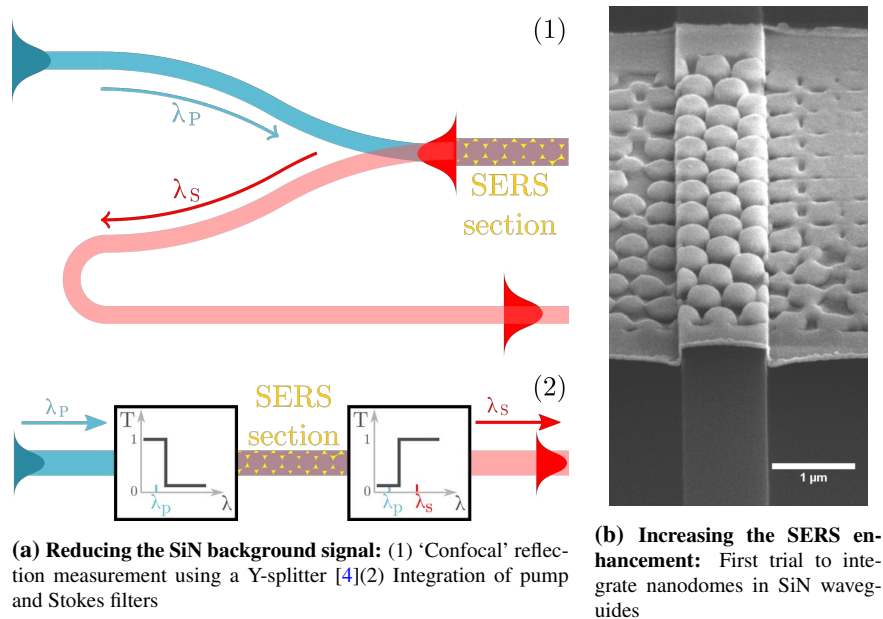
Figure 7.1 Strategies to increase the on-chip SERS signal-to-noise ratio.

Gold-nanodome patterned microchips were used for a label-free intracellular detection of extraneous molecules We fabricated a new type of semi-colloidal SERS particles: a monodisperse collection of microchips with top-down patterned gold-nanostructures for time-constant SERS enhancement. For this purpose, we

cut micrometer-sized planar disks out a gold-nanodome patterned surface using optical lithography and a wet underetch. We found that these chips are efficiently ingested by specific mammalian cells. In preliminary tests, we did not find any influence of the microchips on cell mitosis or cell viability. As a proof-of-concept application, we detected the presence of extraneously added Rhodamine 6G in living cells through its SERS spectrum. Following a skeptical point of view, this R6G detection is not an utterly impressive result. We have shown that confocal fluorescence microscopy can provide the same information with much less effort, and R6G is a molecule with a large Raman cross section. However, the same measurement principle could be applied for detecting non-fluorescent molecules, for example to test the cellular uptake of drugs. Many of those contain conjugated electron systems that give them a large Raman cross-section.

What's next? At the time of experiment, the nanodome SERS platform was not fully optimized. The gold layer was too rough and the dimensions of the inter-dome cavity were suboptimal. An immediate tenfold increase in SERS enhancement factor and an improved chip uniformity can be achieved simply by repeating the experiment with our current nanodome platform.

Using a fixed nanodome SERS structure, the chip takes out the variability encountered when using nanoparticles and their aggregates for intracellular sensing. Also, the sputtered gold is free of any surfactants, which are necessary for the stabilization of gold nanoparticles and produce interfering Raman peaks. Nevertheless, a sensitive and quantitative intracellular label-free measurement remains inhibited by other factors, most importantly the adsorption of a protein corona on the gold surface and the likely encapsulation of the chip in a lipid vesicle. Transmission-electron microscopy images of intracellular particles could give exclusion on the latter issue, about which there is controversy in literature. Whether or not a specific molecule will be detected not only depends on its concentration, but also on its ability to reach the SERS microchip and the charge-based interactions with the gold surface. Despite multiple demonstrations of SERS-based intracellular drug detection in literature, I am skeptical about the future of using non-funtionalized gold surfaces for a generic, quantitative and sensitive intracellular detection of molecules.

Functionalization of the nanodome surface with a peptide substrate enabled the SERS-based detection of protease activity. Peptides were designed and fabricated to form a stable monolayer on a gold surface and provide a selective substrate for a specific protease. By incorporating different aromatic amino acids on both sides of the protease cleavage-site, we obtain a ratiometric measurement for protease activity based on the relative intensity of different SERS bands. This method allows distinguishing protease activity from ligand-exchange, an issue that was often neglected in previously published assays. We have unambiguously shown a SERS-based detection of trypsin activity using substrate-coated nanodomes and monitored substrate cleavage in real-time. The current experi-

ments used a lowest trypsin concentration of 8.6 nM, but the sensitivity in terms of protease concentration was not yet fully quantified. We also showed how the peptide design can be modified towards a substrate for endoproteinase Glu-C. In principle, our detection method can be adapted towards a variety of different proteases. However, we observed difficulties with the stability of the peptide-gold chemistry when using serine proteases in a reductive environment. We showed that a self-assembling PEG-alkanethiol monolayer can be used to protect the gold-thiol bond, but have not yet unambiguously demonstrated a real-time, SERS-based measurement of capase-1 activity, the central protease involved in inflammasome activation.

What's next? First, the sensitivity of the current platform for monitoring trypsin activity has to be rigorously quantified. This includes determining the lowest detectable trypsin concentration. Next, the activity of endoproteinase Glu-C on gold-bound peptides has to be demonstrated and quantified. Afterwards, a truly multiplexed detection of trypsin and endoproteinase Glu-C can be demonstrated by functionalizing the gold surface with a mixture of the substrates for both proteases. If successful, all these experiments are to be redone in complex biological buffers. The expertise, materials and technology for these experiments are available in our lab, so interesting results can be expected on the short term. On the longer term, an improved sensitivity may be desirable. Strategies towards this end include increasing the Raman cross-section of the peptide substrate and improving the substrate accessibility by using spacer layers. Also, currently close to 90% of the gold-bound peptides are in a location that negligibly contributes to the total SERS signal. A redesign of the SERS platform or clever labeling tricks as to only have peptides in the SERS hotspots will further increase the sensitivity. With regard to the detection of serine proteases like caspase-1 in a reductive environment, further studies on the peptide monolayer stability are required. Self-assembled PEG-alkanethiol are most promising, but the hexapeptide CCALNN could provide a more easily synthesized alternative. In short, a large set of experimental work is to be done before arriving at the targeted applications like single-cell analysis or protease inhibitor screening. However, the currently available data provides solid proof of the measurement principle. I strongly believe in the potential of this method as a generic protease-activity sensor.

Towards a lab-on-a-chip for SERS-based protease activity screening. The ongoing technological developments on integrated SiN photonic components, together with a strongly increased sensitivity of waveguide-based SERS sensing will enable fully integrated and parallelized SERS experiments on a single chip. Meanwhile, further research may lead to a more sensitive measurement of protease-activity. In my opinion, an extremely promising long-term perspective of this work is to combine both technologies on a single device for a high-throughput, multiplexed analysis of protease activity on consumable chips, schematically illustrated in figure 7.2. Here, multiple waveguides will allow for a parallel readout, while

each waveguide can be functionalized with several peptides for a multiplexed detection of protease activity. Given the low pump power required for waveguide-based SERS (less than 100 μW), a standard 10 mW continuous wave laser could readily allow exciting hundreds of parallel channels. Furthermore, a simultaneous acquisition of 100 spectra on a 2 dimensional CCD or CMOS camera should be feasible by collecting a separate spectrum on each line of the camera as described by Palonpon et al. [5].

These goals are ambitious but not unrealistic within the combined expertise of the VIB-UGent-imec collaboration that was established during this PhD.

(a)

(b)
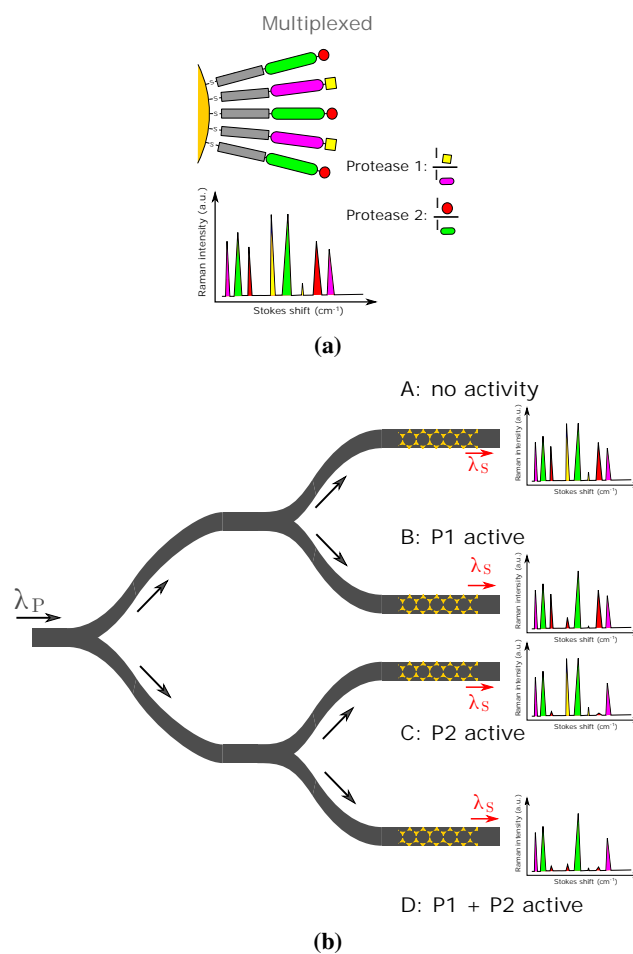
Figure 7.2 Towards an integrated photonics platform for multiplex, parallelized protease detection. (a) Illustration of a multiplexed detection of two peptides. (b) Top view of a possible chip-layout of a waveguide-based, 4-channel SERS measurement. Each channel provides a multiplexed detection of the activity of two proteases (P1 and P2).

References

[1] Jiaqi Li, Chang Chen, Hilde Jans, Xiumei Xu, Niels Verellen, Ingrid Vos, Yasuaki Okumura, Victor V. Moshchalkov, Liesbet Lagae, and Pol Van Dorpe *300 mm Wafer-Level , Ultra-Dense Arrays of Au- Capped Nanopillars with sub-10 nm Gaps as Reliable SERS Substrates* Nanoscale, 6:12391–96, 2014.

[2] Hsin-Yu Wu and Brian T Cunningham *Point-of-care detection and real-time monitoring of intravenously delivered drugs via tubing with an integrated SERS sensor.* Nanoscale, pages 5162–5171, 2014.

[3] Frédéric Peyskens, Ashim Dhakal, Pol Van Dorpe, Nicolas Le Thomas, and Roel Baets *Surface Enhanced Raman Spectroscopy Using a Single Mode Nanophotonic-Plasmonic Platform* ACS Photonics, 3(1):102–108, 2016.

[4] F Peyskens, A Dhakal, P Van Dorpe, N Le Thomas, and R Baets *Surface Enhanced Raman Spectroscopy on Single Mode Nanophotonic-Plasmonic Waveguides* CLEO 2016, 1:3–4, 2016.

[5] Almar F Palonpon, Jun Ando, Hiroyuki Yamakoshi, Kosuke Dodo, Mikiko Sodeoka, Satoshi Kawata, and Katsumasa Fujita *Raman and SERS microscopy for molecular imaging of live cells.* Nature protocols, 8(4):677–92, apr 2013.

A

RAMAN SPECTRA

All Raman spectra were excited with a 785 nm pump wavelength on a WITec Alpha 300R+ confocal Raman microscope. Unless mentioned otherwise, a 600 lpmm grating was used to disperse the Raman spectra onto the CCD camera, resulting in a spectral resolution of approximately 1.5 cm^{-1}.

A.1 Molecules and Materials
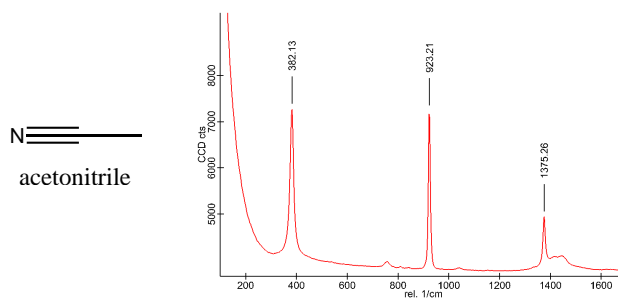
Figure A.1 Acetonitrile
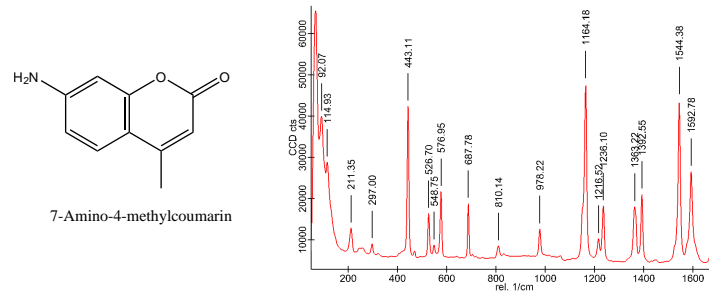
Figure A.2 Amino-methylcoumarine (AMC or amc)
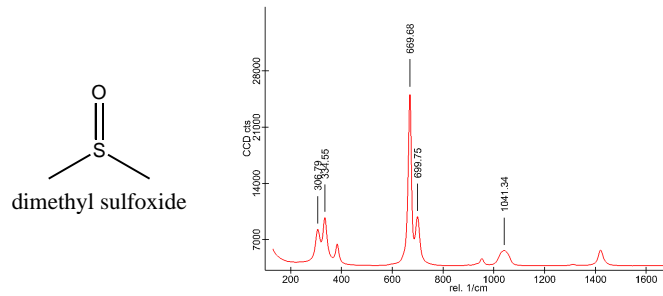
Figure A.3 Dimethyl sulfoxide (DSMO).
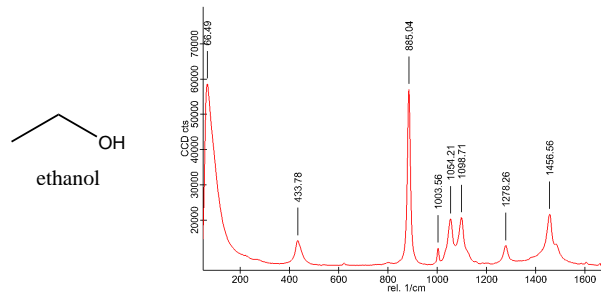
Figure A.4 Ethanol (eOH)
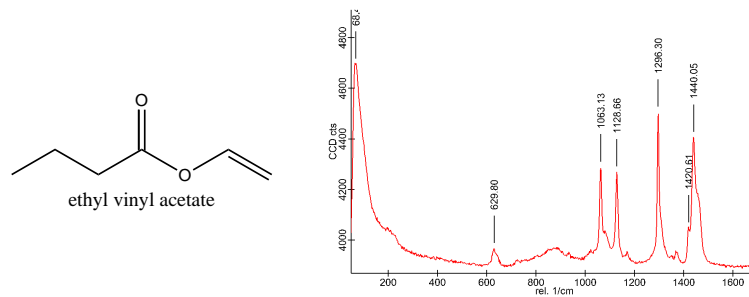
Figure A.5 Ethyl vinyl acetate (EVA, material of 96-well plate sealing mats)
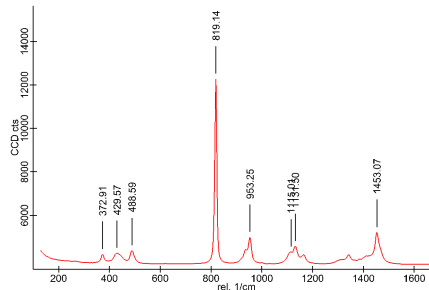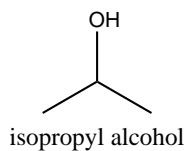
Figure A.6 Isopropyl alcohol (IPA)
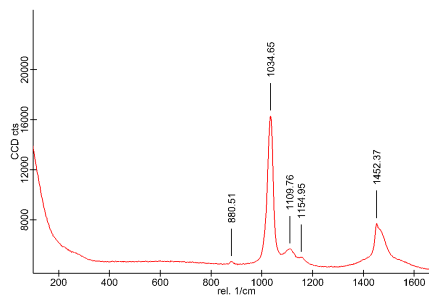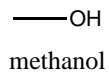
Figure A.7 Methanol (mOH)
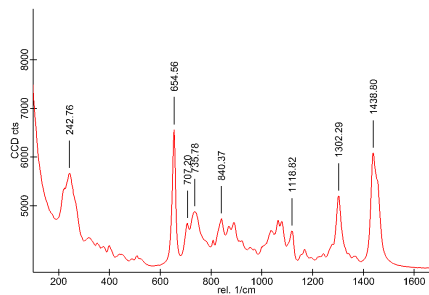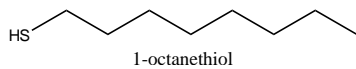
Figure A.8 1-Octanethiol
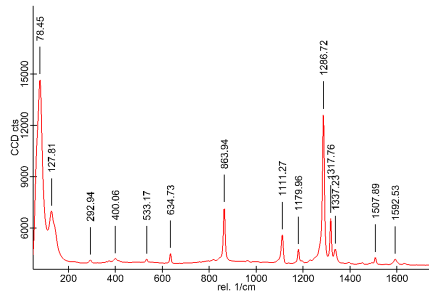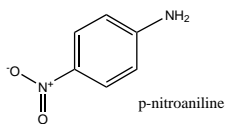
Figure A.9 p-Nitroaniline (pNA)
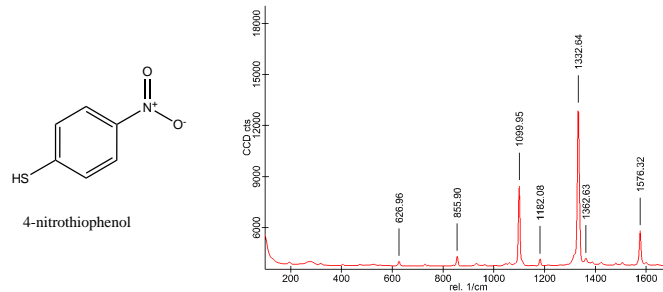
Figure A.10 para-Nitrothiophenol (pNTP) in powderous form.
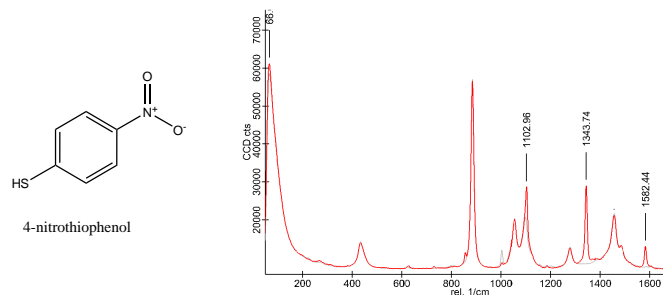
Figure A.11 100 mM p-Nitrothiophenol in ethanol. The light grey curve represents a pure ethanol spectrum, only NTP peaks are indicated. Note that the peak position deviates slightly from solid pNTP.
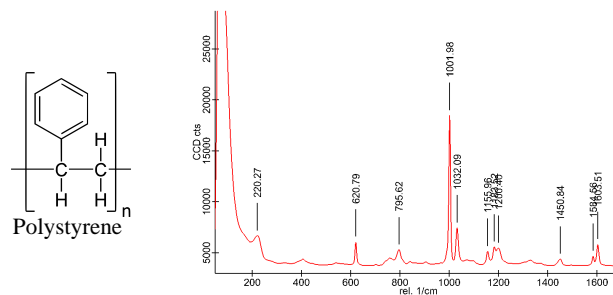
Figure A.12 Polystyrene. The aromatic ring is identical to the one in Phe, resulting in a similar fingerprint
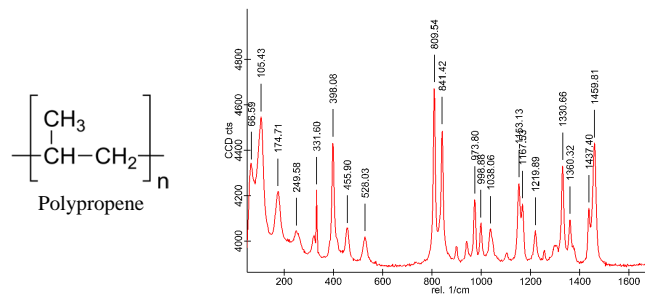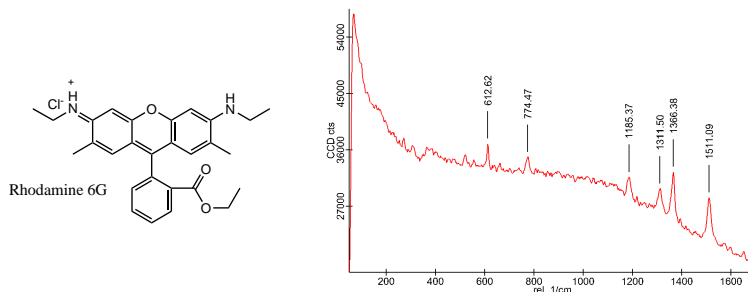

Figure A.13 Polypropylene (PP)

Figure A.14 10 mM Rhodamine 6G (R6G) in water. Notice the fluorescent background.
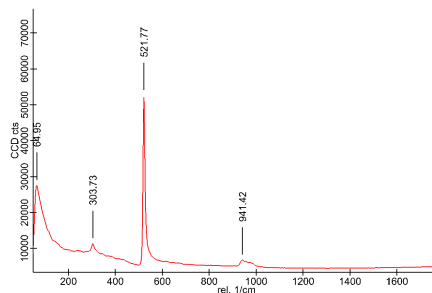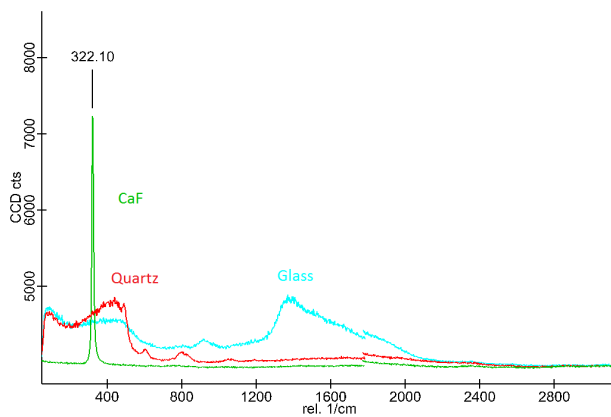

Figure A.15 Silicon (Si)

Figure A.16 Raman background spectra of typical microscope slides. The extremely low background of CaF_2 makes it a superior substrate for many Raman applications. (*The discontinuity around 1700 cm^{-1} is due to a grating shift*).
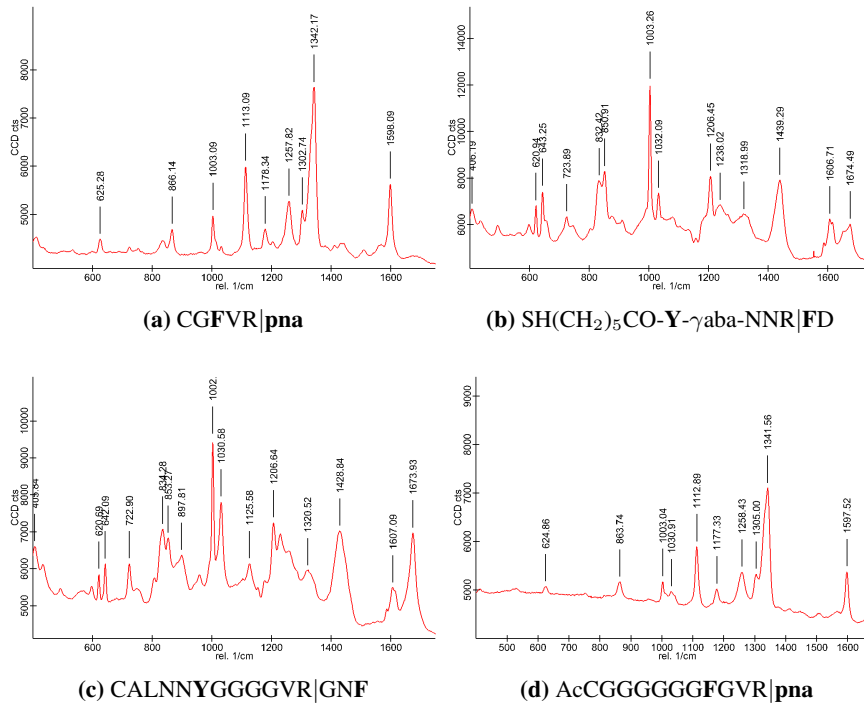
A.2   Peptide substrates

(a) CGFVR|**pna**

(b) SH(CH$_2$)$_5$CO-**Y**-γaba-NNR|**F**D

(c) CALNN**Y**GGGGVR|GN**F**

(d) Ac**C**GGGGGG**F**GVR|**pna**

Figure A.17 Raman spectra of lyophilized trypsin substrates.

(a) SH(CH$_2$)$_5$CO-**Y**-γaba-NNE|**S**WD

(b) CALNN**Y**GGGGNNE|**S**WH
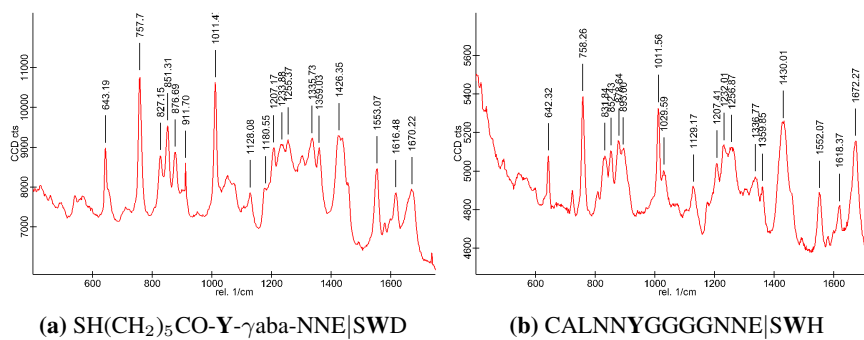
Figure A.18 Raman spectra of lyophilized endoproteinase Glu-C substrates.

(a) **Y**VAD| GC (300 lpmm)

(b) **Y**VAD|**G**FC (300 lpmm)

(c) **Y**VAD|**G**F-PEG-AlkThiol (300 lpmm)

(d) C**F**GGGGG**Y**VAD|**amc**

(e) SH.(CH$_2$)$_5$CO-**F**-γaba-**Y**VAD|**amc**

(f) YVAD|**amc**
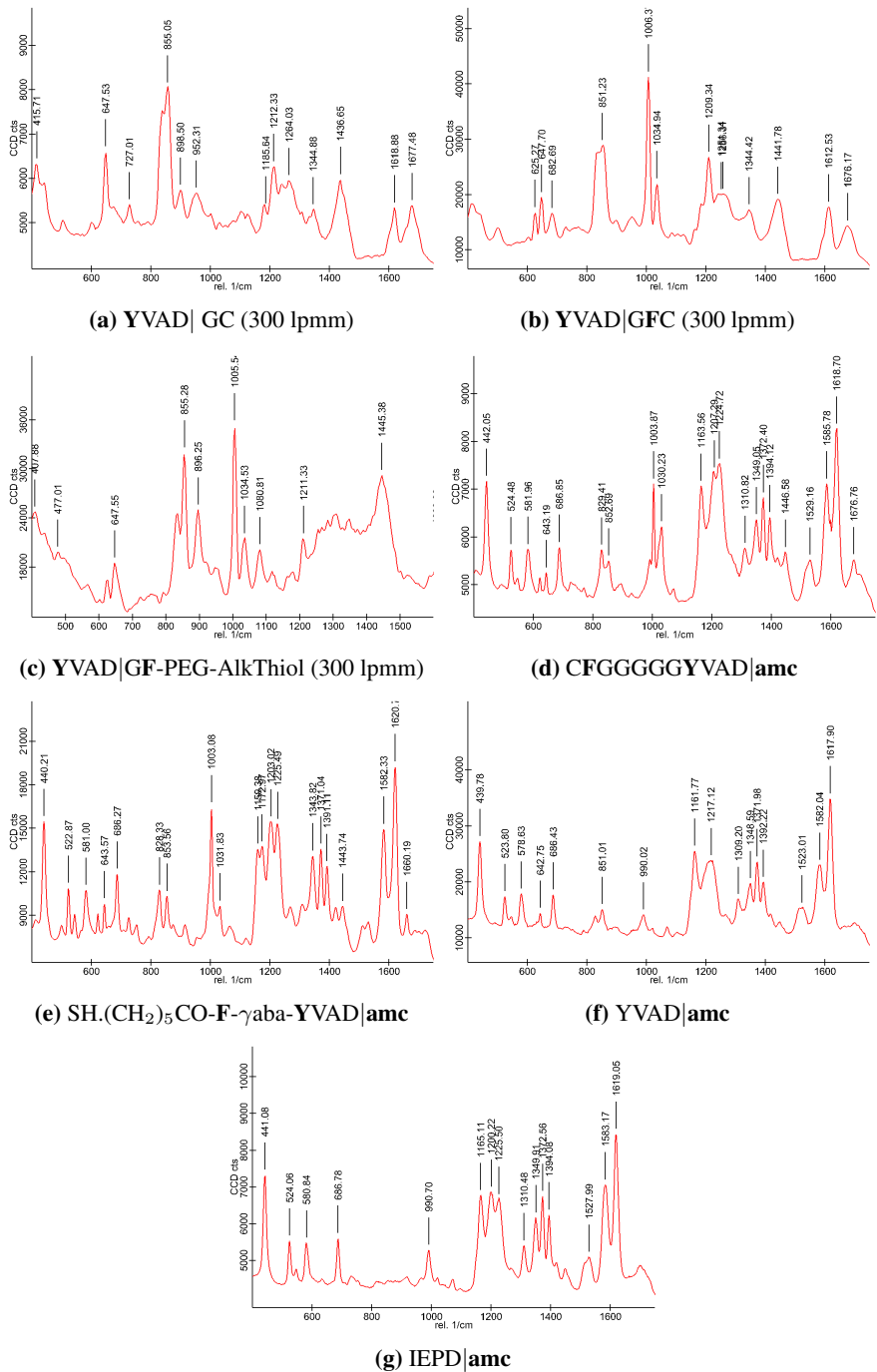
(g) IEPD|**amc**

Figure A.19 Raman spectra of lyophilized caspase-1 substrates. (a-e) Custom made peptides for functionalizing gold surfaces. (f-g) Commercial substrates for fluorescent assays.
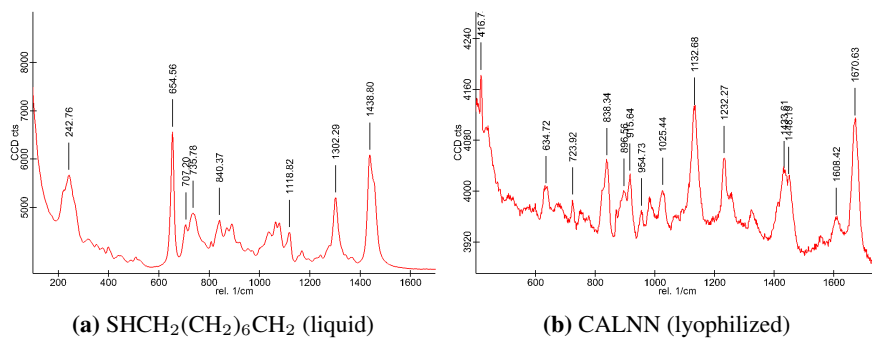
(a) SHCH$_2$(CH$_2$)$_6$CH$_2$ (liquid)   (b) CALNN (lyophilized)

Figure A.20 Raman spectra of lyophylized matrix molecules.